GEOLOGIC SETTING OF LISTWANITE, ATLIN, B.C.: IMPLICATIONS FOR CARBON DIOXIDE SEQUESTRATION AND LODE-GOLD MINERALIZATION

by

LYLE D. HANSEN

B.Sc., The University of Alberta, 2000

A THESIS SUBMITTED IN PARTIAL FULFILMENT OF THE REQUIREMENTS FOR THE DEGREE OF

MASTER OF SCIENCE

in

THE FACULTY OF GRADUATE STUDIES

Geological Sciences

THE UNIVERSITY OF BRITISH COLUMBIA

MAY 2005

ABSTRACT

Listwanite (carbonated-serpentinite), commonly associated with high-grade lode-gold mineralization, binds large quantities of the greenhouse gas carbon dioxide (CO_2). At Atlin, B.C., listwanite distribution is controlled by a basal thrust fault and regional joint/fracture system with four steeply dipping sets. Carbonation proceeded via three sub-reactions fossilized as spatially distinct mineralogical zones. The index minerals, magnesite, talc and quartz, record three metamorphic isograds defining the magnesite-, talc- and quartz-zones. This same overall mineralogical transformation is under consideration for industrial sequestration of CO_2 in a process referred to as mineral carbonation. The carbonate-alteration reactions were isochemical in terms of major non-volatile chemical species, except where quartz-carbonate veining and/or Cr-muscovite are present in areas of intense carbonation (indicating Si^{2+}, Mg^{2+} and K^{+} metasomatism). The progressive destruction of magnetite during listwanite-alteration allowed for the use of a magnetic susceptibility meter in recording reaction progress and helped delineate subtle variations in reaction progress that might otherwise have gone unnoticed in the field.

Although magnesite-zone alteration only accounts for about 5% - 15% of the total carbonation potential for serpentinite, it is widespread and may represent a significant portion of the total bound CO_2. Moreover, the progression of the talc-zone appears to generate fracture permeability. The first two reactions combined can fix approximately half the total carbon sequestration potential for serpentinite with a small associated increase in the volume of solids. The quartz-zone is limited to highly carbonated areas and may be limited in extent due to a large associated gain in solid volume that may act to seal permeability. The first two reaction steps therefore hold the most promise for *in situ* mineral carbonation and could be preferentially driven by controlling the input fluid composition.

Anomalously high gold values are associated with organic hydrocarbons in talc-magnesite rock and depleted $\delta^{13}C$ (ca. -6‰) in carbonate. This combined with $\delta^{18}O$ values of 7‰ to 16‰ for carbonate is consistent with hydrothermal fluids circulating through and scavenging gold from organic-bearing metasedimentary rocks. Alteration is contemporaneous with the nearby Fourth of July Batholith (ca. 170 Ma), which may have

provided a heat source for hydrocarbon maturation and large-scale hydrothermal convection.

TABLE OF CONTENTS

ABSTRACT ii
TABLE OF CONTENTS iv
LIST OF TABLES vii
LIST OF FIGURES viii
LIST OF ABBREVIATIONS xii
LIST OF SYMBOLS xiii
PREFACE xvii
ACKNOWLEDGMENTS xix
CHAPTER I: OVERVIEW 1
1.1 OVERVIEW 1
1.2 REFERENCES 5
CHAPTER II: GEOLOGIC SETTING OF LISTWANITE (CARBONATED-SERPENTINITE) AT ATLIN, BRITISH COLUMBIA: A GEOLOGIC ANALOGUE TO CARBON DIOXIDE SEQUESTRATION 7
2.1 INTRODUCTION 7
2.2 REGIONAL GEOLOGY AND FIELD METHODS 8
2.3 ULTRAMAFIC ROCKS 12
2.4 LISTWANITE 15
2.5 LISTWANITE PETROGRAPHY, GEOCHEMISTRY AND REACTION PATHS 20
2.6 IGNEOUS INTRUSIONS 22
2.7 MAGNETIC PROPERTIES 22
2.8 IMPLICATIONS FOR CO_2 SEQUESTRATION 23
2.8 IMPLICATIONS FOR LODE-GOLD MINERALIZATION 25
2.9 REFERENCES 27
CHAPTER III: STRUCTURAL SETTING, TIMING AND ISOTOPIC CHARACTER OF LISTWANITE (CARBONATED-SERPENTINITE), ATLIN, BRITISH COLUMBIA: IMPLICATIONS FOR LODE-GOLD MINERALIZATION 33

3.1 INTRODUCTION 33
3.2 REGIONAL GEOLOGY AND ROCK UNITS 34
3.3 STRUCTURAL ANALYSIS 36
3.3.1 PRE- TO SYN-OBDUCTION STRUCTURAL ELEMENTS 36
3.3.2 POST-OBDUCTION STRUCTURAL ELEMENTS 41
3.4 IGNEOUS INTRUSIONS 44
3.5 TIMING AND SETTING OF LISTWANITE ALTERATION 50
3.6 ALTERATION ENVIRONMENT 54
3.7 STABLE ISOTOPES 56
3.8 HYDROTHERMAL ORGANIC MATERIAL 60
3.9 SOURCE OF GOLD AND CARBON 60
3.10 CONCLUSIONS 64
3.11 REFERENCES 65
CHAPTER IV: CARBONATED SERPENTINITE (LISTWANITE) ATLIN, BRITISH COLUMBIA: A GEOLOGIC ANALOGUE TO CARBON DIOXIDE SEQUESTRATION **70**
4.1 INTRODUCTION 70
4.2 RELEVANCE TO INDUSTRIAL APPLICATIONS 71
4.3 GEOLOGIC SETTING 72
4.4 STRUCTURAL CONTROL 74
4.5 MINERALOGICAL ZONATION AND REACTION SEQUENCE 74
4.6 GEOCHEMICAL CHANGE DURING LISTWANITIZATION 81
4.7 MAGNETIC SUSCEPTIBILITY 84
4.8 VOLUME STRAIN ACCOMPANYING REACTION 90
4.9 IMPLICATIONS FOR CO_2 SEQUESTRATION 90
4.10 REFERENCES 96
CHAPTER V: MASS BALANCE AND MODELING **102**
5.1 INTRODUCTION 102
5.2 PROTOLITH AND ALTERATION ASSEMBLAGES 106
5.3 ANALYTICAL METHODS 107
5.4 STANDARD ERROR AND WHOLE ROCK GEOCHEMISTRY 107

5.5 DIMENSIONAL ANALYSIS 110
5.6 MASS BALANCE 118
5.7 RESULTS 127
5.8 IMPLICATIONS 132
5.9 COMPARISON TO GRESEN'S ANALYSIS 133
5.10 CONCLUSIONS 133
5.11 REFERENCES 135
CHAPTER VI: CONCLUSIONS **137**
6.1 CONCLUSIONS 137
6.2 REFERENCES 139
APPENDIX A: MISCELLANEOUS TABLES FOR CHAPTER IV **140**
APPENDIX B: MINERALOGY **147**
APPENDIX C: GEOCHEMICAL, STABLE ISOTOPE ANALYSES AND GOLD ASSAY DATA **153**
APPENDIX D: GEOCHRONOLOGIC DATA **163**
APPENDIX E: PROCEDURES AND MISCELLANEOUS INFORMATION **181**
APPENDIX F: SAMPLE LOCATIONS **188**
GEOLOGICAL MAP ..... **insert**

LIST OF TABLES

CHAPTER II

Table 2.1: Mineralogy of carbonated serpentinite from Atlin, B.C. **18**

Table 2.2: Volume changes **24**

CHAPTER III

Table 3.1: Geochronologic data from Atlin area **51**

Table 3.2: Stable isotopic data from various listwanite systems **58**

CHAPTER IV

Table 4.1: Mineralogy of carbonated serpentinite from Atlin, B.C. **76**

Table 4.2: Volume changes **91**

CHAPTER V

Table 5.1: Geochemical analyses of replicates **108**

Table 5.2: Representative geochemical analyses of ultramafic rocks from Atlin, B.C. **109**

Table 5.3: Lowest rank from datasets using unweighted SVD **114**

Table 5.4: Lowest rank from datasets using weighted SVD **114**

Table 5.5: Lowest rank from datasets using iterative weighted SVD **117**

Table 5.6: Lowest rank of each group using each SVD technique at 3σ **119**

LIST OF FIGURES

CHAPTER I

Figure 1.1: Location map of Atlin, B.C. **2**

CHAPTER II

Figure 2.1: Bedrock map of the Atlin area **9**

Figure 2.2: Composite image, detailed geologic, magnetic susceptibility, and calculated CO_2 maps of a 2 m by 2 m area containing fracture-controlled zones of listwanite **10**

Figure 2.3: Aeromagnetic map of the Atlin area **11**

Figure 2.4: Outcrop and transmitted light images of the harzburgite and serpentinite units **13**

Figure 2.5: Equal area stereonet plots of the harzburgite and bastite foliation and magnetite-serpentinite and quartz carbonate veins **14**

Figure 2.6: a) Fracture-controlled listwanite. b) Basal décollement-controlled listwanite and post-alteration dikes **16**

Figure 2.7: Areal view and geological map showing recessive-weathering lineaments **19**

Figure 2.8: Simplified flow chart illustrating reaction path for listwanite **21**

CHAPTER III

Figure 3.1: Bedrock map of the Atlin area **35**

Figure 3.2: Stereonet plots and imagery illustrating the orientations of the S_0 and S_1 structural fabrics **37**

Figure 3.3: Stereonet plots and images illustrating the orientation of the S_2 structural fabric **38**

Figure 3.4: Areal view and geological map showing recessive-weathering lineaments **39**

Figure 3.5: Photomicrograph of sheared serpentinite showing reverse sense of shear **40**

Figure 3.6: Stereonet plot and image showing four joint and fracture orientations controlling listwanite **42**

Figure 3.7: Stereonets plots illustrating orientations of the regional joint and fracture system **43**

Figure 3.8: Stereonet plot and images showing serpentine-magnesite veins **45**

Figure 3.9: Stereonet plot and image showing quartz-carbonate veins **46**

Figure 3.10: Image of bladed carbonate in listwanite **47**

Figure 3.11: Map of 10 m by 10 m area and stereonet plot of quartz-carbonate veins contained within the same map area **48**

Figure 3.12: Total alkali vs. SiO_2 (TAS) plot of dike samples **49**

Figure 3.13: Simplified flow chart illustrating the geological history of the Atlin area **52**

Figure 3.14: Schematic block diagram illustrating the structural controls of listwanite and dikes **55**

Figure 3.15: $\delta^{18}O$ - $\delta^{13}C$ plot of isotopic data from carbonate in listwanite **57**

Figure 3.16: Composite image and detailed geologic maps of a 2 m by 2 m area containing fracture-controlled zones of listwanite **59**

Figure 3.17: Images of organic matter from Atlin and Nahlin fault localities .. **61**

Figure 3.18: Plots of Au assay results, CO_2 content, and $\delta^{13}C$ **62**

CHAPTER IV

Figure 4.1: Simplified geological map of the Atlin area **73**

Figure 4.2: Simplified flow chart illustrating reaction path for listwanite **77**

Figure 4.3: Back-scattered scanning electron microscope images showing minerals formed during progressive listwanite alteration **78**

Figure 4.4: Ternary phase and fluid H_2O - CO_2 activity diagrams of the listwanite system **80**

Figure 4.5: Wt% MgO - SiO_2 circle diagrams **82**

Figure 4.6: Ratio of residual error to standard error in whole rock geochemistry of carbonated samples **85**

Figure 4.7: Plot of magnetic susceptibility and whole rock CO_2 content **87**

Figure 4.8: Composite image, detailed geologic, magnetic susceptibility, and calculated CO_2 maps of a 2 m by 2 m area containing fracture-controlled zones of listwanite **88**

Figure 4.9: Measured and calculated wt% CO_2 across transect A-B from Figure 2.2b **89**

Figure 4.10: Relationship of fracture permeability in advance of a reaction undergoing a gain in the volume of solids **92**

Figure 4.11: H_2O - CO_2 fluid diagram at 250 bars and 60°C **95**

CHAPTER V

Figure 5.1: Simplified flow chart illustrating reaction path for listwanite **103**

Figure 5.2: Wt% MgO - SiO_2 circle diagrams and ternary diagram of listwanite system **104**

Figure 5.3: SVD solutions to a hypothetical two dimensional dataset using weighted and unweighted techniques **112**

Figure 5.4: SVD solutions to a hypothetical two dimensional dataset using weighted and weighted-iterative techniques **115**

Figure 5.5: Residual over analytical error calculated using an unconstrained system of equations and a MgO - SiO_2 diagram of the protolith, altered rock data and model protoliths calculated using unconstrained system of equations **121**

Figure 5.6: Residual over analytical error calculated using a constrained system of equations **124**

Figure 5.7: Mass factor vs. wt% CO_2 diagram and MgO - SiO_2 diagram of the protolith, altered rock data and model protolith calculated using the constrained system of equations **125**

Figure 5.8: Mass factor vs. wt% CO_2 diagram and MgO - SiO_2 diagram of the protolith, altered rock data and model protolith calculated using the constrained-weighted system of equations **128**

Figure 5.9: Residual over analytical error calculated using constrained and weighted system of equations **129**

Figure 5.10: Residual over analytical error calculated using constrained and weighted system of equations for rank reduced datasets **131**

Figure 5.11: Plots of a) mass factor and wt% CO_2 and b) residual over analytical error calculated using Gresens' analysis and the model protoliths calculated using the constrained-weighted system of equation **134**

LIST OF ABBREVIATIONS

AAC – Atlin Accretionary Complex

AOA – Atlin Ophiolitic Assemblage

FOJB – Fourth of July Batholith

GPS – Global positioning system

PCIGR – Pacific Centre for Isotopic and Geochemical Research

ppm – Parts per million

ppb – Parts per billion

SVD – Singular value decomposition

TIMS – Thermal ionization mass spectrometry

VPDB – Vienna Pee Dee Belemnite

VSMOW – Vienna Standard Mean Ocean Water

XRD – X-ray diffractometer

XRF – X-ray fluorescence

LIST OF SYMBOLS

Wt% – Weight percent oxide

NAD 83 – North American Datum 83

S_0 – Compositional layering within the harzburgite unit

S_1 – Fabric defined by flattened and stretched orthopyroxene crystals within harzburgite unit

S_2 – Fabric defined by sheared and stretched bastite (serpentinized orthopyroxene) within the serpentinite unit.

R_1, R_2, R_3 – Denotes reactions 1 to 3 (Chapter II and IV)

R_A, R_B – Denotes reactions A to B (Chapter IV)

A_1, A_2, A_3, A_4 – Denotes mineral assemblages 1 to 4 (Chapters II and IV)

L_a, L_b, L_c, L_d – Denotes the four main steeply-dipping listwanite zone trends

M_1, M_2, M_3 – Denotes the generation of magnesite produced during each of the three listwanite carbonation reactions (R_1 to R_3 respectively)

ΔVs^* (rxn) – Change in volume of solid material of the reaction in question

ΔVs (rock) – Change in volume of solid material of a rock

σ – One standard deviation

d/l – Detection limit

proto – Protolith

min – Minimum

max – Maximum

Ma – million years

MINERALS

Atg – Antigorite

Brc – Brucite

Cal – Calcite

Chl – Chlorite

Chr – Chromite

Dol – Dolomite

En_{90} – Orthopyroxene (90% enstatite end member)

Fo_{90} – Olivine (90% forsterite end member)

Liz – Lizardite

Mgs – Magnesite

Mgt – Magnetite

Ol – Olivine

Opx – Orthopyroxene

Qtz – Quartz

Srp – Serpentine

Tlc – Talc

SYMBOLS USED IN CHAPTER V

A, b, Aeq, beq, C, d – The constrained linear system of equations

Alt – Altered Sample

Alt_{wt}^{proto} – *Alt* weighted by the covariance matrix of the 46 samples of the protolith group.

Co – Coefficient

cov_{err} – Covariance matrix defined by replicate analyses

cov_{proto} – Covariance matrix defined by the protolith group of samples

e – Number of elements in the dataset

E – Denotes an element

ll – Lower limit of an element defined by the protolith group

ll^{wt} – Lower limit of an element defined by the protolith group weighted by the covariance matrix of the 46 samples of the protolith group

m – Denotes an element

mf – Mass factor

MP – Model Protolith

MP_{wt}^{proto} – Model protolith weighted by the covariance matrix of the 46 samples of the protolith group.

n – Denotes a sample

P – Matrix of the basis vectors of the protolith group

P_{wt}^{proto} – *P* weighted by the covariance matrix of the 46 samples of the protolith group

pu – Upper limit placed on the protolith composition

pu_{wt}^{proto} – Weighted upper limit placed on the protolith composition

pl – Lower limit placed on the protolith composition

pl_{wt}^{proto} – Weighted lower limit placed on the protolith composition

R – Rank of a matrix

s – Number of samples in a dataset

S – Matrix representing a dataset

S_{wt}^{err} – Matrix S weighted by cov_{err}

$Sapprox$ – SVD approximation of S

$Sapprox_{wt}^{err}$ – SVD approximation of S_{wt}^{err}

$Sapprox*$ – Approximation of a modified $Sapprox$ or $Sapprox_{wt}^{err}$ matrix

$Serr$ – Vector containing the standard errors of the dataset

ul – Upper limit of an element defined by the protolith group

ul^{wt} – Upper limit of an element defined by the protolith group weighted by the covariance matrix of the 46 samples of the protolith group

$unwt_{err}$ – Matrix to unweighted data weighted by cov_{err}

wt_{err} – Matrix to weight a dataset by cov_{err}

wt_{proto} – Matrix to weight a dataset by cov_{proto}

x – Contains the coefficients Co that when multiplied with P gives a 'best fit' to Alt

z – Number of basis vectors in P

σ^{proto} – Covariance between two elements in the protolith group of samples

σ^{err} – Covariance between the analyses of two elements

PREFACE

This thesis is composed of four body chapters, two of which have been published and two of which are in preparation for publication. Chapter II is published as a Current Research paper through the Geological Survey of Canada and is entitled "Geological Setting of Listwanite (Carbonated Serpentinite) at Atlin, British Columbia: Implications for CO_2 Sequestration and Lode-gold Mineralization." This paper summarizes the geology including the geological units, an incomplete listing of structural elements and geophysical properties discovered or used during the first season of geological mapping and sampling. This paper was co-authored by Dr. Bob Anderson and Dr. Gregory Dipple who helped revise the manuscript and provided support and expertise in the field and Kyoko Nakano who provided field and laborator y assistance. Chapter III is unpublished and elaborates on the first paper in describing the structural controls, timing and origin of altering fluids and discusses potential scenarios for the anomalous gold contents detected in the Atlin listwanite. The U-Pb (zircon) analysis, $^{40}Ar/^{39}Ar$ analyses, and stable isotope analyses for carbonate were performed by Richard Friedman, Thomas Ullrich and Janet Gabites respectively. Chapter IV is published in The Canadian Mineralogist and is entitled "Carbonated Serpentinite (listwanite) at Atlin, British Columbia: A Geological Analogue to Carbon Dioxide Sequestration." It describes the metamorphic reactions, geochemistry and petrology of the alteration assemblages in detail. It was co-authored by Dr. Gregory Dipple who supervised and aided in revisions, Dr. Terry Gordon who provided the geochemical mass balance calculations and Dawn Kllett who, for her undergraduate Honours thesis at the University of British Columbia, examined mineral assemblages and magnetic susceptibility of alteration. My subsequent analysis substantially revised and refined the mineral assemblages. Chapter V outlines a new geochemical space-based mass balance technique. It is a simplified and altered version of Terry Gordon's geochemical mass balance technique and demonstrates that the listwanite alteration at Atlin was an isochemical process. The map in the insert is a published Geological Survey of Canada Open File map, which I produced and digitized with the help of Stephen Williams and Bob Anderson. The authorship, final or expected, is given at the beginning of each chapter, except for the Open File insert where the

authorship is given on the map. Dr. Greg Dipple and Dr. Bob Anderson secured the funding, and provided supervision, for this project.

ACKNOWLEDGEMENTS

This research was funded by a Natural Sciences and Engineering Council of Canada Discovery Grant, by the Oil, Gas and Energy Branch of Environment Canada, and by the Innovative Research Initiative for Greenhouse Gas Mitigation, a program under the Climate Change Action Plan 2000, and administered under Environment Canada and Natural Resources Canada, Earth Sciences Sector. It was conducted under the auspices of Activity 3a, "CO_2 Storage by Mineral Carbonation Reactions: Kinetic and Mechanical Insights from Natural Analogues" under the Earth Sciences Sector Climate Change Program, Project CC480, entitled "Monitoring methods and assessment of carbon sequestration over Canada's landmass."

I would like to thank Bill Reynen, Environment Canada, for encouraging the initiation of this project and Mitch Mihalynuk, British Columbia Geological Survey Branch, for his help and expertise at Atlin, including logistics, data sharing, and aerial photography. Carmel Lowe of the Pacific Geoscience Centre first suggested using magnetic susceptibility to map alteration. Kyoko Nakano provided invaluable field and laboratory assistance, and Sasha Wilson performed Raman analysis. Dawn Kellett is thanked for all her insightful ideas generated during her honours thesis studying the carbonated ultramafic bedrock at Atlin. I thank A. E. Williams-Jones, L. P. Baumgartner, D. Pattison and R. Martin for their insights and comments during the review process of Chapter IV. Stephen Williams of the Geological Survey of Canada at Vancouver provided expertise and help in digitizing my map. I have benefited greatly from Terry Gordon for his geochemical and mathematical expertise. James Scoates provided excellent feedback in the final review of my thesis. I would like to thank Bob Anderson of the Geological Survey of Canada at Vancouver for his invaluable contributions during the review process of much of this thesis and for his insight both at the office and in the field. Finally I would like to thank Greg Dipple for his insightful guidance over the last two and a half years and who took the chance at bring me to Vancouver and getting me involved in such an interesting project.

CHAPTER I: INTRODUCTION

1.1 INTRODUCTION

Listwanite (carbonated-serpentinite), (e.g. Ash, 2001; Hansen *et al.*, 2004; Chapter II) is commonly associated with high-grade lode-gold mineralization and binds large quantities of carbon dioxide, a greenhouse gas. It forms from the same overall mineral transformation proposed for mineral carbonation, an industrial form of CO_2 sequestration. The Mother Lode gold district in California (Wittkopp, 1983) and the Abitibi greenstone belt of the Superior Province of Canada (Schandl and Naldrett, 1992) are two of the most well known examples of mesothermal listwanite-associated lode-gold in North America. In general, the richest gold grades within these deposits are associated with, or in close proximity to carbonate-altered ultramafic rocks (e.g. Ash 2001). Significant debate exists over the role ultramafic rocks and their carbonate-altered equivalents play in lode-gold mineralization. Additionally, the artificial alteration of serpentine and olivine to carbonate, a process known as mineral carbonation, has the potential to fix vast quantities of anthropogenic carbon dioxide (CO_2), a greenhouse gas that has been implicated in global warming (Seifritz, 1990). Globally, mineral carbonation offers virtually unlimited capacity and the promise of safe, permanent storage of CO_2, with little risk of accidental release (Guthrie *et al.*, 2001).

The objectives of this thesis are to document the mineral transformations, geochemical alteration, structural relationships, timing, environmental conditions and stable isotopic signatures for the listwanite alteration at Atlin, British Columbia (Fig. 1.1). Results of this study have resulted in a much better understanding of listwanite-systems in general and have spawned numerous ideas for optimizing *in situ* mineral carbonation systems where CO_2 is directly injected into an ultramafic body or aquifer. This study has also resulted in a better understanding of the development of the high-grade gold lodes associated with listwanite systems.

Chapter II, a previously published paper with the Geological Survey of Canada, highlights the geologic setting, geological units, geophysical properties and structural controls of the listwanite deposits at Atlin. This setting is elaborated in Chapter III,

Figure 1.1: Location of Atlin and the Atlin map area (NTS 104N), northwestern British Columbia. Main rivers are shown in blue and main highways in black.

which presents a detailed structural analysis, detailed geological history, and stable isotopic study highlighting the possible fluid flow patterns and a discussion on the possible origins for the lode-gold mineralization.

Chapters II and III have identified that in addition to the basal thrust fault (Ash, 1994) there exists a regional joint/fracture system with four steeply-dipping fracture sets that control the spatial distribution of listwanite. Gold is not only associated with zones of intense listwanite alteration (e.g. Ash, 2001), but also with organic material. Stable isotopic evidence and petrography have detected an organic signature of carbonate within the listwanite and indicate that the fluids have likely interacted with metasedimentary rock material. Gold may have been mobilized by hydrogen sulphide complexes, derived from organic material and redeposited in areas of intense carbonate alteration. Magnetite stability is strongly influenced by serpentinization (magnetite-producing) and listwanite alteration (magnetite-destroying). This allowed for the employment of a magnetic susceptibility metre as an aid to mapping serpentinized or carbonated fractures.

Chapter IV, a previously published paper in Canadian Mineralogist, discusses the petrology, mineralogical transformations and geochemical alteration based on a limited dataset of 23 samples. Here it was described how listwanite alteration proceeded via three sub-reactions fossilized spatially into distinct mineralogical zones. The first appearance of the index minerals, magnesite, talc and quartz define three metamorphic isograds and the magnesite-, talc- and quartz-zones. The three reactions were carbonation- (de)hydration reactions, were isochemical with respect to non-volatile chemical species, and were controlled by the CO_2 content of the infiltrating fluid. The magnesite- and talc-zone reactions are likely the most suitable for the development of *in situ* mineral carbonation injection systems because of their small associated gain in solid volume and the potential development of permeability caused by fracturing as the talc-zone reaction progresses.

Chapter V supplements Chapter IV in introducing a new geochemical mass balance technique, based on the work of Gordon (2003). This technique was applied to a larger dataset of 160 samples. The novelty of this approach is that it calculates a model protolith for each altered sample that is constrained within a defined chemical space. Results strongly suggest that, with the exception of intensely altered rocks, listwanite

alteration at Atlin occurred without the modification of the major non-volatile component of the rocks. A handful of samples that have undergone complete to near-complete carbonate alteration contain extensive quartz-carbonate veining and Cr-muscovite is present in hand sample and indicates limited Si^{2+}, Mg^{2+} and K^{+} metasomatism.

1.2: REFERENCES

Ash, C. H. (1994): Origin and Tectonic Setting of Ophiolitic Ultramafic and Related Rocks in the Atlin Area, British Columbia (NTS 104N); B.C. Ministry of Energy, Mines and Petroleum Resources, Bulletin 94, 48 p.

Ash, C. H. (2001): Relationship Between Ophiolites and Gold-Quartz Veins in the North American Cordillera; British Columbia Department of Energy, Mines and Petroleum Resources, Bulletin 108, 140 p.

Gordon, T.M. (2003): Algebraic Generalization of the Graphical Gresens and Pearce Methods for Identification of Geochemical Mass-Transfer Processes. (abstract), Vancouver 2003 Abstracts, CD-ROM, GAC-MAC-SEG, Vancouver 2003 Annual General Meeting, Vancouver, B.C., 28-146, ISSN 0701-8738, ISBN: 0-919216-86-2.

Guthrie, G. D., Carey, J. W., Bergfeld, D., Byer, D., Chipera, S., Ziock, H. and Lackner, K. S. (2001). Geochemical Aspects of the Carbonation of Magnesium Silicates in an Aqueous Medium. Proceedings of the First National Conference on Carbon Sequestration, May 14-17, 2001, Washington, DC, session 6C, 14 pages.

Hansen, L. D., Dipple, G. M., Anderson, R. G. and Nakano, K. F. (2004): Geologic Setting of Carbonate Metasomatised Serpentinite (Listwanite) at Atlin, British Columbia: Implications for CO_2 Sequestration and Lode-Gold Mineralization. in Current Research, Geological Survey of Canada, Paper 2004-A5, 12 pages.

Schandl, E. S. and Naldrett, A. J. (1992): CO_2 Metasomatism of Serpentinites, South of Timmins, Ontario; Canadian Mineralogist, v. 30, p. 93-108.

Seifritz, W. (1990): CO_2 Disposal by Means of Silicates. Nature, 345, 486.

Wittkopp, R. W. (1983): Hypothesis for the Localization of Gold in Quartz Veins, Allegheny District. California Geology, 36-6, 123-127.

CHAPTER II: GEOLOGICAL SETTING OF LISTWANITE (CARBONATED SERPENTINITE) AT ATLIN, BRITISH COLUMBIA: IMPLICATIONS FOR CO_2 SEQUESTRATION AND LODE-GOLD MINERALIZATION[1]

2.1 INTRODUCTION

Listwanite forms from the reaction of ultramafic rocks with carbon dioxide (CO_2)-bearing fluid. It is also a natural analogue to the geologic sequestration of the greenhouse gas CO_2 by mineral carbonation. Mineral carbonation reactions bind CO_2 within carbonate minerals by reaction with Mg^{2+} derived from serpentine and olivine. Globally, mineral carbonation offers virtually unlimited capacity and the promise of safe, permanent storage of CO_2 (Guthrie *et al.*, 2001). *In situ* mineral carbonation, the direct injection of CO_2 into large subsurface ultramafic formations, allows for reaction times of tens to hundreds of years (Guthrie *et al.*, 2001). Historically, listwanite is also known for its spatial association with lode-gold mineralization (e.g. Wittkopp, 1983; Schandl and Naldrett, 1992; Ash, 2001). Our goal in studying listwanite is to document reaction environments, pathways, catalysts and reaction mechanics and uncover fluid flow patterns and evidence for gold mobility. This information will aid in the development of *in situ* mineral carbonation systems and refine listwanite lode-gold deposit models.

Here we document the structural controls, mineral reactions, geochemical alteration, and permeability system that accompanied listwanite formation near Atlin, located in northwestern British Columbia. Evidence for carbonation, indicated by Mg-carbonate minerals, is present for metres to tens of metres into wallrock adjacent to controlling fractures. Our field mapping and sampling show that listwanite occurs primarily along the basal décollement of an allochthonous ultramafic body and a transecting joint- and fracture-system. Listwanite-alteration and serpentinization both affect magnetite stability. As a consequence, magnetic susceptibility was successfully tested as a tool to map the degree of serpentinization and carbonation reaction.

[1] A version of this chapter has been published as: Hansen, L.D., Anderson, R.G., Dipple, G.M. and Nakano, K. (2004): Geological Setting of Listwanite (Carbonated Serpentinite) at Atlin, British Columbia: Implications for CO_2 Sequestration and Lode-gold Mineralization, Geological Survey of Canada, Current Research, 2004-A5, 12 p.

2.2 REGIONAL GEOLOGY AND FIELD METHODS

The Atlin Ultramafic Allochthon (Ash and Arksey, 1990a) was first mapped by Aitken (1959) as an ultramafic intrusion. Ash and Arksey (1990a) reinterpreted the rocks as the tectonically emplaced residual upper mantle section of oceanic lithosphere. The ultramafic rocks, combined with associated oceanic rocks, including metabasalt and pelagic sedimentary rocks and mafic to ultramafic cumulates, form an assemblage of fault-bounded and dismembered, but geologically related, sub-units. The Atlin Ophiolitic Assemblage (Ash and Arksey, 1990a) includes the ultramafic and mafic rocks, whereas the sedimentary accretionary rocks comprise the Atlin Accretionary Complex (Ash and Arksey, 1990a). Both were obducted onto the Stikine and Cache Creek terranes during Early to Middle-Jurassic amalgamation and accretion. This study focuses on the listwanite occurrences within the ultramafic section. Previous geological work around Atlin is described by Aitken (1959), Monger (1975, 1977a, b), Monger *et al.* (1978), Bloodgood *et al.* (1989), Mihalynuk *et al.* (1992), Ash and Arksey (1990a, b), Ash *et al.* (1991) and Ash (1994, 2001).

Geochemical and other studies of the Atlin listwanite include: detailed petrography and geochemistry (Kellett, 2002; Hansen *et al.*, 2003a, b, 2005; Chapter IV); mineralogical and geochemical studies of lode-gold prospects around the Atlin camp (Lueck, 1985; Newton, 1985); a fluid inclusion study (Andrew, 1985); mineral chemistry of the principal minerals in the harzburgite (Ash, 1994); and ^{40}Ar-^{39}Ar and K-Ar geochronological ages of Cr-muscovite (Ash, 2001) interpreted as cooling ages related to Middle Jurassic batholiths.

The map of Ash (1994) was the basis for choosing the study area and the foundation for the 1:6000 scale mapping of the listwanite within the Atlin Ultramafic Allochthon (Fig. 2.1). The nature and geometry of the structural zones were mapped at 1:20 scale from a well-preserved listwanite zone on the west flank of Monarch Mountain (Fig. 2.2). All mapping was aided by an aeromagnetic map (Fig. 2.3), a magnetic susceptibility meter and standard GPS techniques. All locations are given as UTM eastings and northings using the 1983 North American Datum (NAD 83).

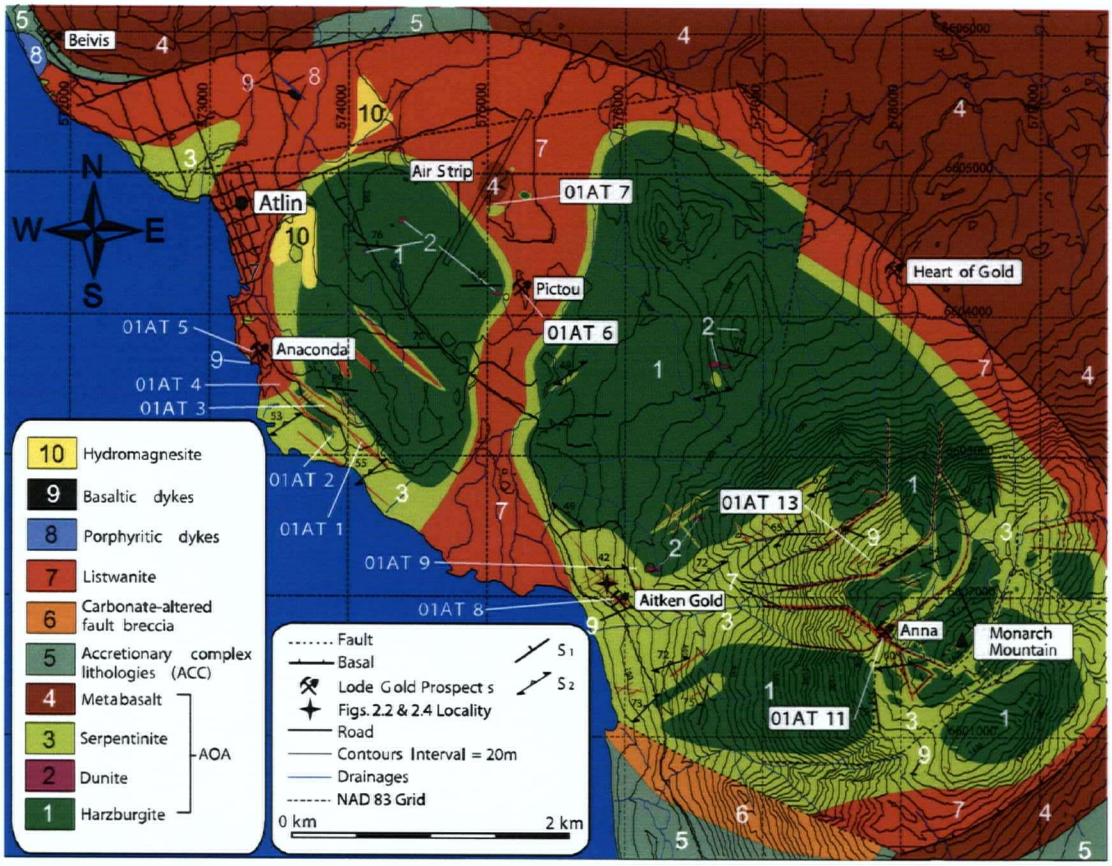

Figure 2.1: Simplified geologic map of the study area showing the distribution of listwanite near Atlin area (this paper; Hansen *et al.*, 2003b; Ash, 1994). AOA and AAC are Atlin Ophiolitic Assemblage and Atlin Accretionary Complex, respectively, of Ash and Arksey (1990a). Sample locations are denoted 01AT XX.

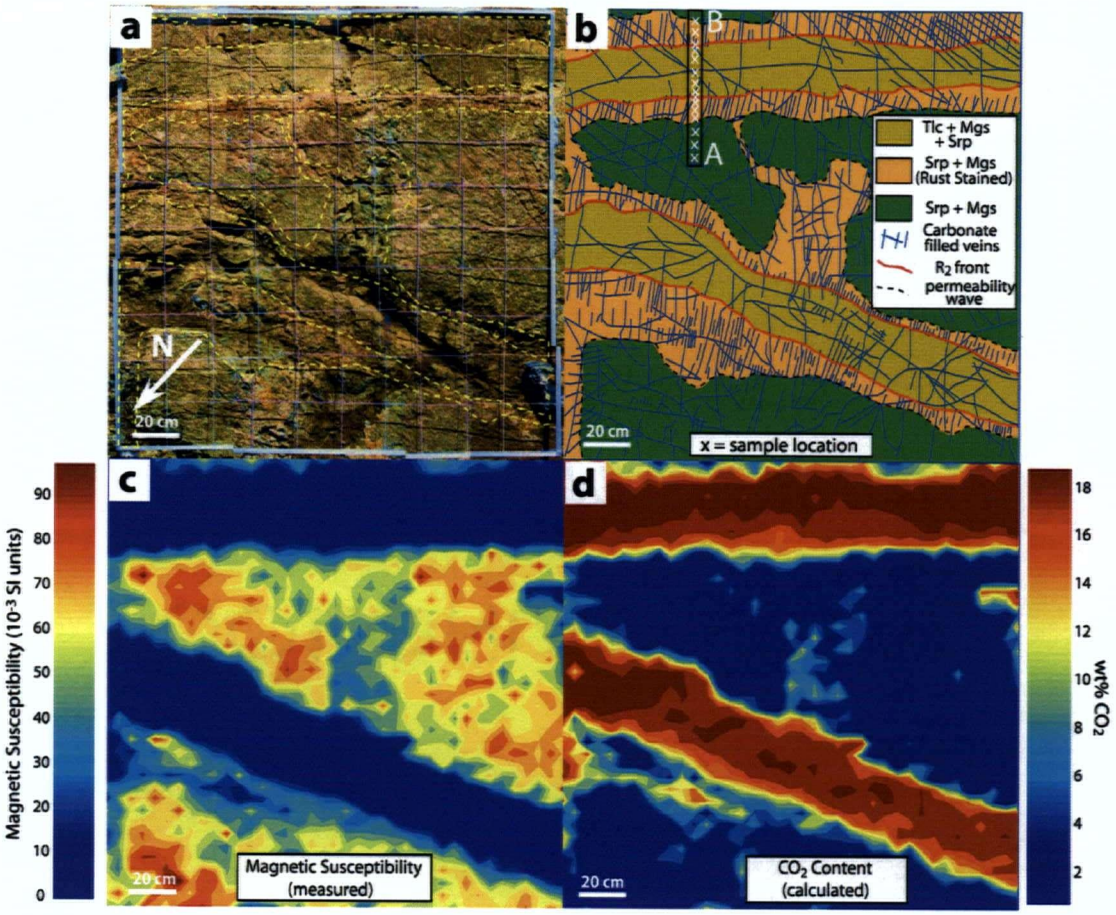

Figure 2.2: a) Composite image of a 2 by 2 metre pavement outcropping on the western slope of Monarch Mountain (E 575887, N 6602098, NAD 83). Dashed yellow lines are contacts in Figure 2.2b. b) Detailed geologic map of the listwanite zone mapped at 1:20 scale. Sample locations and section A-B correspond to those of Figure 3.7. c) Magnetic susceptibility map composed of ca. 1550 measurements, showing the correlation of magnetic susceptibility with map units in Figure 2.2b. d) Whole rock Wt% CO_2 map calculated using Eq_1 following Hansen *et al.* (2005), Chapter IV.

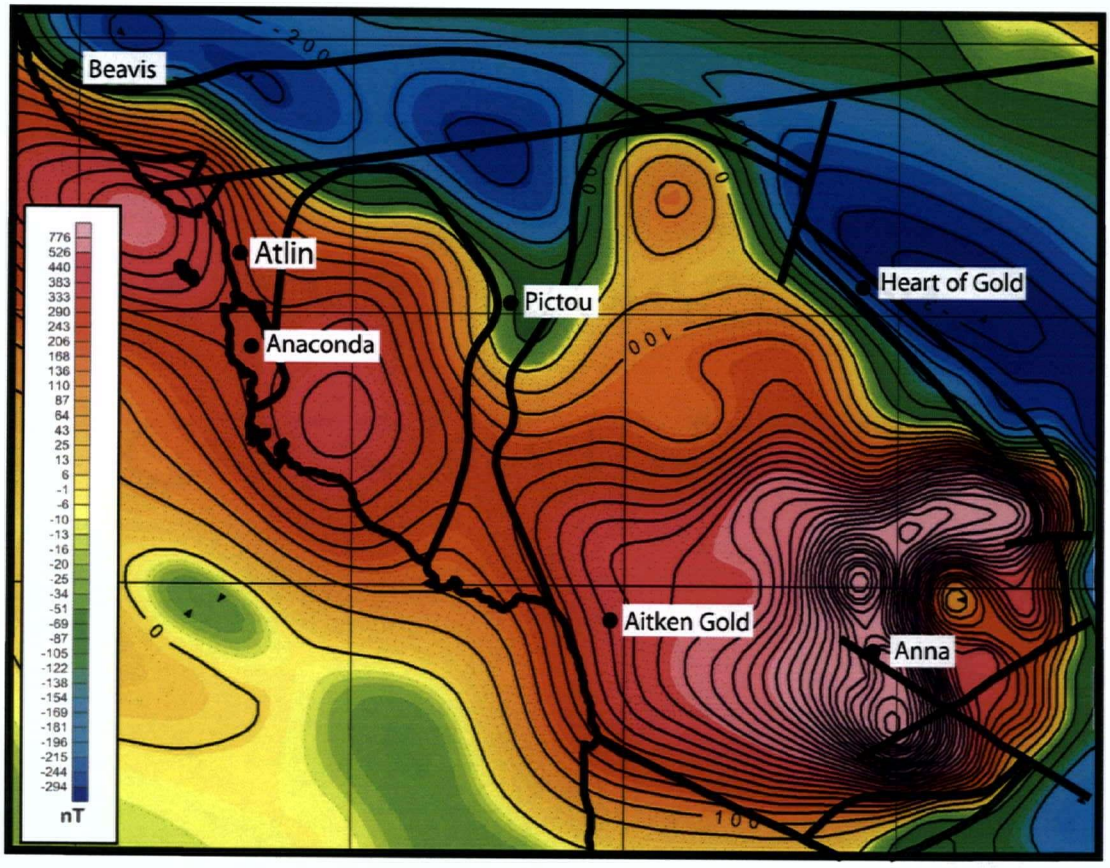

Figure 2.3: Aeromagnetic map of the study area and contacts to the main geological units in Figure 2.1. Aeromagnetic lows correspond to known zones of listwanite. Aeromagnetic data acquired from the National Geophysical Data Base and is maintained by the Geological Survey of Canada. Image generated by C. Lowe (GSC-Pacific).

2.3 ULTRAMAFIC ROCKS

The Atlin Ultramafic Allochthon, composed of serpentinized harzburgite, underlies an area of about 25 km^2 (Fig. 2.1) and comprises variably serpentinized, carbonitized and deformed harzburgite with minor dunite lenses and pyroxenite veins. It is a tectonic klippe, separated from the Atlin Accretionary Complex lithologies by a basal décollement termed the Monarch Mountain Thrust Fault (Ash and Arksey, 1990a). Serpentinization is most intensely developed near the basal décollement and adjacent to joints and fractures that crosscut the body (Fig. 2.1). The serpentine minerals are dominantly antigorite +/- minor chrysotile that occurs within fractures. The harzburgitic ultramafic rocks are divided into two units based on the degree of serpentinization.

The harzburgite unit includes all weakly- to moderately-serpentinized harzburgite (Fig. 2.4a, b). The freshest harzburgite is located at the west-central section on the plateau of Monarch Mountain where serpentine is <30 volume percent (Fig. 2.4b). It is characteristically studded with 5-40 volume percent resistant red-brown orthopyroxene grains (2-10 mm in diameter), commonly pseudomorphed by serpentine, within a recessive dun-brown weathering, partially serpentinized olivine matrix. This unit forms rounded and jointed outcrops. Fresh surfaces are dark green with the orthopyroxene crystals distinguished by their vitreous luster and cleavage. Compositional layering (S_0) is defined by alternating 1 to 10 cm orthopyroxene-rich and -poor layers. Flattening of orthopyroxene grains defines a weakly to moderately developed planar S_1 tectonite fabric (Fig 2.5a) and parallels S_0 where present together.

The serpentinite unit is intensely to completely serpentinized harzburgite (Fig. 2.4c, d). The contact is gradational, commonly making it difficult to differentiate serpentinite from harzburgite. The weathering colour of serpentinite is variable grey to near black, green, and blue. Lichen-free surfaces are spotted due to the presence of dark bastite after orthopyroxene. Commonly a well-developed S_2 fabric, oriented 244° / 54° NW (Figs. 2.4c, 2.5b), is developed and defined by flattened and sheared bastite spots (serpentinized orthopyroxene). Relict orthopyroxene is mantled by bastite. The best examples of serpentinite occur along the lower west flank of Monarch Mountain, where

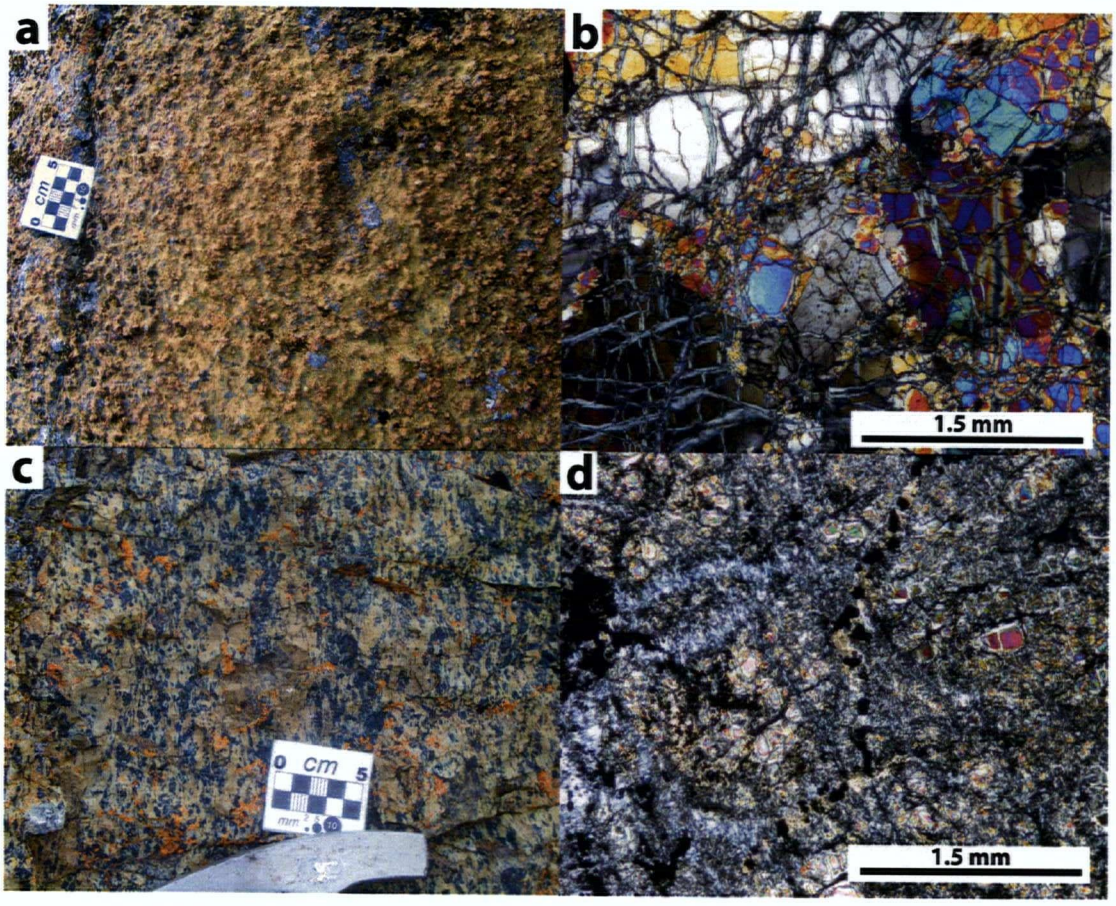

Figure 2.4: a) Resistant orthopyroxene within recessive, partially serpentinized olivine matrix; typical of weakly serpentinized harzburgite. b) Photomicrograph of freshest harzburgite under cross-polars. c) Moderately foliated serpentinite defined by the flattening of bastite spots. d) Photomicrograph of typical serpentinite under cross-polars.

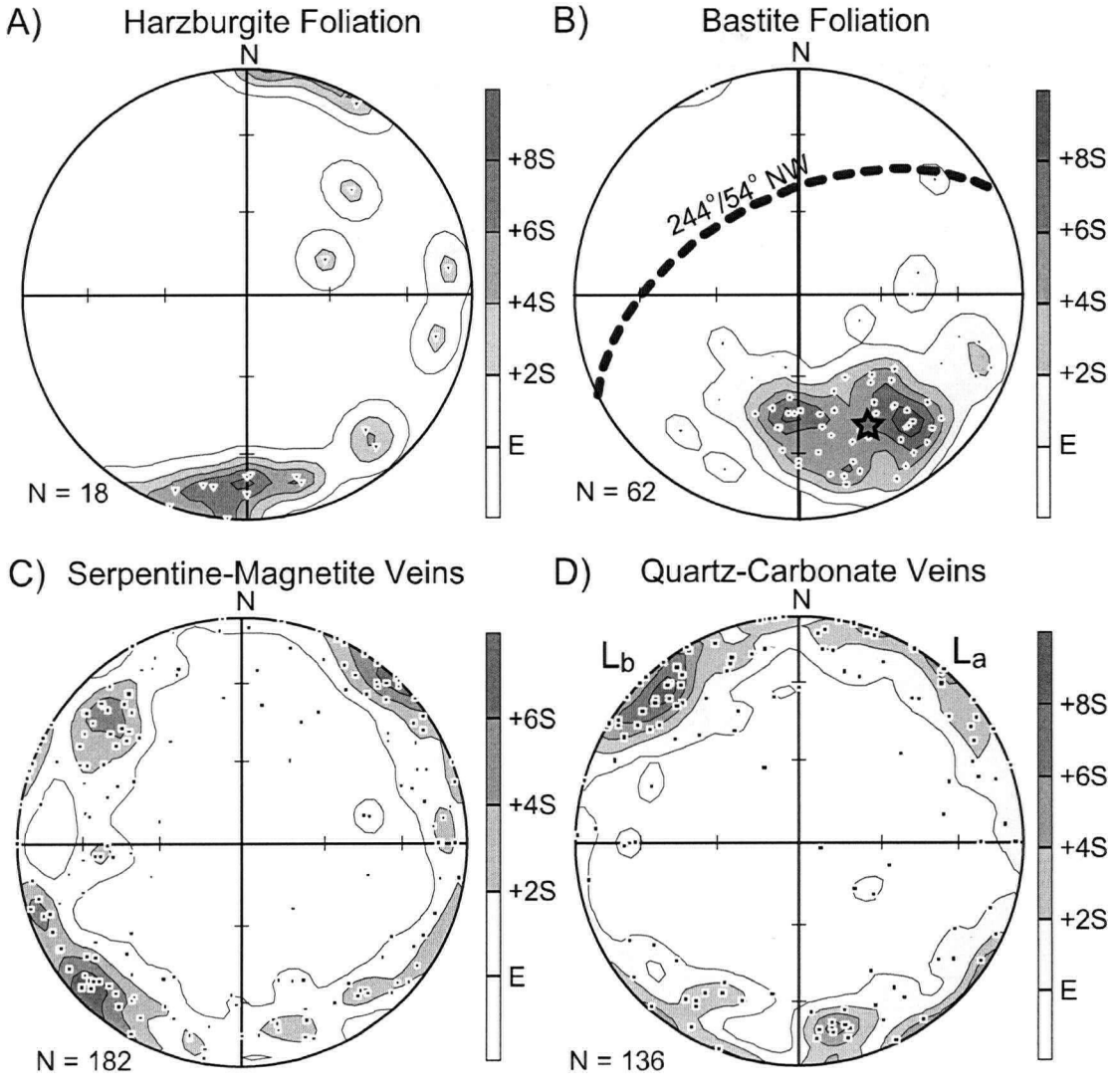

Figure 2.5: Structural data (poles to planes on equal area stereonets) of: a) Harzburgite foliation (S_1) defined by flattening of orthopyroxene grains; b) Bastite foliation (S_2) defined by flattened and sheared bastite spots. Great circle represents the average foliation; c) Magnetite-serpentine veinlets; d) quartz-carbonate veins associated with high-grade listwanite.

the bastite foliation is common, and on the lake shore north of Atlin where well-polished rocks have a spotted green and dark blue texture.

Dunite lenses and pyroxenite veins, commonly too small to show in Figure 2.1, make up a small proportion of the map area. The lenses within the Atlin Ultramafic Allochthon range from less than 1 m to about 100 m in length and form smooth 'dun' brown weathering outcrops. Dunite is commonly highly fractured forming rubble within outcrops of more resistant harzburgite. The long axes of the lenses occur within the planar S_1 fabric of the harzburgite. Pyroxenite veins are generally 1 to 5 cm thick and generally are concordant with the S_1 foliation fabric. However, they are often isoclinally folded and cut by later pyroxenite veins indicating they were emplaced pre- to post-deformation (Ash, 1994). The axial surfaces of the isoclinal folds parallel the tectonite fabric of the harzburgite.

The orientation of the S_2 fabric, mullion structures reported by Ash and Arksey (1990a) and southeasterly striking geological units to the south and to the east of the map area (Ash, 1994) suggest shortening along an northwest-southeast axis with "thrusting" to southeast (Ash and Arksey, 1990a). To the northwest, there is an area of geologic units striking northwest; listwanite controlling joints and fractures are dominantly oriented parallel to these two directions.

2.4 LISTWANITE

Listwanite in Russian and Eastern European literature (e.g. Rose, 1837; Ploshko, 1963; Kashkai and Allakhverdiev, 1965; Halls and Zhao, 1995) is a term used to describe distinctive, rusty-red weathering quartz-carbonate-chromium muscovite rocks produced during the carbonate-alteration of ultramafic rocks. Listwanite and other mineral assemblages produced during the same carbonation process as listwanite are termed listwanite series assemblages and are akin to the rocks of this study (Fig. 2.6). In North America, listwanite is more broadly defined as; "a carbonitized and variably silicified serpentinite, occurring as dikes in ophiolite complexes" (Jackson, 1997). Unfortunately this definition is inappropriate for use at Atlin because it implies metasomatism which has been discounted at Atlin (Hansen *et al.*, 2003a, b, 2005; Chapters IV, V). Furthermore, listwanite-alteration is a multi-step process (Hansen *et al.*, 2005; Chapter

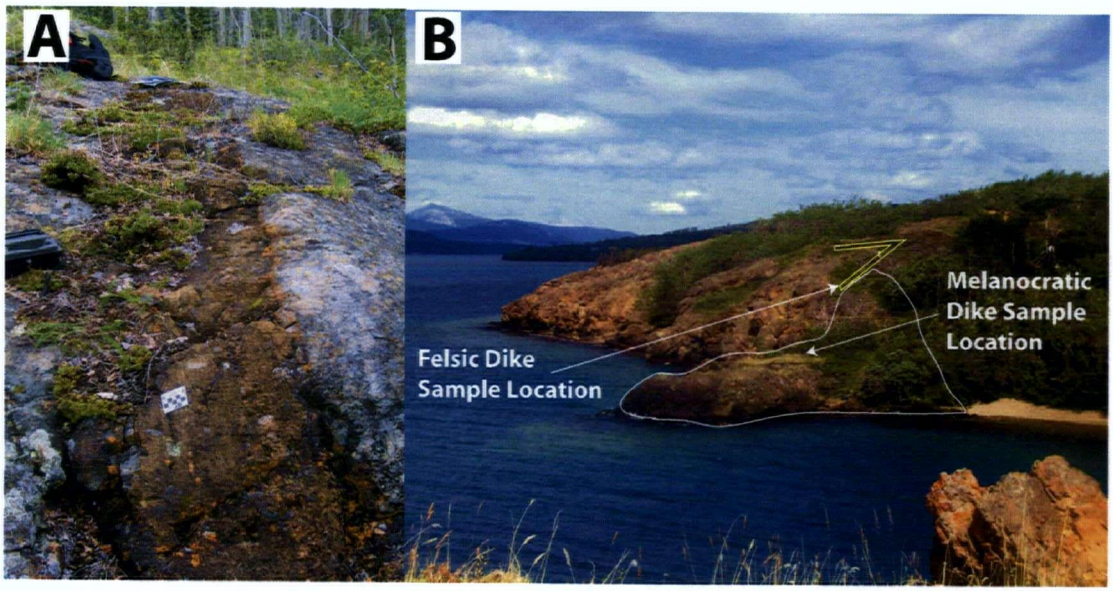

Figure 2.6: a) View to northwest of well-preserved, rusty-brown, talc-magnesite listwanite zone (L_b) which is about 50 cm thick. Scale = 5 cm. b) View to the north of a large area of distinctive rusty red listwanite associated with the basal décollement (below water) along eastern shore of Atlin Lake. The small peninsula in the centre of the image is underlain by a melanocratic basaltic dike. Evergreen tree just to the left of the centre of the photograph is approximately 8 metres tall.

IV) and intermediate mineral assemblages do not contain quartz (Table 2.1). The other common North American term "silica carbonate alteration", used to describe these deposits, is also not suitable for the same reasons. Consequently, our usage of listwanite refers to any carbonate-altered serpentinite. Halls and Zhao (1995) discuss listwanite terminology in greater detail.

At Atlin, listwanite occurs along the shallowly-dipping lower boundary of the Atlin Ultramafic Allochthon (Figs. 2.1 and 2.6b). Any brecciation appears to predate listwanite-alteration. Listwanite is also common along steeply-dipping joints and fractures dominantly trending about 140° (L_a trend) and 50° (L_b trend) (Figs. 2.1, 2.5d, 2.6a). Fracture-controlled listwanite is generally expressed as lineament depressions, commonly vegetated and filled with overburden. Rusty-red weathering side walls confirm they are underlain by listwanite. The lineament and listwanite association is clearly seen at the head of the Monarch Mountain hiking trail on Warm Bay road (Fig. 2.7).

Within the harzburgite unit, the margins of surface lineaments are commonly marked by chalky blue-green weathering serpentine alteration suggesting that they mark structural weaknesses that acted to focus fluids. The serpentinization along fractures is overprinted by listwanite. Small serpentine-magnetite veinlets, usually less than 1 cm thick, cut harzburgite, dunite and serpentinite. Structural measurements indicate that the dominant orientations of the veinlets are collinear with lineament and listwanite trends (Fig. 2.5c, d).

Generally, L_a listwanite zones are fewer but more extensive, pervasively carbonated and contain more stockwork quartz-carbonate veins and Cr-muscovite than L_b zones. The highest concentration of L_a zones transects the map area, extending from about 700 m south of Atlin to the west side of Monarch Mountain, about 3 km southeast of town (Fig. 2.1). It may mark the locus of a broad fault or fracture zone. The Anna and Aitken gold prospects, the only showings in the map area clearly not associated with the basal décollement, are both associated with L_a-trending listwanite zones and Cr-muscovite. Subsequent mapping has defined two other trends and are described in detail in Chapter III.

Table 2.1: Mineralogy of carbonated serpentinite from Atlin, BC

Sample	Chr	Mgt	Brc	Ol	Srp	Mgs	Tlc	Qtz		CO_2 (wt%)
01AT-8-1	x	x			x				A_1	0.06
01AT-13-1	x	x			x				A_1	0.10
01AT-3-1	x	x	x		x				A_1	0.21
01AT-10-1	x	x	x	x	x				A_1	0.15
01AT-10-2	x	x	x	x	x	x[v]			A_1	0.26
01AT-2-2	x	x	x	x	x				A_1	0.33
01AT-9-1	x	x		x	x	x			R_1	2.10
01AT-11-1	x	x		x	x	x			R_1	2.57
01AT-1-9	x	x			x	x			A_2	3.37
01AT-6-3	x	x			x	x			A_2	4.00
01AT-1-8	x	x			x	x			A_2	4.60
01AT-13-2	x	x			x	x			A_2	7.12
01AT-11-2	x	x			x	x			A_2	9.60
01AT-7-3	x	x			x	x	x		R_2	3.40
01AT-1-7	x	x			x	x	x		R_2	7.19
01AT-1-6	x	x			x	x	x		R_2	9.54
01AT-9-2	x				x	x	x		R_2	17.26
01AT-7-1	x					x	x	x	R_3	21.83
01AT-5-4	x	x[y]				x	x	x	R_3	28.01
01AT-1-5	x	x[z]			x[w]	x	x	x	R_3	34.00
01AT-4-1*	x					x	x	x	R_3	34.34
01AT-5-2	x					x		x	A_4	35.20
01AT-6-1*	x					x		x	A_4	36.19

[v] only occurs in small veins
[w] occurs in small isolated patches
[y] armored relicts and late mantling of chromite and pyrite
[z] magnetite in late fractures and late mantling of chromite
* sample contains Cr-muscovite
Sample locations in Appendix F.

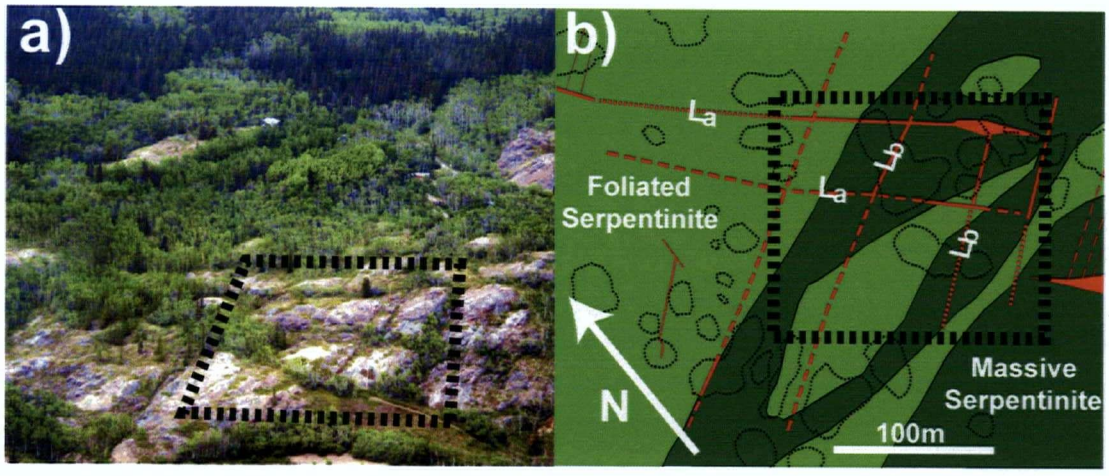

Figure 2.7: a) Aerial view to the northeast showing recessive weathering lineaments representing L_a and L_b orientations associated with listwanite at head of Monarch Mountain Hiking trail (photo by M. Mihalynuk, August 2003) (E 575900, N 6602100, NAD 83). b) Geologic map of the area in Figure 2.7a.

2.5 LISTWANITE PETROGRAPHY, GEOCHEMISTRY AND REACTION PATH

Listwanite at Atlin is zoned mineralogically outward from the controlling fracture permeability network and tracks the migration of three sequential and isochemical carbonation-(de)hydration reactions (Hansen *et al.*, 2005; Chapter IV). The most distal reaction (R_1) was detected geochemically and petrographically (Table 2.1) and involves the breakdown of olivine +/- brucite (assemblage A_1, Fig. 2.8) to magnesite-antigorite (A_2). The magnesite-antigorite rocks commonly resemble serpentinite (A_1) but in outcrop typically contain small carbonate veinlets. The low abundance of olivine in serpentinite (A_1) limits reaction R_1. Antigorite-magnesite grades into talc-magnesite (A_3) produced via reaction R_2. It is soft, has a waxy feel and commonly weathers to a distinctive smooth but irregular dark-red surface. Quartz plus magnesite (A_4) is present in completely carbonated areas that resulted from the carbonation of talc (R_3). The quartz-magnesite zone weathers to a rough orange-red surface. Minor chromite present in serpentinite survives all three reactions. The reactions (R) are:

$$34\ Mg_2SiO_4 + 20\ CO_2 + 31\ H_2O \rightarrow Mg_{48}Si_{34}O_{85}(OH)_{62} + 20\ MgCO_3 \qquad \mathbf{(R_1)}$$

Olivine → Antigorite + Magnesite

$$2\ Mg_{48}Si_{34}O_{85}(OH)_{62} + 45\ CO_2 \rightarrow 45\ MgCO_3 + 17\ Mg_3Si_4O_{10}(OH)_2 + 45\ H_2O \qquad \mathbf{(R_2)}$$

Antigorite → Magnesite + Talc

$$Mg_3Si4O_{10}(OH)_2 + 3\ CO_2 \rightarrow 3\ MgCO_3 + 4\ SiO_2 + H_2O \qquad \mathbf{(R_3)}$$

Talc → Magnesite + Quartz

Olivine is not present with talc and quartz does not occur with serpentine indicating the three reactions have occurred in sequence. The mineral zonation is therefore amenable to the mapping of metamorphic isograds: the magnesite, talc and quartz isograds indicate the first appearance of magnesite, talc and quartz, respectively. The highly altered cores of listwanite zones may contain stockwork quartz-carbonate veins, bright-green Cr-muscovite (mariposite, fuchsite), sulfide (mainly pyrite)

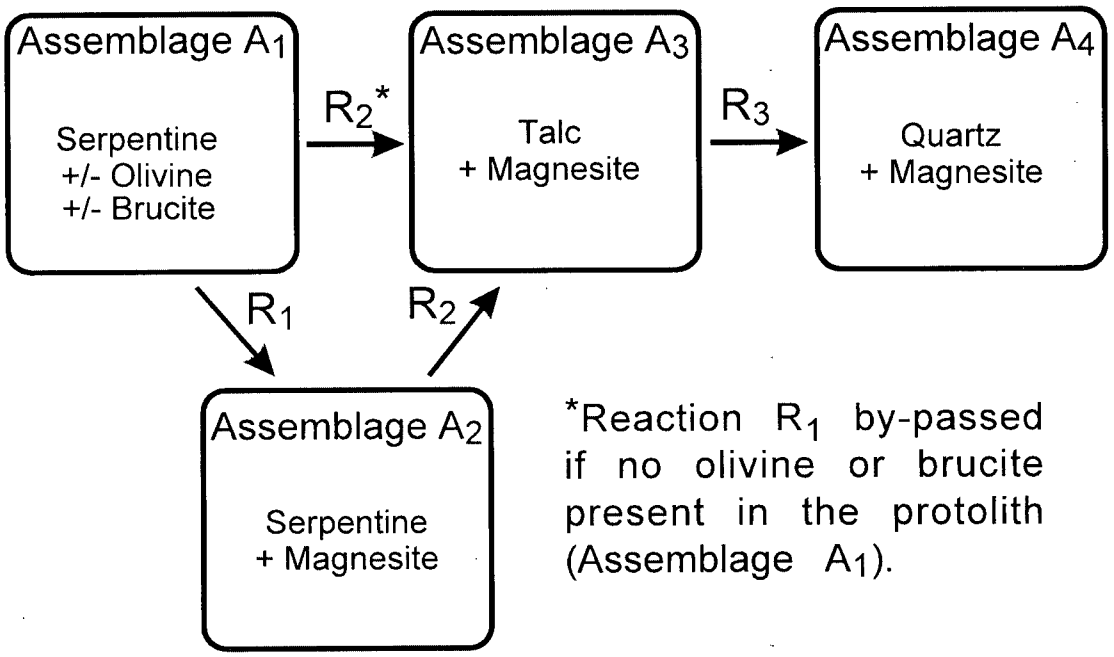

Figure 2.8: Simplified flow chart for the reaction path of the Atlin listwanite system during progressive carbonation of serpentinite. A detailed description of the reactions is provided in Hansen *et al.* (2005), Chapter IV.

mineralization and anomalous Au values (e.g Ash, 2001). Cr-muscovite results from limited chromite destruction and the addition of K^+. Though Ca^{2+} addition is common in listwanite systems (e.g. Aydal, 1990), our studies have been unable to detect it at Atlin.

2.6 IGNEOUS INTRUSIONS

At least three distinct phases of dikes are present in the map area. They include a melanocratic medium-grained hornblende diabase, a medium- to coarse-grained light-grey porphyritic feldspar-, quartz-dacite and a grey-brown porphyritic plagioclase-, K-feldspar-, biotite-, hornblende- and quartz- dacite. All contain sulfide minerals, mostly pyrite. Locally they are carbonated, but clearly cross-cut the listwanite. This cross-cutting relation is clearly seen about 500 m south of Atlin near the Anaconda lode-gold prospect (Fig. 2.5b). Xenoliths of listwanite occur within the mafic dike phase at this location. Dikes are commonly spatially associated with listwanite and surface lineaments. Regional crustal weaknesses have likely provided the same guides to magma ascent as they did for fluids associated with earlier episodes of serpentinization and listwanite generation. A U-Pb geochronological analysis of the light-grey dacite and a fresh ^{40}Ar-^{39}Ar geochronological biotite sample from the grey-brown phase, both of which crosscut listwanite, are reported in Chapter III. These two dates further constrain the age and duration of the listwanite genesis at Atlin and show a temporal correlation with the widespread Middle Jurassic plutonism in the area, potential sources of gold-rich fluid.

2.7 MAGNETIC PROPERTIES

Magnetite forms during the serpentinization of olivine and is destroyed during carbonate-alteration. During serpentinization, iron contained in harzburgitic (roughly Fo_{90}) olivine is preferentially excluded from serpentine resulting in the formation of magnetite (Toft *et al.*, 1990). Magnetite occurs as rim overgrowths on chromite and as disseminated grains aligned in foliation planes and in fractures. All increase the magnetic susceptibility of the serpentinite rocks. Magnetic susceptibility varies strongly between the harzburgite unit (2 to 50 (10^{-3} SI units)) and serpentinite unit (>50 to as high as 150

(10^{-3} SI units)). This observation is useful for differentiating between the two units in lichen-covered areas where the degree of serpentinization is not easily discernable.

Magnetite is progressively consumed during reaction R_2 (Hansen *et al.*, 2005; Chapter IV). The Fe derived from the breakdown of magnetite was accommodated in magnesite (Hansen *et al.* 2005; Chapter IV). Magnetic susceptibility is usually at the lower detection limit of a hand-held magnetic susceptibility meter ($1x10^{-5}$ SI units) in rock containing >20 wt% CO_2, corresponding to complete progress of reaction R_2. A magnetic susceptibility contour map, including ca. 1550 magnetic susceptibility measurements from the detailed mapping area of a L_b listwanite zone, illustrates the association of magnetic susceptibility with mineralogy (Fig. 2.2c). Following Hansen *et al.* (2005; Chapter IV), a CO_2 content map was calculated from the magnetic susceptibility map (Fig. 2.2d) and tracks whole rock CO_2 content to within 5 wt%.

Airborne magnetic surveys are able to detect areas of vast carbonate-alteration (e.g. Ash, 1994; Lowe and Anderson, 2002). Areas of listwanite-alteration in Figure 2.1 correspond to aeromagnetic lows in Figure 2.3. The basal décollement, which traces from just north of Atlin to the Heart of Gold prospect then along the east to south slopes of Monarch Mountain, is easily distinguished on the aeromagnetic map (Figs. 2.1, 2.3). The aeromagnetic saddles in Fig. 2.3 through and just south of Atlin and through the Pictou prospect correspond to areas of known listwanite.

2.8 IMPLICATIONS FOR CO_2 SEQUESTRATION

The overall mineral transformation in listwanite-alteration is the same as that proposed for sequestration of CO_2 in minerals, but in nature proceeds through a series of sub-reactions fossilized as spatially distinct zones. Direct carbonation of olivine +/- brucite (R_1) was previously unrecognized at Atlin and records carbonation of intact bedrock many tens of metres from the primary fracture permeability system. Initial carbonation of olivine by reaction R_1 is likely due to the higher reactivity of olivine (+/- brucite) to that of serpentine in the presence of a CO_2-bearing fluid (Lackner *et al.*, 1995; Guthrie *et al.*, 2001) and the small solid volume increase associated with the carbonation of small amounts of relict olivine (Table 2.2). Though reaction R_1 only accounts for about 5-15 % the carbonation potential for the serpentinite at Atlin (Table 2.1), because it

Table 2.2: Volume Changes

Reaction	ΔVs* (rxn)	ΔVs (rock**)
R_{1a}: Ol → Srp + Mgs	55.1%	4.2%
R_{1b}: Brc → Mgs	13.8%	0.4%
R_2: Srp → Tlc + Mgs	2.6%	2.3%
R_3: Tlc → Qtz + Mgs	28.5%	16.2%

* Calculated from Berman (1988) at 250°C and 500 bars (Chapter IV)

** Assuming 2.5% brucite and 7.5% relict olivine by volume.

is widespread, it may have sequestered a significant portion of the total CO_2 contained in the Atlin listwanite system.

Each of the three carbonation reactions involves an increase in the volume of solids, therefore each has the potential to create or destroy permeability. Reaction R_2 binds large quantities of CO_2 with small associated loss of porosity and permeability (Tables 2.1, 2.2). Moreover, the progression of reaction R_2 may create a permeability front in advance of it, promoting further carbonation. The development of carbonate-filled veins orthogonal to the R_2 reaction front in Figures 2.2a and b may represent fracture permeability generated in tension (Hansen *et al.*, 2005; Chapter IV). The mechanical model of Jamtveit *et al.* (2000) predicts the development of high permeability zones downstream of an advancing reaction undergoing a solid volume increase. Indeed, the pattern of reaction and vein formation in Figures 2.2a and b resembles the model prediction. The distribution of tensile fractures approximately marks the outer extent of rust-weathering serpentinite suggesting they have enhanced percolation of reactive CO_2-bearing fluid into the wall rock.

Complete carbonation to magnesite plus quartz (A_4) is generally limited to the cores of the largest systems. The large solid volume gain associated with reaction R_3 may seal the fluid percolation pathways and limit the usefulness of *in situ* mineral carbonation systems. For this reason, reactions R_1 and R_2, which combined account for about half of the carbonation potential for serpentinite (Table 2.2), may hold the most promise for *in situ* carbonation of minerals. The stability of the three reaction steps is controlled by the activity of CO_2 in the fluid phase (Hansen *et al.*, 2005; Chapter IV). Therefore, industrial mineral carbonation systems could potentially be tailored to drive only those reactions that minimize porosity loss and maximize permeability generation in the subsurface.

2.9 IMPLICATIONS FOR LODE-GOLD MINERALIZATION

A positive correlation of Au with K-altered quartz-carbonate listwanite has been noted in listwanite systems worldwide (e.g. Ploshko, 1963; Buisson and LeBlanc, 1987; Ash and Arksey, 1991). Ploshko (1963) also noted an association of K-alteration in listwanite systems with felsic igneous intrusions in the northern Caucasus. Similarly,

Ash (2001) noted a general correlation in ophiolite-hosted Au occurrences with granitic intrusions in the Canadian Cordillera. Granitic intrusions could promote listwanite development by providing a heat source to drive fluid circulation, by serving as a fluid source, and possibly as a source for gold and other metals.

Middle Jurassic plutonism is widespread to the south and immediately north of the listwanite occurrences. Southern plutons include the Mount McMaster and Llangorse Mountain batholiths (172 +/- 0.3 Ma and 171 +/- 0.3 Ma (U-Pb, zircon) respectively (Anderson *et al.*, 2003)) 45-60 km south of Atlin. The south margin of the large, multi-phase Middle Jurassic Fourth of July batholith (FOJB) occurs a few kilometres to the north of the Atlin Ultramafic Allochthon. The batholith's U-Pb zircon age range of 166-174 Ma (Mihalynuk *et al.*, 1992) overlaps the age range of Cr-muscovite in the listwanite (168-172 Ma (^{40}Ar-^{39}Ar); Ash, 2001). Streams that drain the FOJB contain stream sediments with anomalous Au contents (Jackaman, 2000) suggesting that the intrusion was a possible source for Au and other metals. A small stock correlated with the FOJB crops out between Monarch Mountain and Union Mountain (Ash, 1994). New isotopic ages for dikes in the study area show a direct correlation to the FOJB (Chapter III). Magmatic-hydrothermal activity associated with the FOJB may have contributed to gold mineralization in the Atlin area.

Lode-gold prospects near Atlin are spatially associated with the most intense Cr-muscovite-bearing listwanite zones along the basal décollement and in the L_a orientation. L_a listwanite zones therefore may be preferential targets for future exploration. Listwanite-alteration destroys magnetite. Zones of listwanite appear as magnetic lows on aeromagnetic survey maps (Fig. 2.3). Ground surveying with a magnetic susceptibility meter could help identify subtle to cryptic carbonation which may aid in vectoring to potential lode-gold deposits.

2.10 REFERENCES

Aitken, J. D. (1959): Atlin Map Area, British Columbia; Geological Survey of Canada, Memoir 307, 89 pages and accompanying map at 1:253 440 scale.

Anderson, R. G., Lowe, C. and Villeneuve, M. E. (2003): Nature, Age, Setting, and Mineral Potential of Some Mesozoic Plutons in Central and Northwestern Atlin Map Area (NTS 104N), Northwestern B.C.; (abstract); Vancouver 2003 Abstracts, CD-ROM, GAC-MAC-SEG Vancouver 2003 Annual General Meeting, Vancouver, B.C., v. 28, abstract no. 600, ISSN 0701-8738, ISBN: 0-919216-86-2.

Andrew, K. (1985): Fluid Inclusion and Chemical Studies of Gold-Quartz Veins in the Atlin Camp, Northwestern British Columbia; unpublished B.Sc. thesis, Department of Geological Sciences, Vancouver, B.C., Canada, 116 p.

Ash, C. H. (1994): Origin and Tectonic Setting of Ophiolitic Ultramafic and Related Rocks in the Atlin Area, British Columbia (NTS 104N); B.C. Ministry of Energy, Mines and Petroleum Resources, Bulletin 94, 48 p.

Ash, C. H. (2001): Relationship Between Ophiolites and Gold-Quartz Veins in the North American Cordillera; British Columbia Department of Energy, Mines and Petroleum Resources, Bulletin 108, 140 p.

Ash, C. H. and Arksey, R. L. (1990a): The Atlin Ultramafic Allochthon: Ophiolite Basement Within the Cache Creek Terrane; Tectonic and Metallogenic Significance (104N/12); Geological Fieldwork 1989, B.C. Department of Energy and Mines, Paper 1990-1, p. 365-374.

Ash, C. H. and Arksey, R. L. (1990b): The Listwanite-Lode Gold Association in British Columbia; Geological Fieldwork 1989, B.C. Department of Energy and Mines, Paper 1990-1, p. 359-364.

Ash, C. H., Macdonald, R. W. J. and Arksey, R. L. (1991): Towards a Deposit Model for Ophiolite Related Mesothermal Gold in British Columbia; Geological Fieldwork 1991, BC Department of Energy and Mines, Paper 1992-1, p. 253-260.

Aydal, D. (1990): Gold-Bearing Listwaenites in the Arag Massif, Kastamonu, Turkey; Terra Nova, v. 2, p. 43-52.

Berman, R. G. (1988): Internally-Consistent Thermodynamic Data for Minerals in the System: Na_2O-K_2O-CaO-FeO-Al_2O_3-SiO_2-TiO_2-H_2O-CO_2; Journal of Petrology, v. 29, Part 2, p. 445-522.

Bloodgood, M. A., Rees, C. J., and Lefebure, D. V. (1989): Geology and Mineralization of the Atlin Area, Northwestern British Columbia (104N/11W and 12E); Geological Fieldwork 1988, B.C. Department of Energy and Mines Paper 1989-1, p. 311-322.

Buisson, G. and LeBlanc, M. (1986): Gold-Bearing Listwaenites (Carbonitized Ultramafic Rocks) From Ophiolite Complexes; in Metallogeny of Basic and Ultrabasic Rocks, Gallagher, M., Ixer, R., Neary, C. and Prichard, H., Editors, The Institution of Mining and Metallurgy, pages 121-131.

Buisson, G. and LeBlanc, M. (1987): Gold in Mantle Peridotites from Upper Proterozoic Ophiolites in Arabia, Mali, and Morocco; Economic Geology, v. 82, p. 2091-2097.

Guthrie, G. D., Carey, J. W., Bergfeld, D., Byer, D., Chipera, S., Ziock, H. and Lackner, K. S. (2001): Geochemical Aspects of the Carbonation of Magnesium Silicates in an Aqueous Medium; Proceedings of the First National Conference on Carbon Sequestration, May 14-17, 2001, Washington, DC, session 6C, 14 pages.

Halls, C. and Zhao, R. (1995): Listvenite and Related Rocks: Perspectives on Terminology and Mineralogy With Reference to an Occurrence at Cregganbaun, Co. Mayo, Republic of Ireland; Mineralium Deposita, v. 30, p. 303-313.

Hansen, L. D., Dipple, G. M., and Anderson, R. G. (2003a): Carbonate Altered Serpentinites of Atlin, BC: A Two Stepped Analoge to CO_2 Sequestration; (abstract); Geological Society of America, 2003 annual meeting, Seattle, WA; Abstracts with Programs - Geological Society of America; Session 144-14.

Hansen, L. D., Dipple, G. M., and Gordon, T. M. (2003b): Carbonate-Altered Serpentinites, Atlin, BC: A Natural Analog to CO_2 Sequestration; (abstract); Vancouver 2003 Abstracts, CD-ROM, GAC-MAC-SEG Vancouver 2003 Annual General Meeting, Vancouver, B.C., v. 28, abstract no. 494, ISSN 0701-8738, ISBN: 0-919216-86-2.

Hansen, L. D., Dipple, G. M., Gordon, T. M. and Kellett, D. A. (2005): Carbonated Serpentinite (Listwanite) at Atlin, British Columbia: a Geological Analogue to Carbon Dioxide Sequestration, Canadian Mineralogist, v. 43, part 1, p. 675-689.

Jackaman, W. (2000): British Columbia Regional Geochemical Survey, NTS 104N/1 - Atlin; British Columbia Ministry of Energy and Mines, BC RGS 51.

Jackson, J. A. (1997): Glossary of Geology, Fourth Edition; American Geological Institute, Alexandria, Virginia, 769 p.

Jamtveit, B., Austrheim, H., and Malthe-Sørenssen, A. (2000): Accelerated Hydration of the Earth's Deep Crust Induced by Stress Perturbations; Nature, v. 408, p. 75-87.

Kashkai, A. M. and Allakhverdiev, I. (1965): Listwanites: Their Origin and Classification; U. S. Geological Survey, Library, Reston, VA, United States, 146 p., Translated from the Russian, Listvenity, ikh genezis i klassifikatsiya, Akad. Nauk AZ SSR, Inst. Geol. Baku, 1965.

Kellett, D. A. (2002): Geochemical and Geophysical Monitors of Reaction Progress During Carbonate Alteration of Serpentinite at Atlin, British Columbia; unpublished B.Sc. thesis, Department of Earth and Ocean Sciences, Vancouver, B.C., Canada, 48 p.

Lackner, K. S., Wendt, C. H., Butt, D. P., Joyce, E. L. and Sharp, D. H. (1995): Carbon Dioxide Disposal in Carbonate Minerals; Energy, v. 20, 1153-1170.

Lowe, C and Anderson, R G. (2002): Preliminary Interpretations of New Aeromagnetic Data For the Atlin Map Area, British Columbia; Geological Survey of Canada, Current Research, no. 2002-A17, 11 p.

Lueck, B. A. (1985): Geology of Carbonitized Fault Zones on the Anna Claims and Their Relationship to Gold Deposits, Atlin, British Columbia; unpublished B.Sc. thesis, Department of Geological Sciences, Vancouver, B.C., Canada, 55 p.

Mihalynuk, M. G., Smith, M., Gabites, J. E., Runkle, D. and Lefebure, D. (1992): Age of Emplacement and Basement Character of the Cache Creek Terrane as Constrained by New Isotopic and Geochemical Data; Canadian Journal of Earth Sciences, v. 29, p. 2463-2477.

Monger, J. W. H. (1975): Upper Paleozoic Rocks of the Atlin Terrane; Geological Survey of Canada, Paper 74-47, 63 p.

Monger, J. W. H. (1977a): Upper Paleozoic Rocks of Northwestern British Columbia; in Current Research, Part A, Geological Survey of Canada, Paper 77-1A, p. 255-262.

Monger, J. W. H. (1977b): Upper Paleozoic Rocks of the Western Canadian Cordillera and Their Bearing on the Cordilleran Evolution; Canadian Journal of Earth Sciences, v. 14, p. 1832-1859.

Monger, J.W.H., Richards, T.A. and Paterson, I.A. (1978): The Hinterland Belt of the Canadian Cordillera: New Data From Northern and Central British Columbia; Canadian Journal of Earth Sciences, v. 15, p. 823-830.

Newton, D. (1985): A Study of Carbonate Alteration of Serpentinites Around Au and Ag Bearing Quartz Veins in the Atlin Camp, British Columbia; unpublished B.Sc. thesis, Department of Geological Sciences, Vancouver, B.C., Canada, 85 p.

Ploshko, V. V. (1963): Listwaenitization and Carbonitization at Terminal Stages of Urushten Igneous Complex, North Caucasus, International Geology Review, v. 7, p. 446-463.

Rose, G. (1837): Mineralogisch-Geognostistiche Reise Nach Dem Ural, dem Altai und dem Kaspischen Meere. v. 1: Reise nach dem nordlichen Ural und dem Altai. Berlin, C.W. Eichoff (Verlag der Sanderschen Buchhandlung), xxx plus 641 p. and plates I-VII.

Schandl, E. S. and Naldrett, A. J. (1992): CO_2 Metasomatism of Serpentinites, South of Timmins, Ontario; Canadian Mineralogist, v. 30, p. 93-108.

Toft, P. B., Arkani-Hamed, J. and Haggerty, S. E. (1990): The Effects of Serpentinization on Density and Magnetic Susceptibility: A Petrophysical Model; Physics of the Earth and Planetary Interiors, v. 65, p. 137-157.

Wittkopp, R. W. (1983): Hypothesis for The Localization of Gold in Quartz Veins, Allegheny District; California Geology, p. 123-127.

CHAPTER III: STRUCTURAL SETTING AND TIMING OF LISTWANITE (CARBONATED SERPENTINITE), ATLIN, BRITISH COLUMBIA: IMPLICATIONS FOR LODE-GOLD MINERALIZATION.

3.1 INTRODUCTION

Listwanite, a carbonate-altered ultramafic rock (e.g. Hansen *et al.*, 2004; Chapter II; Ash, 2001), is commonly spatially associated with high-grade lode-gold mineralization. The Mother Lode gold district in California (Wittkopp, 1983) and the Abitibi greenstone belt of the Superior Province of Canada (Schandl and Naldrett, 1992) are two of the best known examples of mesothermal listwanite-associated lode-gold in North America. In general, the richest gold grades within these deposits are associated with, or in close proximity to, carbonate-altered ultramafic rocks (e.g. Ash, 2001). Significant debate exists over the role ultramafic rocks and their carbonate-altered equivalents play in lode-gold mineralization. Buisson and LeBlanc (1987) suggest a model where by ultramafic rocks are stripped of gold by CO_2-bearing hydrothermal fluids during the initial stages of carbonation and redeposited in areas of intense carbonate alteration, quartz-carbonate veining and K^+ metasomatism recorded by the development of Cr-muscovite. An alternative model poses that gold is stripped from tectonically thickened packages of oceanic, volcanic and sedimentary rocks by large-scale hydrothermal convection and redeposited within or near the alkaline environment of K-metasomatized (Cr-muscovite bearing) zones of listwanite (e.g. Ash *et al.*, 1991). The main difference between the two models is the source of gold.

This chapter builds on Chapter II by elaborating upon the structural controls, mineral reactions, geochemical alteration, tectonic setting, stable isotope and geochronologic evolution of the extensive listwanite-altered serpentinite rocks in the vicinity of Atlin, located in northwestern British Columbia. This information is used to assess the various scenarios for mesothermal listwanite-associated lode-gold deposition. Field mapping in the summers of 2003 and 2004 shows that listwanite is spatially distributed primarily along the basal décollement of an allochthonous ultramafic body and along a steeply-dipping late syn- to post-obduction regional joint and fracture system.

Evidence for carbonation, indicated by the presence of Mg-carbonate minerals, is present for metres to tens of metres into wallrock adjacent to these fluid-controlling fractures. Stable isotope and gold assay data support a model where gold is scavenged from either nearby felsic batholiths or the structurally lower accretionary complex materials by hydrocarbon-bearing fluids. Geochronologic evidence indicates that the nearby Fourth of July Batholith (FOJB) is contemporaneous with the listwanite alteration and therefore has likely acted as the heat source for hydrocarbon maturation and hydrothermal convection.

3.2 REGIONAL GEOLOGY AND ROCK UNITS

The Atlin Ultramafic Allochthon (Ash and Arksey, 1990) underlies an area of about 25 km^2 (Fig. 3.1, insert) and comprises variably serpentinized, carbonated and deformed harzburgite along with minor dunite lenses and pyroxenite veins. The ultramafic body forms a tectonic klippe, separated from the Atlin Accretionary Complex lithologies by a basal décollement termed the Monarch Mountain Thrust Fault (Ash and Arksey, 1990). Serpentinization is most intensely developed near the basal décollement and adjacent to a penetrative joint and fracture system that cuts both the ultramafic and structurally lower lithologies. The serpentine minerals are dominantly antigorite +/- minor lizardite and fracture-filling chrysotile.

Harzburgitic ultramafic rocks are divided into the harzburgite and serpentinite units based on the degree of serpentinization and are discussed in Hansen *et al.* (2004) and Chapter II. Other rock types associated with the harzburgitic ultramafic body include metavolcanic rocks, limestone, chert and argillite, which occur structurally below the ultramafic rocks. They are not central to this study and are discussed in detail by Ash (1994).

Listwanite is zoned mineralogically outward from fluid-controlling fractures (discussed below). The zonation tracks the migration of three isochemical carbonation-(de)hydration reactions (Hansen *et al.*, 2005; Chapter IV). The magnesite-, talc- and quartz-zones are separable by metamorphic isograds (reactions R_1 to R_3; Hansen *et al.*, 2005; Chapter IV) defined by the first appearance of magnesite, talc and quartz respectively. The three reactions occurred in sequence and are isochemical (Hansen *et al.*, 2005; Chapter IV), except in the intensely altered cores where stockwork quartz-

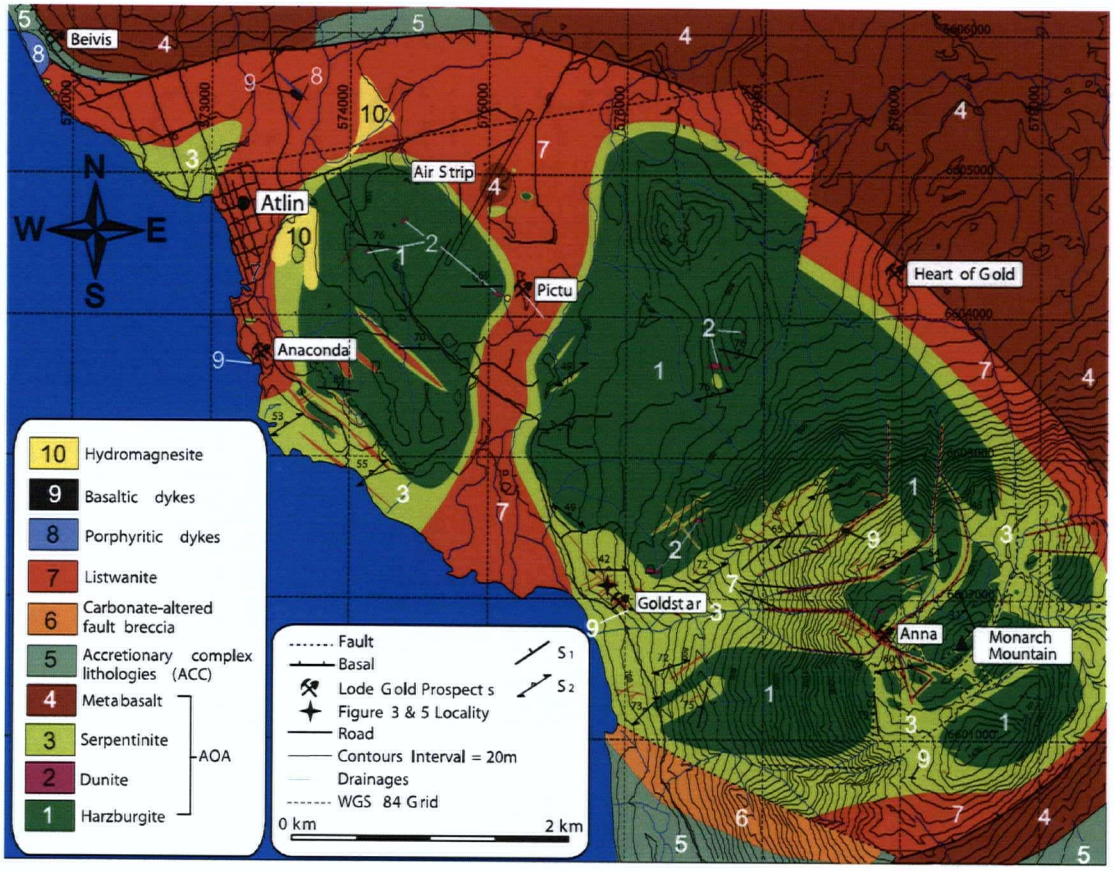

Figure 3.1: Simplified geologic map of the study area showing the distribution of listwanite near Atlin area (this paper; Hansen *et al.*, 2003b; Ash, 1994). AOA and AAC are Atlin Ophiolitic Assemblage and Atlin Accretionary Complex, respectively, of Ash and Arksey (1990a).

carbonate veins, bright-green Cr-muscovite (mariposite, fuchsite), sulfide (mainly pyrite) and anomalous Au values are common.

3.3 STRUCTURAL ANALYSIS

There are a number of different structural elements that were identified within the map area. They are broadly divided into two groups: those which do not influence listwanite distribution (pre- and early syn-obduction) and those which do (syn- and post-obduction).

3.3.1 PRE- TO SYN-OBDUCTION STRUCTURAL ELEMENTS

Compositional layering (S_0) occurs within the harzburgite unit and is defined by alternating 1 to 10 cm orthopyroxene-rich and -poor layers (Figs. 3.2a, d). Flattening of orthopyroxene grains defines a weakly to moderately developed planar S_1 tectonite fabric (Figs. 3.2b, e). Where present together, S_0 parallels S_1. The orientation of these two fabrics changes from moderately to steeply dipping towards the northwest in the northwestern map area to moderately to steeply dipping towards the west in the southeast map area (Figs. 3.2d, e). This could be the result of kilometer-scale folding, faulting and/or rotation within the ultramafic unit. These two fabrics are interpreted to have formed prior to obduction during sea floor spreading-related processes (Ash, 1994).

Commonly a well-developed S_2 fabric, oriented 244° / 54° NW (Fig. 3.3a, c), occurs and is defined by flattened and sheared bastite spots in highly serpentinized zones. This fabric likely represents zones of shear which were active during obduction of the ultramafic body (Ash, 1994). These shear zones are cross-cut by later serpentine- and listwanite-filled lineaments (Fig. 3.4). The S_2 fabric is most common on the lower west flank of Monarch Mountain. Visual analysis of an oriented thin section within the sheared bastite indicates northwest-southeast compression with top to the southeast movement (Fig. 3.5). This observation is constituent with reported mullion structures (Ash and Arksey, 1990), northeast-southwest striking geological units south and east of the map area (Ash, 1994) and with a narrow zone of faults oriented about 231° / 57° NW located about 1 km south of the ultramafic body's south contact.

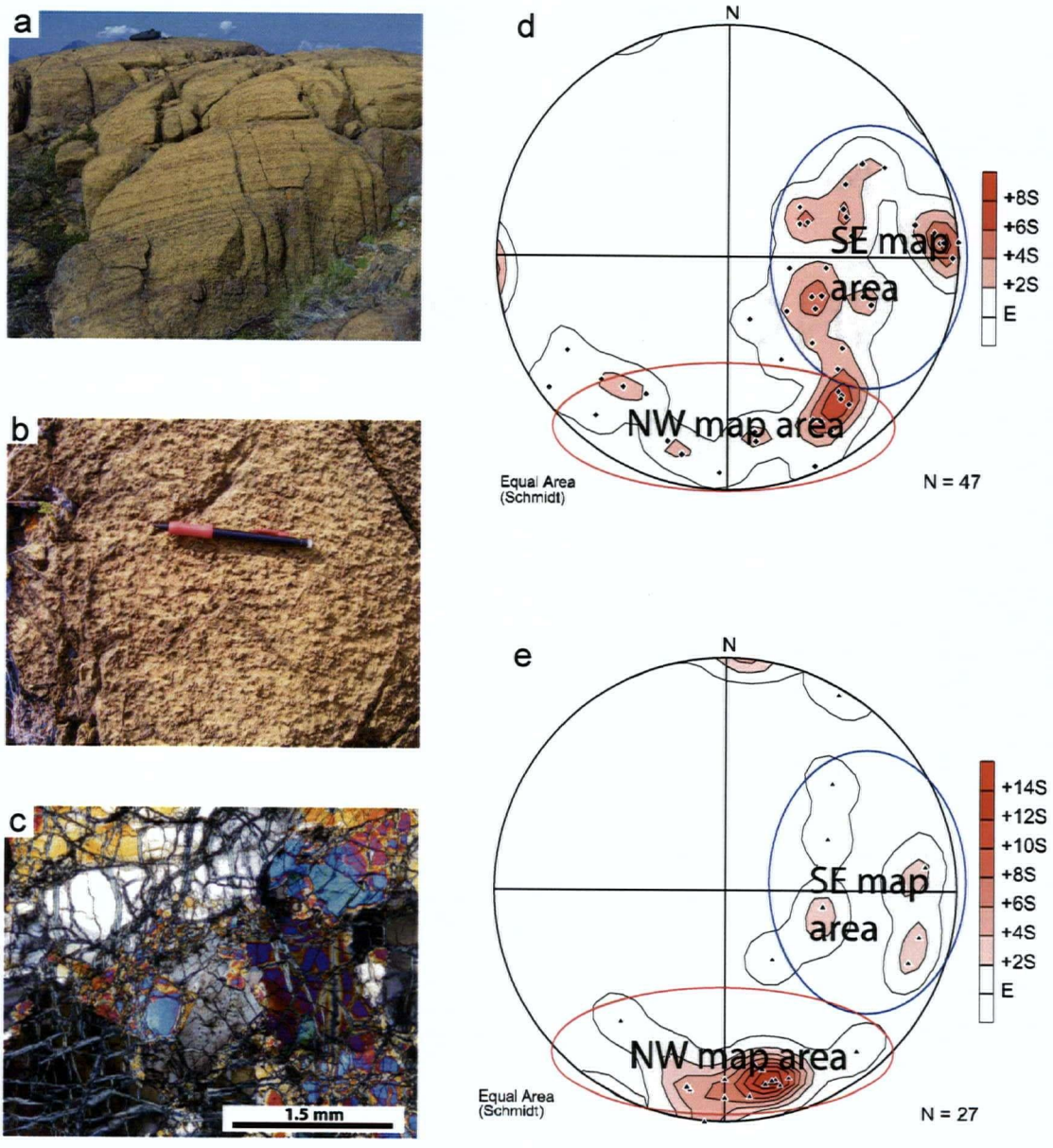

Figure 3.2: Structural data (poles to planes on equal area stereonets) of: a) Photograph showing prominent compositional layering on Monarch Mountain. b) Photograph of harzburgite fabric (pen parallels fabric). c) Photomicrograph of freshest harzburgite under cross-polars. d) Equal area stereonet plot (poles to planes) of compositional banding within harzburgite. e) Equal area stereonet (poles to planes) of harzburgite fabric defined by the flattening of orthopyroxene crystals.

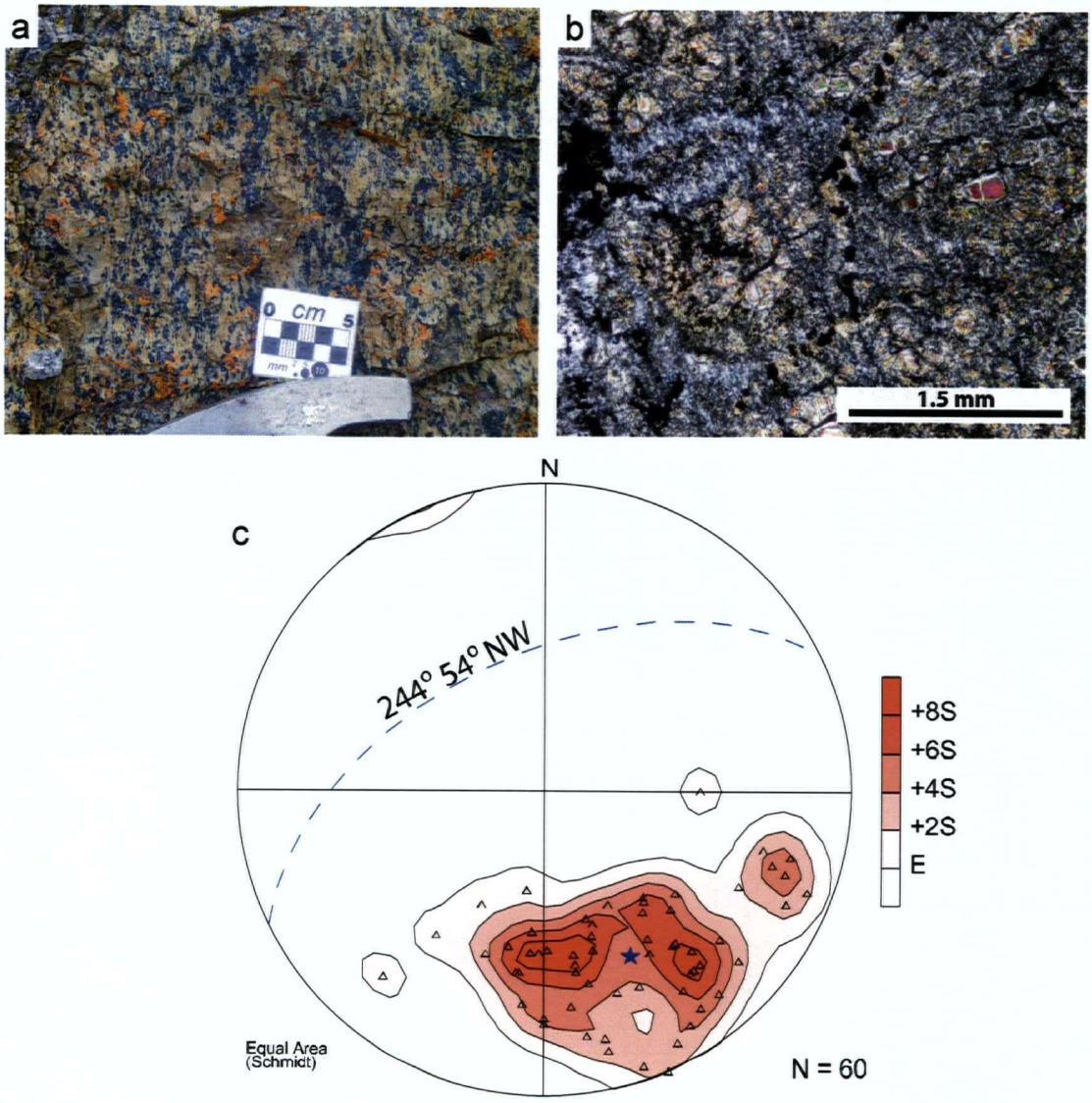

Figure 3.3: a) Photograph of foliated serpentinite defined by the flattening of bastite spots. b) Photomicrograph of typical serpentinite under cross-polars. c) Structural data (poles to planes on equal area stereonet) of bastite foliation defined by flattened and sheared bastite spots.

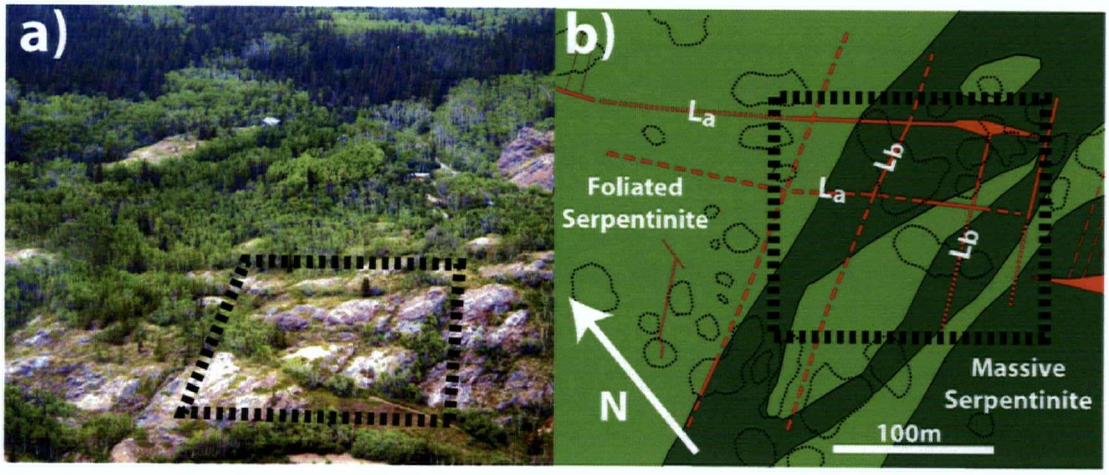

Figure 3.4: a) Aerial view to the northeast showing recessive weathering lineaments representing L_a and L_b orientations associated with listwanite at head of Monarch Mountain Hiking trail (photo by M. Mihalynuk, August 2003) (E 575900, N 6602100, NAD 83). b) Geologic map of the area in Fig. 3.4a.

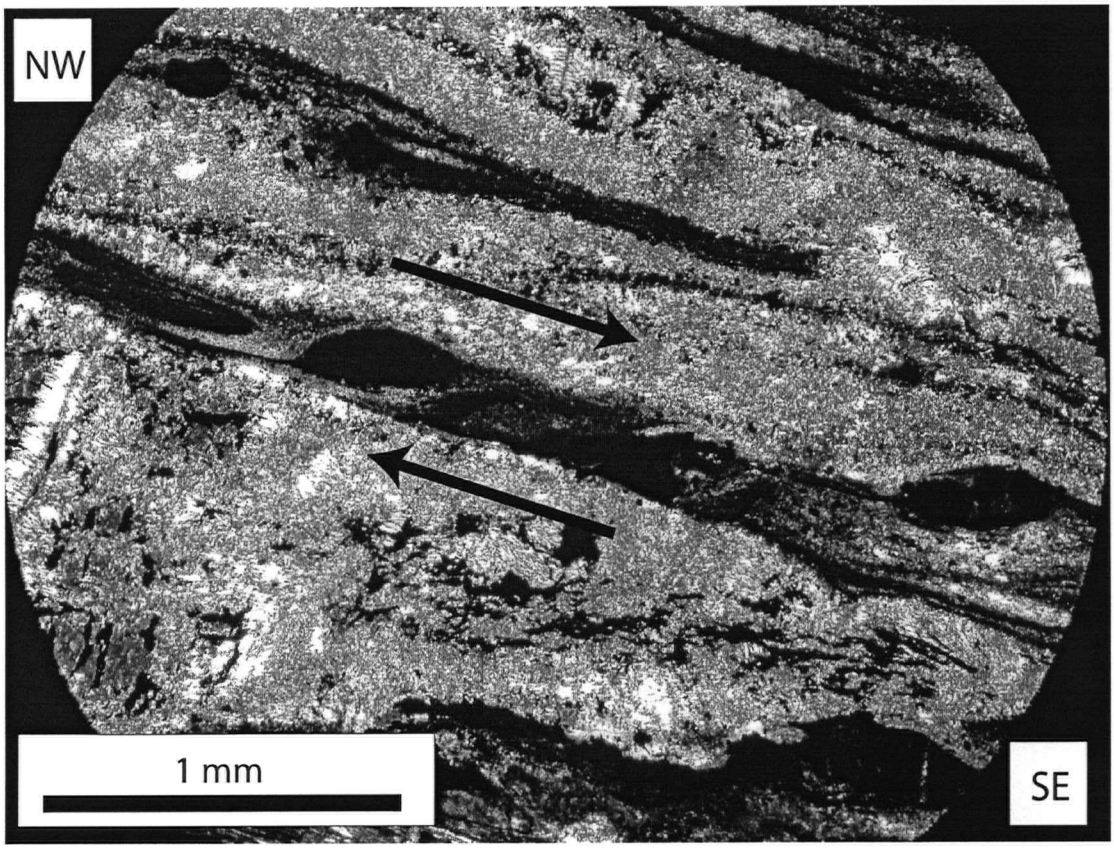

Figure 3.5: Plane polarized light photograph of oriented thin section showing sheared serpentinite and kinematic indicators that suggest apparent top to the right movement (i.e. reverse movement). Horizontal is roughly in line with the direction labels. Sample location is E 575660, N 6602200, NAD 83.

3.3.2 LATE SYN- TO POST-OBDUCTION STRUCTURAL ELEMENTS

In addition to the basal décollement, it is clear that a regional fracture/joint system provided high-permeability guides for CO_2-bearing fluids, and thus the controls on the spatial distribution of listwanite (Fig. 3.1). As illustrated in Figures 3.1 and 3.6, listwanite zones, unrelated to the basal décollement, are oriented in four steeply-dipping planar directions spanning 360° and have about a 45° spacing. These four orientations are referred to as L_a (140° trend), L_b (50° trend), L_c (N-trending) and L_d (E-trending).

Fracture-controlled, planar zones of listwanite are generally expressed as lineament depressions, which are commonly vegetated and filled with overburden. Rusty-red weathering side walls suggest they are underlain by listwanite. Additionally, the margins of surface lineaments are commonly marked by chalky blue-green weathering serpentine-alteration suggesting that they mark structural weaknesses that acted to focus fluids. This association highlights the focusing of CO_2-bearing fluid along planar structural weaknesses, and permits extrapolation of listwanite zones into areas of vegetation and overburden. The L_a and L_b trends tend to be the most commonly identified listwanite zones in the field. Generally, L_a zones are the most extensive and contain the most stockwork quartz-carbonate veins and Cr-muscovite. A consistent cross-cutting relationship between each trend was not identified. Thus, if multiple generations of listwanite exist, they are not reflected by the various orientations.

Four sets of joints and fractures in the Atlin Ultramafic Allochthon are orientated parallel with those of the listwanite zones and lineaments (Figs. 3.7a). The spacing of the four steeply-dipping joints and fractures are 45° apart. Intensely serpentinized outcrops commonly have closer spaced fractures than fresher harzburgitic rocks, but the orientations of the fractures and joints in both geologic units are similar. Likewise, fractures and joints from the structurally lower metabasalts and Atlin Accretionary Complex lithologies are concordant with those in the Atlin Ultramafic Allochthon (Fig. 3.7b). Furthermore, the joint and fracture network cross-cuts the S_2 fabric (Fig. 3.4b).

Small serpentine-magnetite veinlets cut the harzburgite, dunite and serpentinite units and are typically less than 1 cm thick, but may be as much as 10 cm thick. The dominant orientations of the veinlets are broadly coincident with the listwanite zone

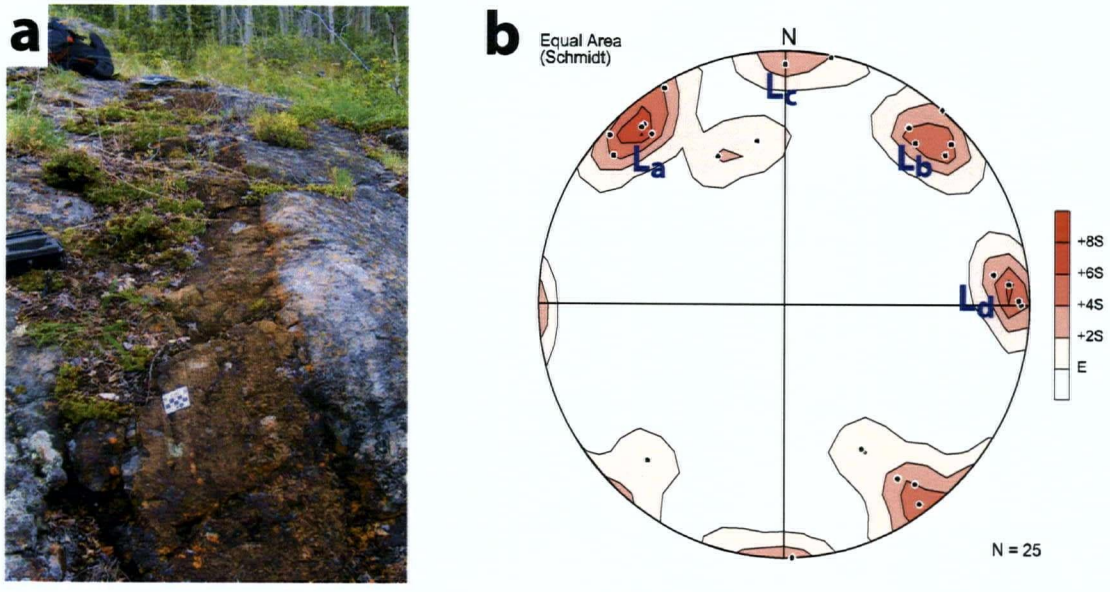

Figure 3.6: a) View to northwest of a well-preserved, rusty-brown, talc-magnesite listwanite zone (L_b) which is about 50 cm thick. Scale = 5cm. b) Equal area stereonet (poles to planes) of planar listwanite zones similar to those in Figure 3.6a.

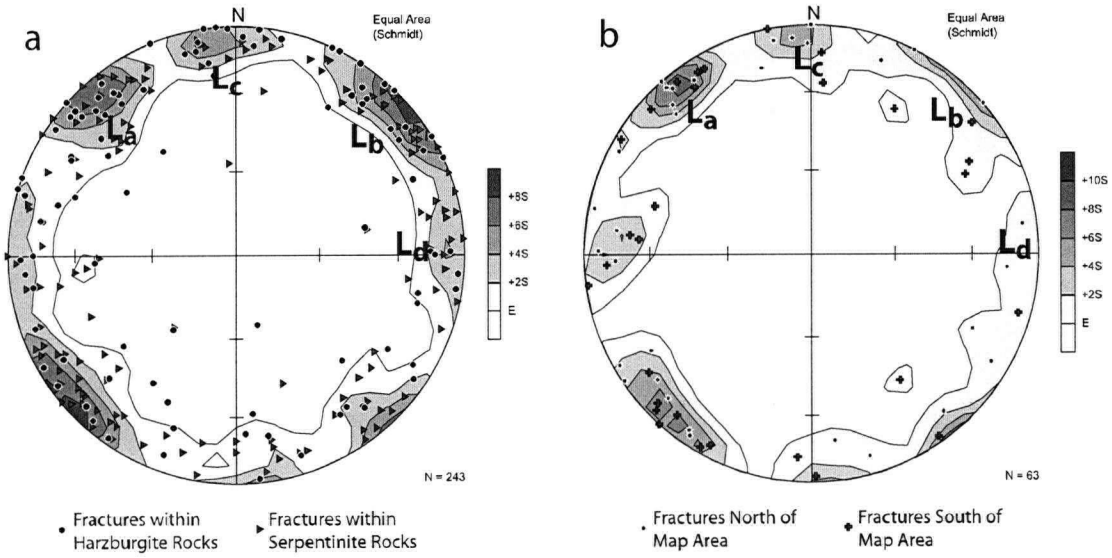

Figure 3.7: a) Equal area stereonet plot (poles to planes) of fractures and joints within the ultramafic rock units (Atlin Ultramafic Allochthon). b) Equal area stereonet plot (poles to planes) of fractures and joints within the underlying Atlin Accretionary Complex lithologies (metabasalt, argillite, chert).

orientations and joint/fracture system (Figs. 3.7 and 3.8). This supports at least one late serpentinization event which may or may not be related to the listwanite alteration.

Intense areas of listwanite-alteration commonly contain densely-spaced stock work quartz-carbonate veins (Fig. 3.9). As with other late syn- to post-obduction structures, most veins are vertical to sub-vertical and strike in the same orientations as the listwanite zones, lineaments, fracture sets and serpentine-magnetite veinlets. The veins commonly display evidence for open fracture-filling including sugary and vuggy quartz and bladed carbonates (Fig. 3.10). Figure 3.11 illustrates that the orientations of the quartz-carbonate veins mapped both regionally and on an outcrop scale are sub-parallel to the other regional structures.

3.4 IGNEOUS INTRUSIONS

Geochemical and petrographic analyses and isotopic ages confirm that at least three distinct phases of dikes are present in the map area depicted in Figure 3.1. The bulk chemical composition of the dike phases are plotted in Figure 3.12. All three phases are locally carbonate-altered where they intrude listwanite, but most are unaltered and appear to cross-cut the listwanite. Additionally, all dike phases are either spatially associated with listwanite-altered areas or surface lineaments parallel to the regional fracture and joint system. Much, if not all of the carbonate alteration within dikes could have resulted from the intrusion of dikes into the carbonate-rich material (i.e. listwanite). The association of dikes with listwanite and lineaments suggests that the fracture/joint system responsible for controlling the post-obduction listwanite and serpentinization also provided structural guides for magma ascent.

The most abundant, widespread and generally least carbonate-altered phase is melanocratic, medium- to coarse-grained diabase dikes that contain plagioclase, clinopyroxene, orthopyroxene, hornblende and sulfide. The alteration mineralogy of this unit includes chlorite, actinolite and carbonate. Xenoliths of intensely-carbonated listwanite occur within the relatively unaltered diabase which has intruded intensely carbonate-altered rock. Where diabase cuts zones of intense listwanite alteration it remains relatively unaltered. These observations suggest that the diabase dikes postdate carbonate alteration.

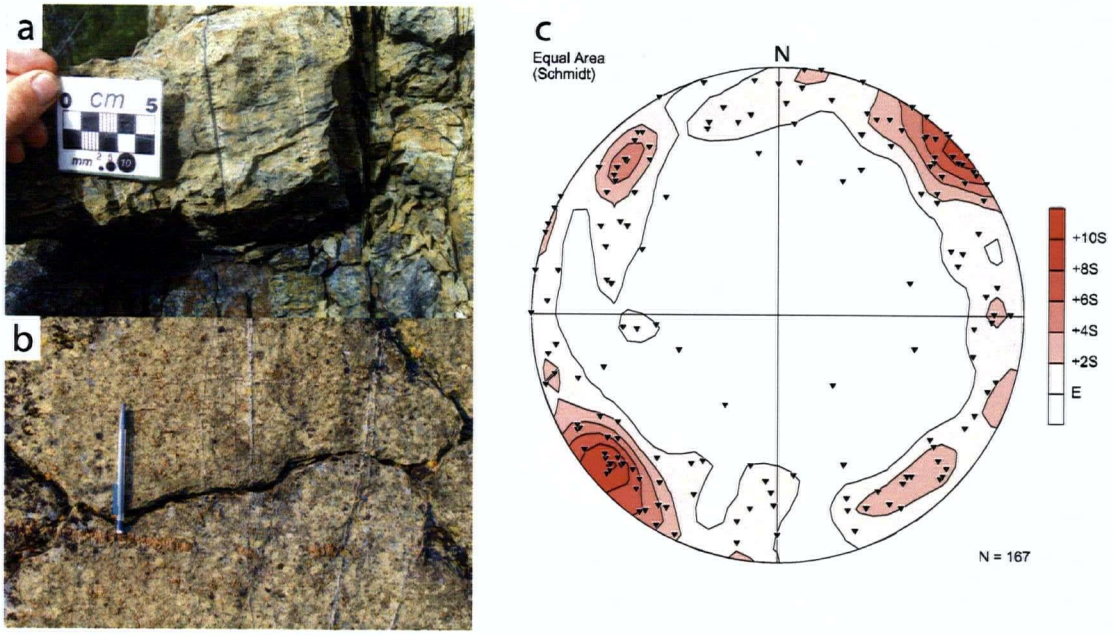

Figure 3.8: a) Photograph of serpentine-magnetite veins in harzburgite. b) Photograph of serpentine-magnetite veins in serpentinite. c) Equal area stereonet (poles to planes) of serpentine-magnetite veins.

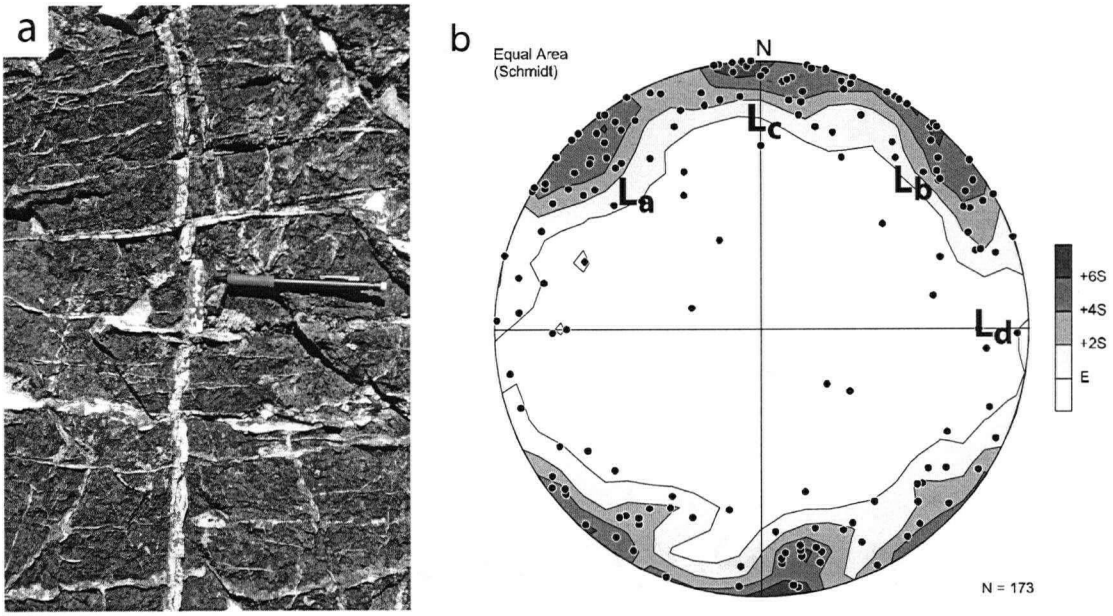

Figure 3.9: a) Photograph of stockwork quartz-carbonate veins within zones of intense listwanite alteration. Pen tip is pointed approximately to the north. b) Equal area stereonet (poles to planes) of quartz-carbonate veins within listwanite unit. Approximate orientations of listwanite zones are given by symbols L_a – L_d.

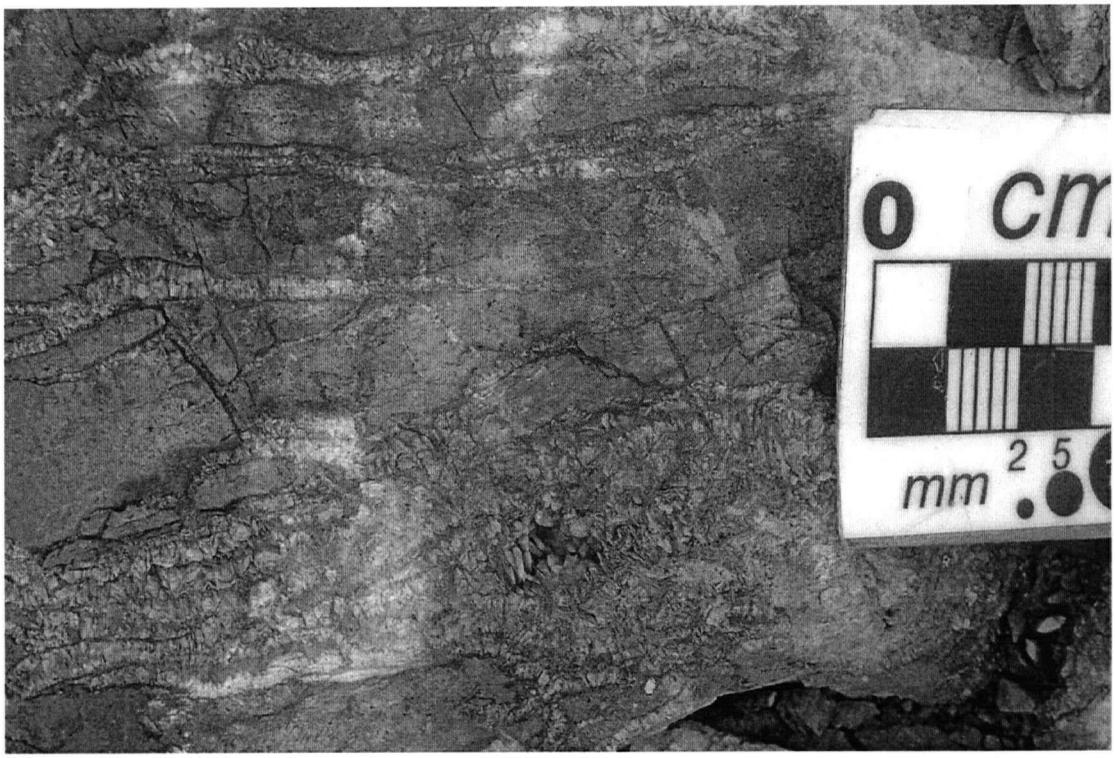

Figure 3.10: Photograph of bladed carbonate within listwanite.

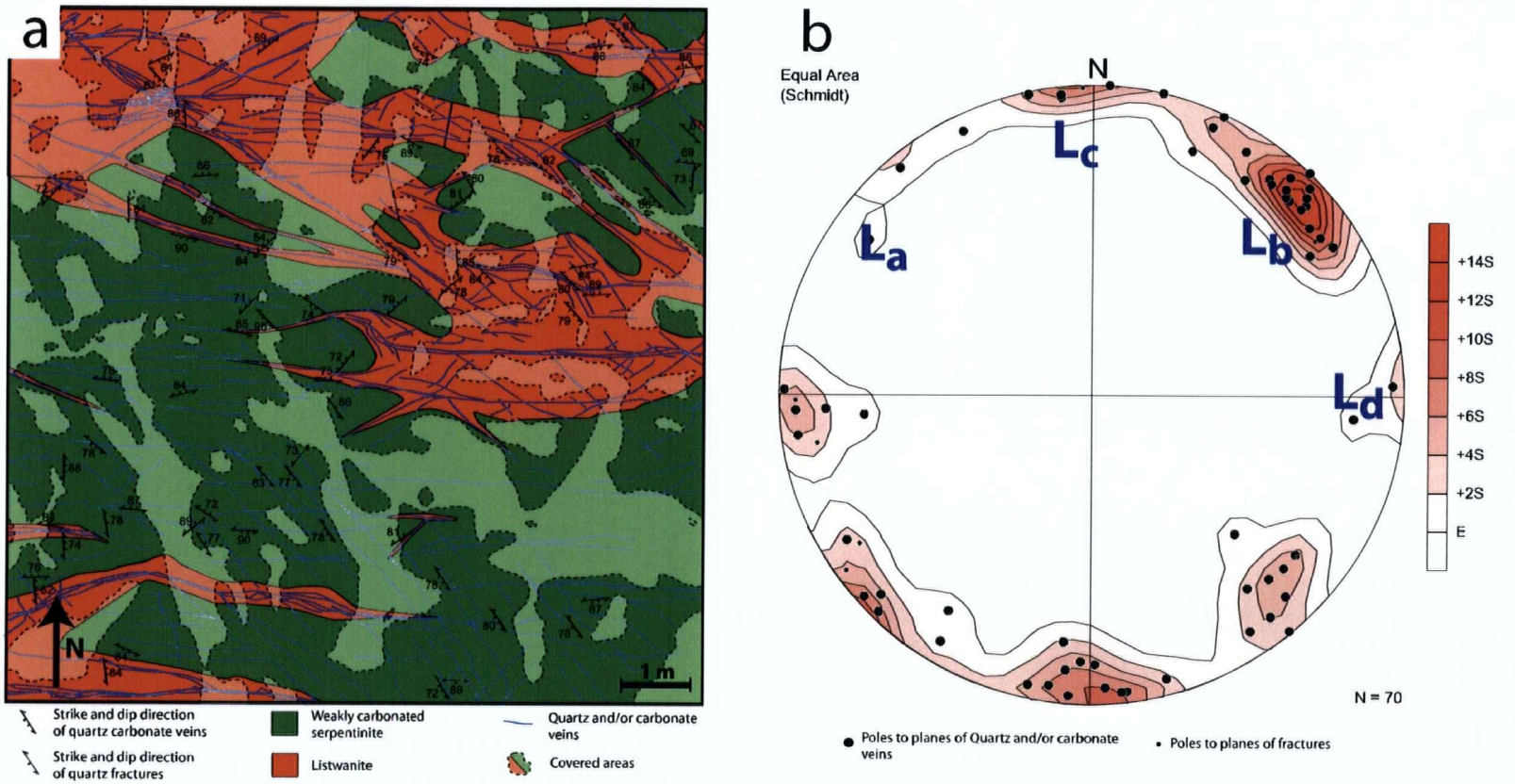

Figure 3.11: a) 10 m by 10 m geologic map of a talc-magnesite to quartz-magnesite listwanite zone. Structural measurements of quartz-carbonate veins have been plotted on the map. b) Equal area stereonet (poles to planes) of quartz-carbonate veins obtained from the area depicted in Figure 3.11a. The general orientations of the listwanite zones are given by the symbols $L_a - L_d$.

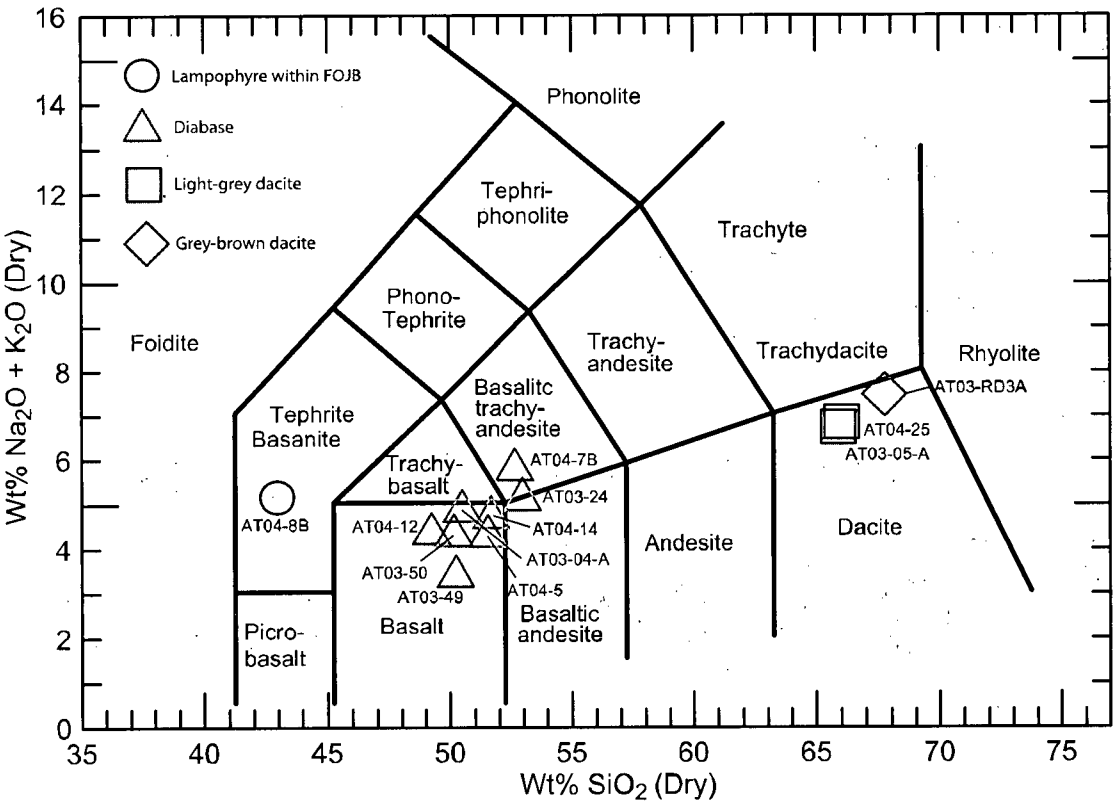

Figure 3.12: Total alkali vs. SiO_2 (TAS) plot (LeBas et al., 1986) of dike samples collected within the map area depicted in Figure 3.1. The two exceptions are AT04-7B and AT04-8B, which were collected from dikes within the Fourth of July Batholith on the road cut near Como Lake. All analyses have been renormalized to 100 wt% excluding volatile chemical species.

A light grey, felsic porphyritic dacite is the next most abundant intrusive phase and was always found associated with listwanite. Phenocrysts include plagioclase, K-feldspar and quartz (as "quartz-eyes"). This unit is commonly highly carbonated and sericitized creating a ground-mass of carbonate, quartz and an interlocking mesh of sericite. Pyrite and chalcopyrite are common and locally account for a few modal percent of the rock. The timing of emplacement of this unit with respect to the carbonate alteration is uncertain, but the dacite dikes appear to cut through listwanite and no listwanite-associated quartz-carbonate veins were found which crosscut it. More precise evidence for the timing derives from the geochronologic evidence (discussed below) that indicates that these dikes are younger than the age range determined for the carbonate alteration.

The third and least abundant igneous phase is a grey-brown medium- to coarse-grained porphyritic dacite dike that contains, in order of decreasing abundance, plagioclase, K-feldspar, biotite, quartz and hornblende phenocrysts. This unit appears to be restricted to the north-central part of the study area just off Highway 7 (Fig. 3.1). All phenocrysts are subhedral to euhedral and display clear evidence for resorption. This unit, as with the diabase, is relatively unaltered in areas of intense listwanite alteration, suggesting it postdates carbonation. These relationships are also corroborated by geochronologic evidence (discussed below) indicating that the unit is younger than the most intense carbonate alteration.

3.5 TIMING AND SETTING OF LISTWANITE ALTERATION

Two Cr-muscovite samples extracted from listwanite and one fresh euhedral biotite book taken from the grey-brown dacite dike yielded reliable ^{40}Ar-^{39}Ar dates. In addition, a U-Pb zircon date was determined from the light-grey dacite phase. Unfortunately, datable separates of the melanocratic diabase dikes could not be attained. Table 3.1 summarizes age data obtained for this, and all other studies obtained within and immediately adjacent to the map area. Figure 3.13 outlines the simplified geologic history of the area. ^{40}Ar-^{39}Ar and U-Pb data are presented in Appendix F. All geochronologic analyses were performed at the Pacific Centre for Isotopic and

Table 3.1: Geochronologic Analyses from Atlin Area

Sample/Location	Mineral	Rock Type	Source	^{40}Ar-^{39}Ar	K-Ar	U-Pb	Interpretation
01AT-1-2	Cr- Muscovite	Listwanite	This Study	128.0 +/- 1.9	/	/	Carbonate-Alteration
02AT-8-1 (Goldstar)	Cr- Muscovite	Listwanite	This Study	172.7 +/- 2.0	/	/	Carbonate-Alteration
AT03-44-7 (Anna)	Cr- Muscovite	Listwanite	This Study	174.4 +/- 1.4^{+}	/	/	Carbonate-Alteration
Pictou	Cr- Muscovite	Listwanite	Ash (2001)	165 +/- 4	121 +/- 4*	/	Carbonate-Alteration
Yellowjacket	Cr- Muscovite	Listwanite	Ash (2001)	171 +/- 3	/	/	Carbonate-Alteration
Surprise	Cr- Muscovite	Listwanite	Ash (2001)	168 +/- 3	171 +/- 6	/	Carbonate-Alteration
Goldstar	Cr- Muscovite	Listwanite	Ash (2001)	167 +/- 3	156 +/- 5*	/	Carbonate-Alteration
Anna	Cr- Muscovite	Listwanite	Ash (2001)	/	169 +/- 6*	/	Carbonate-Alteration
AT03-28	Biotite	Dacite	This Study	84.0 +/- 0.6	/	/	Cooling 280 °C
AT03-5	Zircon	Dacite	This Study	/	/	150.7 +/- 0.6	Crystallization age
FOJB	Zircon	Granitiod	Mihalynuk et al. (1992)	/	/	170.4 +/- 5	Crystallization age
FOJB	Zircon	Granitiod	Mihalynuk et al. (1992)	/	/	171.5 +/- 3.3	Crystallization age
FOJB	Hornblende	Granitiod	Harris et al. (2003)	172.7 +/- 1.7	/	/	Cooling 500 °C
FOJB	Biotite	Granitiod	Harris et al. (2003)	165.1 +/- 1.6	/	/	Cooling 280 °C
FOJB	Biotite	Lamprophyre	Harris et al. (2003)	161.8 +/- 1.6	/	/	Cooling 280 °C
FOJB	Biotite	Lamprophyre	Harris et al. (2003)	165.3 +/- 1.6	/	/	Cooling 280 °C
SLB	Zircon	Granitiod	Mihalynuk et al. (1992)	/	/	83.8 +/- 5	Crystallization age
MMB	Zircon	Granitiod	Anderson et al. (2003)	/	/	172 +/- 0.3	Crystallization age
LMB	Zircon	Granitiod	Anderson et al. (2003)	/	/	171 +/- 0.3	Crystallization age
M/U Stock	Biotite	Granitiod	Hunt & Roddick (1988)	/	167 +/- 3	/	Cooling 280 °C

* Considered whole rock ages. All others are ages determined from separates. $^{+}$ denotes integrated age (all other Ar-Ar ages are plateau ages) FOJB = Fourth of July Batholith, SLB = Surprise Lake Batholith, M/U Stock = unnamed stock between Monarch & Union mountains, MMB = Mount McMaster Batholith, LMB = Llangorse Mountain Batholith. Suspect ages are shaded grey.

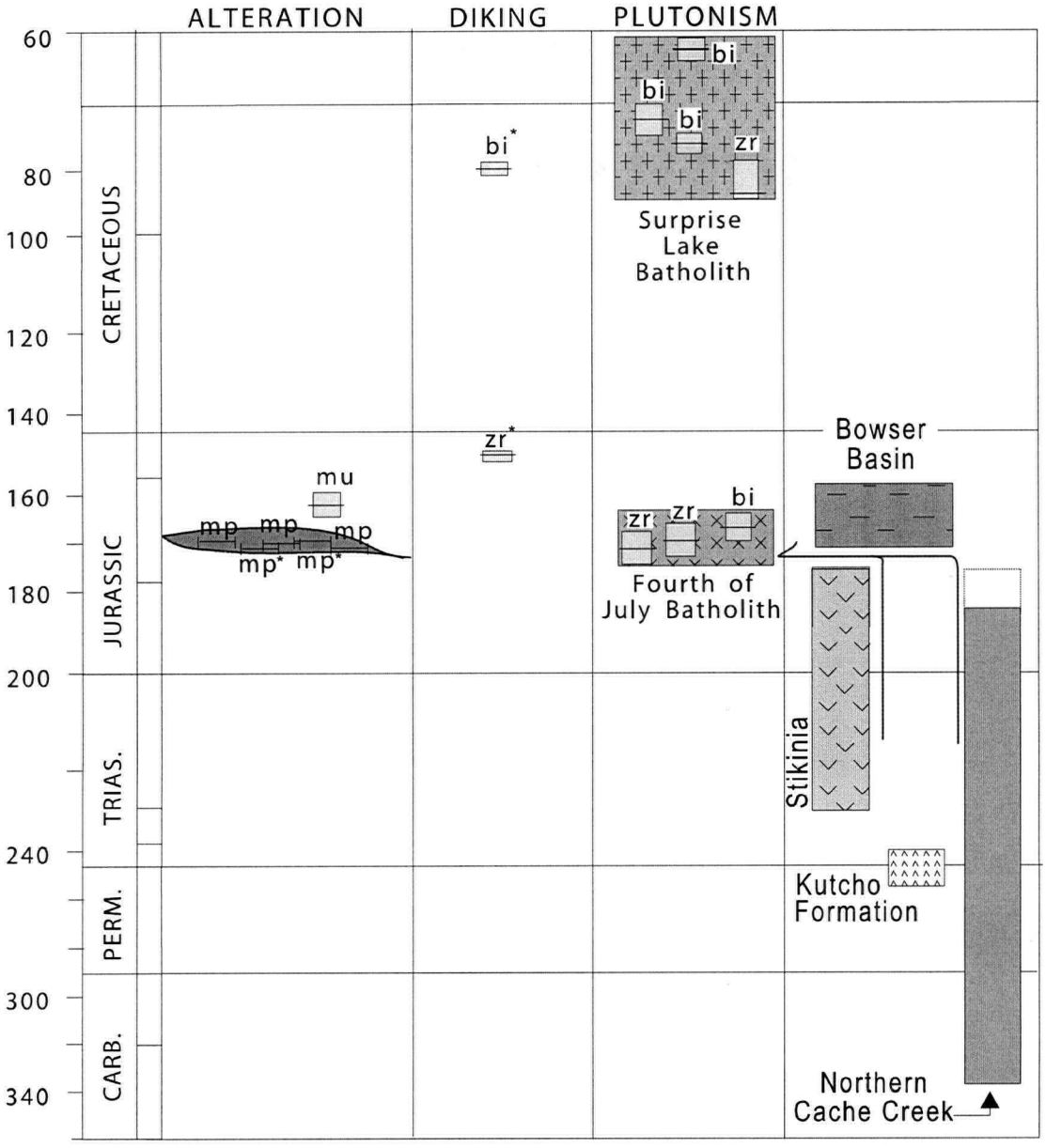

Figure 3.13: Simplified flow chart illustrating the geological history of the Atlin area. The symbols bi, mu, and mp represent $^{40}Ar/^{39}Ar$ dates acquired from biotite, muscovite, and Cr-muscovite (mariposite) respectively while zr denotes U-Pb zircon dates. * denotes analyses acquired from this study. Chart modified from Ash (2001).

Geochemical Research (PCIGR) at the University of British Columbia. All supporting data is located in Appendix D.

The reliable ^{40}Ar / ^{39}Ar Cr-muscovite dates of this study and Ash (2001) (Table 3.1, Fig. 3.13) suggest a primary listwanite alteration event at about 170 Ma, but possibly spanned a few million years (174 - 167 Ma). These ages are in excellent agreement with the U-Pb zircon age of 172 +/- 3 Ma for the FOJB (Mihalynuk *et al.*, 1992), and 167 +/- 3 Ma for a K-Ar biotite (cooling 280°C) from a small stock between Monarch and Union mountains. The overlapping age range of the plutonism and joint- and fracture-controlled listwanite suggests that unloading (erosion) had commenced prior to that time and that the plutonism was the local energy source responsible for mobilizing listwanite-forming hydrothermal fluids. Aalenian (ca. 178 - 174 Ma, Okulitch, 2001, and references therein) sediments of Cache Creek affinity recorded within the Bowser Basin to the southeast are interpreted to record the initial erosion as thrusts of the Cache Creek terrane were loaded onto Stikinia (Ricketts *et al.*, 1992).

Two samples of Cr-muscovite have ^{40}Ar-^{39}Ar plateau ages different from the others. Sample AT03-44-7 produced a plateau age of 188 +/- 1.8 Ma which is older than the expected age of obduction at ca. 170 Ma. There are numerous reasons for the anomalously high plateau age. One possibility is recoil where ^{39}K atoms are converted to ^{39}Ar atoms of sufficient energy to eject the atoms from the mineral phase that is being irradiated (Esser *et al.*, 2004). Another is excess Ar (T.D. Ulrich, 2005 pers. comm.). However an integrated age of 174.4 +/- 1.4 Ma is in agreement with other Cr-muscovite ages and is likely the true age of this sample. Sample 01AT1-2 produced a plateau age of 128 Ma which, though younger than expected, could represent a thermally reset age (T.D. Ulrich, 2005 pers. comm.).

The timing of listwanite alteration is constrained to have occurred synchronously or immediately after the collision of Stikinia with the northern Cache Creek terrane as determined by structural relationships and geochronologic analysis. As discussed earlier, the listwanite alteration is structurally controlled by four steeply-dipping sets of post-obduction joints and fractures with approximately 45° spacing. This pattern is consistent with a vertical maximum principle stress (σ_1). The joints and fractures are present within the ultramafic rocks, the underlying accretionary lithologies and also cross-cut the syn-

obduction S_2 fabric. Thus, the development of the fracture/joint system, and later listwanite alteration, is likely associated with unloading of the Atlin Ultramafic Allochthon after and/or in the very late stages of the collision of Cache Creek with Stikinia. Localized carbonate-flooded and altered breccia in the vicinity of the basal décollement and along a two km-long ridge on the southwest portion of Monarch Mountain suggests that carbonation postdates the main phase of tectonism.

Zircons extracted from the light-grey dacite phase yielded a date of 150.7 +/- 0.4 Ma (U-Pb, zircon) which is interpreted the age of crystalization. This age is unusual as there is very little known igneous activity in the area at this time (Mihalynuk, 1999). However, this places an upper limit on listwanite alteration at 150 Ma, and confirms that this phase is not associated with the FOJB. The fresh euhedral biotite book extracted from the grey-brown dacite yielded an ^{40}Ar-^{39}Ar plateau age of 84.0 +/- 0.6 Ma which is contemporaneous with and likely related to the Surprise Lake Batholith (83.8 +/- 5 Ma, U-Pb zircon date, Table 3.1) which outcrops about 18 km east of Atlin. Unfortunately, an age could not be determined for the diabase phase.

The cross-cutting relationships, geochronologic and structural analyses clearly demonstrate the setting of listwanite alteration. Figure 3.14 shows schematically that the carbonate-alteration is controlled by a post-obduction fracture-joint system and that the igneous intrusions post-date both. A similar association of carbonate alteration with a basal thrust and along steeply dipping joints and fractures is documented within the Voltri ophiolite at Liguria, Italy (Buisson and Leblanc, 1986).

3.6 ALTERATION ENVIRONMENT

The temperature of alteration is constrained by fluid inclusion analysis of quartz-carbonate veins to be in the range of 210°C to 280°C. Vapour to liquid homogenization temperatures ($Th_{L\text{-}V(L)}$) of 210°C to 240°C were measured from low salinity (<5wt% equivalent NaCl) fluid inclusions that show no evidence for phase separation (Andrew 1985). This is consistent with other listwanite systems including the Bridge River area of B.C. at 240°C (Madu *et al.*, 1990); the Timmins area of Ontario at ca. 250°C (Schandl and Wicks, 1991); and a listwanite occurrence in Morocco at 150°C to 300°C (Buisson and Lablanc, 1985). Pressure estimates for the Atlin listwanite alteration are poorly

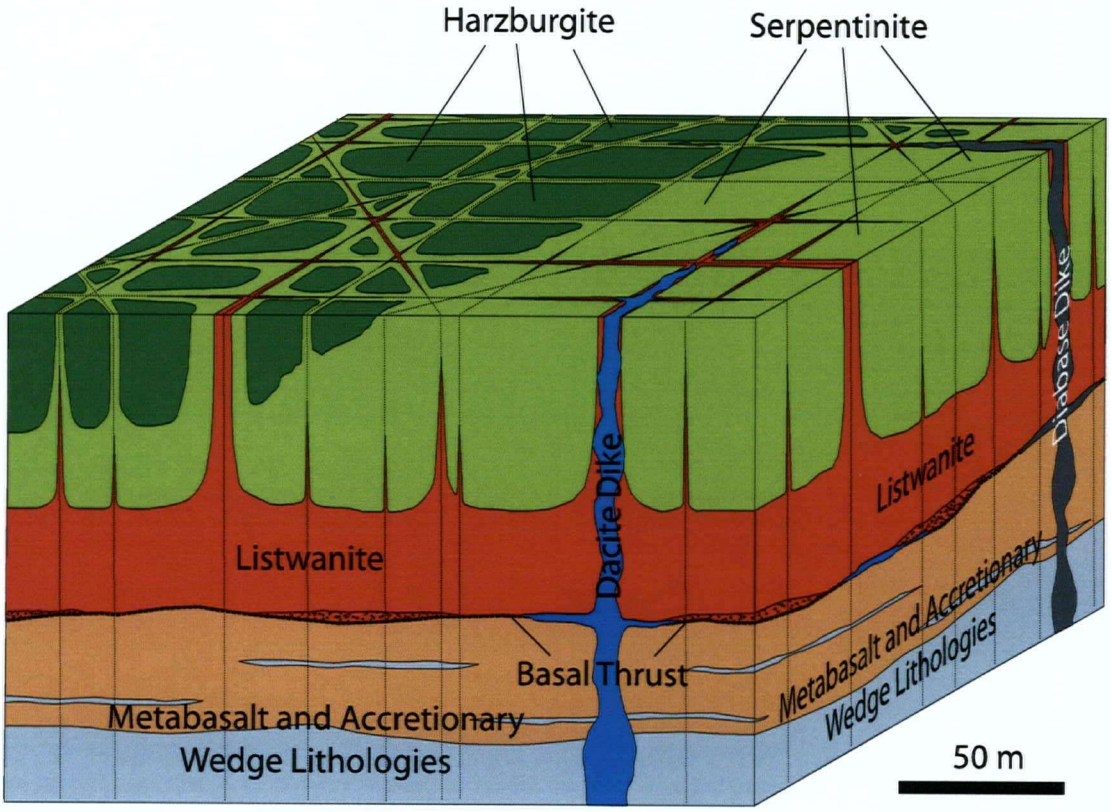

Figure 3.14: Schematic block diagram illustrating that post-obduction fractures and joints controlled the distribution of later listwanite alteration and dike emplacement. Dikes post-date the listwanite-alteration.

constrained. Al-in-hornblende geobarometry by Harris *et al.* (2003) suggests a depth of about 6 - 8 km (ca. 1.5 - 2.2 kbar lithostatic) for the southern section of the FOJB which outcrops less than 2 km north of the Atlin Ultramafic Allochthon. Given that the batholith and listwanite alteration are contemporaneous, listwanite was likely formed at the same depth or slightly shallower than this part of the FOJB. The joint/fracture controls, open space-filling nature and bladed carbonate within quartz and/or carbonate veins (Fig. 3.10) are consistent with a relatively shallow and sub-lithostatic to hydrostatic (ca. 600 - 800 bars at 6 - 8 km depth assuming a hydrostatic gradient of 100 bars/km depth) hydrothermal environment.

3.7 STABLE ISOTOPES

The stable isotope compositions of O and C in carbonate minerals from weakly to completely carbonate-altered samples were measured at the PCIGR in an attempt to decipher the origin of the carbon and altering fluid. Three different episodes of magnesite generation (M_1 to M_3) were produced during the three listwanite reactions (R_1 to R_3). In addition, stable isotopic data was acquired from one sample of hard black organic material ($\delta^{13}C$ = -27.16‰) taken from the listwanite occurrence proximal to the northwest trending Nahlin fault located approximately 60 km to the south-southeast of Atlin. Figure 3.15 illustrates the results from Atlin and Table 3.2 shows a generalized comparison with other listwanite systems. In general, results from this study and from other listwanite systems are broadly similar and likely indicate a similar hydrothermal environment and origin for CO_2-bearing fluids. The results are discussed below.

The boxes in Figure 3.15 enclose the stable isotopic results from the approximately 10 cm-thick transect A-B through the listwanite zone (depicted in Figure 3.16) and show the outcrop-scale change in isotopic composition during carbonate alteration. Regionally, magnesite-, talc- and quartz-zone carbonate all span a range of $\delta^{13}C$ from -1 to -7‰ VPDB and $\delta^{18}O$ from 6 to 16‰ VSMOW. Within outcrop AT03-20, however, there is a clear difference in the stable isotope composition of the talc- and magnesite-zones. The talc-zone is depleted in ^{13}C and enriched in ^{18}O relative to magnesite-zone samples. About 20% carbonate in the talc-zone has formed prior to the first appearance of talc (M_1 magnesite, estimated from data in Appendix C). Thus, the

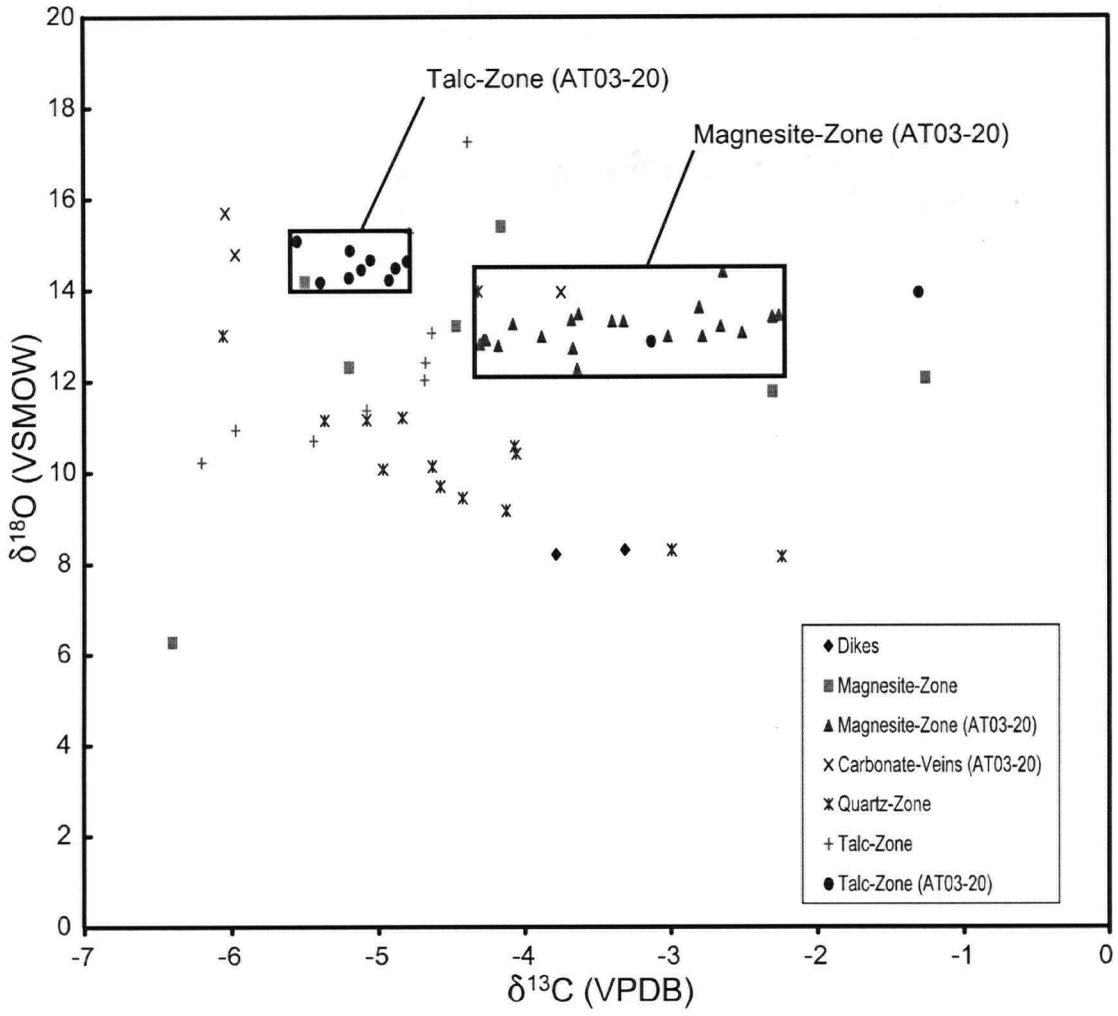

Figure 3.15: Stable isotope compositions from carbonate within the listwanite in the Atlin area. The closed boxes enclose samples taken from within and near the 2 by 2 metre area shown in Figure 3.16.

Table 3.2: Stable isotopic compositions from various listwanite systems

Location	n	$\delta^{13}C_{(VPDB)}$ ‰	$\delta^{18}O_{(VSMOW)}$ ‰	$\delta D_{(VSMOW)}$ ‰	Notes	Reference
Atlin	5	-	5.7 (3.8 to 7.7)	-	Silicate (A_1)	This Study
Atlin	28	-3.5 (-2.3 to -6.4)	12.9 (6.3 to 15.4)	-	Mgs & Dol (R_1-A_2)	This Study
Atlin	9	-4.8 (-0.3 to -6.2)	12.1 (10.2 to 17.3)	-	Carbonate (R_2-A_3)	This Study
Atlin	14	-4.4 (-2.2 to -6.1)	10.5 (8.3 to 14.0)	-	Carbonate (R_3-A_4)	This Study
Atlin	14	-4.6 (-1.3 to -5.6)	13.9 (12.9 to 15.1)	-	Carbonate (R_2-A_3)^x	This Study
Atlin	3	-5.3 (-3.8 to -6.0)	14.8 (14.0 to 15.7)	-	Mgs-Dol Vein from R_2	This Study
Atlin	1	-3.3	8.3	-	Carbonated Diabase	This Study
Atlin	1	-3.8	8.2	-	Carbonated Dacite	This Study
Nahlin Fault	1	-27.2	-	-	Pyrobitumen	This Study
Morocco	N/A	ca. -4	ca. 18	-	Mgs in Listwanite	Buison and Leblanc (1985)
Bridge River, B.C.	N/A	(-8.6 to -10.7)	13.2 +/- 1.5*	-136 to -142	Fluid Inclusions	Madu et al. (1990)
Bridge River, B.C.	N/A	(-5.1 to -6.7)	(24 to 25)	-	Carbonate in Listwanite	Madu et al. (1990)
Timmins, Ont.	N/A	(-7.5 to -7.9)	(11.7 to 16.5)	-	Mgs in Mgs-Tlc rock	Schandl and Wicks (1991)

*Calculated from quartz-H_2O equilibrium and fractionation factor of 3.7
^{x} denotes samples containing black organic material
Compositions are given as an average and/or range given within parenthesis

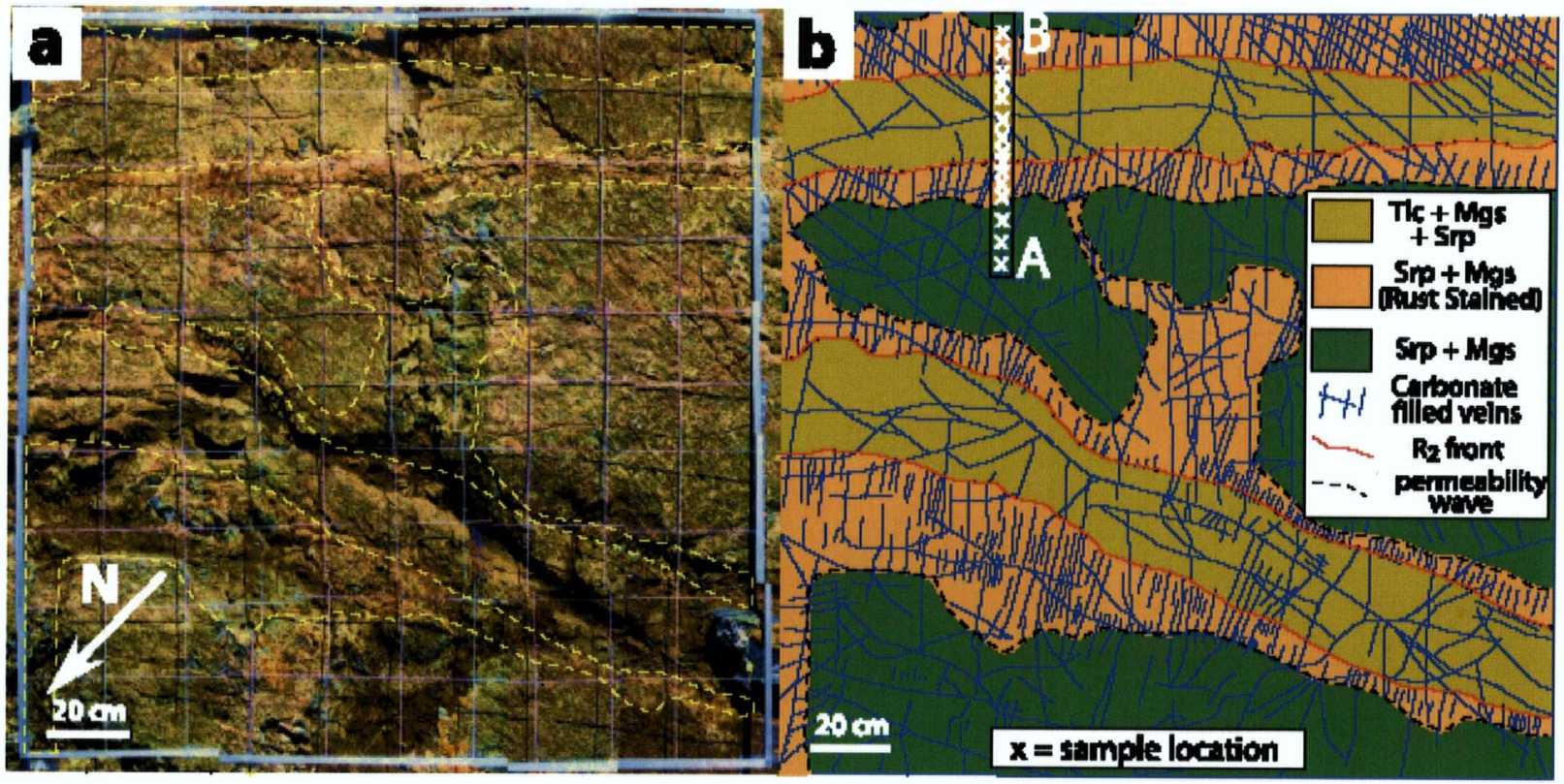

Figure 3.16: a) Composite image of a 2 by 2 metre pavement outcropping on the western slope of Monarch Mountain (E 575887, N 6602098, NAD 83). Dashed yellow lines are contacts in Figure 3.16b. b) Detailed geologic map of the listwanite zone mapped at 1:20 scale.

actual composition of M_2 could plot at about $\delta^{13}C$ = -6‰ and $\delta^{18}O$ = 15.5‰. The talc-zone samples also contain inclusions of black organic carbon.

3.8 HYDROTHERMAL ORGANIC MATERIAL

Carbon isotope data and the presence of hydrothermally mobilized organic material within listwanite (Fig. 3.17) implicate hydrothermal circulation through metasedimentary material. The $\delta^{13}C$ of around -6‰ for carbonate approaches an organic signature. Furthermore, the $\delta^{13}C$ of -27‰ for organic material sampled from the Nahlin fault (Fig. 3.17a) is the expected value of petroleum derived from vegetation (Campbell and Larson, 1998, and references therein) and is similar to that acquired from hydrothermal petroleum by Rasmussen and Buick (2000) and Simoneit (2002). Similar-looking material was found within listwanite at Atlin (Figure 3.17b) and in carbon-rich veins material at the Erickson mine near Cassiar, B.C. (Sketchley and Sinclair, 1987). All three B.C. localities are associated with ultramafic material sutured to the edge of the northern Cache Creek Terrane. Fluid inclusion analyses reported by Madu *et al.* (1990); Buisson and Leblanc (1987) and Schandl and Wicks (1991) indicate CH_4 within the altering fluid of their respective field studies. The only obvious nearby source for organic material is the Atlin Accretionary Complex (AAC).

3.9 SOURCE FOR GOLD AND CARBON

Potential sources for gold include: the ultramafic rocks, underlying accretionary complex lithologies, and the Middle Jurassic igneous batholiths (particularly the nearby FOJB). In addition to the stable isotopic study, 40 samples were submitted for gold assaying with the results shown in Figure 3.18. Gold assay results were acquired by fire assay and IPCES at ALS Chemex laboratories in North Vancouver, British Columbia. Ten samples from each reaction zone (i.e. protolith samples, magnesite-, talc- and quartz-zone samples) were analyzed. In order to assess the potential nugget effect of gold in these samples, replicates and a standard were submitted. Unfortunately, the masses of rock powder from magnesite- and talc-zone samples were inadequate to submit replicate samples. For these two zones, five samples from each group were taken from a 70 by 10 cm area within the grid-mapped outcrop depicted in Figure 3.16.

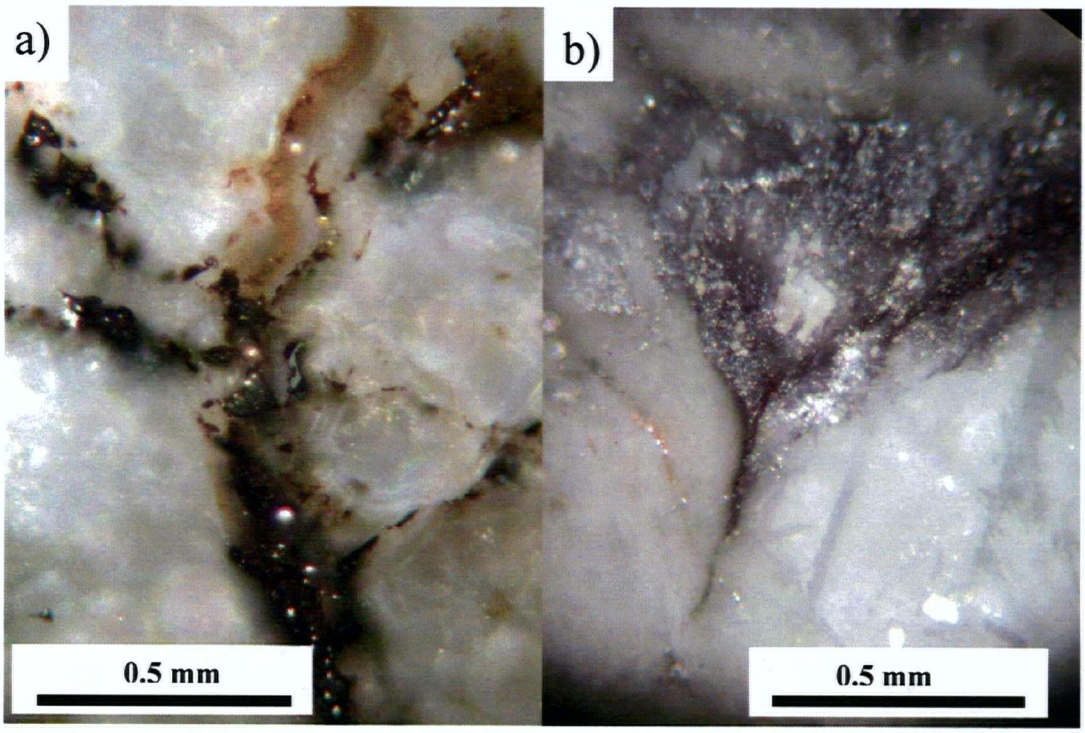

Figure 3.17: Reflected light photomicrographs of: a) organic material within veins in quartz-zone listwanite sampled from the Nahlin fault to the southeast of Atlin. b) organic material occupying a vein within talc-zone of the listwanite zone depicted in Figure 3.16. Note that the bright specs are sulfide and they are associated with the dark organic material.

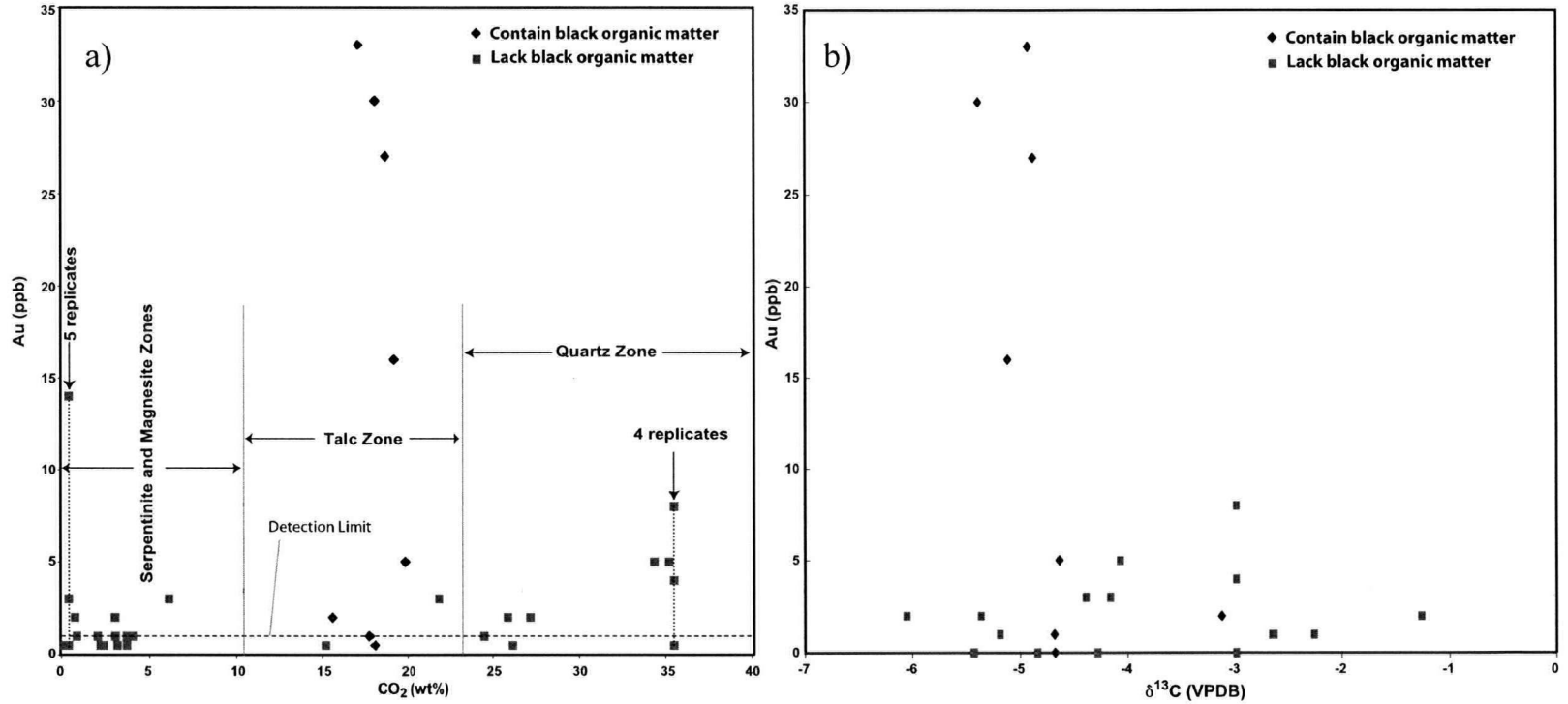

Figure 3.18: Gold content of samples verses a) whole rock CO_2. b) $\delta^{13}C$ in carbonate minerals.

Buisson and Leblanc (1987) suggest that gold, concentrated within oxides (i.e. magnetite), is released and mobilized during the talc-generating reaction that destroys magnetite. The amount released from the ultramafic rocks during this step was suggested to be about 2.7 ppb. If 2.7 ppb was released during talc-zone alteration, the amount of gold released from the Atlin Ultramafic Allochthon would amount to about 141,000 oz gold. This number is based on a 25 km^2 ultramafic body with a 50 m-thick listwanite zone at its base, 50% of which is talc-zone. Although this number is significant, no leaching of Au in the talc-zone was detected at Atlin (Fig. 3.18). In fact the assay results indicate that talc-zone samples are either similar to, or elevated in, Au relative to that of serpentinite. Thus, leaching of Au has likely not occurred within the talc-zone at Atlin.

Ash *et al.* (1992) consider an alternate model that involves the leaching of gold from a tectonically thickened package of oceanic crustal rocks which have undergone partial melting at deeper levels of the crust that in turn drove large-scale hydrothermal convection. There are many lines of evidence that suggest gold was either derived from fluid exsolved from Middle Jurassic batholiths and/or leached from accretionary wedge lithologies during hydrothermal circulation driven by the large-scale igneous activity. Firstly, the U-Pb zircon age range of the FOJB completely overlaps the age range of Cr-muscovite in the listwanite (Table 3.1). Streams that drain the FOJB contain stream sediments with anomalous Au contents (Jackaman, 2000). Ash *et al.,* (1992) noted that most listwanite-associated lode-gold camps in B.C. are associated with syn- to post-accretionary felsic magmatism.

The large range in $\delta^{18}O$ suggests that there was interaction of listwanite-altering hydrothermal fluids with the heterolithic sedimentary and carbonate material of the AAC. Listwanite samples elevated in gold contain organic material and are depleted in $\delta^{13}C$ (Fig. 3.18). These observations suggest the gold was exsolved from the FOJB and/or scavenged from the ACC, possibly as bisulfide complexes, considered the most important group of ligands in transporting gold in hydrothermal fluids (Mikucki, 1998, and references therein). The correlation of organic material and gold suggests a possible role for organic material in the transportation and/or deposition of gold and sulfide.

3.10 CONCLUSION

The listwanite alteration within the Atlin Ultramafic Allochthon at Atlin, B.C., is spatially controlled by a basal thrust fault (e.g. Ash, 1994; Hansen *et al.*, 2004; Chapter II) and regional joint/fracture system with four steeply-dipping fracture sets spaced about 45° apart (Hansen *et al.* 2004, Chapters II and III). The U-Pb (zircon) and ^{40}Ar-^{39}Ar (Cr-muscovite) isotopic ages of the nearby FOJB and the listwanite alteration respectively (Ash, 2001; Mihalynuk *et al.*, 1992; This Study) indicate that the two events were contemporaneous and likely related and occurred at about 170 Ma. The most depleted $\delta^{13}C$ within magnesite is around -6‰ which is consistent with an organic signature and is supported by the presence of organic material within listwanite-altered rocks. The large range in $\delta^{18}O$ of between 6.3‰ and 17.3‰ suggests interaction of the altering fluids with the pelagic sedimentary rocks of the Atlin Accretionary Complex (AAC). The only obvious nearby source of organic material is the pelagic units of the AAC. These results suggest large-scale hydrothermal circulation of fluids, driven by the FOJB, through the metasedimentary, metavolcanic and carbonate rocks of the AAC. These fluids acted to mobilized and incorporated organic material which then infiltrated and carbonate altered the ultramafic rock material of the Atlin Ultramafic Allochthon.

Anomalous gold values are associated with organic material and low $\delta^{13}C$ values. The gold content of the three listwanite zones are at or above that for the parental serpentinite. These observations and analyses are consistent with gold having been scavenged from the underlying accretionary complex lithologies or derived from the contemporaneous and nearby FOJB rather than being scavenged from the ultramafic rocks.

3.11 REFERENCES

Andrew, K. (1985): Fluid Inclusion and Chemical Studies of Gold-Quartz Veins in the Atlin Camp, Northwestern British Columbia; Unpublished B.Sc. thesis, Department of Geological Sciences, Vancouver, B.C., Canada, 116 p.

Anderson, R. G., Lowe, C. and Villeneuve, M. E. (2003): Nature, Age, Setting, and Mineral Potential of Some Mesozoic Plutons in Central and Northwestern Atlin Map Area (NTS 104N), Northwestern B.C.; (abstract); Vancouver 2003 Abstracts, CD-ROM, GAC-MAC-SEG Vancouver 2003 Annual General Meeting, Vancouver, B.C., v. 28, abstract no. 600, ISSN 0701-8738, ISBN: 0-919216-86-2.

Ash, C. H. (1994): Origin and Tectonic Setting of Ophiolitic Ultramafic and Related Rocks in the Atlin Area, British Columbia (NTS 104N); B.C. Ministry of Energy, Mines and Petroleum Resources, Bulletin 94, 48 p.

Ash, C. H. (2001): Relationship Between Ophiolites and Gold-Quartz Veins in the North American Cordillera; British Columbia Department of Energy, Mines and Petroleum Resources, Bulletin 108, 140 p.

Ash, C. H. and Arksey, R. L. (1990): The Atlin Ultramafic Allochthon: Ophiolite Basement Within the Cache Creek Terrane; Tectonic and Metallogenic Significance (104N/12); Geological Fieldwork 1989, B.C. Department of Energy and Mines, Paper 1990-1, p. 365-374.

Ash, C. H., Macdonald, R. W. J. and Arksey, R. L. (1991): Towards a Deposit Model for Ophiolite Related Mesothermal Gold in British Columbia; Geological Fieldwork 1991, BC Department of Energy and Mines, Paper 1992-1, p. 253-260.

Buisson, G. and LeBlanc, M. (1986): Gold-Bearing Listwaenites (Carbonitized Ultramafic Rocks) from Ophiolite Complexes; in Metallogeny of Basic and Ultrabasic Rocks, Gallagher, M., Ixer, R., Neary, C. and Prichard, H., Editors, The Institution of Mining and Metallurgy, pages 121-131.

Campbell, A.R. and Larsen, P. (1998): Introduction to Stable Isotope Applications in Hydrothermal Systems. In: Techniques in Hydrothermal Ore Deposit Geology. Editors: J. Richardson and P. Larsen. Reviews in Economic Geology, 10, 173-193.

Buisson, G. and LeBlanc, M. (1987): Gold in Mantle Peridotites from Upper Proterozoic Ophiolites in Arabia, Mali, and Morocco; Economic Geology, v. 82, p. 2091-2097.

Buisson, G. and Leblanc, M. (1985): Gold in Carbonatized Ultramafic Rocks from Ophiolite Complexes; Economic Geology, 80, 2028-2029.

Esser, R. P., McIntosh, W. C. and Mack, G. H. (2003): $^{40}Ar/^{39}Ar$ Geochronology Results from Clasts from Late from Late Cretaceous/Early Tertiary Units of the Caballo Mountains, New Mexico; New Mexico Bureau of Geology and Mineral Resources, Memoir 49, 22 pages.

Hansen, L.D., Dipple, G. M., Kellett, D. A. And Gordon, T. M. (2005): Carbonate-Altered Serpentinite: A Geologic Analogue to Carbon Dioxide Sequestration, Canadian Mineralogist, v. 43, part 1, p. 225-239.

Hansen, L. D., Dipple, G. M., Anderson, R. G. and Nakano, K. F. (2004): Geologic Setting of Carbonate Metasomatised Serpentinite (Listwanite) at Atlin, British Columbia: implications for CO_2 sequestration and lode-gold mineralization. In Current Research, Geological Survey of Canada, Paper 2004-A5, 12 pages.

Harris, M. J., Symons, D. T., Blackburn, W. H., Hart, C. J., Villenueve, M. (2003): Travels of the Cache Creek Terrane: a Paleomagnetic, Geobarometric and $^{40}Ar/^{39}Ar$ Study of the Jurassic Fourth of July Batholith, Canadian Cordillera; Tectonophysics, 362, 137-159.

Hunt, P.A. and Roddick, J.C. (1988): A Compilation of K-Ar Ages, Report 18; In Radiogenic Age and Isotopic Studies, Report 2, Geological Survey of Canada, Paper 88-2, 127-153.

Jackaman, W. (2000): British Columbia Regional Geochemical Survey, NTS 104N/1 - Atlin; British Columbia Ministry of Energy and Mines, BC RGS 51.

Madu, B. E., Nesbitt, B. E. and Muehlenbachs, K. (1990): A Mesothermal Gold-Stibnite-Quartz Vein Occurrence in the Canadian Cordillera. Economic Geology, 85, 1260-1268.

Matsuhisa, Y., Goldsmith, J. R. and Clayton, R. N. (1979): Oxygen Isotope Fractionation in the System Quartz-Albite-Anorthite-Water, Geochimica et Cosmochimica Acta, 43, 1131-1140.

Mihalynuk, M.G. (1999): Geology and Mineral Resources of the Tagish Lake Area (NTS 104M/8, 9, 10E, 15 and 140N/12W), Northwestern British Columbia; British Columbia Department of Energy, Mines and Petroleum Resources, Bulletin 105, 217 p.

Mihalynuk, M. G., Smith, M., Gabites, J. E., Runkle, D. and Lefebure, D. (1992): Age of Emplacement and Basement Character of the Cache Creek Terrane as Constrained by New Isotopic and Geochemical Data; Canadian Journal of Earth Sciences, 29, p. 2463-2477.

Mikucki, E. J.(1998): Hydrothermal Transport and Deposition Processes in Archean Lode-Gold Systems: a Review; Ore Geology Reviews, 13, 307-321.

Okulitch, A.V. (2001): Geological Time Scale, 2001. Geological Survey of Canada, Open File 3040 (National Earth Science Series, Geological Atlas) – REVISION

Rasmussen, B. and Buick, R. (2000): Oily Old Ores: Evidence for Hydrothermal Petroleum Generation in an Archean Volcanogenic Massive Sulfide Deposit; Geology, 28, 731-734.

Ricketts, D.B., Evenchick, C.A., Anderson, R.G. and Murphy, D.C. (1992): Bowser Basin, Northern British Columbia: Constraints on the Timing of Initial Subsidence and Stikinia - North America Terrane Interactions; Geology, 20, 1119-1122.

Rytuba, J. J. (1993): Epithermal Precious-Metal and Mercury Deposits in the Sonoma and Clear Lake Volcanic Fields, California, In Rytuba, J. J., ed., Active geothermal systems and gold-mercury deposits in the Sonoma-Clear Lake volcanic fields: Soc. Econ. Geol. Guidebook Series, 16, 38-51.

Schandl, E. S. and Wicks, F. J. (1991): Two Stages of CO_2 Metasomatism at the Munro mine, Munro Township, Ontario: Evidence from Fluid-Inclusion, Stable-Isotope, and Mineralogical Studies. Canadian Journal of Earth Sciences, 28, 721-728.

Schandl, E. S. and Naldrett, A. J. (1992): CO_2 Metasomatism of Serpentinites, South of Timmins, Ontario; Canadian Mineralogist, v. 30, p. 93-108.

Simoneit, B. (2002): Carbon Isotope Systematics of Individual Hydrocarbons in Hydrothermal Petroleum from Middle Valley, Northeastern Pacific Ocean; Applied Geochemistry, 17, 1429-1433.

Sketchley, D. A. and Sinclair, A, J. (1987): Multi-Element Lithogeochemistry of Alteration Associated with Gold-Quartz Veins of the Erickson Mine, Cassiar District (104P/4); Geological Fieldwork 1991, BC Department of Energy and Mines, Paper 1987-1, p. 57-63.

Wittkopp, R. W. (1983): Hypothesis for the Localization of Gold in Quartz Veins, Allegheny District; California Geology, p. 123-127.

CHAPTER IV: CARBONATED SERPENTINITE (LISTWANITE) AT ATLIN, BRITISH COLUMBIA: A GEOLOGICAL ANALOGUE TO CARBON DIOXIDE SEQUESTRATION.[1]

4.1 INTRODUCTION

The presence of low-temperature carbonated ultramafic rocks in nature suggests that conditions favourable for mineral carbonation exist at shallow levels of the crust. In mineral carbonation, CO_2 is chemically bound within a carbonate mineral structure by reaction with Mg^{2+} or Ca^{2+} derived from silicate minerals. Fossil analogues to mineral carbonation systems are common in ultramafic terranes throughout the world and produce a suite of metamorphic rocks composed of serpentine, magnesite, talc and quartz-bearing mineral assemblages. These rocks are known as listwanite (Kashkai and Allakhverdiev, 1965) or silica-carbonate alteration (Sherlock *et al.*, 1993). Listwanite has historically been studied because it is common spatial association with lode-gold mineralization (e.g. Ash, 2001; Schandl and Naldrett, 1992; Wittkopp, 1983). Liswanite metamorphism has generally been considered a highly metasomatic process that leads to wholesale changes in bulk rock composition (Schandl and Naldrett, 1992, Sherlock *et al.*, 1993).

Here we document the mineral reactions, geochemical alteration, and permeability system accompanying listwanite formation near Atlin, British Columbia. Listwanite distribution is controlled structurally by a pre-existing joint and fracture network, which served as high-permeability pathways for percolation of CO_2-bearing fluid. Evidence for carbonation, indicated by Mg-carbonate minerals, is present for tens of metres into wallrock adjacent to controlling fractures. The permeability structure of these systems is therefore similar to that of proposed industrial-scale *in situ* mineral carbonation systems, which would utilize joints and fractures as a permeability network. Pervasive listwanite formation adjacent to the fracture systems was isochemical in all

[1] A version of this chapter has been published as: Hansen, L.D., Dipple, G.M., Gordon, T.M. and Kellett, D.A. (2005): Carbonated Serpentinite (listwanite) at Atlin, British Columbia: A Geological Analogue to Carbon Dioxide Sequestration, Canadian Mineralogist, Vol. 43, pp. 225-239.

major chemical species except H_2O and CO_2, and the overall mineralogical transformation is the same as $R_{A \text{ and } B}$ (see reactions below). These deposits therefore serve as a geological analogue to mineral carbonation. The carbonation process is recorded as mineralogical zonation separated by reaction fronts, which permits each reaction to be examined in isolation. Reactions can therefore be examined individually for their CO_2 sequestration potential and impact on porosity and permeability.

$$Mg_3Si_2O_5(OH)_4 + 3\ CO_2 \rightarrow 3\ MgCO_3 + 2\ SiO_2 + 2\ H_2O \qquad (\mathbf{R_A})$$

(Serpentine → Magnesite + Quartz)

$$Mg_2SiO_4 + 2\ CO_2 \rightarrow 2\ MgCO_3 + SiO_2 \qquad (\mathbf{R_B})$$

(Olivine → Magnesite + Quartz)

4.2 RELEVANCE TO INDUSTRIAL APPLICATIONS

The carbonation of serpentine and forsterite (Mg-olivine), to stable Mg-carbonate minerals is of environmental interest because of its ability to fix anthropogenic carbon dioxide (CO_2) (Seifritz, 1990). Globally, mineral carbonation offers virtually unlimited capacity and the promise of safe, permanent storage of CO_2, with little risk of accidental release (Guthrie *et al.*, 2001). Proposed industrial implementation of mineral carbonation includes the capture of CO_2 from a point source such as a coal-fired power plant, and transport by pipeline to a reaction facility for storage. Reaction could occur within an industrial chemical reactor by carbonation of ultramafic rock mined from a quarry. However, this process demands highly efficient and rapid mineral transformation (O'Connor *et al.*, 2001). Alternatively, direct injection of CO_2 into large subsurface ultramafic formations allows for reaction times of tens to hundreds of years (Guthrie *et al.*, 2001), in a process known as *in situ* mineral carbonation.

Numerous magnesium silicate carbonation schemes have been tested in the laboratory (Goff and Lackner, 1998; Goldberg *et al.*, 2001; O'Connor *et al.*, 2001; Wu *et*

al. 2001; Zevenhoven and Kohlmann, 2001), and all involve chemical reactions such as R_A and R_B. To date, the rate of reaction in the laboratory has been reported to be up to about 80% conversion of serpentine to silica and magnesite in 30 minutes at 155°C and 185 bar (O'Connor *et al.*, 2001). However this is still too sluggish and the process too costly to accommodate industrial CO_2 output within industrial reactors. *In situ* mineral carbonation could proceed at a more leisurely pace; however there are no reliable mineral carbonation experiments in CO_2 injection systems (Matter *et al.*, 2002). Reaction path modelling predicts that CO_2 injection into serpentine reservoirs (at 250 bars and 60°C) would result in substantial CO_2 sequestration in a few 10's of years (Cipolli *et al.*, 2004). Moreover, the large increase in the volume of solids (21% for serpentine and 80% for olivine) associated with $R_{A \text{ and } B}$ may reduce the sequestration capacity of the reservoir by destroying permeability at the injection site.

4.3 GEOLOGICAL SETTING

The ultramafic rocks at Atlin represent a tectonically emplaced upper mantle section of oceanic lithosphere (Ash and Arksey, 1990a) composed predominantly of harzburgite and minor dunite, now mostly transformed to serpentinite and listwanite. Aitken (1959), Ash and Arksey (1990a), Hansen *et al.* (2004) and Chapters II and III documented the structural controls of listwanite distribution (Fig. 4.1, insert). Listwanite overprints serpentinite foliation formed during ophiolite obduction, indicating that listwanite formation postdates the emplacement of ophiolitic material onto the Stikine and Cache Creek terranes (Ash 1994). The timing of listwanite genesis in the Atlin area is also constrained by ^{40}Ar-^{39}Ar age determination of chromium-muscovite to be in the range of ca. 168 – 172 Ma (Ash, 2001). Further details on the regional geology near Atlin are provided in Monger (1975, 1977a, b), Monger *et al.* (1978), Bloodgood *et al.* (1989), Ash and Arksey (1990b), Ash *et al.* (1991), Mihalynuk *et al.* (1992) and Ash (1994).

The temperature of formation is constrained by fluid inclusion analysis of quartz-carbonate veins to be in the range of 210 - 280°C. Homogenization temperatures ($Th_{L\text{-}V(L)}$) of 210 to 240°C were measured from low salinity (< 5wt% equivalent NaCl) fluid inclusions that show no evidence for phase separation (Andrew, 1985). Fracture-

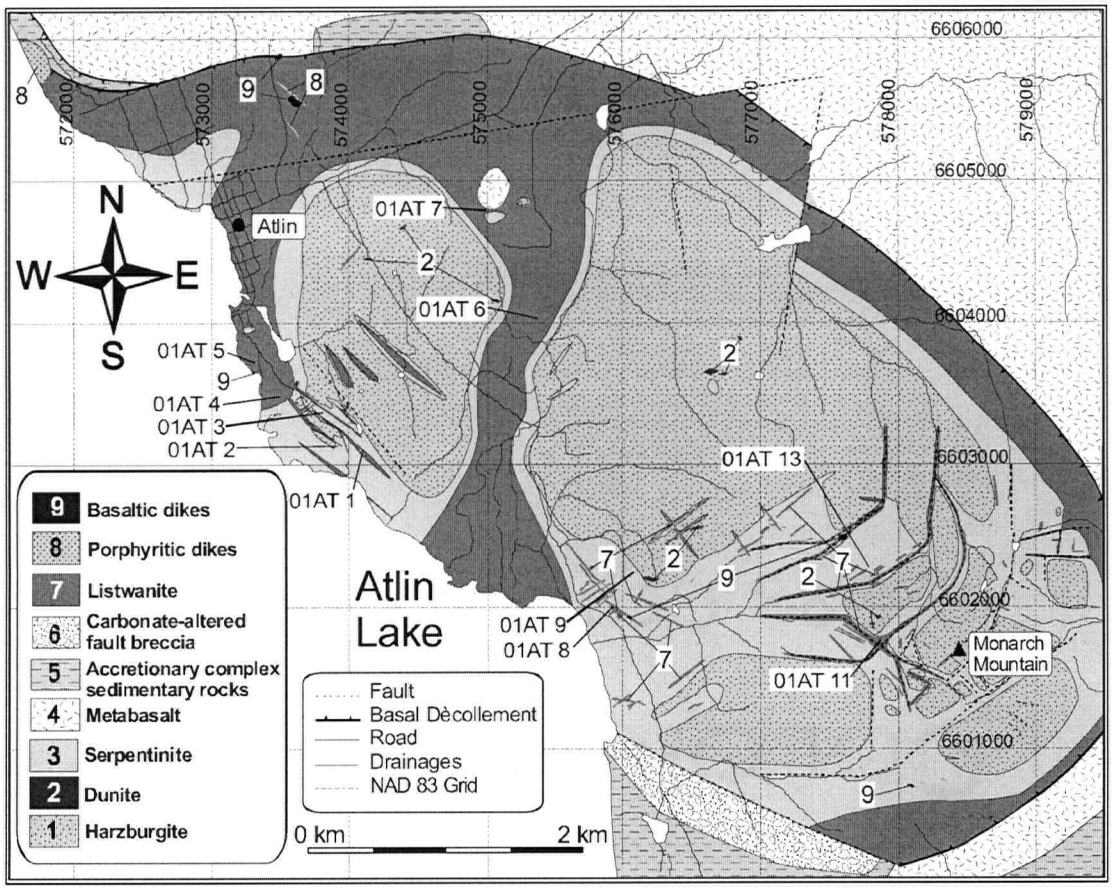

Figure 4.1: Simplified geologic map of the Atlin, B.C. area, illustrating the distribution of listwanite along the basal décollement and a fault/fracture permeability network (modified from Ash 1994, Chapter II and Hansen *et al.* 2003b).

controlled listwanite likely formed under sub-lithostatic fluid pressure which is assumed to be approximately 500 bars. Listwanite is very common in ultramafic bodies; two other well known occurrences include the Timmins area of Ontario (e.g. Schandl and Naldrett, 1992) and the Mother Lode camp in California (e.g. Wittkopp, 1983). Madu *et al.* (1990) and Schandl and Wicks (1991) report similar temperatures of formation from other listwanite occurrences.

4.4 STRUCTURAL CONTROL

Our field mapping confirms structural control of listwanite distribution along the basal décollement and along a transecting network of steeply-dipping joint and fractures sets (e.g. Hansen *et al.* 2004; Chapter II; Chapter III; Fig. 4.1). Although the joint and fracture systems served as the primary conduit for infiltration of CO_2-bearing fluid, pervasive carbonate alteration extends from a few centimetres to many tens of metres outward from the primary structural controls into intact bedrock. The most distal carbonation persists heterogeneously throughout the map area and cannot be accurately represented at the scale of Figure 4.1 where only the more focused and intense carbonation is mapped as listwanite. The reaction halos thus extend beyond the area mapped as listwanite, but the spatial distribution of more intensely carbonated rocks serves to illustrate the structural control of fluid infiltration. Mineralogical zonation within the halos is a record of the pathway of the carbonation reaction.

4.5 MINERALIGICAL ZONATION AND REACTION SEQUENCE

The Atlin ultramafic rocks are depleted mantle harzburgitic material formed during adiabatic melt extraction beneath a mid-ocean ridge (Ash and Arksey, 1990a). The melt extraction process and serpentinization event(s) have left the residual harzburgite chemically heterogeneous prior to listwanite metamorphism. The variation in modal orthopyroxene (opx) is a record of the original harzburgite heterogeneity. Serpentinization reactions consumed olivine + orthopyroxene to form serpentine + magnetite. The extent of serpentization generally exceeds 70% by volume. Serpentine pseudomorphs of opx are common.

The mineral content of serpentinite and listwanite was determined by X-ray diffraction (XRD) and optical and scanning electron microscopy (Table 4.1). Serpentine within uncarbonated samples was confirmed as antigorite by XRD and Raman spectroscopy (Rinaudo and Gastaldi, 2003). Uncarbonated antigorite +/- relict olivine, brucite and orthopyroxene assemblages were transformed to assemblages containing antigorite, magnesite, talc and quartz. The mineral assemblages track the migration of three carbonation reactions summarized in Figure 4.2. In sum, these reactions result in the overall transformations recorded in reactions $R_{A \text{ and } B}$. The physical separation of the reaction fronts allows each reaction to be examined in isolation. The boundaries separating each mineral assemblage are reaction isograds in the sense of Carmichael (1970).

The most distal carbonation reactions are volumetrically minor and involve the breakdown of relict olivine via reaction R_{1a} to antigorite and magnesite (Fig. 4.3a, assemblage A_2 of Fig. 4.2):

$$34\ Mg_2SiO_4 + 20\ CO_2 + 31\ H_2O \rightarrow Mg_{48}Si_{34}O_{85}(OH)_{62} + 20\ MgCO_3 \qquad (\mathbf{R_{1a}})$$

Olivine → Antigorite + Magnesite

O'Hanley and Wicks (1995) documented reaction of olivine to lizardite and subsequent transformation to antigorite at Cassiar, B.C. We have been unable to confirm the presence of lizardite in samples recording reaction R_{1a}. Lacking evidence to the contrary, we therefore consider all serpentine to be antigorite.

Trace amounts of brucite are present in some A_1 assemblages but are not found in samples containing magnesite. Carbonation of olivine-bearing samples may therefore also have included the reaction:

$$Mg(OH)_2 + CO_2 \rightarrow MgCO_3 + H_2O \qquad (\mathbf{R_{1b}})$$

Brucite → Magnesite

Table 4.1: Mineralogy of carbonated serpentinite from Atlin, BC

Sample	Chr	Mgt	Brc	Ol	Srp	Mgs	Tlc	Qtz		CO_2 (wt%)
01AT-8-1	x	x			x				A_1	0.06
01AT-13-1	x	x			x				A_1	0.10
01AT-3-1	x	x	x		x				A_1	0.21
01AT-10-1	x	x	x	x	x				A_1	0.15
01AT-10-2	x	x	x	x	x	x[v]			A_1	0.26
01AT-2-2	x	x	x	x	x				A_1	0.33
01AT-9-1	x	x		x	x	x			R_1	2.10
01AT-11-1	x	x		x	x	x			R_1	2.57
01AT-1-9	x	x			x	x			A_2	3.37
01AT-6-3	x	x			x	x			A_2	4.00
01AT-1-8	x	x			x	x			A_2	4.60
01AT-13-2	x	x			x	x			A_2	7.12
01AT-11-2	x	x			x	x			A_2	9.60
01AT-7-3	x	x			x	x	x		R_2	3.40
01AT-1-7	x	x			x	x	x		R_2	7.19
01AT-1-6	x	x			x	x	x		R_2	9.54
01AT-9-2	x				x	x	x		R_2	17.26
01AT-7-1	x					x	x	x	R_3	21.83
01AT-5-4	x	x[y]				x	x	x	R_3	28.01
01AT-1-5	x	x[z]			x[w]	x	x	x	R_3	34.00
01AT-4-1*	x					x	x	x	R_3	34.34
01AT-5-2	x					x		x	A_4	35.20
01AT-6-1*	x					x		x	A_4	36.19

[v] only occurs in small veins
[w] occurs in small isolated patches
[y] armored relicts and late mantling of chromite and pyrite
[z] magnetite in late fractures and late mantling of chromite
* sample contains Cr-muscovite
Sample locations in Appendix F.

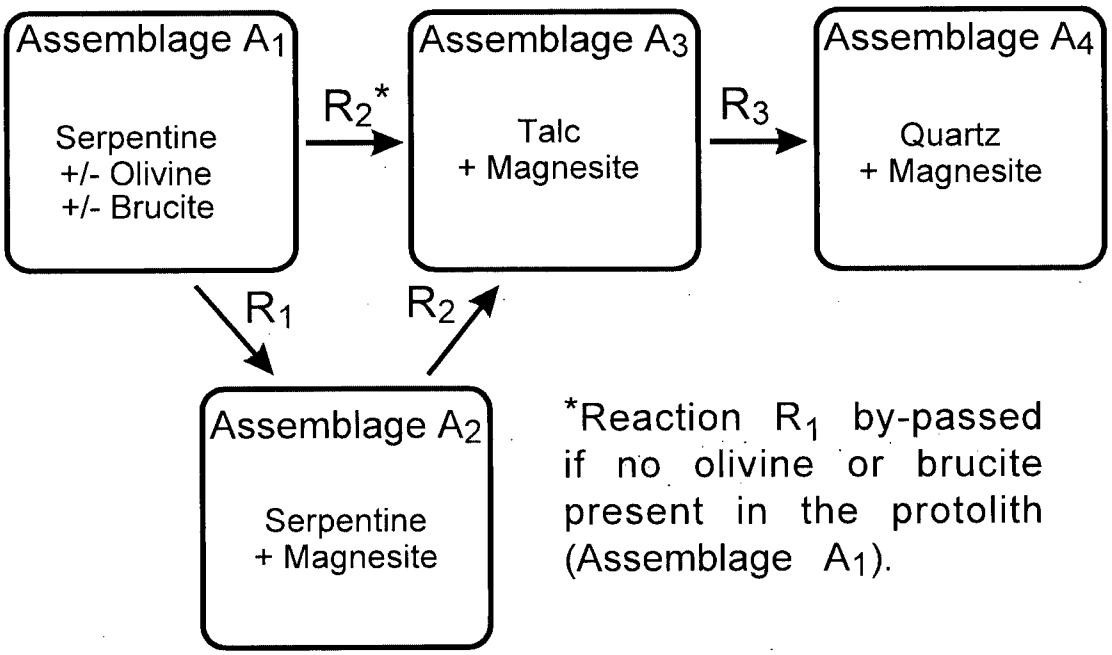

Figure 4.2: Simplified flow chart for the reaction path of the Atlin listwanite system during progressive carbonation of serpentinite.

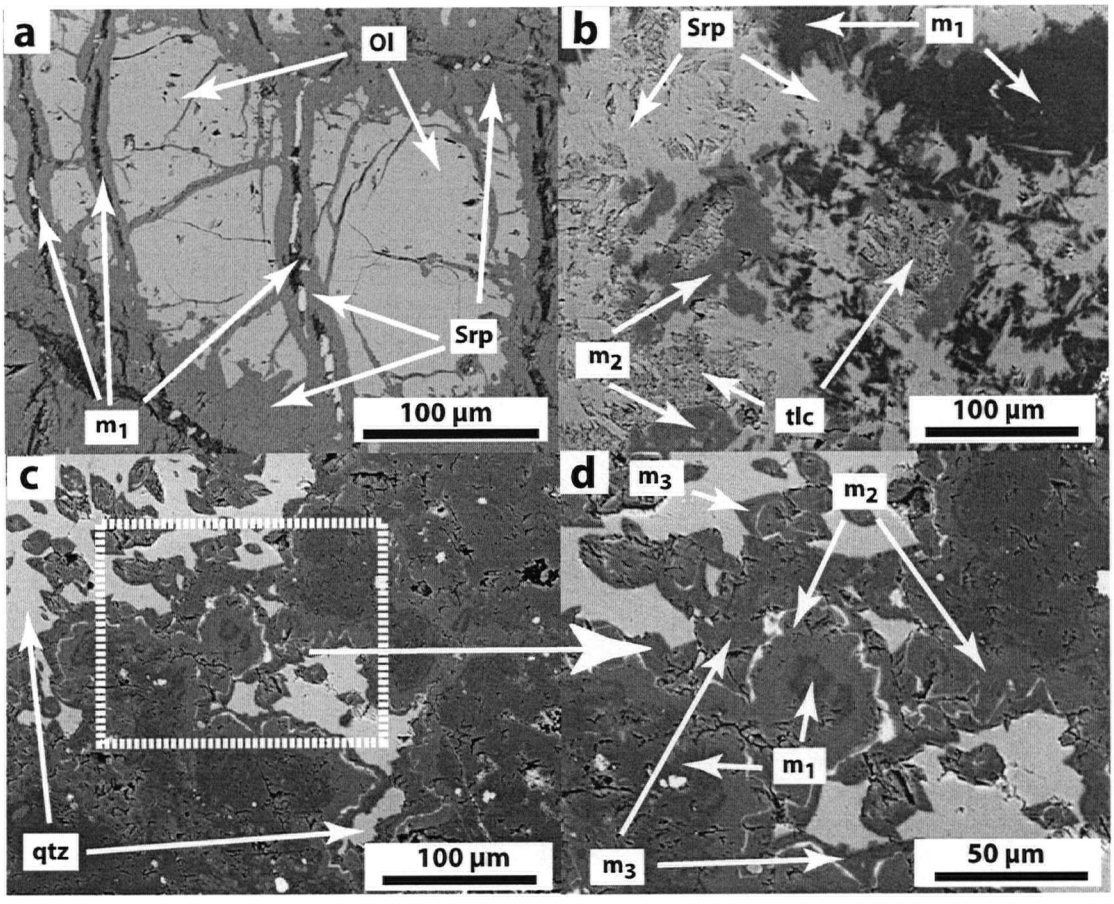

Figure 4.3: Backscattered scanning electron images showing progressive carbonation during listwanite genesis. a): Reaction R_{1b}: olivine to serpentine and magnesite (M_1) + magnetite. b): Reaction R_2: antigorite to magnesite (M_2) + talc. c): Reaction R_3: magnesite (M_3) + quartz assemblage. d): Close-up of (c). M_1, M_2 and M_3 are interpreted to represent magnesite generated during reactions R_1, R_2 and R_3 respectively. Note that magnesite M_2 rims M_1 and that M_3 rims M_2 and forms euhedral boundaries with quartz. Light grey magnesite has a higher mean atomic mass and higher Fe content than dark grey magnesite.

Coexisting products and reactants of R_{1b} have not been observed in any samples collected from Atlin. For simplicity, reactions R_{1a} and R_{1b} will be considered together as reaction R_1.

Reaction R_1 generally accommodates less than ca. 5 wt % CO_2 (Table 4.1) and is limited in progress by olivine (+/- brucite) abundance prior to carbonation. Formation of magnesite at the expense of olivine (+/- brucite) can be driven by a modest increase in the activity of CO_2 in the fluid phase with negligible decrease in activity of H_2O (Fig. 4.4b). Early, distal carbonation of brucite and olivine is consistent with the observed higher reactivity of olivine and brucite relative to serpentine in mineral carbonation experiments (Guthrie *et al.*, 2001; Lackner *et al.*, 1995).

The formation of magnesite plus talc (Assemblage A_3) and destruction of antigorite (Fig. 4.3b) marks a major carbonation front and occurs throughout most of the area mapped as listwanite in Figure 4.1. Carbonation proceeded via the reaction:

$$2\ Mg_{48}Si_{34}O_{85}(OH)_{62} + 45\ CO_2 \rightarrow 45\ MgCO_3 + 17\ Mg_3Si_4O_{10}(OH)_2 + 45\ H_2O \qquad \mathbf{(R_2)}$$

Antigorite → Magnesite + Talc

which combined with reaction R_1, accounts for about half of the overall carbonation potential for the serpentinite rocks at Atlin (up to about 20 wt %, Table 4.1, Fig. 4.4a). It also marks a further increase in the CO_2 content of the fluid phase (Fig. 4.4b). The cores of large listwanite systems consist of magnesite plus quartz (Assemblage A_4, Fig. 4.2), which formed by the reaction R_3 at the highest activity of CO_2 in the fluid phase (Fig. 4.4b).

$$Mg_3Si_4O_{10}(OH)_2 + 3\ CO_2 \rightarrow 3\ MgCO_3 + 4\ SiO_2 + H_2O \qquad \mathbf{(R_3)}$$

Talc → Magnesite + Quartz

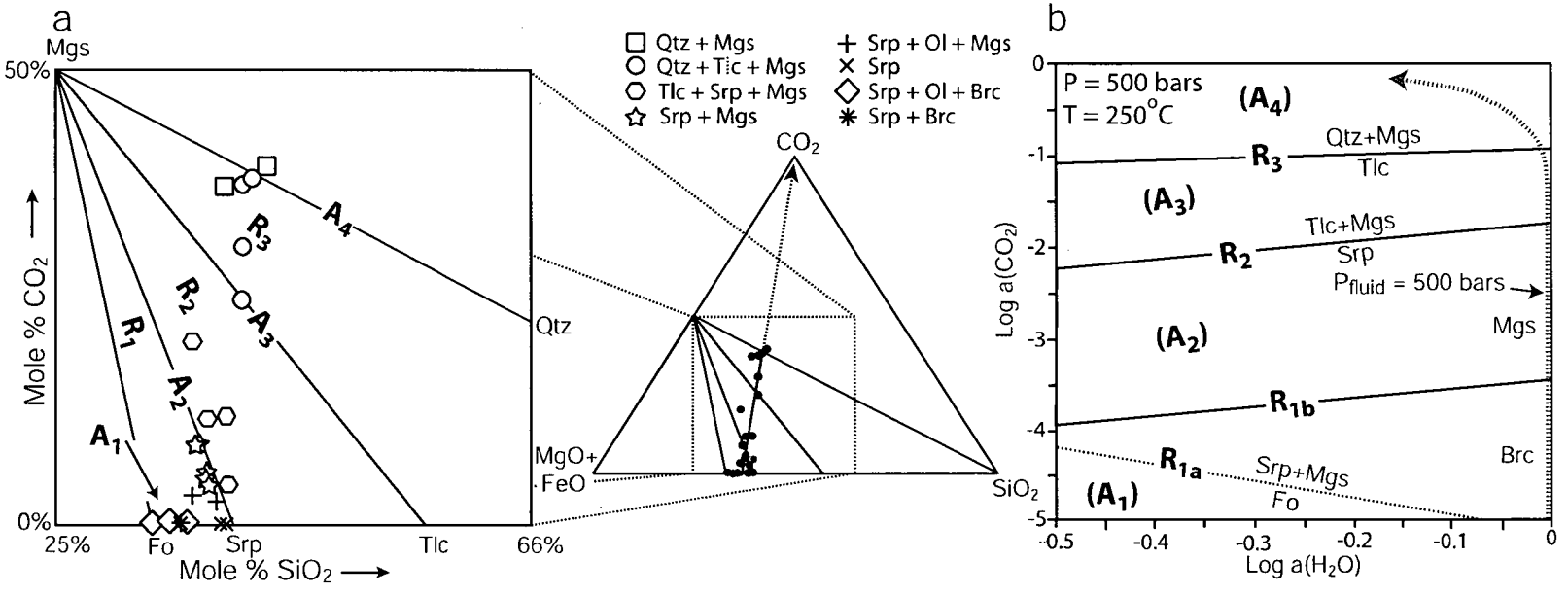

Figure 4.4: a) Ternary phase diagram comparing the observed mineral content and whole rock composition in a MgO+FeO-SiO_2-CO_2 ternary diagram projected from H_2O. b) Mineral stability in the system MgO-SiO_2-CO_2-H_2O as a function of activity of H_2O and CO_2 in the fluid phase calculated using PTAX and the mineral database of Berman (1988). The dashed line is the metastable extension of reaction R_{1a}. The arrowed dashed line is the path of P_{fluid} = 500 bars for a binary H_2O-CO_2 fluid, calculated with the CORK equation of state (Holland and Powell 1991).

Thus, the overall mineral transformation of serpentine and olivine to quartz and magnesite is the same as that recorded in reactions $R_{A \text{ and } B}$. Total carbonation of serpentinite leads to CO_2 contents in excess of 36 wt% on a whole-rock basis (Table 4.1). Reactions R_1, R_2 and R_3 record an increase in activity of CO_2 in an H_2O-rich fluid (Fig. 4.4b).

Reactions R_1 to R_3 produce magnesite of different compositions that are discernible with back-scattered electron imaging because of differences in mean atomic mass. Energy-dispersive spectroscopy confirms that increasing mean atomic mass is due primarily to an increase in Fe content of magnesite. Magnesite M_1 formed during R_1 exhibits euhedral faces with serpentine and is overgrown by M_2 magnesite with a higher Fe content associated with talc (Fig. 4.4b). The dark cores to magnesite in Figures 4.3c, d are likewise interpreted to record M_1 magnesite growth overprinted by magnesite formed by reaction R_2. Dark rims of M_3 magnesite in Figure 4.3d contain less Fe than M_2 magnesite and forms euhedral contacts with quartz.

4.6 GEOCHEMICAL CHANGE DURING LISTWANITIZATION

The mineralogical transformations in reactions R_1 to R_3 can be achieved through (de)hydration-carbonation reactions and no modification of the major oxide chemical composition of serpentinite. Previous studies of listwanite, however, have argued for pervasive chemical change accompanying carbonation (Schandl and Naldrett, 1992; Sherlock *et al.*, 1993; Buisson and LeBlanc, 1985). Indeed the term silica-carbonate alteration that is commonly applied to these systems implies metasomatism. If the mineral reactions at Atlin involve substantial mobility of major non-volatile species, then this system may not serve as a useful analogue for mineral carbonation processes.

Whole-rock chemical compositions from Atlin (data in Appendix A) are consistent with the hypothesis that carbonation was not accompanied by chemical changes of major non-volatile chemical species. Decreases in wt% MgO and SiO_2, which combined make up about 90% of the non-volatile component of the Atlin rocks, correlate with an increase in CO_2 content at a constant $MgO:SiO_2$ ratio (Fig. 4.5). This trend is consistent with the immobility and passive depletion of Si and Mg during mass increase (CO_2 addition). Serpentinite and listwanite overlap completely in composition if

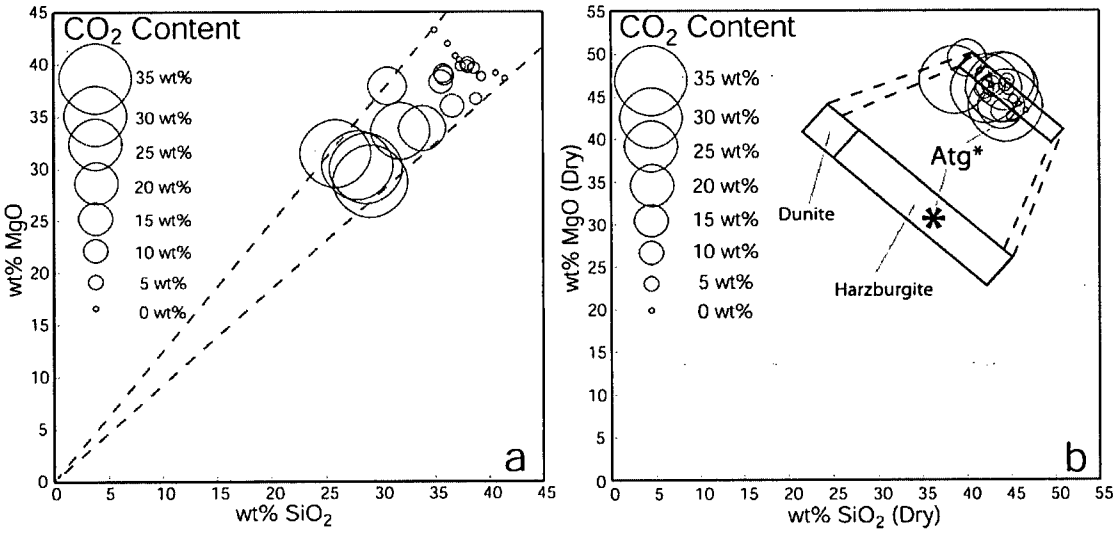

Figure 4.5: a) Weight percent MgO plotted vs. SiO_2. Circle size is proportional to CO_2 content. Data is in Appendix A. The observed trend is consistent with the passive dilution of MgO and SiO_2 by increase in CO_2 content. Dashed lines represent the chemical range defined by the protolith samples and passive dilution. b) MgO and SiO_2 whole rock compositions renormalized to 100% (excluding H_2O and CO_2). Carbonated and uncarbonated samples plot on calculated dunite and harzburgite compositions (using Fo_{90} and En_{90} compositions for olivine and orthopyroxene, respectively). Note that the MgO and SiO_2 contents of serpentinite and listwanite are indistinguishable. *Denotes an antigorite-rich rock which contains 7 wt% magnetite (estimated from the data in Appendix A) created during the complete serpentinization of Fo_{90}/En_{90} rich rocks.

major oxide compositions are renormalized to 100% excluding H_2O and CO_2 (Fig. 4.5b). The variation of SiO_2:MgO ratio within the suite of rocks may be a function of the degree of initial serpentinization, or the amount of initial orthopyroxene (Fig 4.5b).

Whole-rock geochemical compositions were tested against model sequestration reactions R_{1a}, R_{1b}, R_2 and R_3 using the method of Gordon (2003), a new geochemical mass balance technique that quantitatively accounts for protolith heterogeneity. The six samples with assemblage A_1 (Table 4.1) and the lowest CO_2 content (<0.5 wt%; Appendix A) were chosen to define the protolith. The protolith for each carbonated rock was modeled as a linear combination of these six so that compositional heterogeneities in the protolith did not propagate into the assessment of the carbonation. The remaining samples were divided into three groups. Seven samples without talc or quartz were considered to have experienced only reactions R_{1a} and R_{1b}, four samples with talc but no quartz were considered to have experienced reactions R_{1a}, R_{1b} and R_2, and the remaining six quartz-bearing samples were considered to have experienced the full suite of reactions.

Reaction R_{1a} requires the model mass-transfer vector for the seven low-CO_2 samples be zero for all species except C and H. For these samples, the model ratio of C added to H added is 20:62. Model reactions R_{1b}, R_2 and R_3 have the ratios of C added to H added of 1:-2, 1:-2 and 3:-2 respectively. A linear algebraic basis (Strang, 1993) for the vector space orthogonal to the model mass-transfer vectors (invariant space) can be obtained by simple manipulations using linear algebra. The basis contains linear combinations of elements unaffected by the proposed mass-transfer reactions. Because more than one reaction is involved in each group of samples, the possibility of various extents of reaction of R_{1a}, R_{1b}, R_2 and R_3 means that this method does not constrain the C/H ratio of the mass-transfer vector.

Given the composition of a carbonated rock, the mass-transfer vector must have an origin that can be described by a linear combination of the vectors in protolith space and be orthogonal to vectors in invariant space. This approach provides a vector equation, the least-squares solution of which provides a "best fit" protolith composition and "best fit" mass-transfer vector for each carbonated rock.

The success of the model sequestration reactions in predicting the observed composition of a modified rock can be judged by comparing the residuals of the least-squares solution with the errors permitted by analytical uncertainties determined from replicate analyses. These results are shown in Figure 4.6. Positive residuals indicate that the altered rock contains more of that element than permitted by the hypothesis. In general, the isochemical reaction model provides a good fit to the data. Residuals for Si, Ti, Fe, Mg, Na, K, P, and V return a good to excellent fit, generally within 3 standard errors (see Appendix A). The variation in the composition of these elements in listwanite can be fully explained by the variability of the protolith rocks and the dilution effect of mass addition. The model protolith subspace and simple sequestration reactions do not adequately describe the variation in Al, Mn, Ca, Cr, Ni and Zn, which all show large residuals. The failure of the model to explain the compositional variation in these elements is most likely due to inadequate geochemical characterization of protolith variability due to the small number of protolith samples. The residuals are generally both positive and negative and show no systematic variation with degree of carbonation. Moreover, Al, Cr, Ni and Zn are relatively immobile compared to many other major elements such as Mg and Fe in hydrothermal systems. There is no convincing evidence for chemical mobility beyond the volatile species. A more extensive database and geochemical mass balance calculation in Chapter V provides for a more thorough examination of the protolith and alteration.

4.7 MAGNETIC SUSCEPTIBILITY

R_1 carbonation occurs many tens of metres from major fracture systems but is generally not evident in the field. We have been unable to map the distribution of magnesite formed after olivine breakdown, for example, because this reaction is commonly not discernable in hand sample. The magnetic susceptibility of serpentinite is relatively high because of the formation of magnetite during serpentinization of harzburgite and dunite (e.g., Toft *et al.*, 1990). There is also evidence for magnetite generation during reaction R_1 (Fig. 4.3a). Generally magnetite forms rim overgrowths on chromite and as disseminated grains aligned in foliation planes and in fractures.

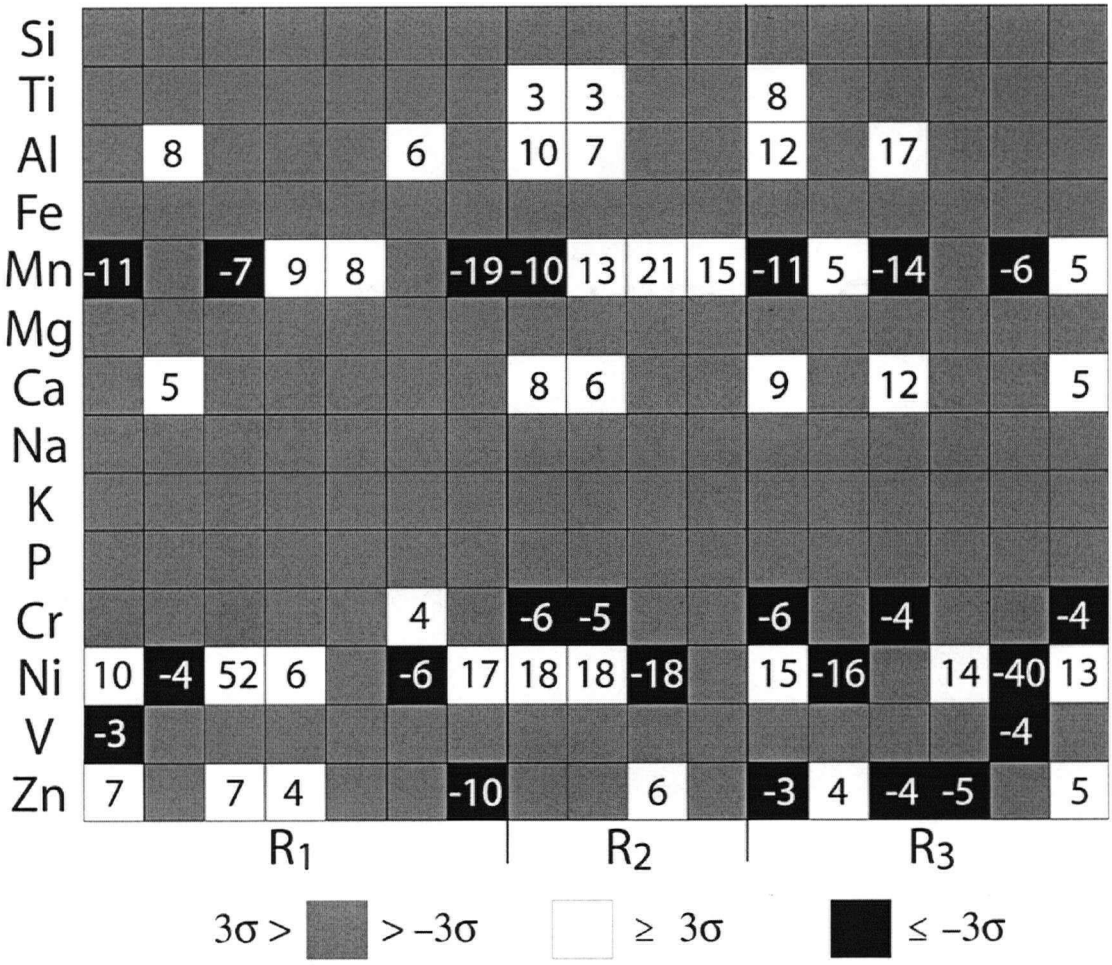

Figure 4.6: Ratio of residual error to standard error in whole rock chemical composition of carbonated samples. Residual error is the difference between compositions predicted by reactions R_1-R_3 and measured compositions. Values of the ratio that exceed three standard errors (positive/negative) indicate an excess/deficiency of the species which cannot be accounted for by the model sequestration reactions ($R_{1a\&b}$, R_2 and R_3). Table of all residuals is included in the appendix.

Magnetite was subsequently destroyed during carbonation (Table 4.1) and is completely consumed by the final stages of reaction R_2.

Mass balance calculations indicate that Fe is conserved during carbonation of serpentinite. Fe liberated by magnetite destruction must therefore be hosted within another mineral. The increase in Fe content of magnesite in M_2 is consistent with conservation of Fe during magnetite destruction. There is a corresponding decrease in whole rock magnetic susceptibility in samples recording reaction R_2 (Fig. 4.7).

We have exploited the correlation of whole-rock CO_2 content and magnetic susceptibility (Fig. 4.7) to develop a semi-quantitative measure of reaction progress that can be employed in the field. Magnetic susceptibility of outcrops and hand specimens were measured with an Exploranium KT-9 Kappameter. Although fully carbonated rocks contain > 35 wt% CO_2, virtually all magnetic susceptibility appears to have been destroyed by about 20 wt% CO_2, which corresponds to the completion of reaction R_2. Magnetic susceptibility of serpentinite is heterogeneous and reflects the degree of initial serpentinization. A least squares fit to the data yields a semi-quantitative relationship between magnetic susceptibility and CO_2, and thus reaction progress:

$$\text{Magnetic Susceptibility } (10^{-3} \text{ S.I. units}) = 61.003 - 3.0544(\text{wt\% } CO_2) \qquad (4.1)$$

To test the utility of this relationship in mapping reaction progress, a 2 by 2 metre pavement of variably carbonated serpentinite was mapped and analyzed in the field for magnetic susceptibility (approx. 1550 analyses, Fig. 4.8). Fracture-controlled talc + magnesite + minor serpentine (R_2) transects the pavements in two discrete reaction zones that are flanked by distal antigorite + magnesite assemblages (A_2). The mineralogical zonation at this locale corresponds to discrete changes in magnetic susceptibility. The distinction between serpentinite and rusty serpentinite in the field is very subtle, yet this alteration is prominent in magnetic susceptibility. Measured whole rock CO_2 content for samples along transect A-B is within 5% of CO_2 content calculated from magnetic susceptibility and (Equation 4.1, Fig. 4.9). Calculated CO_2 content increases continuously within the zone of rust-weathering serpentinite, implying a gradation in reaction progress across this zone. However, whole rock geochemistry through the section indicates an

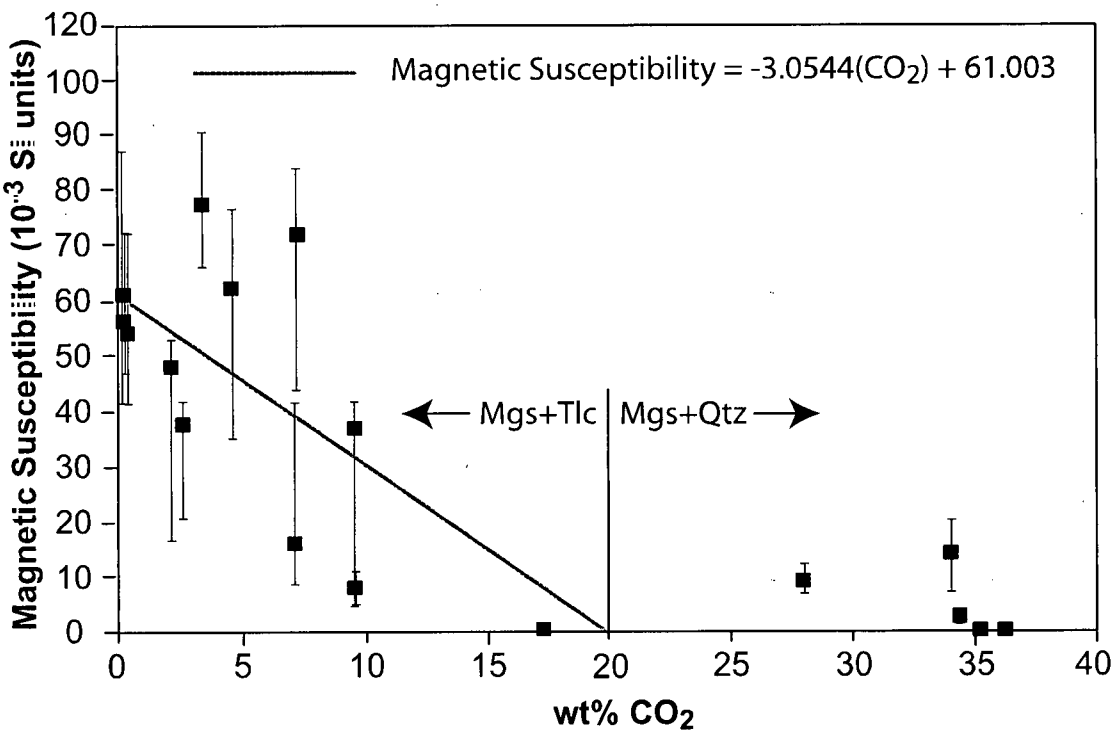

Figure 4.7: Magnetic susceptibility vs. whole rock wt% CO_2. Linear fit was constrained to intersect zero magnetic susceptibility at 20 wt% CO_2, which approximately marks the maximum CO_2 content of rocks that record complete progress of reaction R_2.

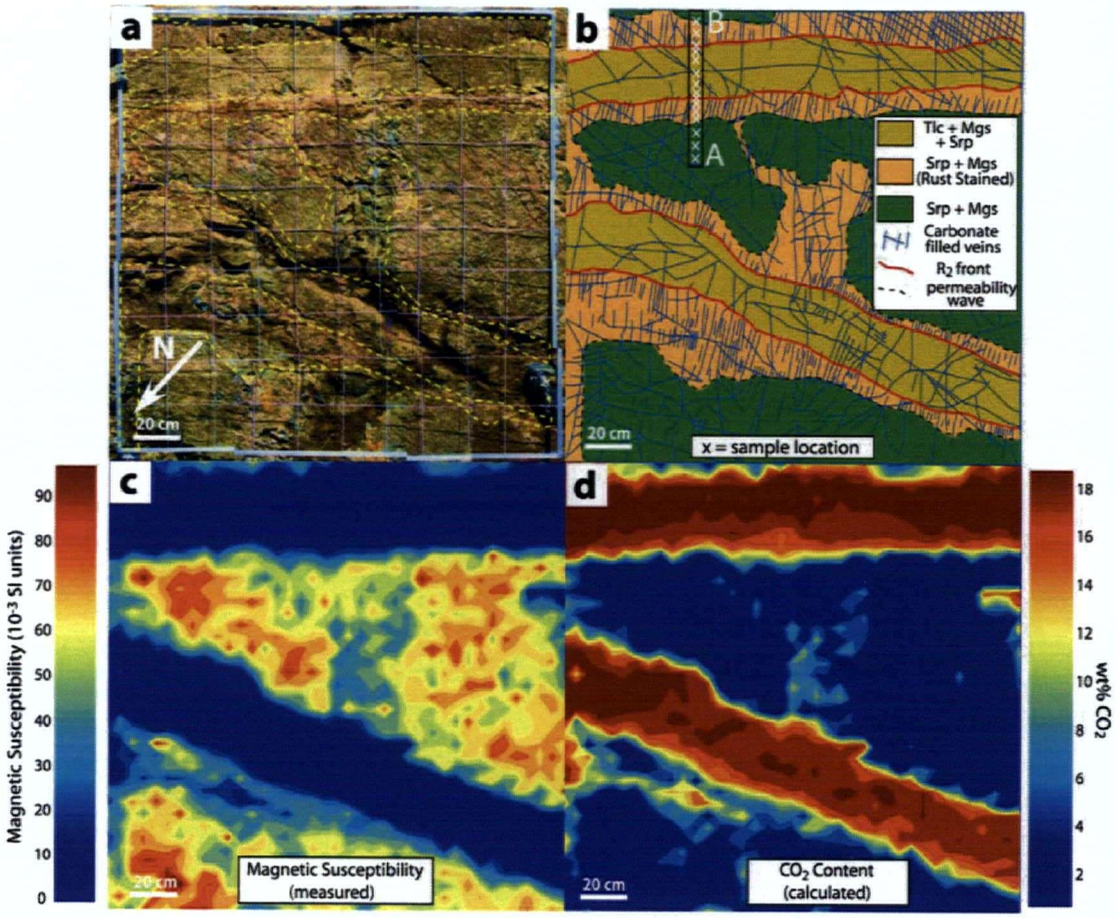

Figure 4.8: a) Composite image of a 2 by 2 metre pavement outcropping on the western slope of Monarch Mountain (E 575887, N 6602098, NAD 83). Dashed yellow lines are contacts in Figure 2.2b. b) Detailed geologic map of the listwanite zone mapped at 1:20 scale. Sample locations and section A-B correspond to those of Figure 3.7. c) Magnetic susceptibility map composed of ca. 1550 measurements, showing the correlation of magnetic susceptibility with map units in Figure 2.2b. d) Whole rock Wt% CO_2 map calculated using Eq_1 following Hansen *et al.* (2005), Chapter IV.

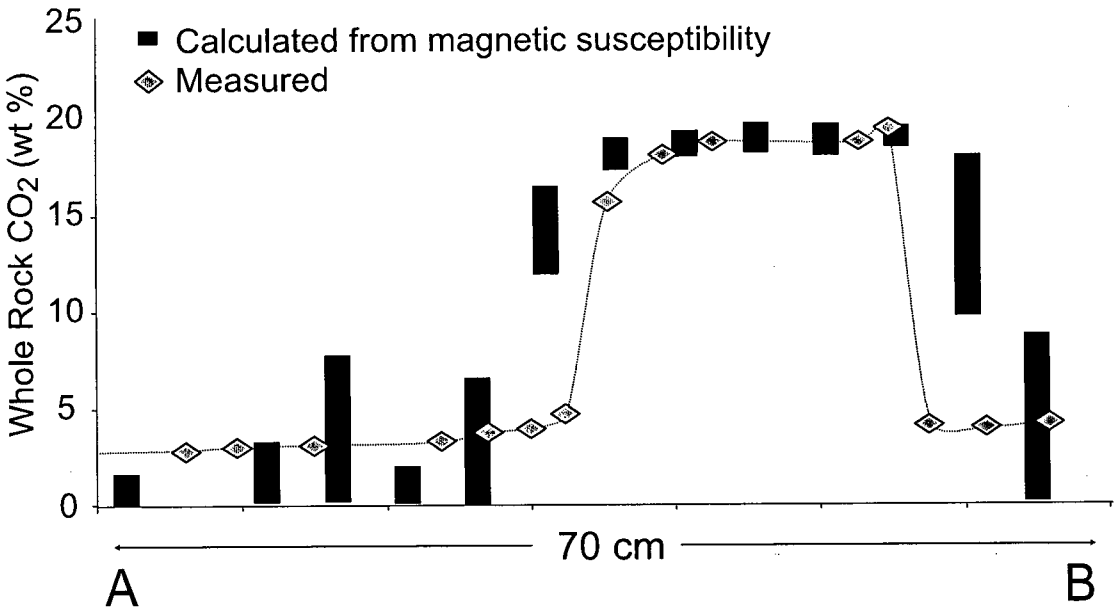

Figure 4.9: Measured and calculated wt% CO_2 across A-B from Figure 2.2b. Wt% CO_2 calculated using Eq_1 and magnetic susceptibility data of Figure 2.2c. The range in calculated CO_2 content reflects the full range of four magnetic susceptibility measurements at each location.

abrupt change in CO_2 content (Fig. 4.9). The gradation in magnetic susceptibility at the reaction front could either reflect the resolution of the magnetic susceptibility metre or the progressive destruction of magnetite not directly linked to progress of carbonation reaction. Regardless, magnetic susceptibility maps provide semi-quantitative estimates of reaction progress in the field and are invaluable in discerning the geometry of reaction fronts associated with reaction R_2.

4.8 VOLUME STRAIN ACCOMPANYING REACTION

The carbonation reactions involve an increase in the volume of solids (Table 4.2); each reaction therefore has the potential to create or destroy porosity and permeability. The development of carbonate veins orthogonal to the outer limit of talc plus magnesite reaction in Figures 4.8a, b likely developed in tension. The mechanical model of Jamtveit *et al.* (2000) predicts the development of high-permeability zones downstream of reactions that produce a net solid volume increase (Fig. 4.10). Indeed, the pattern of carbonation and vein formation in Figures 4.8a, b resembles the patterns produced by the Jamtveit *et al.* model. If vein formation outboard of the talc-magnesite reaction front records tension and mechanical coupling of swelling during reaction R_2, then the volume strain of the two processes should balance, at least approximately. Volume strain was calculated by measuring vein thickness (7.6 +/- 3.8 mm) and density in the rusty serpentinite zone of Figure 4.8. The calculated volume increase of 3.6 +/- 1.8% compares well with the solid volume change of reaction R_2 (2.3 % in a serpentinite rock with 7.5% relict olivine). The distribution of carbonate-filled tension gashes appears to control the outer extent of formation of rusty serpentinite alteration and thus likely has enhanced percolation of reactive fluid into intact wallrock.

4.9 IMPLICATIONS FOR CO_2 SEQUESTRATION

Direct carbonation of olivine (+/- brucite) was previously unrecognized at Atlin and records infiltration and carbonation of intact bedrock many tens to hundreds of metres from the primary fracture-controlled permeability system. The relative ease by which fluid infiltrated intact bedrock may be due to the inherently high reactivity of olivine and brucite and by the small solid volume increase associated with carbonation of

Table 4.2: Volume Changes

Reaction	ΔVs* (rxn)	ΔVs (rock**)
R_{1a}: Ol → Srp + Mgs	55.1%	4.2%
R_{1b}: Brc → Mgs	13.8%	0.4%
R_2: Srp → Tlc + Mgs	2.6%	2.3%
R_3: Tlc → Qtz + Mgs	28.5%	16.2%

* Calculated from Berman (1988) at 250°C and 500 bars (Chapter IV)

** Assuming 2.5% brucite and 7.5% relict olivine by volume.

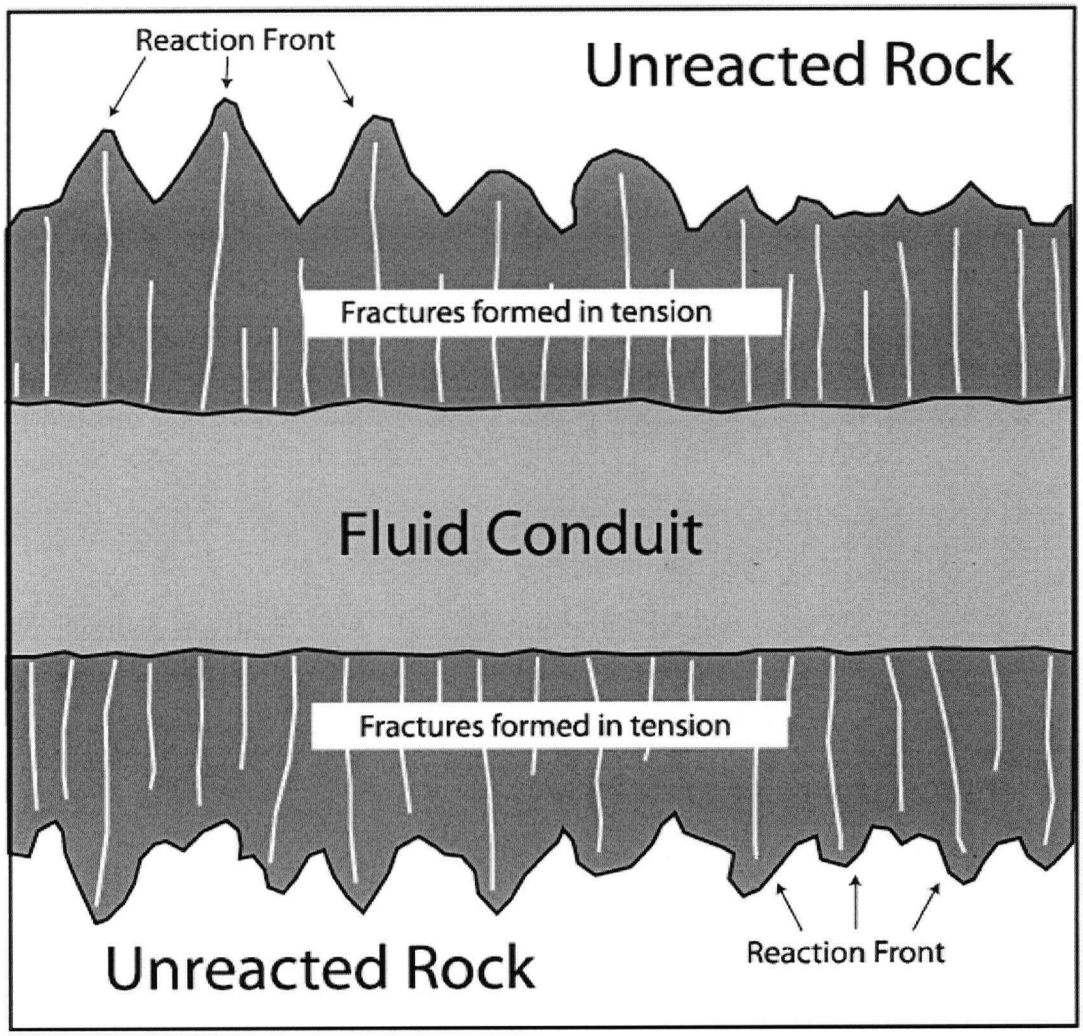

Figure 4.10: Distribution of fracture permeability in advance of a reaction, predicted by the mechanical model of Jamtveit *et al.* (2000). In the model, tension fracture permeability results from an overall increase in solid volume during reaction. Modified from Jamtveit *et al.* (2000).

small amounts of brucite and relict olivine. The extent of reaction R_1 indicates that the primary permeability of serpentinite at Atlin was sufficient for fluid infiltration and progress of R_1. However, the large increase in solid volume of R_1 may limit its usefulness for fluid infiltration in olivine-rich bedrock. From Table 4.1, the direct carbonation of brucite and olivine to magnesite plus serpentine only accounts for about 5 – 15 % of the carbonation potential for the serpentinite at Atlin. However, because products of reaction R_1 are widespread, it may have sequestered a significant portion of the total CO_2 content of the Atlin listwanite system.

The listwanite is best developed along a regional joint and fracture system as well as a basal thrust fault (Chapter III), hence the Altin Ultramafic Allochthon had good potential for carbonation due to the structural preparation. This suggests that the potential of an ultramafic body for CO_2 sequestration is directly linked to its original fracture permeability because without it, the carbonation potential is limited regardless of the efficiency of the various CO_2-sequestering reactions.

The carbonation of antigorite to magnesite and talc binds large quantities of CO_2 with small associated gain in the volume of solid material. Moreover, within intact bedrock, the progress of this reaction may create a permeability front in advance of the reaction front, promoting further fluid infiltration and reaction. Reactions R_1 and R_2, which combined account for about half of the carbonation potential for serpentinite (Table 4.1), may hold the most promise for industrial-scale *in situ* carbonation of minerals. Complete carbonation of serpentinite to magnesite plus quartz is generally limited to the fractured cores of the largest listwanite systems. Products of reaction R_3 generally are not developed far into intact bedrock, which may have been incapable of accommodating the large increase in solid volume associated with this reaction. This indicates that carbonation to magnesite plus quartz may limit the sequestration capacity of *in situ* mineral-carbonation systems by destroying porosity and permeability in the vicinity of injection sites. The reaction path models of Cipolli *et al.* (2004) predict significant conversion of serpentine within *in situ* mineral carbonation systems to carbonate and chalcedony (microcrystalline quartz) within a few 10's of years. Their model assumes direct transformation of serpentine to chalcedony and magnesite at 250 bars and 60°C based on the conditions of the Gruppo di Voltri serpentinite aquifer at

Genova, Italy. Our investigations at Atlin and Figure 4.11 suggest that carbonation within the subsurface under these conditions would more likely proceed via a series of reactions (R_1 to R_3). Moreover, as indicated above, reactions R_1 and R_2 involve a relatively small increase in the volume of solids limiting porosity destruction yet still sequester half the CO_2 as complete carbonation to quartz plus magnesite. The stability of carbonation reactions are controlled by the activity of CO_2 in the fluid phase and Figure 4.11 indicates that the fluid chemistry favorable for driving R_1 and R_2 is a CO_2-rich aqueous fluid. Industrial mineral carbonation processes could therefore be engineered to control the input gas composition so as to preferentially drive carbonation reactions that minimize porosity loss and maximize permeability generation in the subsurface.

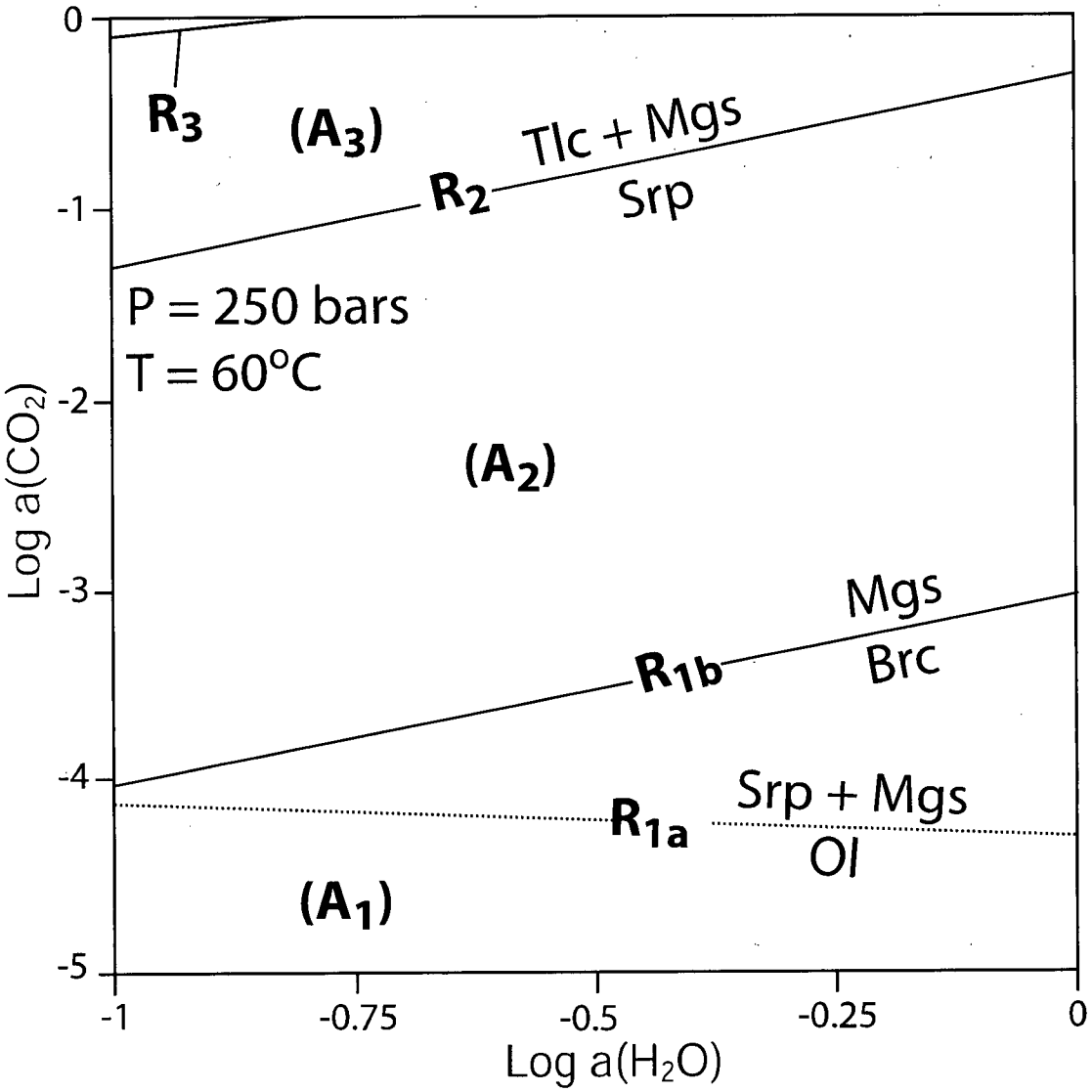

Figure 4.11: Mineral stability in the system MgO- SiO_2-CO_2-H_2O as a function of activity of H_2O and CO_2 in the fluid phase calculated at the Gruppo di Voltri serpentinite aquifer at Genova, Italy (P = 250 bars, T = 60°C, Cipolli *et al.* 2004). Calculated using PTAX and the mineral database of Berman (1988).

4.10 REFERENCES

Aitken, J. D. (1959): Atlin Map Area, British Columbia. Geological Survey of Canada, Memoir 307: 89 pages.

Andrew, K. (1985): Fluid Inclusion and Chemical Studies of Gold-Quartz Veins in the Atlin Camp, Northwestern British Columbia. B.Sc. Thesis, Department of Geological Sciences, University of British Columbia, Vancouver, B.C., Canada, 116 pages.

Ash, C. H. (1994): Origin and Tectonic Setting of Ophiolitic Ultramafic and Related Rocks in the Atlin Area, British Columbia (NTS 104N). B.C. Ministry of Energy, Mines and Petroleum Resources, Bulletin 94, 48 Pages.

Ash, C. H. (2001): Relationship Between Ophiolites and Gold-Quartz Veins in the North American Cordillera. Department of Energy, Mines and Petroleum Resources, Bulletin 108, 140 pages.

Ash, C. H. and Arksey, R. L. (1990a): The Atlin Ultramafic Allochthon: Ophiolite Basement Within the Cache Creek Terrane; Tectonic and Metallogenic Significance (104N/12). Geological Fieldwork 1989, B.C. Department of Energy and Mines, Paper 1990-1, 365-374.

Ash, C. H. and Arksey, R. L. (1990b): The Listwanite-Lode Gold Association in British Columbia. Geological Fieldwork 1989, B.C. Department of Energy and Mines, Paper 1990-1, 359-364.

Ash, C. H., MacDonald, R. W. and Arksey, R. L. (1991): Towards a Deposit Model for Ophiolite Related Mesothermal Gold in British Columbia. Geological Fieldwork 1991, B.C. Department of Energy and Mines, Paper 1992-1, 253-260.

Berman, R. G. (1988): Internally-Consistent Thermodynamic Data for Minerals in the System: Na_2O-K_2O-CaO-FeO-Al_2O_3-SiO_2-TiO_2-H_2O-CO_2. Journal of Petrology, 29-2, 445-522.

Bloodgood, M. A., Rees, C. J. and Lefebure, D. V. (1989): Geology and Mineralization of the Atlin Area, Northwestern British Columbia (104N/11W and 12E). Geological Fieldwork 1988, B.C. Department of Energy and Mines, Paper 1989-1, 311-322.

Buission, G. and LeBlanc, M. (1985): Gold in Carbonatized Ultramafic Rocks from Ophiolite Complexes. Economic Geology, 80, 2028-2029.

Carmichael, D.M., (1970): Intersecting Isograds in the Whetstone Lake area, Ontario. Journal of Petrology, 11, 147- 181.

Cipolli, G., Gambardella, B., Marini, L., Ottonello, G. and Zuccolini, M. V. (2004): Geochemistry of High-pH Waters from Serpentinites of the Gruppo di Voltri (Genova, Italy) and Reaction Path Modeling of CO_2 Sequestration in Serpentinite Aquifers. Applied Geochemistry, 19, 787-802.

Goff, F. and Lackner, K. S. (1998): Carbon Dioxide Sequestering Using Ultramafic Rocks. Environmental Geosciences, 5-3, 89-101.

Goldberg, P., Chen, Z. Y., O'Connor, W. K., Walters, R. P. and Ziock, H. (2001): CO_2 Mineral Sequestration Studies in US. Proceedings of the First National Conference on Carbon Sequestration, May 14-17, 2001, Washington, DC, session 6C, 10 pages.

Gordon, T.M. (2003): Algebraic Generalization of the Graphical Gresen and Pearce Methods for Identification of Geochemical Mass-Transfer Processes. (abstract), Vancouver 2003 Abstracts, CD-ROM, GAC-MAC-SEG, Vancouver 2003 Annual General Meeting, Vancouver, B.C., 28-146, ISSN 0701-8738, ISBN: 0-919216-86-2.

Guthrie, G. D., Carey, J. W., Bergfeld, D., Byer, D., Chipera, S., Ziock, H. and Lackner, K. S. (2001). Geochemical Aspects of the Carbonation of Magnesium Silicates in an Aqueous Medium. Proceedings of the First National Conference on Carbon Sequestration, May 14-17, 2001, Washington, DC, session 6C, 14 pages.

Hansen, L. D., Dipple, G. M., Anderson, R. G. and Nakano, K. F. (2004): Geologic Setting of Carbonate Metasomatised Serpentinite (Listwanite) at Atlin, British Columbia: Implications for CO_2 Sequestration and Lode-Gold Mineralization. In Current Research, Geological Survey of Canada, Paper 2004-A5, 12 pages.

Hansen, L. D., Dipple, G. M. and Anderson, R. G. (2003b): Carbonate Altered Serpentinites of Atlin, BC: A Two Stepped Analogue to CO_2 Sequestration. (abstract), Programs with Abstracts, GSA Annual Meeting & Exposition, Seattle, WA, 133-14, 329.

Holland, T and Powell, R. (1991): A Compensated-Redlich-Kwong (CORK) Equation For Volumes and Fugacities of CO_2 and H_2O in the Range 1 bar to 50 kbar and 100-1600 C. Contributions to Mineralogy and Petrology, 109, 265-273.

Jamtveit, B., Austrheim, H. and Malthe-Sorenssen, A. (2000): Accelerated Hydration of the Earth's Deep Crust Induced by Stress Perturbations. Nature, 408, 75-78.

Kashkai, A. M. and Allakhverdiev, I. (1965): Listwanites: Their Origin and Classification. U. S. Geol. Surv., Libr., Reston, VA, United States, 146 pages, Translated from the Russian, Listvenity, ikh genezis i klassifikatsiya, Akad. Nauk AZ SSR, Inst. Geol. Baku, 1965

Lackner, K. S., Wendt, C. H., Butt, D. P., Joyce, E. L. and Sharp, D. H. (1995): Carbon Dioxide Disposal in Carbonate Minerals. Energy, 20, 1153-1170.

Madu, B. E., Nesbitt, B. E. and Muehlenbachs, K. (1990): A Mesothermal Gold-Stibnite-Quartz Vein Occurrence in the Canadian Cordillera. Economic Geology, 85, 1260-1268.

Matter, J. M., Takahashi, T., Goldberg, D., Morin, R. H. and Stute, M. (2002): Secure, Long-Term Geological Carbon Sequestration in Mafic Rocks: Results from Field and Laboratory Experiments. (abstract), Programs with Abstracts, GSA Annual Meeting & Exposition, Denver, CO, 135-5.

Mihalynuk, M. G., Smith, M., Gabites, J. E., Runkle, D. and Lefebure, D. (1992): Age of Emplacement and Basement Character of the Cache Creek Terrane as Constrained by New Isotopic and Geochemical Data. Canadian Journal of Earth Sciences, 29, 2463-2477.

Monger, J. W. H. (1975): Upper Paleozoic Rocks of the Atlin Terrane. Geological Survey of Canada, Paper 74-47, 63 pages.

Monger, J. W. H. (1977a): Upper Paleozoic Rocks of Northwestern British Columbia. In Current Research, Part A, Geological Survey of Canada, Paper 77-1A, 255-262.

Monger, J. W. H. (1977b): Upper Paleozoic Rocks of the Western Canadian Cordillera and Their Bearing on the Cordilleran Evolution. Canadian Journal of Earth Sciences, 14, 1832-1859.

Monger, J. W. H., Richards, T. A. and Paterson, I. A. (1978): The Hinterland Belt of the Canadian Cordillera: New Data from Northern and Central British Columbia. Canadian Journal of Earth Sciences, 15, 823-830.

O'Connor, W. K., Dahlin, D. C., Nilsen, D. N., Rush, G. E., Walterd, R. P. and Turner, P. C. (2001): Carbon Dioxide Sequestration by Direct Mineral Carbonation: Results From Studies and Current Status. Proceedings of the First National Conference on Carbon Sequestration, May 14-17, 2001, Washington, DC, session 6C, 10 pages.

O'Hanley, D. S. and Wicks, F. J. (1995): Conditions of Formation of Lizardite, Chrysotile and Antigorite, Cassiar, British Columbia. Canadian Mineralogist, 33, 753-773.

Rinaudo, C. and Gastaldi, D. (2003): Characterization of Chrysotile, Antigorite and Lizardite by FT-Raman Spectroscopy. Canadian Mineralogist, 41, 883-890.

Schandl, E. S. and Wicks, F. J. (1991): Two Stages of CO_2 Metasomatism at the Munro Mine, Munro Township, Ontario: Evidence from Fluid-Inclusion, Stable-Isotope, and Mineralogical Studies. Canadian Journal of Earth Sciences, 28, 721-728.

Schandl, E. S and Naldrett, A. J. (1992): CO_2 Metasomatism of Serpentinites, South of Timmins, Ontario. Canadian Mineralogist, 30, 93-108.

Seifritz, W. (1990): CO_2 Disposal by Means of Silicates. Nature, 345, 486.

Sherlock, R. L., Logan, M. A. V., and Jowett, E. C. (1993): Silica Carbonate Alteration of Serpentinite, Implications for the Association of Precious Metal and Mercury Mineralization in the Coast Ranges. Society of Economic Geologists Guidebook Series, 16, 90-116.

Strang, G. (1993): Introduction to Linear Algebra. Wellesley-Cambridge Press.

Todt, P. B., Arkani-Hamed, J. and Haggerty, S. E. (1990): The Effects of Serpentinization on Density and Magnetic Susceptibility: A Petrophysical Model. Physics of the Earth and Planetary Interiors, 65, 137-157.

Wittkopp, R. W. (1983): Hypothesis for the Localization of Gold in Quartz Veins, Allegheny District. California Geology, 36-6, 123-127.

Wu, J., Sheen, J., Chen, S. and Fan, Y. (2001): Feasibility of CO_2 Fixation Via Artificial Rock Weathering. Industrial and Engineering Chemical Research, 40, 3902-3905.

Zeverhoven, R. and Kohlmann, J. (2001): CO_2 Sequestration by Magnesium Silicate Mineral Carbonation in Finland. Second Nordic Minisymposium on Carbon Dioxide Capture and Storage, Gotenborg (October 26, 2001): http://www.entek.chalmers.se/~anly/symp/symp2001.html.

CHAPTER V: GEOCHEMICAL MASS BALANCE USING A PROTOLITH SPACE

5.1 INTRODUCTION

There are a number of methods currently available for assessing the geochemical mass balance between altered samples and unaltered protolith material. The most widely employed methods are the system of linear equations of Gresens (1967), the graphical method of Grant (1987) and the bootstrap method of Ague and Van Haren (1996). All of the aforementioned methods require that a chemically heterogeneous protolith be represented by a single composition and at best assess the impact of protolith heterogeneity through propagation of the variance of the protolith composition (e.g. Ague and Van Haren, 1996). Furthermore, at least one chemical species must be assumed to be immobile when assessing the alteration. Here I outline an alternate method, following Gordon (2003), in which a model protolith (*MP*) is calculated for each altered sample and is allowed to span a defined geochemical space. Any difference between the altered sample and the *MP* thus is considered alteration. This mass balance approach is applied to chemical alteration of carbonate altered serpentinite, also known as listwanite alteration (e.g. Hansen *et al.*, 2004; Chapter II), at Atlin, British Columbia.

In Hansen *et al.* (2005) and Chapter IV it was demonstrated using a data set of 23 samples that the formation of listwanite at Atlin occurred in three sequential reaction steps (Fig. 5.1), and that the alteration was isochemical. MgO vs. SiO_2 and ternary diagrams (Fig. 5.2), as well as a mass balance technique similar to that outlined below, were used to determine that the most significant process that affected the major non-volatile chemical species alteration was passive dilution caused by mass gain as CO_2 content increased. Misfits in Al, Mn, Ca, Cr, Ni and Zn between model protoliths and observed compositions were considered to have resulted from the incomplete geochemical characterization of the protolith. Here a much larger data set of 160 samples, including 45 samples of protolith material, are used to rigorously test a geochemical space-based mass balance technique. This method indicates that the major non-volatile chemical constituents remained unaltered except in extremely carbonated

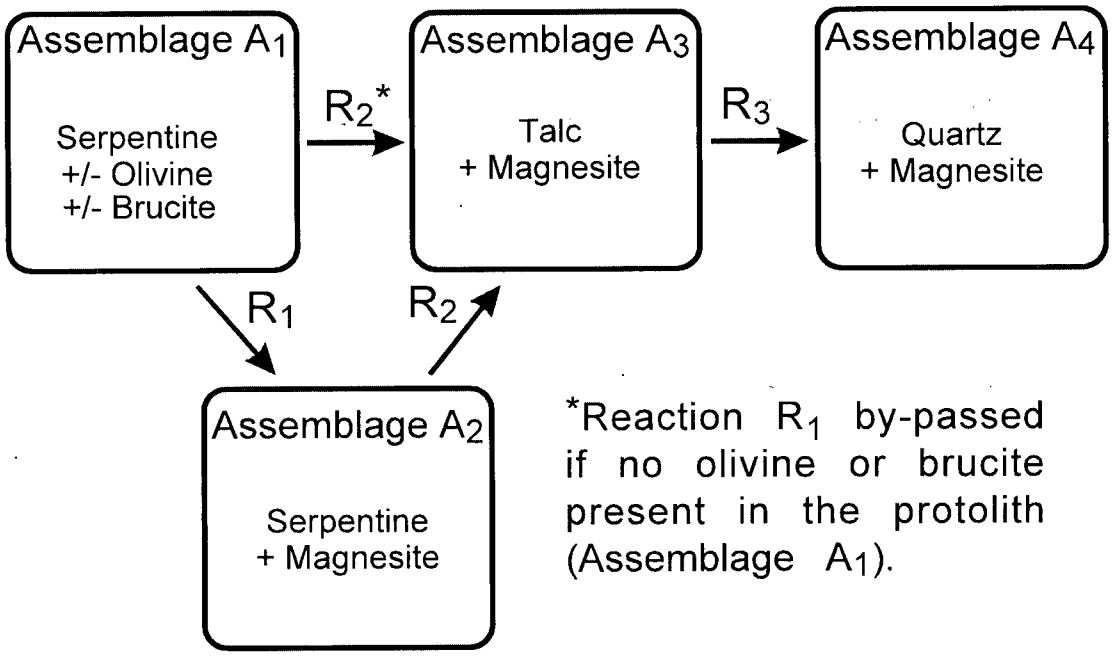

Figure 5.1: Simplified flow chart for the reaction path of the Atlin listwanite system during progressive carbonation of serpentinite. The detailed description of the reactions and mineral assemblages is given in Chapter IV.

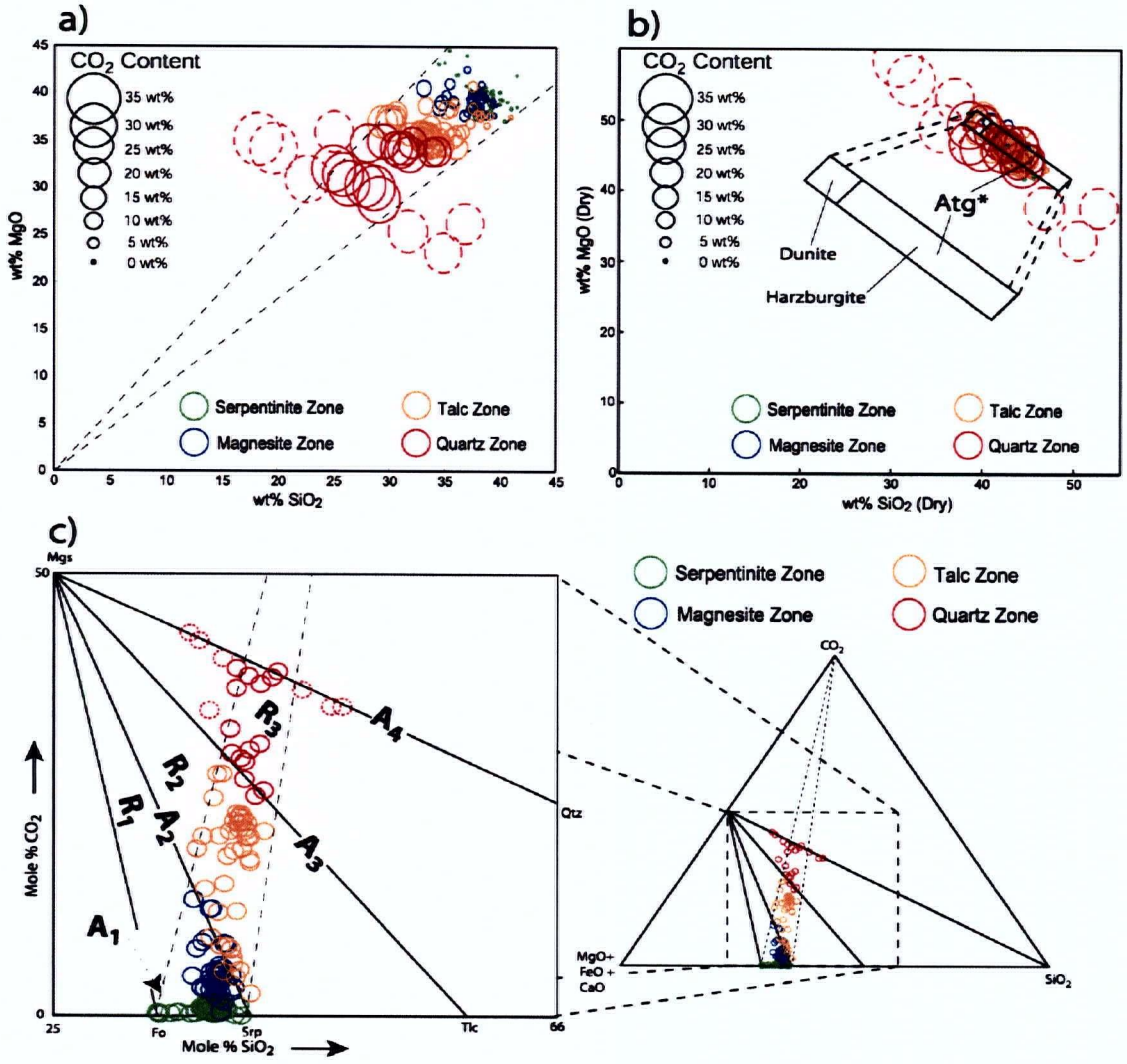
a)
CO2 Content
35 wt%
30 wt%
25 wt%
20 wt%
15 wt%
10 wt%
5 wt%
0 wt%
wt% MgO
wt% SiO2
Serpentinite Zone
Talc Zone
Magnesite Zone
Quartz Zone
b)
CO2 Content
35 wt%
30 wt%
25 wt%
20 wt%
15 wt%
10 wt%
5 wt%
0 wt%
wt% MgO (Dry)
wt% SiO2 (Dry)
Atg*
Dunite
Harzburgite
Serpentinite Zone
Talc Zone
Magnesite Zone
Quartz Zone
c)
Mgs
Mole % CO2
Mole % SiO2
Fo
Srp
Tlc
Qtz
R1
R2
R3
A1
A2
A3
A4
Serpentinite Zone
Talc Zone
Magnesite Zone
Quartz Zone
CO2
MgO+
FeO+
CaO
SiO2

Figure 5.2: a) Wt% MgO plotted vs. SiO_2. Circle size is proportional to CO_2 content. Data is in Appendix C. The observed trend is consistent with the passive dilution of MgO and SiO_2 by increase in CO_2 content except for seven outliers (dashed circles) which are near-completely to completely carbonate-altered. Dashed lined represent the chemical range defined by the protolith material and passive dilution. b) MgO and SiO_2 whole rock compositions renormalized to 100% (excluding H_2O and CO_2). Carbonated and uncarbonated samples plot on calculated dunite and harzburgite compositions (using Fo_{90} and En_{90} compositions for olivine and orthopyroxene respectively). Note that the MgO and SiO_2 contents of serpentinite and listwanite are indistinguishable. *Denotes an antigorite rich rock which contains 7 wt% magnetite (estimated from the whole rock geochemical data in Appendix C) created during the complete serpentinization of Fo^{90}/En^{90} rich rocks. c) Ternary phase diagram comparing the observed mineral content and whole rock composition in a MgO+FeO+CaO-SiO_2-CO_2 ternary diagram projected from H_2O.

areas where extensive quartz-carbonate veining (Si^{2+} - Mg^{2+} metasomatism) and limited K^+ (Cr-muscovite) and possibly Ca^{2+} metasomatism occurred.

5.2 PROTOLITH & ALTERATION ASSEMBLAGES

The geochemical dataset was collected from the Atlin Ultramafic Complex which contains depleted mantle harzburgite formed during adiabatic melt extraction beneath a mid-ocean ridge (Ash and Arksey, 1990). The melt extraction process and subsequent serpentinization event(s) have left the residual harzburgite chemically heterogeneous prior to listwanite metamorphism. The variation in modal orthopyroxene (opx) is a likely record of the original harzburgite heterogeneity (Fig. 5.2b).

Samples are divided, on the basis of mineral content, into five groups including protolith serpentinized harzburgite and four mineralogically distinct alteration assemblages (Fig. 5.2) of Hansen et al. (2005; Chapter IV). The data from Chapter IV is augmented by additional geochemical and mineralogical data on all 160 samples (Appendixes B and C). The serpentinized harzburgitic to dunitic protolith material is chemically variable. All samples contain measurable CO_2, even the freshest harzburgite samples. Thus, serpentinite samples without magnesite (A_1) and that contain less than 1 wt% CO_2 are considered protolith samples while those with greater than 1 wt% are considered altered samples. The most likely chemical species to be affected during a small amount of CO_2 addition is Ca in dolomite with or without calcite veins. If all CO_2 addition is attributed to carbonate addition, 1 wt% CO_2 would require the addition of about 1.2 wt% CaO if all the carbonate is calcite or 0.6 wt% if it is all dolomite. Given that the maximum amount of CaO in the 46 protolith samples is 1.96 wt% with only 0.59 wt% CO_2, it is very likely that the chemical range in CaO (and all other chemical species) reflects to some degree protolith heterogeneities (e.g. clinopyroxene content with respect to CaO).

Group A_1 samples do not contain magnesite and therefore have not undergone any of the three listwanite alteration reactions of Hansen *et al.* (2005). However they do contain up to 3.17 wt% CO_2. High CO_2 contents correlate with dolomite and/or calcite veining which is prevalent within serpentinite away from obvious carbonate alteration. These samples are excluded from the assessment of protolith heterogeneity. The altered

suite that I assessed includes samples without magnesite (A_1), and three groups separated by the metamorphic isograds defined by the first appearance of magnesite (R_1, A_2), talc (R_2, A_3) and quartz (R_3, A_4). For simplicity, the five groups are labelled protolith, serpentinite zone, magnesite zone, talc zone, and quartz zone. All geochemical data is converted from wt% oxide to moles/Kg of rock for each element. Fe is likely present in variable oxidation states because it is hosted in olivine, pyroxene, serpentine, magnetite and magnesite. Total whole rock Fe is represented as Fe^{3+} total. The generalized mineralogy for each zone is illustrated in Figure 5.1 (see Appendix B for complete mineralogy).

5.3 ANALYTICAL METHODS

Bulk geochemical samples were crushed and powdered in a tungsten carbide shatterbox. Powders were sent to the Geochemical Laboratories at McGill University, Montreal, PQ for bulk geochemical analysis by X-ray fluorescence. The results are included in Appendix C. The samples were analyzed for major, minor and trace elements, CO_2 content by induction furnace, and total volatile content by loss on ignition (L.O.I.).

The semi-quantitative mineralogy was determined from rock powders using a Siemens Diffraktometer D5000 X-Ray Diffractometer (XRD) at The University of British Columbia. Powders were further reduced in grain size using an aluminum oxide mortar and pestle in ethanol and uniformly smeared onto glass slides for analysis. Where possible, XRD-determined mineralogy was cross-checked with standard transmission light petrography, back scattered electron imagery and energy dispersive spectrography.

5.4 ERROR & WHOLE ROCK GEOCHEMISTRY

The error on the geochemical analyses was determined from four sets of blind replicates totalling 13 analyses on a single sample over a period of about 14 months. The error σ is reported as one standard deviation for each chemical species as determined from replicates (Table 5.1). Where the detection limit is greater than the variance determined from the replicate analyses for a particular element, the detection limit is substituted for σ. Table 5.2 illustrates representative analyses from each of the

Table 5.1: Geochemical Analyses of Replicates

Sample	SiO_2	TiO_2	Al_2O_3	Fe_2O_3	MnO	MgO	CaO	Na_2O	K_2O	P_2O_5	Cr_2O_3	Ni	V	Zn	LOI	CO_2	Total
AT03-pc2^{i}	38.71	0.013	0.75	8.03	0.108	40.22	0.85	<d/l	0.02	0.007	3827	2277	34	13	11.12	0.41	100.45
AT03-pc2^{i}	38.81	0.012	0.77	8.10	0.107	40.45	0.84	<d/l	0.01	0.006	3902	2289	34	13	11.12	0.41	100.85
AT03-pc2^{i}	38.59	0.013	0.78	8.00	0.109	40.12	0.83	0.01	0.01	0.007	4100	2282	35	13	11.14	0.45	100.25
AT03-pc2^{ii}	38.78	0.013	0.78	8.06	0.108	40.35	0.85	0.06	0.01	0.008	3844	2288	33	13	11.22	0.51	100.86
AT03-pc2^{ii}	38.57	0.013	0.76	8.04	0.107	40.25	0.82	0.06	0.01	0.007	3857	2286	38	16	11.21	0.52	100.47
AT03-pc2^{ii}	38.68	0.012	0.77	8.10	0.109	40.23	0.84	0.07	0.01	0.007	3969	2280	34	13	11.23	0.52	100.69
AT03-pc2^{ii}	38.61	0.013	0.77	8.06	0.107	40.19	0.83	0.07	0.01	0.008	3878	2283	34	13	11.24	0.53	100.53
AT03-pc2^{iii}	38.61	0.014	0.77	8.08	0.106	40.28	0.85	0.04	0.01	0.007	4173	2265	38	14	11.19	0.58	100.61
AT03-pc2^{iii}	38.68	0.012	0.77	8.03	0.107	40.02	0.83	0.05	0.01	0.008	3935	2274	37	14	11.22	0.57	100.36
AT03-pc2^{iii}	38.68	0.013	0.77	8.04	0.108	40.15	0.85	0.05	0.01	0.007	3779	2271	35	12	11.22	0.56	100.51
AT03-pc2^{iv}	38.81	0.013	0.77	8.01	0.109	40.21	0.84	0.08	0.02	0.007	3918	2283	39	13	11.24	0.59	100.73
AT03-pc2^{iv}	38.75	0.012	0.77	8.08	0.111	40.24	0.83	0.06	0.01	0.008	3932	2274	38	14	11.21	0.61	100.71
AT03-pc2^{iv}	38.69	0.015	0.79	8.02	0.110	40.20	0.86	0.09	0.01	0.007	3846	2268	39	13	11.25	0.57	100.66
Σ	0.0808	9E-04	0.01	0.033	0.001	0.104	0.012	0.028	0.004	0.0006	109.93	7.655	2.2	1	0.045	0.07	
d/l	0.006	0.004	0.012	0.003	0.003	0.01	0.002	0.008	0.003	0.0035	15	3	10	2	0.01	0.01	
σ	0.0808	0.004	0.012	0.033	0.003	0.104	0.012	0.028	0.004	0.0035	109.93	7.655	10	2	0.045	0.07	

All chemical species are reported as wt% except Cr_2O_3, Ni, V, Zn which are in ppm. i, ii, iii and iv denote replicates from four different times over a 14 month period. Σ = standard deviation.d/l = detection limit. σ = error.

Table 5.2: Representative Geochemical Analyses of Ultramafic Rocks

Sample	SiO_2	TiO_2	Al_2O_3	Fe_2O_3	MnO	MgO	CaO	Na_2O	K_2O	P_2O_5	Cr_2O_3	Ni	V	Zn	LOI	CO_2	Total	
01AT-8-1	41.50	0.012	0.14	7.99	0.098	38.61	0.02	0.03	0.01	0.012	3617	2191	23	25	11.65	0.06	100.66	Proto
01AT-10-1	34.98	0.010	0.09	8.08	0.105	43.25	0.06	<d/l	0.01	0.010	4274	2637	19	31	13.50	0.15	100.77	Proto
01AT-10-2	37.29	0.010	0.40	7.96	0.113	40.39	0.37	<d/l	0.01	0.009	4540	2315	31	33	13.14	0.26	100.38	Proto
AT04-6B	36.05	0.012	0.12	7.67	0.093	41.93	0.02	0.10	0.01	0.008	4757	2529	26	6	13.99	0.38	100.73	Proto
AT03-44-23	39.91	0.014	0.84	8.04	0.056	38.87	0.26	0.08	0.01	0.008	4086	2344	36	14	12.13	0.49	100.87	Proto
AT03-21-PCb	38.67	0.012	0.73	8.13	0.112	40.57	0.80	0.05	0.01	0.008	3938	2302	31	13	11.04	0.58	100.76	Srp-zone
AT03-21-Ma	38.33	0.012	0.68	8.05	0.106	40.48	0.80	0.06	0.01	0.007	3204	2320	33	8	11.63	0.68	100.72	Srp-zone
AT03-21-PFc	38.21	0.013	0.69	7.96	0.104	40.01	0.63	0.04	0.01	0.007	3283	2250	33	5	12.54	0.82	100.77	Srp-zone
AT03-44-14	40.40	0.014	0.95	8.03	0.099	37.18	1.18	0.06	0.01	0.008	3866	2208	38	11	12.24	0.89	100.78	Srp-zone
AT03-20-PE1a	38.65	0.015	0.87	8.22	0.115	40.27	0.74	0.06	0.01	0.008	3789	2361	42	14	11.06	1.31	100.64	Srp-zone
AT03-20-PD1a	37.96	0.013	0.96	7.67	0.105	38.57	0.90	0.06	0.01	0.008	3693	2144	40	10	13.95	2.29	100.79	Mgs-Zone
AT03-44-36	37.30	0.013	0.55	7.81	0.091	39.41	0.37	0.07	0.01	0.008	3815	2396	26	17	14.59	3.95	100.85	Mgs-Zone
AT03-44-5	34.74	0.009	0.08	7.29	0.088	39.04	0.03	0.04	0.01	0.007	3441	2240	14	16	18.90	9.91	100.81	Mgs-Zone
AT03-44-15	39.35	0.014	1.06	8.41	0.115	39.22	0.81	0.05	0.01	0.007	3793	2238	44	16	11.12	2.22	100.78	Mgs-Zone
AT03-44-37	37.02	0.011	0.10	7.06	0.090	42.51	0.04	0.05	0.01	0.007	4362	2602	12	9	13.09	3.7	100.69	Mgs-Zone
AT04-20F	30.14	0.009	0.05	6.64	0.086	36.73	0.05	0.06	0.01	0.008	2254	2355	<d/l	<d/l	26.42	24.72	100.66	Tlc-Zone
AT03-20-ij2b	38.23	0.012	0.89	7.32	0.066	37.50	0.54	0.02	0.01	0.008	3733	2201	35	12	15.05	4.67	100.24	Tlc-Zone
AT03-44-1	33.30	0.010	0.18	7.46	0.105	38.72	0.07	0.05	0.01	0.007	3875	2130	21	22	20.34	11.9	100.86	Tlc-Zone
AT03-20-CD2d	34.58	0.013	0.89	6.92	0.107	35.20	0.88	0.06	0.01	0.007	3653	1960	33	16	21.18	15.88	100.41	Tlc-Zone
AT03-20-ij3c	33.86	0.012	0.87	6.82	0.115	34.55	0.77	0.02	0.01	0.007	3646	1944	39	13	22.53	18.65	100.13	Tlc-Zone
01AT-6-1	28.84	0.009	0.24	4.80	0.071	28.88	2.05	0.03	0.03	0.006	3206	1793	14	28	34.63	35.17	100.09	Qtz-Zone
01AT-5-2	28.65	0.009	0.07	5.69	0.065	30.03	0.18	0.02	0.01	0.008	3359	1502	<d/l	17	34.99	35.20	100.21	Qtz-Zone
AT03-44-9	34.34	0.009	0.32	6.48	0.111	33.94	0.12	0.07	0.01	0.007	3232	1377	24	35	24.57	22.45	100.44	Qtz-Zone
01AT-5-4	31.84	0.008	0.07	5.76	0.066	33.61	0.10	<d/l	0.01	0.011	3110	1760	<d/l	23	28.41	28.01	100.38	Qtz-Zone
01AT-4-1	27.87	0.008	0.14	6.78	0.113	30.33	0.24	<d/l	0.01	0.008	3926	1956	15	21	34.09	34.34	100.18	Qtz-Zone

All data given in wt% oxide except Cr_2O_3, Ni, V and Zn which are reported in ppm.

aforementioned groups defined above. The full table of analyses can be found in Appendix C.

Many analyses contain concentrations for certain elements that are reported as being below the detection limit reported by the laboratory. The mass balance calculations require a species abundance. Any element reported as below the detection limit defined by the laboratory is replaced with half the detection limit reported for that element. Furthermore, H_2O was not directly measured. It was determined by the difference between L.O.I. and CO_2. The variance in H_2O is reported as the variance in L.O.I. defined by the 13 replicate analyses. The accuracy of Na_2O, L.O.I. and CO_2 differ significantly between batches in the replicate analyses. Because the suite of 160 geochemical analyses was collected over two years, the variance produced from all replicates is used in determining the standard error.

5.5 DIMENSIONAL ANALYSIS

The geochemical data are represented in matrix form. The dimensionality of a geochemical matrix is a measure of the number of linearly independent processes, in geochemical space, that formed each group. For example, the protolith group was formed by melt extraction and serpentinization of peridotite then subsequently carbonated to form listwanite and likely metasomatized in the most extremely carbonated cases. Thus, one would expect the dimensionality of the listwanite-altered samples to exceed that of the protolith group, and the quartz-zone group, with extensive quartz-carbonate veining, to be the highest.

The rank (dimensionality) of a matrix is the minimum number of columns (or rows) that when combined in linear combinations can reproduce all other columns and rows in the matrix (e.g. Strang, 1993). These columns span the compositional space defined by the matrix and, if taken in vector form, define a basis for that matrix. Each of the five groups of samples is represented by matrix S of dimension e (rows) by s (columns), where e is equal to the number of elements E in the dataset and s is equal to the number of samples in each group.

$$S = \begin{pmatrix} E_{(1,1)} & \cdots & E_{(1,s)} \\ \vdots & \ddots & \vdots \\ E_{(e,1)} & \cdots & E_{(e,s)} \end{pmatrix}, \quad Serr = \begin{pmatrix} \sigma_{E1} \\ \vdots \\ \sigma_{Ee} \end{pmatrix} \qquad (5.1, 2)$$

The standard errors of the analysed elements in the dataset define an e by 1 vector *Serr*. Because uncertainty exists in the analyses of each chemical constituent, there is the possibility that one or more approximations of S exist that has a lower dimensionality and falls within standard error of the original matrix S. Three techniques useful in reducing a matrix within standard error constraints are outlined below.

Sapprox matrixes are found using singular value decomposition (svd) (e.g. Strang, 1993) where the smallest singular values are changed to 0's while satisfying:

$$\left| S_{(e,s)} - Sapprox_{(e,s)} \right| \leq Serr_{(e)} \quad \text{for all } e \text{ and } s \qquad (5.3)$$

As illustrated in Figure 5.3a, this 'unweighted' technique is limited in its ability to find a *Sapprox* that satisfies (5.3) when attempting the reduction of a hypothetical two dimensional system to a rank of one. The unweighted svd solution only considers variations in S that are perpendicular to the model line. In the unweighted solution, *Approx* falls outside the error ellipses (crosses in Fig. 5.3a) for one sample, even though the error ellipse intersects the solution space (indicated by the thick black line connecting the crosses in Fig. 5.3a).

This can be rectified by using a weighted svd technique where S is weighted by the inverse of the square root of the covariance matrix cov_{err}, defined by the 13 blind replicate analyses (5.4). The diagonals of cov_{err} contain the square of the variance for each element. In the Atlin geochemical datasets the standard error is the greater of the variance and detection limit for each element (Table 5.1), therefore the diagonal values of the cov_{err} must be replaced with square of the standard error.

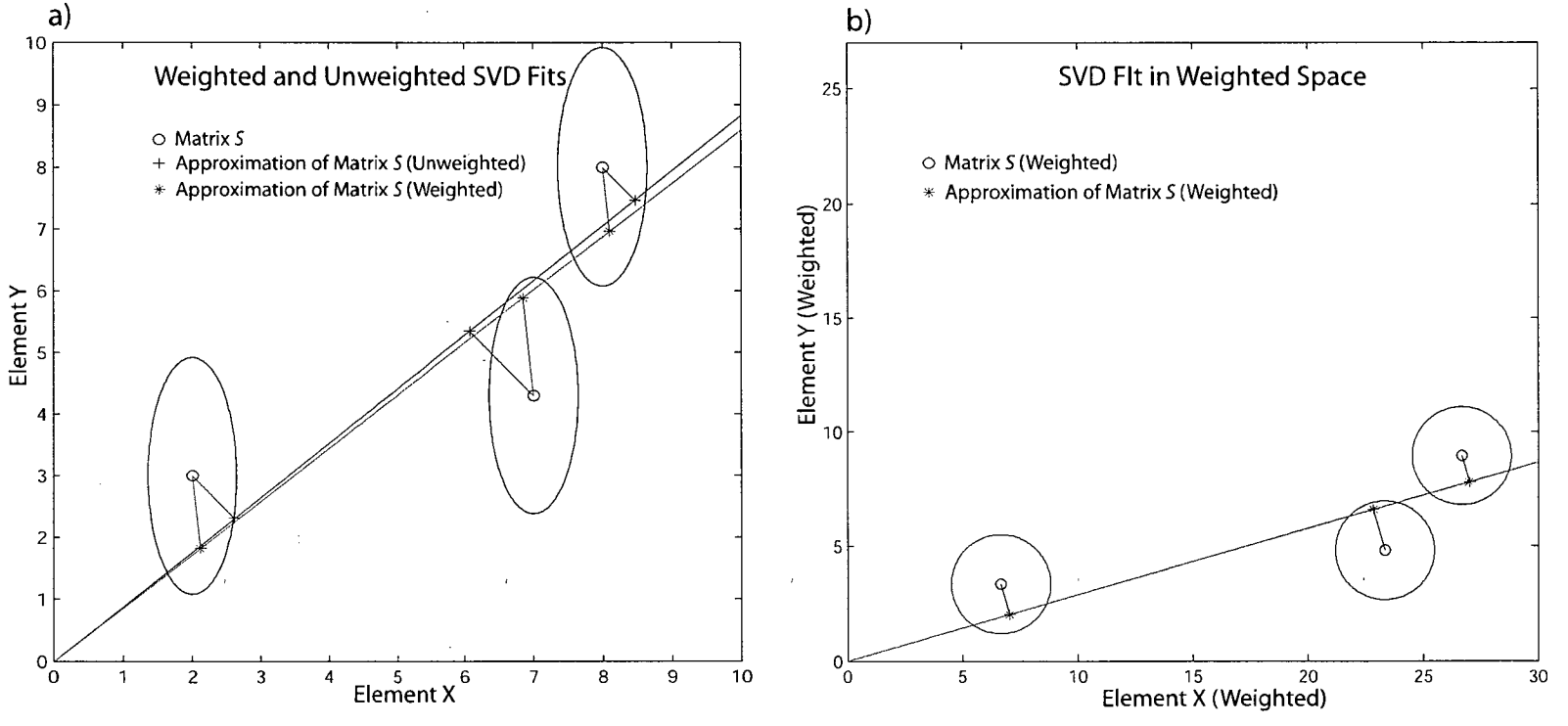

Figure 5.3: a) Actual SVD solutions to a hypothetical two dimensional dataset using both weighted and unweighted SVD where the data is weighted by the inverse of the standard errors. b) Illustrated weighted SVD in weighted space.

$$cov_{err} = \begin{pmatrix} \left(\sigma^{err}_{(E1)}\right)^2 & \sigma^{err}_{(E1,E2)} & \cdots & \sigma^{err}_{(E1,Ee)} \\ \sigma^{err}_{(E2,E1)} & \left(\sigma^{err}_{(E2)}\right)^2 & \cdots & \sigma^{err}_{(E2,Ee)} \\ \vdots & \vdots & \ddots & \vdots \\ \sigma^{err}_{(Ee,E1)} & \sigma^{err}_{(Ee,E2)} & \cdots & \left(\sigma^{err}_{(Ee)}\right)^2 \end{pmatrix} \tag{5.4}$$

$$wt_{err} = \left(\sqrt{\text{cov}_{err}}\right)^{-1}, \qquad S^{err}_{wt} = wt_{err} \cdot S \tag{5.5, 6}$$

$$unwt_{err} = \sqrt{\text{cov}_{err}}, \quad S = unwt_{err} \cdot S^{err}_{wt}, \quad Sapprox = unwt_{err} \cdot Sapprox^{err}_{wt} \tag{5.7, 8, 9}$$

The weighted svd technique finds a *Sapprox* that is one dimensional and falls within the error ellipses of all three samples (stars in Fig. 5.3a).

Rank reduction with weighted and unweighted svd on the geochemical data from Atlin is summarized in Tables 5.3 and 5.4. The original rank of the matrix is 16, reflecting the number of rows (number of chemical species analysed). The degree of rank reduction depends on the size of the error ellipses represented in Tables 5.3 and 5.4 as the number of standard errors. Tables 5.3 and 5.4 show the lowest rank each group could be reduced to within multiples of the σ values using unweighted and weighted data.

The rank of *S* may be further reduced if iterative techniques are used to fully explore the chemical space enclosed within the error ellipses. Figure 5.4a (iteration 1) illustrates another two dimensional hypothetical data set where the weighted svd technique fails to produce an *Sapprox* that is within the defined error. However *Sapprox* matrices do exist that satisfy (5.3). To find a solution within error, the original values from *S* are substituted back into *Sapprox* for all entries that fail criterion (5.3). The modified *Sapprox* is denoted *Sapprox**. Performing weighted svd on *Sapprox** produces a new *Sapprox* which is an approximation of *Sapprox**. This iteration effectively 'pulls' *Sapprox* towards the sample(s) which did not satisfy (5.3) in the previous iteration. After four iterations on this hypothetical two dimensional dataset, the solution in Figure 5.4a (solid black line) is acquired.

Table 5.3: Lowest rank of each group using unweighted SVD

	Proto	Srp-zone	Mgs-zone	Tlc-zone	Qtz-zone
1σ	16	-	16	16	16
2σ	15	-	16	16	16
3σ	15	-	16	15	15*
4σ	15	-	16	15	15*
5σ	15	-	16	14	15*
6σ	14	-	15	14	15*
n	46	9	42	44	19

* contains one or more negative values within the approximation of the dataset. SVD not done on Srp-zone because of the small number of analyses.

Table 5.4: Lowest rank of each group using weighted SVD

	Proto	Srp-zone	Mgs-zone	Tlc-zone	Qtz-zone
1σ	16	-	16	16	15*
2σ	14*	-	15	14*	14*
3σ	10	-	14	12	13*
4σ	10	-	14	11	13*
5σ	9	-	14	11	13*
6σ	9	-	11	11	11*
n	46	9	42	44	19

* contains one or more negative values within the approximation of the dataset. SVD not done on Srp-zone because of the small number of analyses.

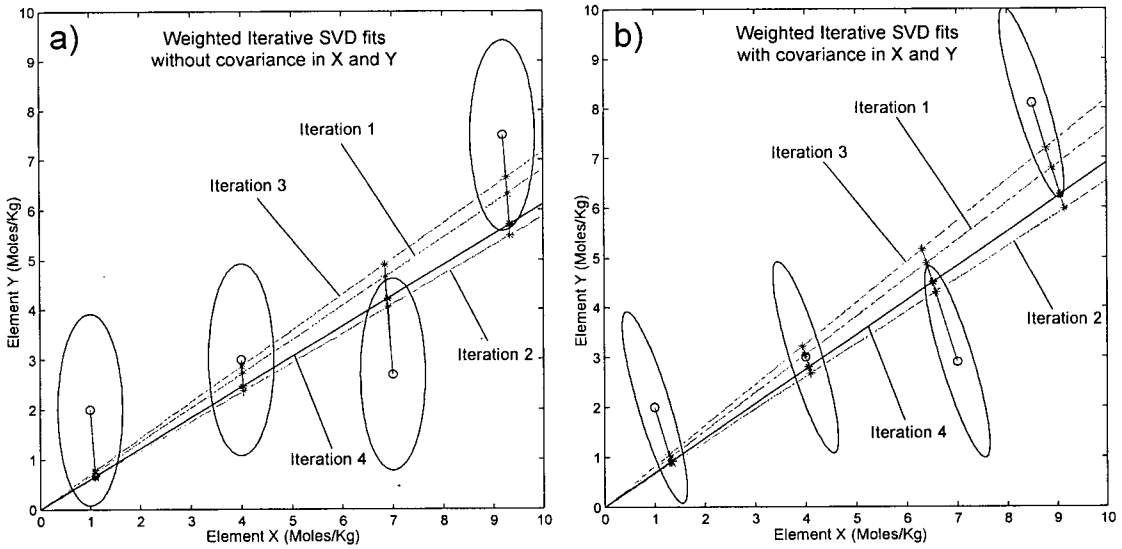

Figure 5.4: SVD solutions to a hypothetical two dimensional dataset using an iterative technique with data weighted by the inverse of the standard error. Two cases are shown. a) shows a situation where there is no covariance between the errors of X and Y. b) shows a situation where covariance does exist in the errors of X and Y. Acceptable solution is found after three iterations. The sample data is in Appendix A.

This procedure was scaled up to the real 16 dimensional datasets defined from Atlin. The iterative technique applies the additional constraint that all values of *Sapprox* be ≥ 0.

$$Sapprox_{(e,s)} \geq 0 \text{ for all } e \text{ and s} \tag{5.10}$$

Each dataset is initially reduced to a rank of $R = 1$ using the weighted data. If *Sapprox* fails inequality (5.3) for any element(s) in a sample then the original data from S are substituted back into *Sapprox* to create *Sapprox**. The iterative process is repeated until an *Sapprox* matrix is found that satisfies (5.3), or a specified number of iterations have been completed. It was found, by trial and error, that 250 iterations was adequate for this study as no difference in rank was produced between this number and 1000 iterations. If no satisfactory *Sapprox* matrix is found, then R is increased by 1 and the process is continued. R is increased in this manner until an *Sapprox* is found that satisfies (5.3) or $R=e$ in which case the dataset could not be reduced in rank. Table 5.5 shows the lowest rank found for each of the four metamorphic zones and their protolith using this technique for various multiples of σ.

In general, the results of the two weighted rank reduction techniques are consistent with the hypothesis that additional processes have affected listwanite-altered samples in addition to those responsible for the development of the heterogeneous protolith. The compositional space required by the protolith sample suite has a lower dimension than that required by the altered rocks. The quartz-zone altered samples have the largest dimensionality. In the magnesite and talc zones, the additional processes most likely include CO_2 addition and H_2O removal. Dolomite veins, common in weakly carbonated samples and often difficult to remove prior to powdering of samples, result in Ca addition and thus is also a possible process. The-quartz zone group of samples is the highest in rank despite the fact that it contains the smallest number of samples. They display significant evidence for metasomatism which includes quartz-carbonate veining (Mg, Si +/- Ca addition/removal) and Cr-muscovite formation (K addition). This apparent chemical mobility is assessed with mass balance calculations on the unmodified

Table 5.5: Lowest rank of each group using iterative weighted SVD

	Proto	Srp-zone	Mgs-zone	Tlc-zone	Qtz-zone
1σ	16	-	16	16	15
2σ	13	-	13	12	13
3σ	11	-	12	11	13
4σ	10	-	11	11	12
5σ	9	-	11	11	11
6σ	9	-	11	10	11
n	46	9	42	44	19

SVD not done on Srp-zone because of the small number of analyses.

full rank datasets and on the 3σ approximation results for unweighted, weighted and weighted iterative svd (Table 5.6).

5.6 MASS BALANCE

The chemical differences, or alteration, between the protolith group and each altered sample can be assessed using least squared linear algebraic manipulations. A least squares change of basis (Strang, 1993) is the heart of the mass balance calculation and is outlined as follows. The change of basis calculation uses a system of linear equations. The column basis for the protolith group is represented as the matrix P.

$$P = \begin{pmatrix} E_{(1,1)} & \cdots & E_{(1,z)} \\ \vdots & \ddots & \vdots \\ E_{(e,1)} & \cdots & E_{(e,z)} \end{pmatrix} \tag{5.11}$$

The subscript z represents the number of basis vectors in P. The composition of each altered sample (n) is designated $Alt_{(n)}$, a 1 by e vector listing moles element per Kg rock. Thus,

$$x_{(n)} = Alt_{(n)} \setminus P \tag{5.12}$$

where the '\' symbol gives the least squares solution to $P \cdot x_{(n)} = Alt_{(n)}$, and provides the vector $x_{(n)}$, containing the coefficients Co that when multiplied with P gives a 'best fit' to $Alt_{(n)}$. This 'best fit' is the model protolith MP that is made up of a linear combination of the basis vectors of P. In other words

$$P \cdot x_{(n)} = MP_{(n)} \approx Alt_{(n)} \tag{5.13}$$

One advantage of this approach is that it identifies a unique protolith composition for each altered sample. The protolith is chosen from the chemical space defined by the basis vectors to all protolith samples and is chosen so as to minimise the misfit between

Table 5.6: Lowest rank of each group using each SVD technique at 3σ

	Proto	Srp-zone	Mgs-zone	Tlc-zone	Qtz-zone
Full Rank	16	-	16	16	16
Unweighted	15	-	16	15	15*
Weighted	10	-	14	12	13*
Weighted iterative	11	-	12	11	13
n	46	9	42	44	19

* contains one or more negative values within the approximation of the dataset

the protolith and altered sample. This approach therefore minimises the amount of alteration. Differences between $MP_{(n)}$ and $Alt_{(n)}$ indicate that the altered sample falls outside the chemical space defined by *P*.

The mineralogical changes during alteration require significant mobility in elements H and C. These two elements were therefore removed from the mass balance calculation to eliminate their influence on the linear least-squares fit. This allows for a more reliable test of the passive dilution hypothesis in that it is now easier to detect changes of non-volatile elements with respect to each other. Thus, $e = 14$ and $z \leq 14$.

Data was rank reduced to within 3σ. Model protoliths for altered samples are compared to altered rock compositions in Figure 5.5a. Each altered sample is represented as a column of boxes, and samples from each group are arranged from left to right on the basis of increasing CO_2 content. The vertical dimension corresponds to the elements. Grey-filled boxes indicate that the elemental abundance in the model protolith and altered sample differ by less than 3σ. White boxes denote elements for which the abundance in the altered sample abundance exceeds that of the model protolith by more than 3σ. Black boxes denote those elements where a deficiency of more than 3σ in the altered rock relative to the model protolith exists.

Geochemical (Fig. 5.2) and petrographical evidence exists for the metasomatism in the most extreme carbonated samples. These include, high density quartz-carbonate veining (Si and Mg metasomatism) and the presence of Cr-muscovite (K metasomatism). However, the change of basis calculation did not detect these elemental alterations (Fig. 5.5). Rather, the most abundant rock-forming elements, such as Mg and Si, display an excellent fit throughout the entire suite of altered samples even though outliers, shown as dashed circles in Figure 5.2, exist. The misfit was forced into the least abundant elements such as Zn and V. This indicates that the geochemical space approach to this point can only detect if altered samples fall outside the sub-space defined by *P*. Two reasons exist for this. One is because to this point there have been no constraints placed on the protolith aside from forcing it to be contained within the sub-space defined by *P*. The second reason is because the most abundant elements have the most control on the fit of *MP* to *Alt*. Figure 5.5b shows an Mg *vs.* Si plot for the calculated model protolith *MP*. It

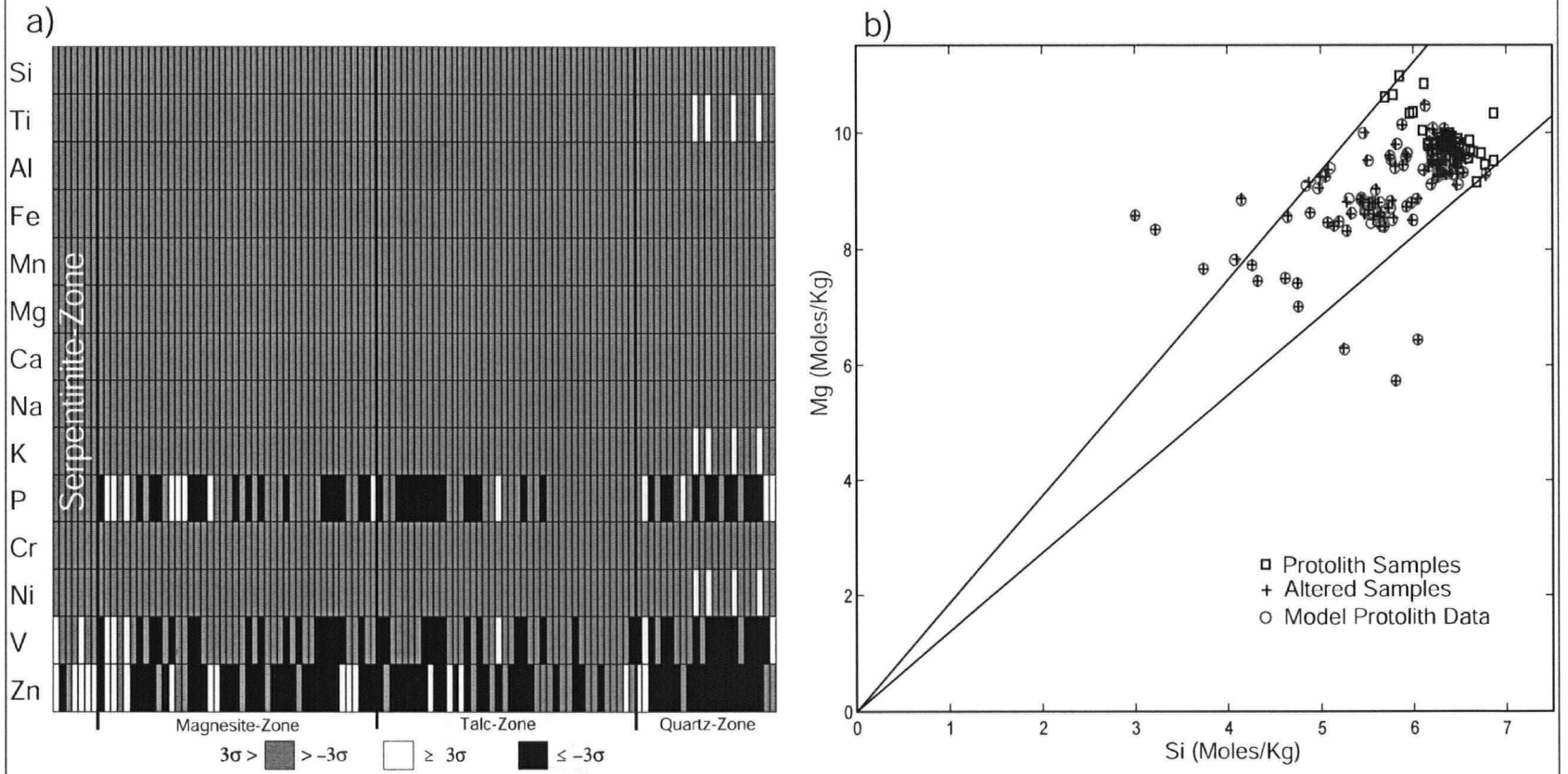

Figure 5.5: a) Residual over standard error calculated using Matlab left division on data reduced in rank to 3σ. b) Mg vs. Si plot illustrating that *MP* mimics the actual data of the altered samples because there are no constraints placed on the chemical make-up of *MP*.

illustrates that these two elements almost perfectly mimic the original data of all altered samples.

To limit the model protoliths to lie within the bounds of the protolith variations, the system of equations were solved with additional linear constraints. Each element in *MP* was constrained to fall within a set chemical range defined by the 46 protolith samples. The upper and lower limits (*ul* and *ll* respectively) of each element define two 1 by *e* vectors termed *pu* and *pl*, respectively.

$$pl = \begin{pmatrix} ll_{E1} \\ \vdots \\ ll_{Ee} \end{pmatrix} \text{ and } pu = \begin{pmatrix} ul_{E1} \\ \vdots \\ ul_{Ee} \end{pmatrix}, \text{ thus } pl \le MP \le pu \text{ for all } e \tag{5.14}$$

Here the minima and maxima of each element within the 46 protolith samples were chosen to define *pl* and *pu*, respectively, rather than a mean +/- one standard deviation. Sampling bias, caused by sampling a significant portion of protolith samples from a relatively small area of the project area, skews the averages of each element. A range defined by minima and maxima avoids this problem by allowing *MP* to be constrained within a protolith geochemical range known to exist.

The new system of equations with the additional linear constraints was solved using the medium scale optimisation option of the Matlab function lsqlin (Coleman *et al.*, 1999). This function employs an active set method similar to that described in Gill *et al.* (1981). The system of equations

$$A \cdot x = b \tag{5.15}$$

is solved in a least squares sense forcing the optional inequality

$$C \cdot x \le d \tag{5.16}$$

and optional equality

$$Aeq \cdot x = beq \tag{5.17}$$

(5.14) and (5.15) are setup in the following way (modified and simplified from Gordon (2003).

$$A = \left(-P \mid Alt_{(n)}\right), \qquad b = \left(0_1 \quad \cdots \quad 0_z\right) \tag{5.18, 19}$$

$$C = \left(\begin{array}{c|c} \dfrac{-P}{P} & \begin{matrix} 0 \\ \vdots \\ 0 \end{matrix} \end{array}\right), \quad d = \begin{pmatrix} -pl \\ pu \end{pmatrix}, \quad x_{(n)} = \begin{pmatrix} Co_{n1} \\ \vdots \\ \dfrac{Co_{nz}}{mf_n} \end{pmatrix} \tag{5.20, 21, 22}$$

Note that (5.15) set up with (5.18) and (5.19) is simply a rearranged form of (5.8) with the addition of the mass factor term *mf* in $x_{(n)}$. If (5.23) is satisfied, *mf* represents the calculated gain in mass of the altered sample.

$$Co_1 + Co_2 + \cdots + Co_z = 1 \tag{5.23}$$

Equation (5.23) forces the protolith or starting martial to add up to 1 (i.e. 1 Kg of starting material), and is satisfied by equality (5.17) where:

$$Aeq = 1 \text{ and } beq = \left(1_1 \quad \cdots \quad 1_z \quad 0\right) \tag{5.24}$$

Thus, one Kg of protolith material forms *mf* Kg of rock following alteration.

Figure 5.6 shows where the residual between *MP* and *Alt* exceeds 3σ, following the calculations (5.15) to (5.24) on the original, full rank data (results for the rank reduced data are shown below). Generally the data fit the model well. In addition, the resultant *mf* for each sample is in agreement with the range of mass factors calculated from whole rock data assuming a passive dilution hypothesis (Fig. 5.7a). The range in mass factors for an altered sample is the minimum and maximum of the sum of the non-

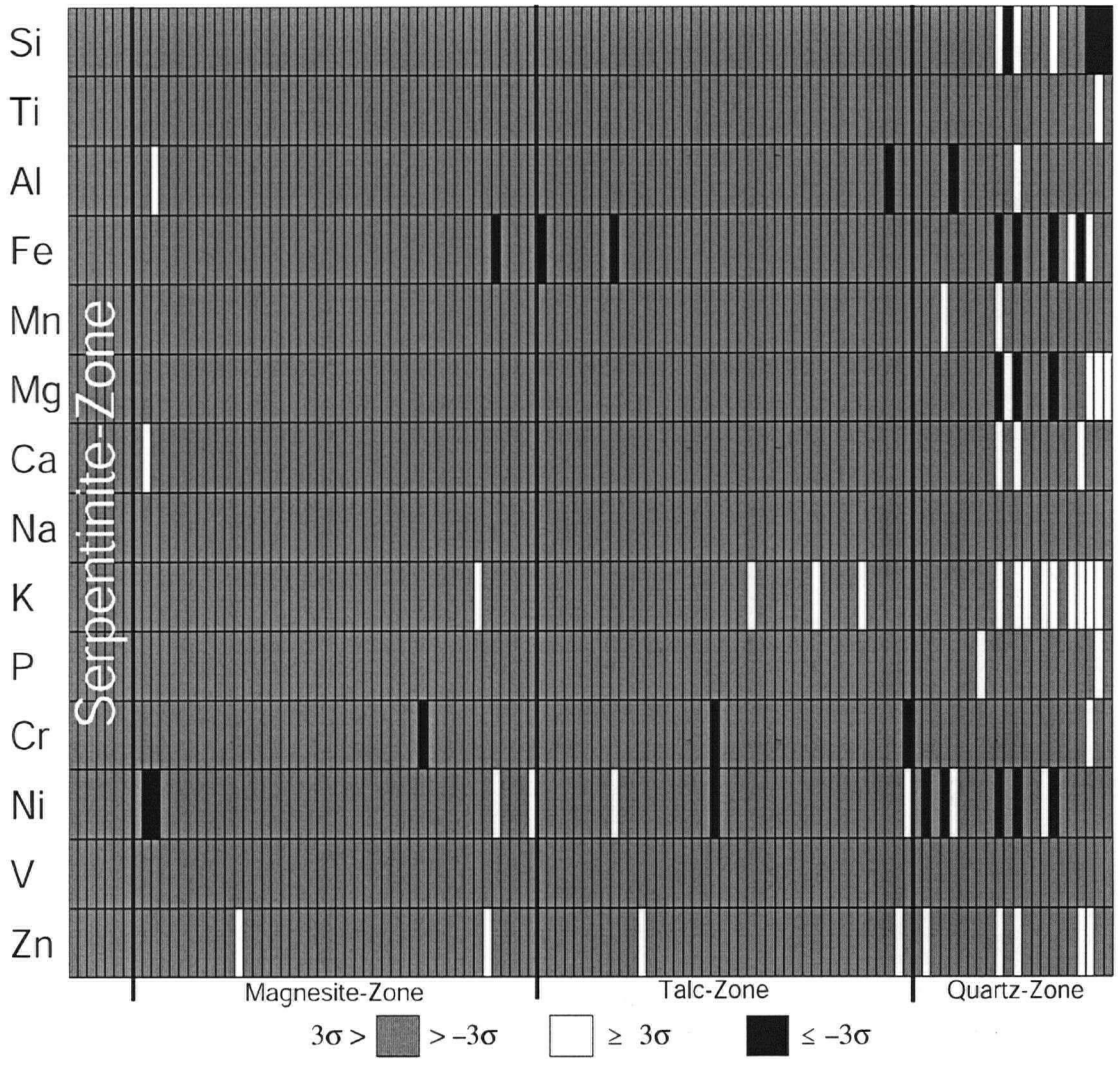

Figure 5.6: Ratio of residual error to standard error in whole rock chemical composition of carbonated samples. Residual error is the difference between model protolith compositions predicted by reactions equations (5.15) to (5.24) and measured compositions of altered samples. Values of the ratio that exceed three standard errors (positive/negative) indicate an excess/deficiency of the species that cannot be accounted for by the given protolith range in composition and the passive dilution hypothesis.

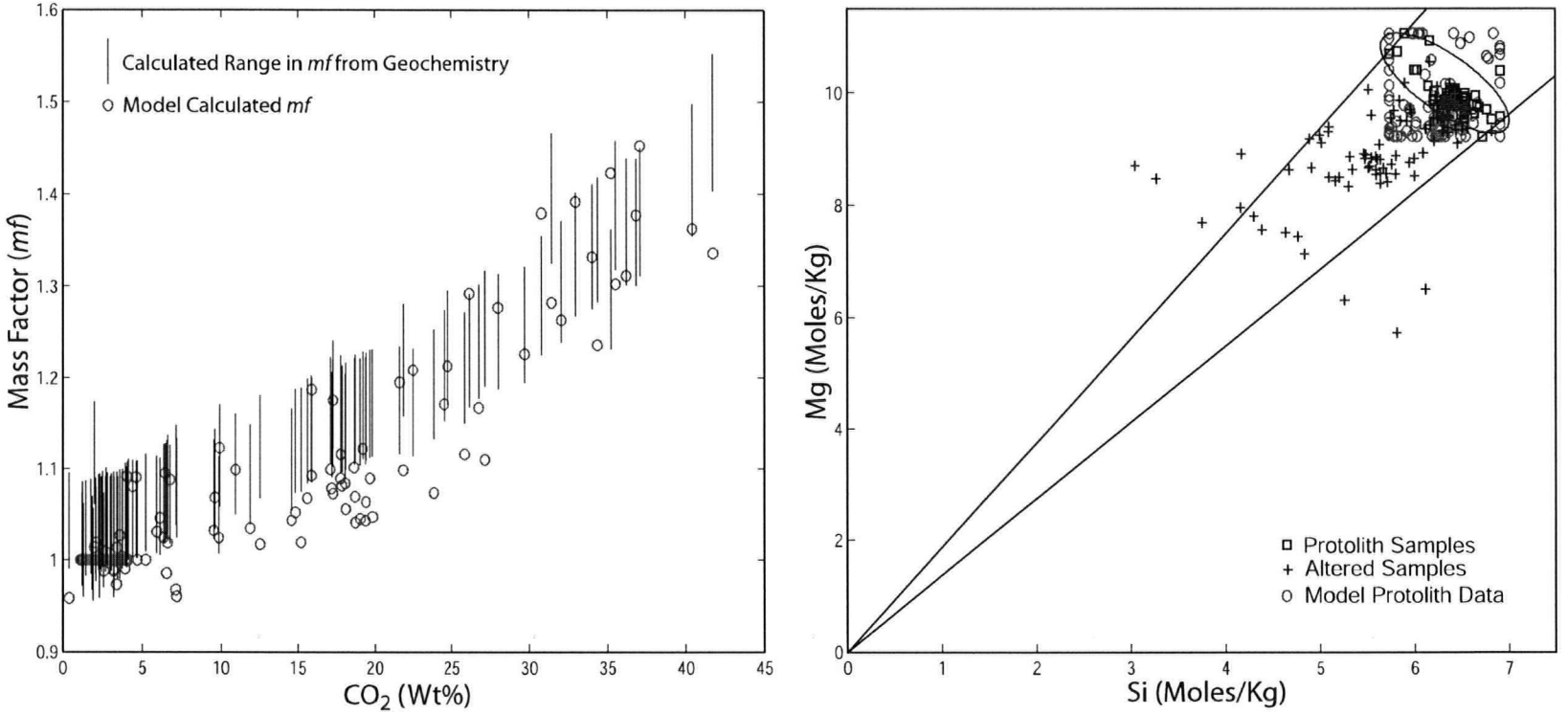

Figure 5.7: a) Gain in mass vs. CO_2 content. Circles represent model calculated *mf*s which are in good agreement with the range calculated from the total dry renormalized geochemistry assuming the passive dilution hypothesis. b) Mg vs. Si diagram showing the altered samples, protolith samples and calculated *MP*s.

volatile component, in wt%, of the 45 protolith samples divided by the same in the altered sample.

Problems become evident when one element from *MP* is plotted verses another (Fig. 5.7b). The model protolith compositions span the rectangular bounds defined by (5.14) and are not restricted to ellipses defined by covariances between elements in the protolith group. This covariance is shown as the ellipse centred on the median of the two elements in Figure 5.7b. This can be partially rectified by adding an additional constraint to inequality (5.16). The addition is similar to (5.20) and (5.21) but instead uses data weighted by the inverse of the square root of the covariance matrix *cov* defined by the protolith group of samples *proto*.

$$cov_{proto} = \begin{pmatrix} \left(\sigma_{(E1)}^{proto}\right)^2 & \sigma_{(E1,E2)}^{proto} & \cdots & \sigma_{(E1,Ee)}^{proto} \\ \sigma_{(E2,E1)}^{proto} & \left(\sigma_{(E2)}^{proto}\right)^2 & \cdots & \sigma_{(E2,Ee)}^{proto} \\ \vdots & \vdots & \ddots & \vdots \\ \sigma_{(Ee,E1)}^{proto} & \sigma_{(Ee,E2)}^{proto} & \cdots & \left(\sigma_{(Ee)}^{proto}\right)^2 \end{pmatrix}, \qquad wt_{proto} = \left(\sqrt{\text{cov}_{proto}}\right)^{-1} \qquad (5.25, 26)$$

$$P_{wt}^{proto} = wt_{proto} \cdot P, \qquad Alt_{wt}^{proto} = wt_{proto} \cdot Alt \qquad (5.26, 27)$$

$$pl_{wt}^{proto} = \begin{pmatrix} ll_{E1}^{wt} \\ \vdots \\ ll_{Ee}^{wt} \end{pmatrix} \;\&\; pu_{wt}^{proto} = \begin{pmatrix} ul_{E1}^{wt} \\ \vdots \\ ul_{Ee}^{wt} \end{pmatrix}, \text{thus } pl_{wt}^{proto} \le MP_{wt}^{proto} \le pu_{wt}^{proto} \text{ for all } e \qquad (5.28)$$

Equations (5.16) and (5.20) become

$$C = \left(\begin{array}{c|c} -P & 0 \\ P & \vdots \\ -P_{wt}^{proto} & \vdots \\ P_{wt}^{proto} & 0 \end{array}\right), \qquad d = \begin{pmatrix} -pl \\ pu \\ -pl_{wt}^{proto} \\ pu_{wt}^{proto} \end{pmatrix} \qquad (5.31, 32)$$

and constrain elements within *MP* to simultaneously plot within the error boxes defined by the unweighted data, and within rhombohedra which roughly mimic the shapes of covariance ellipses. *A*, *b*, *Aeq*, *beq* and *x* remain unchanged.

5.7 RESULTS

The results of the mass balance calculation using unmodified full-rank data sets and with the weighted constraints in place are shown in Figure 5.8 and 5.9. Figure 5.8a shows the model calculated *mf* as a function of the degree of carbonation (CO_2 content) superimposed over the range in mass factors calculated from whole rock data. In general, there is a very good correlation between the two. Figure 5.8b shows the Mg/Si makeup of the protolith samples (boxes), altered samples (crosses) and model protoliths (circles). The model protoliths fall within the rectangular bounds defined by (5.14) and within the rhombohedra defined by (5.28). Figure 5.9 shows a) the residuals (model protoliths subtracted from the altered samples) that fall outside +/- 3σ from the altered rocks and b) residuals that fall outside +/- 10σ highlighting the more extensive alteration. A table of residuals is included in Appendix F. Positive and negative residuals (white and black boxes, respectively) indicate that the altered rock contains more (or less) of that element than permitted by the hypothesis.

In general, the isochemical reaction model provides a very good fit to the data. Excluding the seven almost to completely-carbonated outliers, identified as samples with dashed circles in Figure 5.2, the 12 elements Si, Ti, Al, Fe, Mn, Mg, Ca, Na, K, P, Cr and V return a good to excellent fit, generally within +/- 3σ (Fig. 5.9). Thus, the variation in the composition of these elements can almost exclusively be explained by the variability of the protolith rocks and the dilution effect during mass addition. Where deviation from a perfect fit is displayed, mainly in Zn and Ni, it is both positive and negative throughout the whole suite of alteration and produces no trends. Therefore it is most likely that these two elements were also immobile during the carbonate-alteration. The poor fit in these two elements could be due to inadequate characterization of the protolith. Another possibility is that the calculation forces more of the misfit into the least abundant elements which have the least control on the fit. This could explain the misfit in Zn.

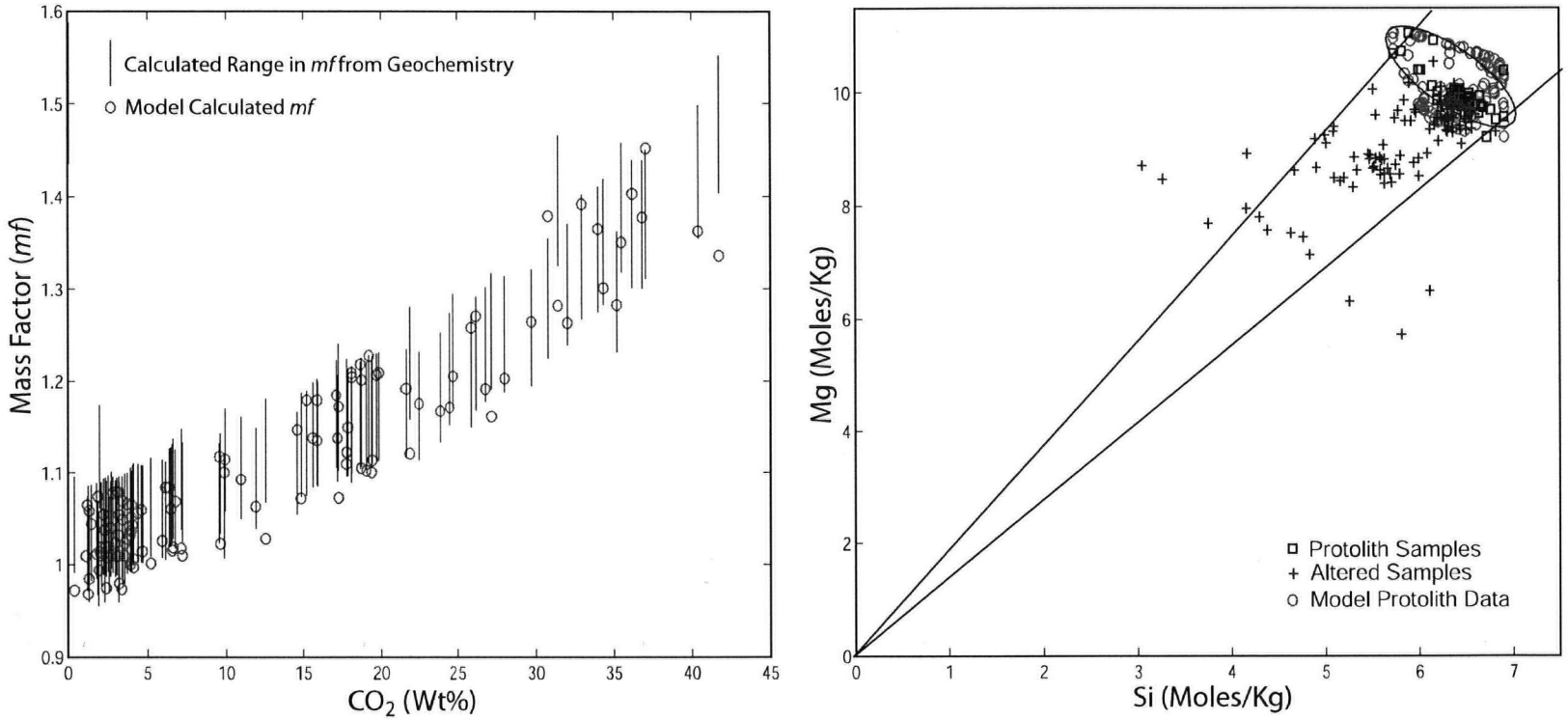

Figure 5.8: a) Gain in mass vs. CO_2 content. Circles represent model calculated *mf*s which are in good agreement with the range calculated from the total dry renormalized geochemistry assuming the passive dilution hypothesis. b) Mg vs. Si diagram showing the altered data, protolith data and calculated *MP*s.

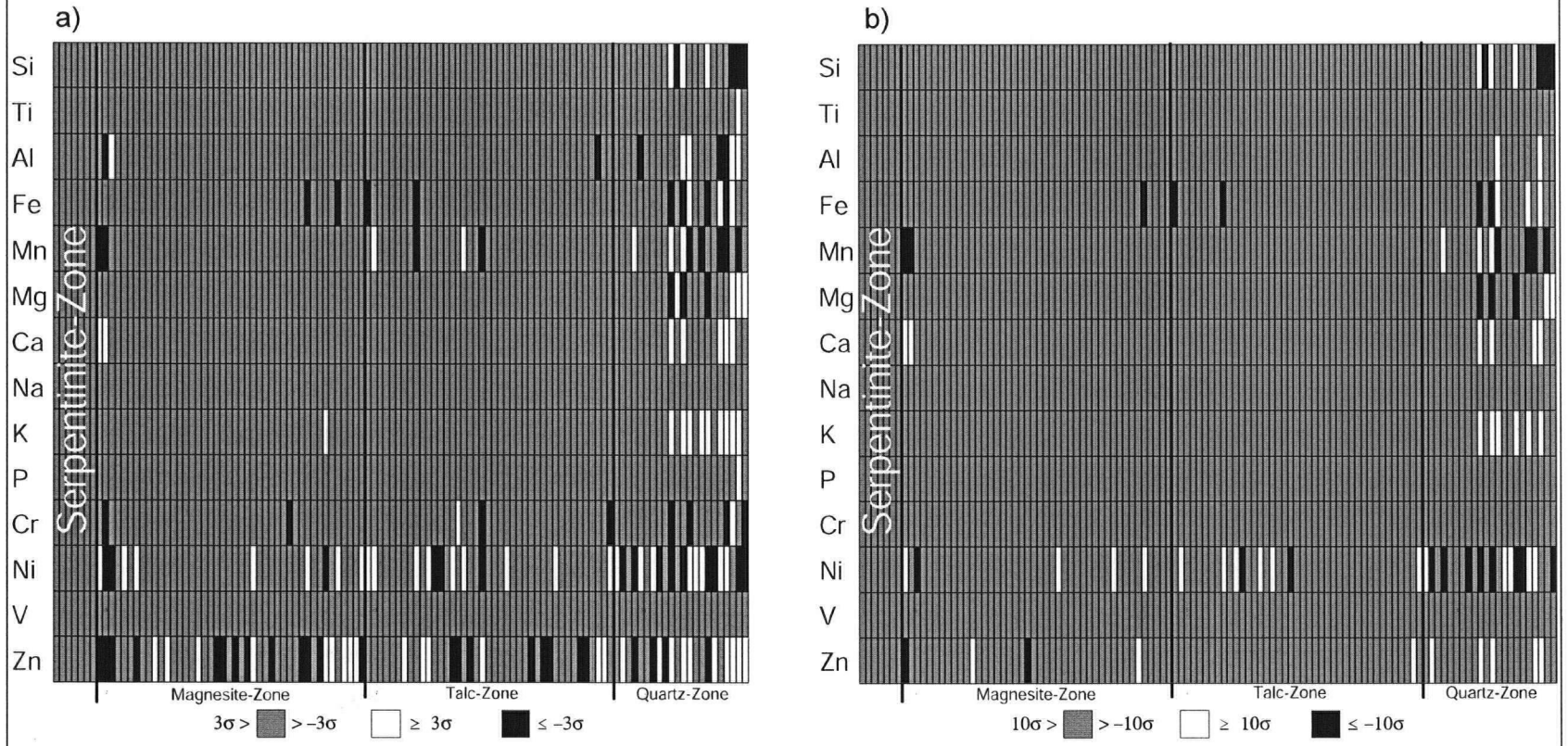

Figure 5.9: Ratio of residual error to standard error in whole rock chemical composition of carbonated samples. Residual error is the difference between model protolith compositions predicted by equations (5.15) to (5.32) and measured compositions of altered samples. a) Values of the ratio that exceed three standard errors (positive/negative) indicate an excess/deficiency of the species that cannot be accounted for by the given protolith range in composition and the passive dilution hypothesis. b) Same as a) except it shows the more significant residuals that exceed 10 standard errors.

Seven samples from the quartz-zone display widespread elemental mobility. High density veins are evident in hand sample and were difficult to remove prior to crushing of the sample for geochemical analysis. In terms of the most abundant rock-forming elements, Figure 5.2 illustrates that only samples that are near completely- to completely-carbonated deviate from the passive dilution trend.

The sporadic positive residuals in Ca can be attributed to a number of different reasons including: the inadequate removal of vein material prior to powdering of samples; inadequate characterization of the protolith (i.e. the abundance of clino-pyroxene); and Ca addition during carbonation in the most highly carbonated samples. Though significant Ca addition has not convincingly been detected in this study, documented cases (e.g. Aydal, 1990) have clearly shown that Ca addition is important in some listwanite systems.

Large positive residuals in K displayed in highly carbonated samples likewise are consistent with mineralogical observations. Bright green Cr-muscovite, a K-bearing mineral, is common in samples that have undergone extreme carbonate alteration and quartz-carbonate veining (Table B1, appendix B). Though K addition occurred during the most intense alteration, it was absent during most of the listwanite alteration.

Figure 5.10 shows the results of the mass balance using the rank reduced datasets where the approximations of the original data was allowed to differ by as much as 3σ from the original unmodified data. The results are almost identical to those acquired from the calculations on the unmodified data. One would except that the smaller amount of basis vectors in the rank reduced datasets would result in a poorer fit. However this is not the case. Likely the dimensionality removed during the rank reduction was negligible indicating that the true dimensionality is indeed less than 16.

The use of data that is reduced in rank is of limited use in this approach of mass balance. Figure 5.5a illustrates that the dimensionality throughout most of the alteration is about the same. Quartz-carbonate veining and Cr-muscovite correspond well with the sudden increase in the misfit in the most extreme carbonate altered samples. Although numerical extraction of the differences in dimensionality between the groups is not yet possible, future mass balance techniques may be able to incorporate this information.

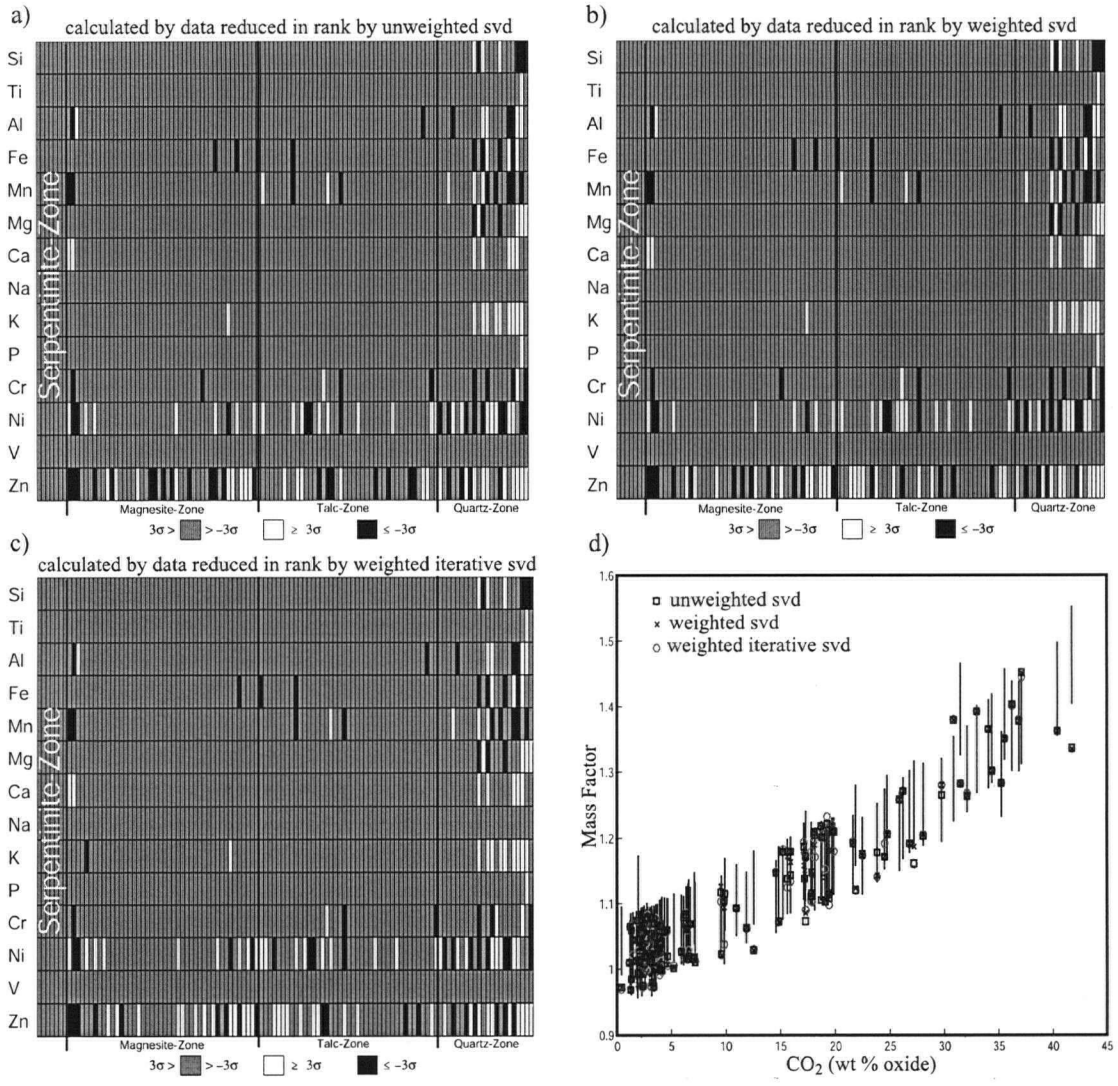

Figure 5.10: Ratio of residual error to standard error in whole rock chemical composition of carbonated samples. Residual error is the difference between model protolith compositions predicted by equations (5.15) to (5.32) and measured compositions of altered samples. Values of the ratio that exceed three standard errors (positive/negative) indicate an excess/deficiency of the species which cannot be accounted for by the given protolith range in composition and the passive dilution hypothesis. a), b and c) correspond to residuals calculated using data reduced in rank to 3σ using the unweighted, weighted and weighted-iterative svd techniques. d) shows the model calculated mass factor as a function of CO_2 content of the rock superimposed over the range in mass factors calculated from the dry chemistry of the rocks.

5.8 IMPLICATIONS

This geochemical mass balance approach has many advantages over other popular mass balance techniques. Possibly the most attractive is this technique calculates a model protolith, constrained to fall within a defined geochemical space, for each altered sample rather than assigning the same average protolith for all altered samples. Any difference between the altered rock and its calculated model protolith, assuming the protolith is chemically characterized adequately, is thus considered to represents alteration.

The calculation is still based on a least-squares best fit. For this reason, significant alteration in major elements tends to cause misfit in those that are well-behaved because the least squares calculation finds the solution that best fits all elements in the altered sample. In other words, misfits in mobile elements are balanced by introducing misfit in immobile elements. For this reason, this geochemical assessment procedure, as outlined beforehand, is best suited to test systems hypothesized to have involved little mobility in non-volatile chemical species, such as the listwanite rocks of this study.

Ideally this technique should also constrain the ratio of each pair of elements (i.e. all possible pairs) in the model protolith to fall within the minimum and maximum ratios for the same pair in the protolith group of samples. This would confine model protoliths to fall within the two lines in Figure 5.7b which define the minimum and maximum ratio of Mg to Si in the protolith group. In theory this constraint is easy to comprehend and define mathematically (5.33); however it is very difficult to impossible using *lsqlin*.

$$\begin{bmatrix} \left(E_1/E_m\right)_{min} \\ \left(E_2/E_m\right)_{min} \\ \vdots \\ \left(E_e/E_m\right)_{min} \end{bmatrix} \leq \begin{bmatrix} \left(E_1/E_m\right)_{MP} \\ \left(E_2/E_m\right)_{MP} \\ \vdots \\ \left(E_e/E_m\right)_{MP} \end{bmatrix} \leq \begin{bmatrix} \left(E_1/E_m\right)_{max} \\ \left(E_2/E_m\right)_{max} \\ \vdots \\ \left(E_e/E_m\right)_{max} \end{bmatrix} \quad \text{for each element } m. \quad (5.33)$$

5.9 COMPARISON TO GRESENS' ANALYSIS

In this section, the geochemical mass balance technique is compared to that of Gresens (1967), probably the most widely applied geochemical mass balance technique. However, instead of using a average protolith for all altered samples, the Gresens (1967) technique as applied here uses the model calculated protoliths on each altered sample calculated from the previous section (using the unaltered datasets). For all but the seven identified outlier samples, represented as dashed circles in Figure 5.2, Si and Mg are assumed to be immobile during the listwanite alteration. The elements used as baseline immobile elements for the seven outliers were chosen on a sample-by-sample basis. Here the two or three most abundant elements which show no residual in Figure 5.9a were used. Results, including the calculated mass factors, are shown in Figure 5.11 and are comparable to the results produced from the constrained weighted mass balance technique from the previous section.

5.10 CONCLUSION

This chapter clearly illustrates, using a new and powerful geochemical space based approach to mass balance, that the listwanite alteration at Atlin primarily involved non-metasomatic (de)hydration/carbonation reactions. The limited cases of clear metasomatism, primarily Si, Mg and K, are backed up with hand sample evidence that includes extensive quartz-carbonate veining and Cr-muscovite generation or can be accounted for by the incomplete characterization of the protolith. One of the major advantages this technique has over other popular mass balance options is that it allows for a protolith, given an allowable geochemical space in which to reside, for each altered sample. Dimensional analysis by the reduction of the datasets in rank is consistent with the hypothesis that additional processes have affected listwanite altered samples in addition to those responsible for the development of the heterogeneous protolith. That is, protolith group has the lowest dimensionality while the quartz-zone has the highest.

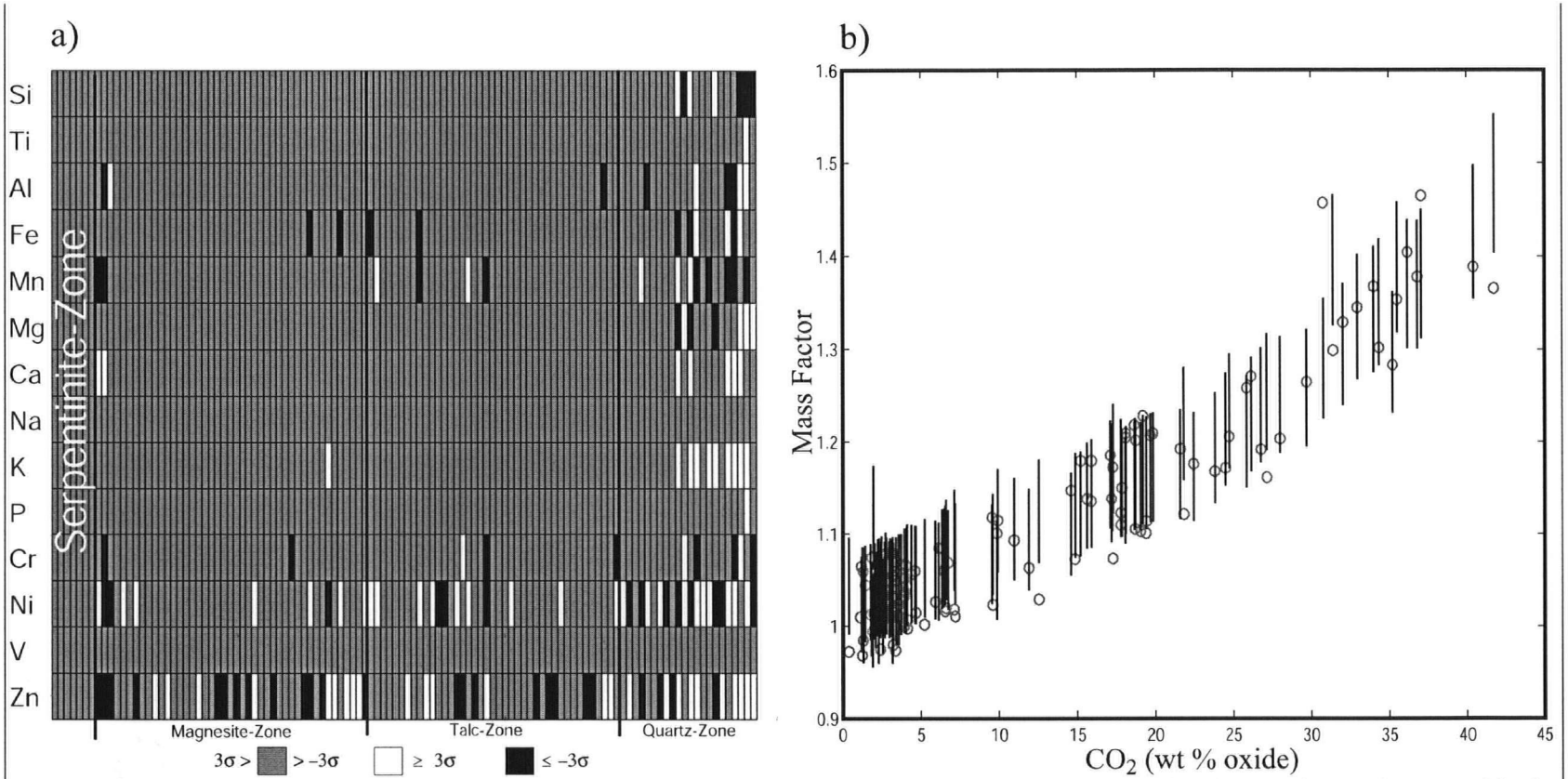

Figure 5.11: a) Ratio of residual error to standard error in whole rock chemical composition of carbonated samples. Residual error is the that calculated using the method of Gresens (1967) assuming Si and Mg are immobile, for all but the identified outliers, and using the model calculated protolith for each altered sample. The most abundant elements, which do not show residuals in Figure 5.9a, are assumed immobile for the seven outliers. b) Gresens' analysis calculated mass factors superimposed on the range in mass factors calculated from the total dry geochemistry assuming the passive dilution hypothesis.

5.10 REFERENCES

Ague, J. J. and Van Haren, J. L. M., 1996, Assessing Metasomatic Mass and Volume Changes Using the Bootstrap, With Application to Deep-Crustal Hydrothermal Alteration of Marble: Economic Geology, v. 91, p. 1169-1182.

Ash, C. H. and Arksey, R. L. (1990a): The Atlin Ultramafic Allochthon: Ophiolite Basement Within the Cache Creek Terrane; Tectonic and Metallogenic Significance (104N/12); Geological Fieldwork 1989, B.C. Department of Energy and Mines, Paper 1990-1, p. 365-374.

Aydal, D. (1990): Gold-Bearing Listwaenites in the Arag Massif, Kastamonu, Turkey; Terra Nova, v. 2, p. 43-52.

Gill, P.E., W. Murray, and M.H. Wright, Practical Optimization, Academic Press, London, UK, 1981.

Coleman, T., Branch, M. and Grace, A. (1999): Optimization Toolbox: for Use with Matlab, Version 2.

Gordon, T.M. (2003): Algebraic Generalization of the Graphical Gresen and Pearce Methods for Identification of Geochemical Mass-Transfer Processes. (abstract), Vancouver 2003 Abstracts, CD-ROM, GAC-MAC-SEG, Vancouver 2003 Annual General Meeting, Vancouver, B.C., 28-146, ISSN 0701-8738, ISBN: 0-919216-86-2.

Grant, J. A. 1986: The Isocon Diagram - A Simple Solution to Gresens Equation for Metasomatic Alteration; Economic Geology, v. 81, p. 1976-1982.

Gresens, R. L. (1967): Composition-Volume Relationships of Metasomatism. *Chemical Geology*, **2**, 47-65.

Hansen, L.D., Dipple, G. M., Kellett, D. A. and Gordon, T. M. (2005): Carbonate-Altered Serpentinite: A Geologic Analog to Carbon Dioxide Sequestration, Canadian Mineralogist, v. 43, part 1, p. 225-239.

Hansen, L. D., Dipple, G. M., Anderson, R. G. and Nakano, K. F. (2004): Geologic Setting of Carbonate Metasomatised Serpentinite (Listwanite) at Atlin, British Columbia: Implications for CO_2 Sequestration and Lode-Gold Mineralization. In Current Research, Geological Survey of Canada, Paper 2004-A5, 12 pages.

Strang, G. (1993): Introduction to Linear Algebra. Wellesley-Cambridge Press.

CHAPTER VI: CONCLUSION

6.1: CONCLUSION

The listwanite alteration within the Atlin Ultramafic Allochthon at Atlin B.C. is spatially controlled by a basal thrust fault (e.g. Ash, 1994; Hansen *et al.*, 2004) and regional joint/fracture system with four steeply-dipping fracture sets spaced about 45° apart (Hansen *et al.*, 2004, Chapters II and III). The alteration proceeded via three sub-reactions fossilized as spatially distinct zones. The index minerals of magnesite, talc and quartz represent three metamorphic isograds defining the magnesite-, talc- and quartz-zones (Hansen *et al.*, 2005; Chapter IV). The major non-volatile chemical constituents remained unaltered during all but the most extreme cases of carbonate alteration where extensive quartz-carbonate veining (Si^{2+} - Mg^{2+} metasomatism) and limited K^{+} (Cr-muscovite) and possibly Ca^{2+} metasomatism occurred (Chapter V). Each carbonation reaction is controlled by the CO_2 content within a CO_2-H_2O fluid.

The isotopic ages of the nearby Fourth of July Batholith (FOJB) and the listwanite alteration are coeval (Ash, 2001; Mihalynuk *et al.*, 1992; Chapter IV) and likely related. The most depleted $\delta^{13}C$ within magnesite is around -6‰ which is consistent with an organic signature and is supported by the presence of organic material within listwanite altered rocks. The large range in $\delta^{18}O$ of between 6.3‰ and 17.3‰ suggests interaction of the altering fluids with the pelagic sedimentary rocks of the Atlin Accretionary Complex (AAC). The only obvious nearby source of organic material is the pelagic units of the AAC. These results suggest large-scale hydrothermal circulation of fluids, driven by the FOJB, through the metasedimentary, metavolcanic and carbonate rocks of the AAC which mobilized and thermally matured organic material and scavenged carbonate which then infiltrated and altered the ultramafic rocks of the Atlin Ultramafic Allochthon.

Anomalous gold values are associated with organic material and low $\delta^{13}C$ values (Chapter IV). The gold content of the three listwanite zones are at or above that for the parental serpentinite. These observations and analyses are consistent with gold having been scavenged from the underlying accretionary complex lithologies or derived from the contemporaneous and nearby FOJB rather than being scavenged from the ultramafic

rocks. Gold is associated with organic material which may have acted as a transporting agent.

Although magnesite-zone alteration, the first reaction, only accounts for about 5 – 15 % of the total carbonation potential of serpentinite, it is spatially heterogeneously widespread and therefore may have sequestered a significant portion of the total bound CO_2 within the Atlin listwanite system. Moreover, within intact bedrock, the progression of the talc-zone reaction generates fracture permeability, and appears to have locally enhanced reaction by generating a permeability wave in advance of it. The magnesite- and talc-zones combined, represent approximately half the carbonation potential for typical serpentinite rock and were produced with a small associated increase in the volume of solids. The quartz-zone, on the other hand, is limited to only the most highly carbonated areas and may be limited in extent due to the large associated gain in solid volume. The first two reaction steps therefore hold the most promise for *in situ* mineral carbonation as they limit porosity loss and potentially can generate permeability. Because the three carbonation reactions are controlled by the CO_2 content of the fluid, industrial injection systems could be tailored to preferentially only drive the first two carbonation reactions.

The listwanite is best developed along a regional joint and fracture system as well as a basal thrust fault (Chapter III), hence the Altin Ultramafic Allochthon had good potential for carbonation due to the structural preparation. This suggests that the potential of any ultramafic body for CO_2 sequestration is directly linked to its original fracture permeability because without it the carbonation potential is limited regardless of the efficiency of the various CO_2-sequestering reactions.

The next logical step in terms of advancing the in situ industrial mineral carbonation injection systems is to use the information gained in this study and incorporating it into a model. Cipolli *et al.* (2004) have modeled a serpentinite aquifer in Italy. Although their results are promising, they assume that serpentinite material is transformed directly to a chalcedony (a form of silica) and magnesite. This study clearly shows that the reaction of serpentinite is more likely to follow a sequence of reactions. The modification of the Cipolli *et al.* (2004) model to incorporate this information could potentially accelerate the carbonation rates high enough to an economically feasible.

6.2 REFERENCES

Ash, C. H. (1994): Origin and Tectonic Setting of Ophiolitic Ultramafic and Related Rocks in the Atlin Area, British Columbia (NTS 104N); B.C. Ministry of Energy, Mines and Petroleum Resources, Bulletin 94, 48 p.

Ash, C. H. (2001): Relationship Between Ophiolites and Gold-Quartz Veins in the North American Cordillera; British Columbia Department of Energy, Mines and Petroleum Resources, Bulletin 108, 140 p.

Cipolli, G., Gambardella, B., Marini, L., Ottonello, G. and Zuccolini, M. V. (2004): Geochemistry of High-pH Waters from Serpentinites of the Gruppo di Voltri (Genova, Italy) and Reaction Path Modeling of CO_2 Sequestration in Serpentinite Aquifers. Applied Geochemistry, 19, 787-802.

Hansen, L.D., Dipple, G. M., Kellett, D. A. And Gordon, T. M. (2005): Carbonate-Altered Serpentinite: A Geologic Analogue to Carbon Dioxide Sequestration, Canadian Mineralogist, v. 43, part 1, p. 225-239.

Hansen, L. D., Dipple, G. M., Anderson, R. G. and Nakano, K. F. (2004): Geologic Setting of Carbonate Metasomatised Serpentinite (Listwanite) at Atlin, British Columbia: Implications for CO_2 Sequestration and Lode-Gold Mineralization. In Current Research, Geological Survey of Canada, Paper 2004-A5, 12 pages.

Mihalynuk, M. G., Smith, M., Gabites, J. E., Runkle, D. and Lefebure, D. (1992): Age of Emplacement and Basement Character of the Cache Creek Terrane as Constrained by New Isotopic and Geochemical Data; Canadian Journal of Earth Sciences, 29, p. 2463-2477.

Appendix A: Miscellaneous Tables for Chapter IV and V

Bulk geochemical samples were crushed using a jaw crusher and powdered in a tungsten carbide shatterbox. Powders were sent to the Geochemical Laboratories at McGill University, Montreal, PQ, for bulk geochemical analysis by X-ray fluorescence. The results are included in Table A1 below. Samples were analyzed for major, minor and trace elements, CO_2 content by induction furnace, and total volatile content by loss on ignition (LOI). The Standard errors used in any calculations in Chapter IV were determined from 7 blind replicate analyses of sample AT03-20-PC2.

Table A1: Whole Rock Geochemical Data

Sample	SiO_2	TiO_2	Al_2O_3	Fe_2O_3	MnO	MgO	CaO	Na_2O	K_2O	P_2O_5	Cr_2O_3	Ni	V	Zn	LOI	Total	CO_2
01AT-8-1	41.50	0.012	0.140	7.990	0.098	38.61	0.02	0.03	0.01	0.012	3617	2191	23	25	11.65	100.66	**0.06**
01AT-13-1	40.64	0.014	1.190	6.930	0.088	39.12	0.15	<d/l	0.01	0.010	3154	2196	46	21	11.90	100.57	**0.10**
01AT-10-1	34.98	0.010	0.090	8.080	0.105	43.25	0.06	<d/l	0.01	0.010	4274	2637	19	31	13.50	100.77	**0.15**
01AT-3-1	36.93	0.010	0.230	8.230	0.090	40.78	0.02	0.01	0.01	0.010	3254	2393	23	28	13.94	100.83	**0.21**
01AT-10-2	37.29	0.010	0.400	7.960	0.113	40.39	0.37	<d/l	0.01	0.009	4540	2315	31	33	13.14	100.38	**0.26**
01AT-2-2	36.21	0.010	0.160	7.900	0.099	41.95	0.37	<d/l	0.01	0.010	4648	2452	20	28	13.16	100.57	**0.33**
01AT-9-1	39.32	0.012	1.080	6.800	0.085	38.81	0.11	0.06	0.01	0.010	4012	2299	36	39	13.50	100.44	**2.10**
01AT-11-1	37.38	0.013	1.110	9.150	0.167	39.78	0.44	0.01	0.01	0.012	3778	2220	50	36	12.10	100.78	**2.57**
01AT-1-9	38.62	0.011	0.270	7.120	0.082	39.62	0.03	0.01	0.02	0.012	4206	2789	17	36	14.10	100.60	**3.37**
01AT-7-3	38.80	0.017	0.910	7.210	0.140	36.69	1.61	0.02	0.01	0.010	3412	2175	33	28	14.04	100.02	**3.40**
01AT-6-3	38.01	0.012	0.340	7.030	0.074	39.77	0.06	<d/l	0.01	0.011	2522	2388	18	25	14.53	100.34	**4.00**
01AT-1-8	38.05	0.011	0.140	6.580	0.070	40.01	0.06	0.02	0.01	0.010	2861	2389	12	7	14.98	100.47	**4.60**
01AT-13-2	35.79	0.013	0.920	8.580	0.139	39.10	0.04	0.03	0.01	0.010	5138	2194	32	39	15.35	100.72	**7.12**
01AT-1-7	35.88	0.011	0.150	8.100	0.083	38.88	0.09	0.11	0.02	0.009	4111	2427	20	12	16.70	100.69	**7.19**
01AT-1-6	36.62	0.014	1.050	7.780	0.110	36.01	0.97	0.02	0.02	0.009	3375	2214	37	31	17.64	100.81	**9.54**
01AT-11-2	35.58	0.011	0.220	7.450	0.121	38.29	0.46	<d/l	0.01	0.009	3969	2004	29	38	17.84	100.59	**9.60**
01AT-9-2	30.63	0.009	0.070	7.110	0.095	37.90	0.23	<d/l	0.01	0.009	3216	2250	17	27	23.80	100.40	**17.26**
01AT-7-1	33.85	0.022	1.090	6.800	0.103	33.85	0.88	0.04	0.01	0.009	3119	2088	41	25	22.91	100.09	**21.83**
01AT-5-4	31.84	0.008	0.070	5.760	0.066	33.61	0.10	<d/l	0.01	0.011	3110	1760	<d/l	23	28.41	100.38	**28.01**
01AT-1-5	25.86	0.010	0.860	7.210	0.088	31.46	0.90	0.05	0.05	0.008	3185	1938	34	28	33.66	100.67	**34.00**
01AT-4-1*	27.87	0.008	0.140	6.780	0.113	30.33	0.24	<d/l	0.01	0.008	3926	1956	15	21	34.09	100.18	**34.34**
01AT-5-2	28.65	0.009	0.070	5.690	0.065	30.03	0.18	0.02	0.01	0.008	3359	1502	<d/l	17	34.99	100.21	**35.20**
01AT-6-1*	29.07	0.009	0.240	4.790	0.072	28.78	2.06	<d/l	0.03	0.007	3177	1794	11	41	34.63	100.18	**36.19**
σ	**0.0939**	**0.0005**	**0.0107**	**0.0364**	**0.0009**	**0.109**	**0.0111**	**0.0438**	**0.0038**	**0.0007**	**95**	**4**	**2**	**1**	**0.0537**		**0.0538**

Units in wt% except Cr_2O_3, Ni, V and Zn which are reported in ppm. *denotes samples which contain Cr-muscovite

σ = standard deviation

Table A2: Ratio of residual to one standard deviation data illustrated in Figure 4.5

	R_1	R_1	R_1	R_1	R_1	R_1	R_1	R_2	R_2	R_2	R_2	R_3	R_3	R_3	R_3	R_3	R_3
Si	-3.E-03	-0.15	1.E-03	5.E-04	1.E-04	-0.12	-0.01	-0.21	-0.15	2.E-04	-4.E-05	-0.24	5.E-04	-0.34	9.E-05	-9.E-04	-0.12
Ti	-1.93	1.78	-1.90	-0.40	-1.16	2.05	1.93	3.14	3.08	1.49	0.61	8.11	-2.02	2.24	1.42	0.77	0.32
Al	0.28	7.73	0.01	-0.03	-0.02	6.10	0.33	10.34	7.20	-0.05	-0.02	11.71	-0.04	17.07	4.E-03	0.04	2.92
Fe	0.02	0.78	4.E-03	-0.01	-0.01	0.59	0.05	1.07	0.73	-0.02	-0.01	1.21	-0.01	1.74	3.E-03	0.01	0.63
Mn	-10.56	0.86	-7.46	9.17	8.01	-0.33	-18.99	-10.27	13.44	20.90	14.85	-10.85	5.22	-13.89	-2.30	-5.71	5.09
Mg	-2.E-04	0.03	-1.E-03	-4.E-05	6.E-05	0.02	8.E-04	0.05	0.03	5.E-04	2.E-04	0.05	2.E-04	0.07	-2.E-04	6.E-04	0.03
Ca	-0.40	5.36	-0.15	0.03	0.03	0.83	0.18	8.34	5.91	0.05	0.06	9.44	-0.02	12.31	0.01	-0.04	5.03
Na	0.73	0.04	-0.11	-0.07	-0.01	0.16	1.15	0.13	0.10	-0.03	0.04	0.28	-0.11	0.24	0.00	0.12	0.01
K	0.04	-0.01	1.38	0.02	0.03	0.01	1.41	0.81	0.01	0.07	0.14	0.11	0.18	2.39	0.19	0.51	0.78
P	0.25	1.61	0.08	-0.61	-1.23	1.16	4.E-03	1.08	0.27	-0.44	-0.03	1.13	-0.04	1.09	1.18	-0.56	-0.38
Cr	2.47	-0.98	0.79	-0.37	-0.32	3.52	0.53	-5.54	-4.71	-0.77	-0.59	-6.29	-0.14	-3.68	0.05	0.34	-3.77
Ni	9.75	-3.68	52.21	5.92	2.54	-5.63	16.61	17.53	17.59	-17.12	0.90	14.68	-16.49	2.06	14.20	-39.94	13.36
V	-3.17	-0.28	-1.46	0.74	0.98	-2.03	-2.03	-1.65	0.63	2.76	1.55	-0.41	-0.08	0.64	-2.58	-3.87	0.85
Zn	7.33	-2.98	6.53	4.10	1.01	-1.58	-10.66	-2.92	1.51	6.46	2.71	-3.42	4.31	-3.63	-4.85	-0.60	4.59

Table A3: Hypothetical data supporting Figures 5.2 and 5.3

Figure 5.2	**1**	**2**	**3**	**4**	**Covariance Matrix**	
X	2.0	7.0	8.0	-	0.09	0.00
Y	3.0	4.3	8.0	-	0.00	0.80
Figure 5.3a						
X	1.0	4.0	7.0	9.2	0.09	0.00
Y	2.0	3.0	2.7	7.5	0.00	0.80
Figure 5.3b						
X	1.0	4.0	7.0	8.5	0.09	-0.23
Y	2.0	3.0	2.9	8.1	-0.23	0.80

Table A4: Residual (moles/Kg) from mass balance using full rank data

	Si	Ti	Al	Fe	Mn	Mg	Ca	Na	K	P	Cr	Ni	V	Zn
1	0.0000	0.0000	0.0000	0.0000	0.0000	0.0000	0.0000	0.0000	0.0000	0.0000	0.0000	0.0000	0.0000	0.0000
2	0.0000	0.0000	0.0000	0.0000	0.0000	0.0000	0.0000	0.0000	0.0000	0.0000	0.0000	0.0000	0.0000	0.0000
3	0.0000	0.0000	0.0000	0.0000	0.0000	0.0000	0.0000	0.0000	0.0000	0.0000	0.0000	0.0000	0.0000	0.0000
4	0.0000	0.0000	0.0000	0.0000	0.0000	0.0000	0.0000	0.0000	0.0000	0.0000	0.0000	0.0000	0.0000	0.0000
5	0.0000	0.0000	0.0000	0.0000	0.0000	0.0000	0.0000	0.0000	0.0000	0.0000	0.0000	0.0000	0.0000	0.0000
6	0.0000	0.0000	0.0000	0.0000	0.0000	0.0000	0.0000	0.0000	0.0000	0.0000	0.0000	0.0000	0.0000	0.0000
7	0.0000	0.0000	0.0000	0.0000	0.0000	0.0000	0.0000	0.0000	0.0000	0.0000	0.0000	0.0000	0.0000	0.0000
8	0.0000	0.0000	0.0000	0.0000	**-0.0093**	0.0000	**0.0313**	0.0000	0.0000	0.0000	0.0000	**0.0027**	0.0000	**-0.0002**
9	0.0000	0.0000	**-0.0007**	0.0000	**-0.0119**	0.0000	**0.0490**	0.0000	0.0000	0.0000	**-0.0019**	**-0.0005**	0.0000	**-0.0002**
10	0.0000	0.0000	**0.0106**	0.0000	0.0000	0.0000	0.0000	0.0000	0.0000	0.0000	0.0000	**-0.0018**	0.0000	**-0.0001**
11	0.0000	0.0000	0.0000	0.0000	0.0000	0.0000	0.0000	0.0000	0.0000	0.0000	0.0000	0.0000	0.0000	0.0000
12	0.0000	0.0000	0.0000	0.0000	0.0000	0.0000	0.0000	0.0000	0.0000	0.0000	0.0000	**0.0004**	0.0000	0.0000
13	0.0000	0.0000	0.0000	0.0000	0.0000	0.0000	0.0000	0.0000	0.0000	0.0000	0.0000	0.0000	0.0000	0.0000
14	0.0000	0.0000	0.0000	0.0000	0.0000	0.0000	0.0000	0.0000	0.0000	0.0000	0.0000	**0.0012**	0.0000	**-0.0001**
15	0.0000	0.0000	0.0000	0.0000	0.0000	0.0000	0.0000	0.0000	0.0000	0.0000	0.0000	0.0000	0.0000	0.0000
16	0.0000	0.0000	0.0000	0.0000	0.0000	0.0000	0.0000	0.0000	0.0000	0.0000	0.0000	0.0000	0.0000	0.0000
17	0.0000	0.0000	0.0000	0.0000	0.0000	0.0000	0.0000	0.0000	0.0000	0.0000	0.0000	0.0000	0.0000	**0.0001**
18	0.0000	0.0000	0.0000	0.0000	0.0000	0.0000	0.0000	0.0000	0.0000	0.0000	0.0000	0.0000	0.0000	0.0000
19	0.0000	0.0000	0.0000	0.0000	0.0000	0.0000	0.0000	0.0000	0.0000	0.0000	0.0000	0.0000	0.0000	**0.0005**
20	0.0000	0.0000	0.0000	0.0000	0.0000	0.0000	0.0000	0.0000	0.0000	0.0000	0.0000	0.0000	0.0000	0.0000
21	0.0000	0.0000	0.0000	0.0000	0.0000	0.0000	0.0000	0.0000	0.0000	0.0000	0.0000	0.0000	0.0000	0.0000
22	0.0000	0.0000	0.0000	0.0000	0.0000	0.0000	0.0000	0.0000	0.0000	0.0000	0.0000	0.0000	0.0000	0.0000
23	0.0000	0.0000	0.0000	0.0000	0.0000	0.0000	0.0000	0.0000	0.0000	0.0000	0.0000	0.0000	0.0000	0.0000
24	0.0000	0.0000	0.0000	0.0000	0.0000	0.0000	0.0000	0.0000	0.0000	0.0000	0.0000	0.0000	0.0000	**0.0001**
25	0.0000	0.0000	0.0000	0.0000	0.0000	0.0000	0.0000	0.0000	0.0000	0.0000	0.0000	0.0000	0.0000	0.0000
26	0.0000	0.0000	0.0000	0.0000	0.0000	0.0000	0.0000	0.0000	0.0000	0.0000	0.0000	0.0000	0.0000	0.0000
27	0.0000	0.0000	0.0000	0.0000	0.0000	0.0000	0.0000	0.0000	0.0000	0.0000	0.0000	0.0000	0.0000	0.0000
28	0.0000	0.0000	0.0000	0.0000	0.0000	0.0000	0.0000	0.0000	0.0000	0.0000	0.0000	0.0000	0.0000	**-0.0003**
29	0.0000	0.0000	0.0000	0.0000	0.0000	0.0000	0.0000	0.0000	0.0000	0.0000	0.0000	0.0000	0.0000	0.0000
30	0.0000	0.0000	0.0000	0.0000	0.0000	0.0000	0.0000	0.0000	0.0000	0.0000	0.0000	0.0000	0.0000	**-0.0001**
31	0.0000	0.0000	0.0000	0.0000	0.0000	0.0000	0.0000	0.0000	0.0000	0.0000	0.0000	0.0000	0.0000	0.0000
32	0.0000	0.0000	0.0000	0.0000	0.0000	0.0000	0.0000	0.0000	0.0000	0.0000	0.0000	0.0000	0.0000	**-0.0002**
33	0.0000	0.0000	0.0000	0.0000	0.0000	0.0000	0.0000	0.0000	0.0000	0.0000	0.0000	**0.0063**	0.0000	**0.0003**
34	0.0000	0.0000	0.0000	0.0000	0.0000	0.0000	0.0000	0.0000	0.0000	0.0000	0.0000	0.0000	0.0000	0.0000
35	0.0000	0.0000	0.0000	0.0000	0.0000	0.0000	0.0000	0.0000	0.0000	0.0000	0.0000	0.0000	0.0000	0.0000
36	0.0000	0.0000	0.0000	0.0000	0.0000	0.0000	0.0000	0.0000	0.0000	0.0000	0.0000	0.0000	0.0000	**-0.0001**
37	0.0000	0.0000	0.0000	0.0000	0.0000	0.0000	0.0000	0.0000	0.0000	0.0000	0.0000	0.0000	0.0000	0.0000
38	0.0000	0.0000	0.0000	0.0000	0.0000	0.0000	0.0000	0.0000	0.0000	0.0000	0.0000	0.0000	0.0000	0.0000
39	0.0000	0.0000	0.0000	0.0000	0.0000	0.0000	0.0000	0.0000	0.0000	0.0000	**-0.0014**	0.0000	0.0000	0.0000
40	0.0000	0.0000	0.0000	0.0000	0.0000	0.0000	0.0000	0.0000	0.0000	0.0000	0.0000	0.0000	0.0000	0.0000
41	0.0000	0.0000	0.0000	0.0000	0.0000	0.0000	0.0000	0.0000	0.0000	0.0000	0.0000	0.0000	0.0000	0.0000
42	0.0000	0.0000	0.0000	**-0.0102**	0.0000	0.0000	0.0000	0.0000	0.0000	0.0000	0.0000	**0.0023**	0.0000	**-0.0001**
43	0.0000	0.0000	0.0000	0.0000	0.0000	0.0000	0.0000	0.0000	0.0000	0.0000	0.0000	0.0000	0.0000	0.0000
44	0.0000	0.0000	0.0000	0.0000	0.0000	0.0000	0.0000	0.0000	0.0000	0.0000	0.0000	0.0000	0.0000	**-0.0002**
45	0.0000	0.0000	0.0000	0.0000	0.0000	0.0000	0.0000	0.0000	**0.0049**	0.0000	0.0000	**-0.0004**	0.0000	**0.0002**

Table A4: (cont.)

	Si	Ti	Al	Fe	Mn	Mg	Ca	Na	K	P	Cr	Ni	V	Zn
46	0.0000	0.0000	0.0000	0.0000	0.0000	0.0000	0.0000	0.0000	0.0000	0.0000	0.0000	0.0000	0.0000	**0.0003**
47	0.0000	0.0000	0.0000	**-0.1407**	0.0000	0.0000	0.0000	0.0000	0.0000	0.0000	0.0000	**0.0019**	0.0000	0.0000
48	0.0000	0.0000	0.0000	0.0000	0.0000	0.0000	0.0000	0.0000	0.0000	0.0000	0.0000	0.0000	0.0000	**0.0001**
49	0.0000	0.0000	0.0000	0.0000	0.0000	0.0000	0.0000	0.0000	0.0000	0.0000	0.0000	0.0000	0.0000	**0.0002**
50	0.0000	0.0000	0.0000	0.0000	0.0000	0.0000	0.0000	0.0000	0.0000	0.0000	0.0000	0.0000	0.0000	**0.0002**
51	0.0000	0.0000	0.0000	0.0000	0.0000	0.0000	0.0000	0.0000	0.0000	0.0000	0.0000	**0.0013**	0.0000	0.0000
52	0.0000	0.0000	0.0000	**-0.0329**	0.0000	0.0000	0.0000	0.0000	0.0000	0.0000	0.0000	**0.0008**	0.0000	0.0000
53	0.0000	0.0000	0.0000	0.0000	**0.0014**	0.0000	0.0000	0.0000	0.0000	0.0000	0.0000	**0.0017**	0.0000	0.0000
54	0.0000	0.0000	0.0000	0.0000	0.0000	0.0000	0.0000	0.0000	0.0000	0.0000	0.0000	0.0000	0.0000	0.0000
55	0.0000	0.0000	0.0000	0.0000	0.0000	0.0000	0.0000	0.0000	0.0000	0.0000	0.0000	0.0000	0.0000	0.0000
56	0.0000	0.0000	0.0000	0.0000	0.0000	0.0000	0.0000	0.0000	0.0000	0.0000	0.0000	0.0000	0.0000	0.0000
57	0.0000	0.0000	0.0000	0.0000	0.0000	0.0000	0.0000	0.0000	0.0000	0.0000	0.0000	0.0000	0.0000	0.0000
58	0.0000	0.0000	0.0000	0.0000	0.0000	0.0000	0.0000	0.0000	0.0000	0.0000	0.0000	0.0000	0.0000	**0.0003**
59	0.0000	0.0000	0.0000	0.0000	0.0000	0.0000	0.0000	0.0000	0.0000	0.0000	0.0000	0.0000	0.0000	0.0000
60	0.0000	0.0000	0.0000	**-0.2178**	**-0.0021**	0.0000	0.0000	0.0000	0.0000	0.0000	0.0000	**0.0051**	0.0000	0.0000
61	0.0000	0.0000	0.0000	0.0000	0.0000	0.0000	0.0000	0.0000	0.0000	0.0000	0.0000	0.0000	0.0000	**0.0001**
62	0.0000	0.0000	0.0000	0.0000	0.0000	0.0000	0.0000	0.0000	0.0000	0.0000	0.0000	**0.0015**	0.0000	**0.0002**
63	0.0000	0.0000	0.0000	0.0000	0.0000	0.0000	0.0000	0.0000	0.0000	0.0000	0.0000	**-0.0014**	0.0000	0.0000
64	0.0000	0.0000	0.0000	0.0000	0.0000	0.0000	0.0000	0.0000	0.0000	0.0000	0.0000	**-0.0006**	0.0000	0.0000
65	0.0000	0.0000	0.0000	0.0000	0.0000	0.0000	0.0000	0.0000	0.0000	0.0000	0.0000	0.0000	0.0000	0.0000
66	0.0000	0.0000	0.0000	0.0000	0.0000	0.0000	0.0000	0.0000	0.0000	0.0000	0.0000	**0.0029**	0.0000	0.0000
67	0.0000	0.0000	0.0000	0.0000	0.0000	0.0000	0.0000	0.0000	0.0000	0.0000	**0.0075**	0.0000	0.0000	0.0000
68	0.0000	0.0000	0.0000	0.0000	**0.0014**	0.0000	0.0000	0.0000	0.0000	0.0000	0.0000	**0.0014**	0.0000	0.0000
69	0.0000	0.0000	0.0000	0.0000	0.0000	0.0000	0.0000	0.0000	0.0000	0.0000	0.0000	0.0000	0.0000	**-0.0002**
70	0.0000	0.0000	0.0000	0.0000	0.0000	0.0000	0.0000	0.0000	0.0000	0.0000	0.0000	0.0000	0.0000	0.0000
71	0.0000	0.0000	0.0000	0.0000	**-0.0008**	0.0000	0.0000	0.0000	0.0000	0.0000	**-0.0094**	**-0.0095**	0.0000	**0.0002**
72	0.0000	0.0000	0.0000	0.0000	0.0000	0.0000	0.0000	0.0000	0.0000	0.0000	0.0000	0.0000	0.0000	0.0000
73	0.0000	0.0000	0.0000	0.0000	0.0000	0.0000	0.0000	0.0000	0.0000	0.0000	0.0000	0.0000	0.0000	0.0000
74	0.0000	0.0000	0.0000	0.0000	0.0000	0.0000	0.0000	0.0000	0.0000	0.0000	0.0000	0.0000	0.0000	0.0000
75	0.0000	0.0000	0.0000	0.0000	0.0000	0.0000	0.0000	0.0000	0.0000	0.0000	0.0000	**0.0008**	0.0000	0.0000
76	0.0000	0.0000	0.0000	0.0000	0.0000	0.0000	0.0000	0.0000	0.0000	0.0000	0.0000	0.0000	0.0000	0.0000
77	0.0000	0.0000	0.0000	0.0000	0.0000	0.0000	0.0000	0.0000	0.0000	0.0000	0.0000	0.0000	0.0000	0.0000
78	0.0000	0.0000	0.0000	0.0000	0.0000	0.0000	0.0000	0.0000	0.0000	0.0000	0.0000	0.0000	0.0000	0.0000
79	0.0000	0.0000	0.0000	0.0000	0.0000	0.0000	0.0000	0.0000	0.0000	0.0000	0.0000	0.0000	0.0000	0.0000
80	0.0000	0.0000	0.0000	0.0000	0.0000	0.0000	0.0000	0.0000	0.0000	0.0000	0.0000	0.0000	0.0000	0.0000
81	0.0000	0.0000	0.0000	0.0000	0.0000	0.0000	0.0000	0.0000	0.0000	0.0000	0.0000	0.0000	0.0000	0.0000
82	0.0000	0.0000	0.0000	0.0000	0.0000	0.0000	0.0000	0.0000	0.0000	0.0000	0.0000	0.0000	0.0000	**-0.0002**
83	0.0000	0.0000	0.0000	0.0000	0.0000	0.0000	0.0000	0.0000	0.0000	0.0000	0.0000	**0.0006**	0.0000	0.0000
84	0.0000	0.0000	0.0000	0.0000	0.0000	0.0000	0.0000	0.0000	0.0000	0.0000	0.0000	0.0000	0.0000	0.0000
85	0.0000	0.0000	0.0000	0.0000	0.0000	0.0000	0.0000	0.0000	0.0000	0.0000	0.0000	0.0000	0.0000	0.0000
86	0.0000	0.0000	0.0000	0.0000	0.0000	0.0000	0.0000	0.0000	0.0000	0.0000	0.0000	0.0000	0.0000	0.0000
87	0.0000	0.0000	0.0000	0.0000	0.0000	0.0000	0.0000	0.0000	0.0000	0.0000	0.0000	0.0000	0.0000	**-0.0002**
88	0.0000	0.0000	0.0000	0.0000	0.0000	0.0000	0.0000	0.0000	0.0000	0.0000	0.0000	0.0000	0.0000	**-0.0001**
89	0.0000	0.0000	0.0000	0.0000	0.0000	0.0000	0.0000	0.0000	0.0000	0.0000	0.0000	0.0000	0.0000	0.0000

Table A4: (cont.)

	Si	Ti	Al	Fe	Mn	Mg	Ca	Na	K	P	Cr	Ni	V	Zn
90	0.0000	0.0000	**-0.0036**	0.0000	0.0000	0.0000	0.0000	0.0000	0.0000	0.0000	0.0000	0.0000	0.0000	**0.0002**
91	0.0000	0.0000	0.0000	0.0000	0.0000	0.0000	0.0000	0.0000	0.0000	0.0000	0.0000	0.0000	0.0000	**0.0007**
92	0.0000	0.0000	0.0000	0.0000	0.0000	0.0000	0.0000	0.0000	0.0000	0.0000	**-0.0069**	**0.0039**	0.0000	0.0000
93	0.0000	0.0000	0.0000	0.0000	0.0000	0.0000	0.0000	0.0000	0.0000	0.0000	0.0000	**0.0024**	0.0000	0.0000
94	0.0000	0.0000	0.0000	0.0000	0.0000	0.0000	0.0000	0.0000	0.0000	0.0000	0.0000	**-0.0085**	0.0000	**0.0005**
95	0.0000	0.0000	0.0000	0.0000	0.0000	0.0000	0.0000	0.0000	0.0000	0.0000	0.0000	0.0000	0.0000	0.0000
96	0.0000	0.0000	0.0000	0.0000	**0.0110**	0.0000	0.0000	0.0000	0.0000	0.0000	0.0000	**-0.0075**	0.0000	0.0000
97	0.0000	0.0000	**-0.0006**	0.0000	0.0000	0.0000	0.0000	0.0000	0.0000	0.0000	0.0000	**0.0008**	0.0000	0.0000
98	0.0000	0.0000	0.0000	0.0000	0.0000	0.0000	0.0000	0.0000	0.0000	0.0000	0.0000	0.0000	0.0000	0.0000
99	0.0000	0.0000	0.0000	0.0000	0.0000	0.0000	0.0000	0.0000	0.0000	0.0000	0.0000	**0.0013**	0.0000	0.0000
100	0.0000	0.0000	0.0000	0.0000	0.0000	0.0000	0.0000	0.0000	0.0000	0.0000	0.0000	**-0.0019**	0.0000	**0.0003**
101	0.0000	0.0000	0.0000	0.0000	0.0000	0.0000	0.0000	0.0000	0.0000	0.0000	0.0000	0.0000	0.0000	0.0000
102	**1.1134**	0.0000	0.0000	**-0.1992**	**0.0210**	**-1.2388**	**1.1090**	0.0000	**0.0520**	0.0000	**-0.0006**	**-0.0076**	0.0000	**0.0006**
103	**-0.4236**	0.0000	0.0000	0.0000	0.0000	**0.2169**	0.0000	0.0000	0.0000	0.0000	0.0000	0.0000	0.0000	0.0000
104	**0.4140**	0.0000	**0.0123**	**-0.1373**	**0.0069**	**-0.3504**	**0.7551**	0.0000	**0.0730**	0.0000	0.0000	**-0.0066**	0.0000	**0.0006**
105	0.0000	0.0000	**0.0618**	**0.0593**	**-0.0051**	0.0000	0.0000	0.0000	**0.0102**	0.0000	**-0.0016**	**0.0008**	0.0000	**0.0001**
106	0.0000	0.0000	0.0000	0.0000	0.0000	0.0000	0.0000	0.0000	0.0000	0.0000	0.0000	**0.0022**	0.0000	0.0000
107	0.0000	0.0000	0.0000	0.0000	**-0.0007**	0.0000	0.0000	0.0000	**0.0053**	0.0000	0.0000	**0.0037**	0.0000	0.0000
108	**0.9357**	0.0000	0.0000	**-0.0093**	0.0000	**-0.7992**	0.0000	0.0000	**0.0312**	0.0000	0.0000	**-0.0078**	0.0000	**-0.0001**
109	0.0000	0.0000	0.0000	0.0000	0.0000	0.0000	0.0000	0.0000	0.0000	0.0000	0.0000	**-0.0037**	0.0000	**0.0001**
110	0.0000	0.0000	**-0.0126**	**0.1559**	**-0.0084**	0.0000	**0.0165**	0.0000	**0.0102**	0.0000	0.0000	**0.0031**	0.0000	0.0000
111	0.0000	0.0000	**-0.0144**	**-0.0139**	**-0.0066**	0.0000	**0.1659**	0.0000	**0.0053**	0.0000	**-0.0006**	**0.0064**	0.0000	**0.0004**
112	**-0.2459**	0.0000	**0.1012**	**0.1454**	0.0000	**0.1187**	**0.0733**	0.0000	**0.0451**	0.0000	**0.0127**	0.0000	0.0000	**0.0006**
113	**-1.2349**	**0.0016**	**0.0161**	0.0000	**-0.0053**	**0.4924**	0.0000	0.0000	**0.0046**	**0.0030**	0.0000	0.0000	0.0000	**0.0001**
114	**-1.6169**	0.0000	0.0000	0.0000	0.0000	**0.5806**	0.0000	0.0000	0.0000	0.0000	**-0.0049**	**-0.0011**	0.0000	**0.0001**

Appendix B: Mineralogy

Table B1: Qualitative mineralogy of carbonated serpentinite from Atlin, BC

Sample	Chr	Mgt	Opx	Brc	Ol	Atg	Liz	Mgs	Tlc	Qtz	Dol	Cal	Chl		CO_2
01AT-8-1	x	x				x	x						x	A_1	0.06
01AT-13-1	x	x				x	x							A_1	0.10
01AT-10-1	x	x		x	x	x	x							A_1	0.15
AT03-44-25	x	x	x		x	x	x							A_1	0.16
01AT-3-1	x	x		x		x	x						x	A_1	0.21
AT03-42	x	x	x	x	x	x			x					A_1	0.22
AT03-44-17	x	x			x	x	x							A_1	0.22
01AT-10-2	x	x	x	x	x	x	x	x[v]			x			A_1	0.26
AT03-44-24	x	x			x	x	x							A_1	0.27
AT03-51C	x	x		x	x	x	x							A_1	0.27
AT04-21b	x	x		x		x	x							A_1	0.30
AT03-44-30	x	x	x	x	x	x	x							A_1	0.32
AT04-3	x	x		x	x	x	x							A_1	0.32
01AT-2-2	x	x		x	x	x	x				x			A_1	0.33
AT04-9	x	x		x		x	x							A_1	0.34
AT04-6B	x	x				x						x		A_1	0.38
AT04-11	x	x				x	x							A_1	0.39
AT03-20-PC2	x	x		x	x	x	x						x	A_1	0.41
AT03-44-26	x	x	x		x	x	x				x			A_1	0.44
AT03-44-34	x	x			x	x	x							A_1	0.44
AT03-20-PC3a	x	x		x	x	x	x							A_1	0.48
AT03-44-23	x	x	x	x		x	x							A_1	0.49
AT03-20-PC1a	x	x		x	x	x	x							A_1	0.53
AT03-21-PCb	x	x	x	x	x	x	x							A_1	0.58
AT04-13	x	x			x	x	x							A_1	0.59
AT04-16	x	x	x	x		x	x				x			A_1	0.61
AT03-20-PA1a	x	x			x	x	x					x		A_1	0.64
AT03-21-PGb	x	x		x	x	x	x							A_1	0.64
AT04-10	x	x	x	x	x	x	x				x			A_1	0.66
AT03-21-Ma	x	x	x	x	x	x	x							A_1	0.68
AT03-21-PCa	x	x	x	x	x	x	x				x			A_1	0.69
AT03-44-35	x	x	x		x	x	x							A_1	0.71
AT03-20-PE3b	x	x	x	x	x	x	x				x			A_1	0.74
AT03-21-PKb	x	x		x	x	x	x				x			A_1	0.74
AT04-23	x	x	x	x		x	x							A_1	0.76
AT03-21-PFb	x	x		x	x	x	x							A_1	0.77
AT03-21-PGa	x	x			x	x	x					x		A_1	0.80
AT03-44-20	x	x			x	x	x				x			A_1	0.80
AT03-21-PFc	x	x		x	x	x	x					x		A_1	0.82
AT03-51E	x	x				x					x			A_1	0.83

Table B1 (continued): Mineralogy of carbonated serpentinite from Atlin, BC

Sample	Chr	Mgt	Opx	Brc	Ol	Atg	Liz	Mgs	Tlc	Qtz	Dol	Cal	Chl		CO_2
AT03-21-PFa	x	x	x	x	x	x	x							A_1	0.86
AT03-20-PE3A	x	x	x		x	x	x				x			A_1	0.87
AT03-21-PKa	x	x		x	x	x	x							A_1	0.88
AT03-44-14	x	x				x						x		A_1	0.89
AT03-20-PD2a	x	x			x	x	x					x		A_1	0.95
AT03-20-PA2b	x	x		x	x	x	x					x		A_1	0.96
AT04-4	x	x				x						x		A_1	1.11
AT03-44-21	x	x			x	x	x				x			A_1	1.20
AT03-20-PE1a	x	x			x	x	x							A_1	1.31
AT03-21-PHb	x	x		x	x	x	x					x		A_1	1.31
AT03-20-PB3b	x	x	x		x	x	x				x			A_1	1.77
AT03-20-PD1b	x	x			x	x	x				x			A_1	1.85
AT03-44-16	x	x	x	x		x	x				x			A_1	3.17
AT03-44-22	x	x				x					x			A_1	3.17
AT03-44-13	x	x			x	x	x	x			x			R_1	0.40
AT03-20-PB2b	x	x			x	x	x	x			x			R_1	1.91
AT03-44-15	x	x	x		x	x	x	x			x			R_1	2.22
01AT-11-1	x	x			x	x	x	x			x			R_1	2.57
AT03-20-CD4d	x	x	x		x	x	x	x			x			R_1	3.21
AT03-44-3	x	x			x	x	x	x			x			R_1	3.42
AT03-20-CD4c	x	x	x		x	x	x	x			x			R_1	3.55
AT03-44-37	x	x		x	x	x		x						R_1	3.70
01AT-13-2	x	x			x	x	x	x						R_1	7.12
AT03-51F	x	x				x		x						A_2	1.25
AT03-44-18	x	x				x	x	x			x	x		A_2	1.44
AT03-44-19	x	x	x			x	x	x			x			A_2	2.06
01AT-9-1	x	x				x	x	x					x	A_2	2.10
AT03-20-PD1a	x	x				x	x	x			x			A_2	2.29
AT03-21-EF1a	x	x	x			x	x	x			x			A_2	2.33
AT03-51D	x	x				x	x	x						A_2	2.40
AT03-20-CD2a	x	x				x	x	x			x			A_2	2.49
AT03-20-PD3a	x	x				x		x			x			A_2	2.67
AT03-20-PD2b	x	x		x		x	x	x			x			A_2	2.72
AT03-20-IJ1a	x	x				x	x	x			x		x	A_2	2.80
AT03-20-IJ1b	x	x				x	x	x			x		x	A_2	2.97
AT03-21-EF1b	x	x				x	x	x			x			A_2	3.04
AT03-20-IJ1c	x	x				x	x	x			x		x	A_2	3.06
AT03-20-CD1a	x	x				x	x	x			x			A_2	3.17
AT03-20-IJ2e	x	x				x	x	x			x		x	A_2	3.20
01AT-1-9	x	x				x	x	x						A_2	3.37

Table B1 (continued): Mineralogy of carbonated serpentinite from Atlin, BC

Sample	Chr	Mgt	Opx	Brc	Ol	Atg	Liz	Mgs	Tlc	Qtz	Dol	Cal	Chl		CO_2
AT03-20-CD2b	x	x				x	x	x			x			A_2	3.57
AT03-20-IJ2d	x	x				x	x	x			x		x	A_2	3.72
AT03-20-IJ2c	x	x				x		x			x			A_2	3.92
AT03-44-36	x	x				x	x	x			x			A_2	3.95
AT03-20-CD1c	x	x				x	x	x			x			A_2	3.98
01AT-6-3	x	x				x	x	x						A_2	4.00
AT03-20-CD1b	x	x				x	x	x			x			A_2	4.05
AT03-20-IJ4d	x	x				x	x	x			x		x	A_2	4.11
AT03-44-29	x	x				x		x						A_2	4.37
01AT-1-8	x	x				x	x	x						A_2	4.60
AT03-51A	x	x				x	x	x			x			A_2	6.11
AT03-44-4	x	x				x		x			x			A_2	6.54
AT03-44-38	x	x				x	x	x						A_2	6.60
AT03-51b	x	x				x	x	x						A_2	6.74
AT03-44-2	x	x				x	x	x						A_2	9.86
AT03-44-5	x	x				x		x						A_2	9.91
AT03-44-39	x	x				x		x						A_2	10.94
AT03-21-EF1c	x	x				x	x	x	x		x			R_2	1.97
01AT-7-3	x	x				x	x	x	x		x		x	R_2	3.40
AT03-20-IJ4c	x	x				x	x	x	x		x			R_2	3.91
AT03-20-IJ4b	x	x				x	x	x	x		x		x	R_2	4.11
AT03-20-IJ2b	x	x				x	x	x	x		x		x	R_2	4.67
AT03-20-CD4b	x	x				x	x	x	x					R_2	5.21
AT03-20-CD2c	x					x	x	x	x		x			R_2	5.91
AT03-44-28	x	x				x		x	x					R_2	6.34
AT03-44-33	x	x				x	x	x	x					R_2	6.45
01AT-1-7	x	x				x	x	x	x					R_2	7.19
01AT-1-6	x	x				x	x	x	x	x	x		x	R_2	9.54
01AT-11-2	x	x				x	x	x	x		x			R_2	9.60
AT03-44-1	x	x				x		x	x					R_2	11.89
AT04-20D	x	x				x		x	x					R_2	12.54
AT03-21-EF2a	x	x				x		x	x		x			R_2	14.58
AT03-21-EF2f	x					x		x	x		x			R_2	14.83
AT03-44-27	x					x	?	x	x		x			R_2	15.20
AT03-20-IJ2a	x	x				x		x	x		x		x	R_2	15.60
AT03-20-CD2d	x					x	?	x	x		x			R_2	15.88
AT03-21-EF2b	x	x				x		x	x		x			R_2	15.89
AT03-20-CD3b	x					x	?	x	x		x			R_2	17.11
AT03-20-CD4a	x					x		x	x		x			R_2	17.19
01AT-9-2	x					x	?	x	x		x			R_2	17.26

Table B1 (continued): Mineralogy of carbonated serpentinite from Atlin, BC

Sample	Chr	Mgt	Opx	Brc	Ol	Atg	Liz	Mgs	Tlc	Qtz	Dol	Cal	Chl		CO_2
AT04-20C	x	x				x	x	x	x		x			R_2	17.27
AT03-21-EF1d	x					x		x	x		x			R_2	17.77
AT03-20-CD3a	x					x	?	x	x		x			R_2	17.78
AT03-44-10	x					x		x	x					R_2	17.86
AT03-20-IJ3a	x					x		x	x		x		x	R_2	18.08
AT03-21-EF1e	x					x		x	x		x			R_2	18.10
AT03-20-IJ3c	x					x		x	x		x			R_2	18.65
AT03-20-IJ3b	x					x		x	x		x		x	R_2	18.70
AT03-21-EF2e	x					x	?	x	x		x			R_2	18.73
AT03-21-EF1f	x					x	?	x	x		x			R_2	19.05
AT03-20-CD3c	x					x	?	x	x		x			R_2	19.22
AT03-21-EF2c	x					x	?	x	x		x			R_2	19.40
AT03-20-IJ4a	x					x		x	x		x		x	R_2	19.43
AT03-20-CD3d	x					x	?	x	x		x			R_2	19.69
AT03-21-EF2d	x					x		x	x		x			R_2	19.85
AT03-44-6	x	x				x		x	x					R_2	21.60
AT03-44-40	x	x				x		x	x					R_2	24.49
AT04-20F	x							x	x					A_3	24.72
01AT-7-1	x							x	x	x	x		x	R_3	21.83
AT03-44-9	x					x	?	x	x	x				R_3	22.45
AT04-20J	x							x	x	x				R_3	23.80
AT03-44-12	x							x	x	x				R_3	25.86
AT04-20N	x	x						x	x	x				R_3	26.16
AT04-20L	x							x	x	x				R_3	26.77
AT04-20I	x							x	x	x				R_3	27.17
01AT-5-4	x	x[y]						x	x	x				R_3	28.01
AT04-20E	x							x	x	x				R_3	29.71
AT03-44-8*	x							x	x	x	x			R_3	30.79
AT04-20M	x							x	x	x				R_3	32.04
AT04-2*	x							x	x	x	x			R_3	32.95
01AT-1-5	x	x[z]				x[w]		x	x	x	x		x	R_3	34.00
01AT-4-1*	x							x	x	x	x			R_3	34.34
AT04-20A	x							x	x	x				R_3	36.82
01AT-1-2*	x							x		x				A_4	31.42
01AT-5-2	x							x		x				A_4	35.20
AT04-20B	x							x		x				A_4	35.50
01AT-6-1*	x							x		x	x			A_4	36.19
AT04-20K*	x							x		x	x			A_4	37.07
AT04-20H	x					x		x		x				A_4	40.40
01AT-5-3*	x							x		x				A_4	41.73

Table B1 (continued): Mineralogy of carbonated serpentinite from Atlin, BC

v only occurs in small veins
w occurs in small isolated patches
y armored relicts & late mantling of chromite and pyrite
z magnetite in late fractures & late mantling of chromite
? Masked in XRD by other phases
* sample contains Cr-muscovite
CO_2 reported in wt%

Appendix C: Geochemical, Stable Isotope Analyses and Gold Assay Data

Table C1: Geochemical Analyses of Ultramafic Rocks

Sample	SiO_2	TiO_2	Al_2O_3	Fe_2O_3	MnO	MgO	CaO	Na_2O	K_2O	P_2O_5	Cr_2O_3	Ni	V		LOI	CO_2	Total
01AT-10-1	34.98	0.010	0.09	8.08	0.105	43.25	0.06	<d/l	0.01	0.010	4274	2637	19	31	13.50	0.15	100.77
01AT-10-2	37.29	0.010	0.40	7.96	0.113	40.39	0.37	<d/l	0.01	0.009	4540	2315	31	33	13.14	0.26	100.38
01AT-11-1	37.38	0.013	1.11	9.15	0.167	39.78	0.44	0.01	0.01	0.012	3778	2220	50	36	12.10	2.57	100.78
01AT-11-2	35.58	0.011	0.22	7.45	0.121	38.29	0.46	<d/l	0.01	0.009	3969	2004	29	38	17.84	9.60	100.59
01AT-1-2	36.75	0.010	0.68	5.27	0.072	26.24	0.28	<d/l	0.13	0.008	2267	1294	23	14	30.72	31.42	100.52
01AT-13-1	40.64	0.014	1.19	6.93	0.088	39.12	0.15	<d/l	0.01	0.010	3154	2196	46	21	11.90	0.10	100.57
01AT-13-2	35.79	0.013	0.92	8.58	0.139	39.10	0.04	0.03	0.01	0.010	5138	2194	32	39	15.35	7.12	100.72
01AT-1-5	25.86	0.010	0.86	7.21	0.088	31.46	0.90	0.05	0.05	0.008	3185	1938	34	28	33.66	34.00	100.67
01AT-1-6	36.62	0.014	1.05	7.78	0.110	36.01	0.97	0.02	0.02	0.009	3375	2214	37	31	17.64	9.54	100.81
01AT-1-7	35.88	0.011	0.15	8.10	0.083	38.88	0.09	0.11	0.02	0.009	4111	2427	20	12	16.70	7.19	100.69
01AT-1-8	38.05	0.011	0.14	6.58	0.070	40.01	0.06	0.02	0.01	0.010	2861	2389	12	7	14.98	4.60	100.47
01AT-1-9	38.62	0.011	0.27	7.12	0.082	39.62	0.03	0.01	0.02	0.012	4206	2789	17	36	14.10	3.37	100.60
01AT-2-2	36.21	0.010	0.16	7.90	0.099	41.95	0.37	<d/l	0.01	0.010	4648	2452	20	28	13.16	0.33	100.57
01AT-3-1	36.93	0.010	0.23	8.23	0.090	40.78	0.02	0.01	0.01	0.010	3254	2393	23	28	13.94	0.21	100.83
01AT-4-1	27.87	0.008	0.14	6.78	0.113	30.33	0.24	<d/l	0.01	0.008	3926	1956	15	21	34.09	34.34	100.18
01AT-5-2	28.65	0.009	0.07	5.69	0.065	30.03	0.18	0.02	0.01	0.008	3359	1502	<d/l	17	34.99	35.20	100.21
01AT-5-3	18.33	0.007	0.14	5.63	0.084	35.10	0.18	<d/l	0.01	0.010	2177	1807	13	16	40.48	41.73	100.35
01AT-5-4	31.84	0.008	0.07	5.76	0.066	33.61	0.10	<d/l	0.01	0.011	3110	1760	<d/l	23	28.41	28.01	100.38
01AT-6-1	28.84	0.009	0.24	4.80	0.071	28.88	2.05	0.03	0.03	0.006	3206	1793	14	28	34.63	35.17	100.09
01AT-6-3	38.01	0.012	0.34	7.03	0.074	39.77	0.06	<d/l	0.01	0.011	2522	2388	18	25	14.53	4.00	100.34
01AT-7-1	33.85	0.022	1.09	6.80	0.103	33.85	0.88	0.04	0.01	0.009	3119	2088	41	25	22.91	21.83	100.09
01AT-7-3	38.80	0.017	0.91	7.21	0.140	36.69	1.61	0.02	0.01	0.010	3412	2175	33	28	14.04	3.40	100.02
01AT-8-1	41.50	0.012	0.14	7.99	0.098	38.61	0.02	0.03	0.01	0.012	3617	2191	23	25	11.65	0.06	100.66
01AT-9-1	39.13	0.013	1.06	6.79	0.085	38.57	0.11	0.04	0.01	0.008	4071	2298	36	20	13.67	1.73	100.13
01AT-9-2	30.58	0.009	0.05	7.06	0.097	37.77	0.23	<d/l	0.01	0.007	3165	2237	16	9	23.95	16.44	100.29
AT03-20-CD1A	38.34	0.013	0.55	7.76	0.091	39.23	0.50	0.05	0.01	0.008	4115	2228	31	9	13.68	3.17	100.87
AT03-20-CD1B	37.28	0.012	0.63	7.69	0.099	38.51	0.76	0.07	0.01	0.008	3419	2175	39	11	14.63	4.05	100.26
AT03-20-CD1C	38.17	0.013	0.73	7.61	0.093	38.67	0.75	0.04	0.01	0.008	3657	2156	39	12	14.25	3.98	100.93
AT03-20-CD2A	39.43	0.012	0.91	7.33	0.074	37.74	0.91	0.09	0.01	0.008	3809	2120	34	13	13.42	2.49	100.53
AT03-20-CD2B	38.72	0.013	0.95	7.36	0.074	37.68	1.01	0.04	0.01	0.007	3838	2086	41	16	14.12	3.57	100.58
AT03-20-CD2C	37.32	0.011	0.92	7.82	0.068	36.88	0.66	0.09	0.01	0.008	3818	2078	41	21	15.87	5.91	100.25
AT03-20-CD2D	34.58	0.013	0.89	6.92	0.107	35.20	0.88	0.06	0.01	0.007	3653	1960	33	16	21.18	15.88	100.41
AT03-20-CD3A	34.23	0.011	0.91	6.83	0.111	34.53	1.10	0.08	0.01	0.006	3693	1919	42	14	21.93	17.78	100.31
AT03-20-CD3B	34.85	0.012	0.86	6.78	0.106	34.51	1.09	0.06	0.01	0.007	3372	1947	35	10	21.45	17.11	100.27
AT03-20-CD3C	33.59	0.012	0.80	6.76	0.116	34.48	1.42	0.08	0.01	0.007	3139	1908	36	8	22.83	19.22	100.61

Table C1: Geochemical Analyses of Ultramafic Rocks (continued)

Sample	SiO_2	TiO_2	Al_2O_3	Fe_2O_3	MnO	MgO	CaO	Na_2O	K_2O	P_2O_5	Cr_2O_3	Ni	V	Zn	LOI	CO_2	Total
AT03-20-CD3D	33.19	0.010	0.76	6.88	0.121	35.04	0.66	0.05	0.01	0.007	2957	1965	32	7	23.09	19.69	100.31
AT03-20-CD4A	31.93	0.012	0.78	7.77	0.112	35.74	0.99	0.08	0.01	0.007	3191	1986	34	13	22.74	17.19	100.69
AT03-20-CD4B	38.21	0.012	0.85	7.47	0.068	37.80	0.30	0.05	0.01	0.007	3454	2162	36	15	15.25	5.21	100.59
AT03-20-CD4C	37.84	0.012	0.88	7.84	0.092	38.55	0.92	0.06	0.01	0.008	3656	2208	40	12	13.22	3.55	100.02
AT03-20-CD4D	38.27	0.012	0.93	7.81	0.091	39.11	0.82	0.07	0.01	0.008	3756	2186	38	12	13.02	3.21	100.75
AT03-20-ij1a	38.15	0.012	0.84	7.82	0.094	38.73	0.83	0.03	0.01	0.008	3374	2238	35	6	13.56	2.80	100.65
AT03-20-ij1b	38.29	0.015	0.78	7.81	0.100	38.54	0.73	<d/l	0.01	0.008	3509	2197	39	10	13.60	2.97	100.46
AT03-20-ij1c	38.20	0.013	0.72	7.68	0.107	38.64	0.75	0.02	0.01	0.008	3552	2172	34	9	13.83	3.06	100.55
AT03-20-ij2a	33.86	0.013	0.85	7.40	0.109	35.56	0.68	0.01	0.01	0.006	3692	2006	36	13	21.21	15.60	100.28
AT03-20-ij2b	38.23	0.012	0.89	7.32	0.066	37.50	0.54	0.02	0.01	0.008	3733	2201	35	12	15.05	4.67	100.24
AT03-20-ij2c	37.91	0.015	0.90	7.74	0.082	38.31	1.04	0.01	0.01	0.008	3858	2198	35	15	14.21	3.92	100.85
AT03-20-ij2d	37.75	0.012	0.89	7.68	0.095	38.37	1.11	0.03	0.01	0.008	3544	2141	40	12	14.15	3.72	100.68
AT03-20-ij2e	37.98	0.015	0.90	7.75	0.101	38.39	0.96	<d/l	0.01	0.008	3729	2168	38	14	13.81	3.20	100.51
AT03-20-ij3a	34.06	0.013	0.87	6.85	0.112	34.92	0.76	0.03	0.01	0.007	3403	1975	34	10	22.22	18.08	100.39
AT03-20-ij3b	33.58	0.011	0.82	6.89	0.116	34.80	0.91	<d/l	0.02	0.007	3331	1986	33	10	22.64	18.70	100.33
AT03-20-ij3c	33.86	0.012	0.87	6.82	0.115	34.55	0.77	0.02	0.01	0.007	3646	1944	39	13	22.53	18.65	100.13
AT03-20-ij4a	33.10	0.011	0.72	6.91	0.119	34.95	0.86	<d/l	0.02	0.006	3574	2023	31	15	23.51	19.43	100.77
AT03-20-ij4b	39.09	0.012	0.97	7.10	0.056	37.67	0.25	<d/l	0.01	0.008	3934	2151	38	15	14.73	4.11	100.51
AT03-20-ij4c	37.94	0.013	0.88	7.62	0.083	37.95	0.89	<d/l	0.02	0.008	3469	2148	39	11	14.50	3.91	100.45
AT03-20-ij4d	37.07	0.012	0.97	7.78	0.091	38.00	1.10	<d/l	0.01	0.008	4363	2152	40	18	14.45	4.11	100.14
AT03-20-PA-1A	39.33	0.014	0.82	8.04	0.110	39.49	0.77	0.03	0.01	0.007	3633	2252	39	7	11.58	0.64	100.79
AT03-20-PA-2B	39.23	0.012	0.87	7.77	0.108	38.82	1.31	0.05	0.01	0.008	3968	2179	41	13	12.10	0.96	100.91
AT03-20-PB-2B	38.68	0.012	0.94	7.86	0.102	39.47	0.84	0.04	0.01	0.008	4138	2210	41	15	11.98	1.91	100.58
AT03-20-PB-3B	38.85	0.014	0.88	8.09	0.104	39.39	0.87	0.09	0.01	0.008	3637	2212	43	9	11.84	1.77	100.74
AT03-20-PC-1A	38.52	0.012	0.71	8.09	0.109	40.23	0.63	0.08	0.01	0.008	3629	2271	35	11	11.86	0.53	100.85
AT03-20-PC-3A	38.51	0.012	0.73	8.16	0.109	40.42	0.67	0.08	0.01	0.007	3512	2289	32	10	11.57	0.48	100.86
AT03-20-PD-1A	37.96	0.013	0.96	7.67	0.105	38.57	0.90	0.06	0.01	0.008	3693	2144	40	10	13.95	2.29	100.79
AT03-20-PD-1B	38.22	0.016	0.97	7.65	0.100	38.69	0.94	0.06	0.01	0.008	3735	2187	36	13	13.52	1.85	100.78
AT03-20-PD-2A	39.21	0.013	0.84	7.72	0.108	38.48	1.24	0.06	0.01	0.007	3918	2142	40	11	12.47	0.95	100.77
AT03-20-PD-2B	37.89	0.012	0.90	7.61	0.113	38.66	0.89	0.07	0.01	0.008	3829	2159	31	15	13.97	2.72	100.74
AT03-20-PD-3A	37.96	0.013	0.93	7.28	0.112	38.48	0.92	0.06	0.01	0.009	3582	2123	34	12	14.20	2.67	100.55
AT03-20-PE-1A	38.65	0.015	0.87	8.22	0.115	40.27	0.74	0.06	0.01	0.008	3789	2361	42	14	11.06	1.31	100.64
AT03-20-PE-3A	39.33	0.015	1.02	8.02	0.116	39.89	1.10	0.05	0.01	0.008	4131	2280	43	15	10.58	0.87	100.79
AT03-20-PE-3B	40.03	0.015	1.18	7.85	0.121	39.38	1.51	0.06	0.01	0.008	4307	2197	52	15	10.04	0.74	100.86
AT03-21-EF1-A	37.90	0.011	0.60	7.81	0.098	39.59	0.44	0.04	0.01	0.007	3941	2247	28	12	13.68	2.33	100.81

Table C1: Geochemical Analyses of Ultramafic Rocks (continued)

Sample	SiO_2	TiO_2	Al_2O_3	Fe_2O_3	MnO	MgO	CaO	Na_2O	K_2O	P_2O_5	Cr_2O_3	Ni	V	Zn	LOI	CO_2	Total
AT03-21-EF1-B	37.81	0.012	0.59	7.75	0.102	39.49	0.55	0.07	0.01	0.008	3749	2235	29	11	13.84	3.04	100.83
AT03-21-EF1-C	40.97	0.012	0.68	6.48	0.057	37.58	0.64	0.06	0.02	0.008	3980	2306	32	6	13.50	1.97	100.64
AT03-21-EF1-D	32.81	0.011	0.54	7.12	0.120	35.95	0.45	0.09	0.01	0.007	3549	1965	25	10	23.04	17.77	100.70
AT03-21-EF1-E	33.68	0.011	0.48	6.89	0.112	35.55	0.52	0.07	0.01	0.006	3102	2028	25	6	22.56	18.1	100.41
AT03-21-EF1-F	32.96	0.009	0.47	6.97	0.104	35.88	0.38	0.09	0.01	0.007	3109	2071	22	7	23.22	19.05	100.62
AT03-21-EF2-A	36.06	0.011	0.47	6.73	0.094	35.63	0.42	0.08	0.01	0.007	3261	2265	27	9	20.37	14.58	100.44
AT03-21-EF2-B	30.59	0.008	0.48	7.67	0.095	37.53	0.92	0.05	0.01	0.007	2303	1645	21	13	23.02	15.89	100.78
AT03-21-EF2-C	33.31	0.011	0.53	6.82	0.101	35.64	0.36	0.07	0.01	0.007	4057	2101	27	14	23.03	19.4	100.51
AT03-21-EF2-D	32.89	0.013	0.52	6.82	0.104	35.62	0.41	0.07	0.01	0.006	3389	2057	22	8	23.46	19.85	100.47
AT03-21-EF2-E	33.56	0.011	0.53	6.80	0.101	35.70	0.53	0.05	0.01	0.007	3606	2169	29	9	22.76	18.73	100.64
AT03-21-EF2-F	35.73	0.011	0.70	6.69	0.091	35.33	0.58	0.08	0.01	0.007	4963	2130	38	19	20.49	14.83	100.43
AT03-21-Ma	38.33	0.012	0.68	8.05	0.106	40.48	0.80	0.06	0.01	0.007	3204	2320	33	8	11.63	0.68	100.72
AT03-21-PC-A	38.61	0.014	0.72	7.92	0.106	40.58	0.69	0.05	0.01	0.008	4589	2339	37	15	11.38	0.69	100.79
AT03-21-PC-B	38.67	0.012	0.73	8.13	0.112	40.57	0.80	0.05	0.01	0.008	3938	2302	31	13	11.04	0.58	100.76
AT03-21-PF-A	38.13	0.012	0.71	7.75	0.109	39.76	0.57	0.03	0.01	0.008	3124	2205	31	12	13.20	0.86	100.83
AT03-21-PF-B	37.98	0.014	0.69	7.72	0.104	39.81	0.44	0.07	0.01	0.008	3175	2240	30	13	13.20	0.77	100.59
AT03-21-PF-C	38.21	0.013	0.69	7.96	0.104	40.01	0.63	0.04	0.01	0.007	3283	2250	33	5	12.54	0.82	100.77
AT03-21-PG-A	38.57	0.012	0.77	7.81	0.103	39.80	0.76	0.09	0.01	0.008	3944	2222	35	14	12.19	0.8	100.74
AT03-21-PG-B	38.10	0.014	0.71	8.15	0.110	40.27	0.53	0.06	0.01	0.007	3426	2300	33	13	12.26	0.64	100.80
AT03-21-PH-B	37.99	0.012	0.69	7.54	0.098	39.50	0.83	0.10	0.01	0.008	3249	2227	30	9	13.27	1.31	100.60
AT03-21-PK-A	37.85	0.014	0.72	8.17	0.108	39.46	0.60	0.07	0.01	0.008	3851	2203	34	14	13.22	0.88	100.84
AT03-21-PK-B	37.71	0.011	0.76	8.26	0.103	39.72	0.52	0.06	0.01	0.007	4926	2263	37	20	12.73	0.74	100.62
AT03-42	41.49	0.017	1.12	8.54	0.122	41.89	1.24	0.10	0.01	0.009	3449	2351	41	11	5.50	0.22	100.62
AT03-44-1	33.30	0.010	0.18	7.46	0.105	38.72	0.07	0.05	0.01	0.007	3875	2130	21	22	20.34	11.89	100.86
AT03-44-10	36.07	0.016	0.81	6.90	0.054	34.38	0.09	0.06	0.01	0.007	3185	2107	32	8	21.50	17.86	100.43
AT03-44-12	31.28	0.008	0.11	7.06	0.193	34.26	0.16	0.04	0.01	0.007	3240	1528	17	12	26.74	25.86	100.35
AT03-44-13	39.68	0.017	1.28	8.26	0.142	38.80	1.09	0.07	0.01	0.008	4312	2072	47	19	10.79	0.4	100.79
AT03-44-14	40.40	0.014	0.95	8.03	0.099	37.18	1.18	0.06	0.01	0.008	3866	2208	38	11	12.24	0.89	100.78
AT03-44-15	39.35	0.014	1.06	8.41	0.115	39.22	0.81	0.05	0.01	0.007	3793	2238	44	16	11.12	2.22	100.78
AT03-44-16	37.84	0.012	0.88	7.70	0.079	37.63	1.98	0.03	0.02	0.008	3905	2324	35	12	13.91	3.17	100.72
AT03-44-17	39.03	0.016	1.11	8.86	0.107	38.75	0.16	0.08	0.01	0.008	3921	2187	45	12	12.21	0.22	100.96
AT03-44-18	38.67	0.013	0.98	8.57	0.085	37.98	1.08	0.06	0.01	0.007	3403	2253	40	7	12.87	1.44	100.90
AT03-44-19	39.36	0.015	1.13	8.28	0.115	39.13	0.88	0.09	0.01	0.007	4011	2218	48	16	11.17	2.06	100.82
AT03-44-2	34.54	0.009	0.10	7.20	0.092	38.50	0.10	0.05	0.01	0.007	3918	2365	18	27	18.81	9.86	100.05
AT03-44-20	39.28	0.013	1.16	8.72	0.165	40.27	0.60	0.09	0.01	0.008	4052	2238	50	24	10.00	0.8	100.95

Table C1: Geochemical Analyses of Ultramafic Rocks (continued)

Sample	SiO_2	TiO_2	Al_2O_3	Fe_2O_3	MnO	MgO	CaO	Na_2O	K_2O	P_2O_5	Cr_2O_3	Ni	V	Zn	LOI	CO_2	Total
AT03-44-21	38.98	0.015	1.05	8.99	0.138	39.03	0.60	0.06	0.01	0.009	4112	2290	48	16	11.20	1.2	100.73
AT03-44-22	37.88	0.014	1.00	7.50	0.068	37.56	2.12	0.06	0.01	0.008	3549	1981	41	8	14.07	3.17	100.85
AT03-44-23	39.91	0.014	0.84	8.04	0.056	38.87	0.26	0.08	0.01	0.008	4086	2344	36	14	12.13	0.49	100.87
AT03-44-24	39.33	0.014	0.98	9.29	0.105	39.10	0.05	0.06	0.01	0.008	3946	2378	41	19	11.31	0.27	100.90
AT03-44-25	39.35	0.014	1.06	9.64	0.105	39.29	0.03	0.05	0.01	0.008	3815	2328	45	17	10.77	0.16	100.95
AT03-44-26	39.96	0.016	1.11	8.49	0.138	40.10	1.13	0.05	0.01	0.007	4060	2246	44	23	9.17	0.44	100.82
AT03-44-27	33.79	0.010	0.29	7.53	0.144	36.59	0.30	0.06	0.01	0.007	3432	2242	26	25	21.21	15.2	100.51
AT03-44-28	37.54	0.009	0.33	7.04	0.110	38.48	0.17	0.06	0.01	0.008	3399	2272	26	13	16.37	6.34	100.70
AT03-44-29	38.40	0.011	0.32	6.39	0.087	39.83	0.07	0.04	0.01	0.008	3553	2502	21	3	14.80	4.37	100.57
AT03-44-3	38.33	0.011	0.12	7.34	0.099	40.92	0.30	0.07	0.01	0.008	3153	2509	18	3	13.03	3.42	100.81
AT03-44-30	40.20	0.013	0.90	8.12	0.120	39.29	0.99	0.10	0.01	0.007	4019	2237	39	12	10.41	0.32	100.79
AT03-44-33	37.51	0.009	0.06	4.80	0.070	40.73	0.03	0.07	0.01	0.008	3610	2713	11	5	16.61	6.45	100.54
AT03-44-34	39.15	0.016	1.06	9.14	0.139	40.02	0.20	0.06	0.02	0.008	3848	2276	41	23	10.51	0.44	100.94
AT03-44-35	39.32	0.015	1.06	8.41	0.132	39.70	1.48	0.07	0.01	0.007	3814	2237	49	17	10.07	0.71	100.89
AT03-44-36	37.30	0.013	0.55	7.81	0.091	39.41	0.37	0.07	0.01	0.008	3815	2396	26	17	14.59	3.95	100.85
AT03-44-37	37.02	0.011	0.10	7.06	0.090	42.51	0.04	0.05	0.01	0.007	4362	2602	12	9	13.09	3.7	100.69
AT03-44-38	37.48	0.011	0.40	6.80	0.086	38.98	0.03	0.06	0.01	0.008	3668	2258	34	42	16.30	6.6	100.77
AT03-44-39	33.11	0.009	0.07	6.45	0.102	40.54	0.04	0.04	0.01	0.007	3640	2496	13	6	19.62	10.94	100.61
AT03-44-4	36.77	0.011	0.32	7.73	0.068	37.72	0.29	0.08	0.04	0.008	3480	2170	30	21	16.51	6.54	100.12
AT03-44-40	29.41	0.009	0.08	6.10	0.060	37.03	0.07	0.06	0.01	0.007	3551	2186	13	41	27.04	24.49	100.46
AT03-44-5	34.74	0.009	0.08	7.29	0.088	39.04	0.03	0.04	0.01	0.007	3441	2240	14	16	18.90	9.91	100.81
AT03-44-6	30.04	0.008	0.03	6.38	0.111	37.29	0.09	0.05	0.01	0.006	3692	2176	13	27	25.56	21.60	100.17
AT03-44-8	34.94	0.012	0.76	3.80	0.177	23.11	5.93	0.07	0.19	0.006	2497	1215	25	35	30.38	30.79	99.75
AT03-44-9	34.34	0.009	0.32	6.48	0.111	33.94	0.12	0.07	0.01	0.007	3232	1377	24	35	24.57	22.45	100.44
AT03-51-A	35.13	0.008	0.09	8.16	0.099	39.77	0.18	0.02	0.01	0.009	3565	2396	19	<d/l	16.68	6.11	100.75
AT03-51-B	35.45	0.009	0.10	5.34	0.115	40.99	0.03	0.08	0.01	0.008	4269	2543	20	13	17.55	6.74	100.37
AT03-51-C	37.02	0.010	0.10	8.34	0.118	44.04	0.03	0.05	0.01	0.007	4275	2520	15	7	10.41	0.27	100.82
AT03-51-D	37.39	0.010	0.42	7.86	0.102	40.06	0.11	0.09	0.01	0.008	3768	2281	29	11	14.14	2.4	100.81
AT03-51-E	39.26	0.013	1.03	7.55	0.103	38.97	0.40	0.07	0.01	0.008	3779	2189	39	12	12.76	0.83	100.78
AT03-51-F	39.23	0.013	0.77	7.32	0.090	39.25	0.05	0.06	0.01	0.009	4618	2324	30	20	13.20	1.25	100.70
AT03-PC2	38.71	0.013	0.75	8.03	0.108	40.22	0.85	<d/l	0.02	0.007	3827	2277	34	13	11.12	0.41	100.41
AT04-10	38.73	0.012	0.92	8.24	0.111	39.62	1.10	0.06	0.01	0.008	3446	2177	38	16	11.32	0.66	100.70
AT04-11	38.80	0.013	0.69	7.89	0.082	39.34	0.09	0.08	0.01	0.009	3337	2246	39	29	12.97	0.39	100.54
AT04-13	40.97	0.018	0.98	8.66	0.132	38.43	1.96	0.09	0.01	0.008	3929	2226	45	9	8.93	0.59	100.81
AT04-16	38.42	0.017	0.96	7.86	0.105	39.61	0.73	0.06	0.02	0.008	3754	2234	34	13	12.42	0.61	100.81

Table C1: Geochemical Analyses of Ultramafic Rocks (continued)

Sample	SiO_2	TiO_2	Al_2O_3	Fe_2O_3	MnO	MgO	CaO	Na_2O	K_2O	P_2O_5	Cr_2O_3	Ni	V	Zn	LOI	CO_2	Total
AT04-2	31.60	0.015	0.90	4.12	0.109	25.47	4.45	0.05	0.26	0.006	3037	1242	35	42	32.38	32.95	99.80
AT04-20A	25.01	0.008	0.23	6.66	0.073	32.08	0.15	0.05	0.03	0.007	3530	2114	22	7	35.79	36.82	100.66
AT04-20B	26.36	0.011	0.34	7.88	0.067	30.52	0.20	0.05	0.05	0.008	3785	1999	27	17	34.68	35.50	100.75
AT04-20C	34.88	0.010	0.33	6.46	0.070	35.82	0.17	0.08	0.02	0.006	3553	2194	23	9	22.22	17.27	100.64
AT04-20D	35.18	0.012	0.38	6.81	0.073	38.30	0.08	0.06	0.01	0.007	3789	2250	27	19	19.36	12.54	100.88
AT04-20E	28.10	0.009	0.14	6.29	0.118	34.78	0.09	0.08	0.01	0.006	3586	2078	15	<d/l	30.47	29.71	100.66
AT04-20F	30.14	0.009	0.05	6.64	0.086	36.73	0.05	0.06	0.01	0.008	2254	2355	<d/l	<d/l	26.42	24.72	100.66
AT04-20H	19.66	0.022	0.43	6.04	0.067	34.16	0.21	0.07	0.03	0.021	3489	1961	19	9	39.30	40.40	100.56
AT04-20I	31.04	0.008	0.16	6.30	0.064	34.01	0.07	0.05	0.01	0.007	4342	2180	24	2	28.15	27.17	100.52
AT04-20J	32.09	0.010	0.09	6.95	0.077	34.83	0.04	0.07	0.01	0.007	3828	2162	15	<d/l	25.67	23.80	100.44
AT04-20K	22.57	0.009	0.79	7.22	0.117	31.02	0.92	0.06	0.16	0.008	4081	1851	38	41	36.88	37.07	100.36
AT04-20L	29.51	0.008	0.10	6.74	0.091	34.97	0.10	0.06	0.01	0.006	3887	2066	12	3	28.36	26.77	100.55
AT04-20M	25.06	0.008	0.09	5.91	0.079	35.96	0.06	0.03	0.01	0.007	4043	2088	12	5	32.77	32.04	100.60
AT04-20N	30.63	0.008	0.04	7.34	0.084	34.25	0.05	0.05	0.01	0.007	3347	2157	12	2	27.46	26.16	100.48
AT04-21B	38.51	0.013	0.74	7.96	0.110	39.72	0.02	0.05	0.01	0.008	4010	2226	36	18	12.71	0.30	100.48
AT04-23	37.26	0.011	0.36	7.93	0.107	39.85	0.34	0.05	0.01	0.007	3725	2283	27	11	14.27	0.76	100.80
AT04-4	39.08	0.014	1.05	8.51	0.108	38.26	0.73	0.09	0.01	0.009	3776	2254	51	12	12.35	1.11	100.82
AT04-6B	36.05	0.012	0.12	7.67	0.093	41.93	0.02	0.10	0.01	0.008	4757	2529	26	6	13.99	0.38	100.73
AT04-9	34.45	0.011	0.10	7.45	0.095	43.10	0.03	0.04	0.01	0.008	4118	2610	18	8	14.83	0.34	100.80
AT04-3	35.43	0.013	0.12	7.59	0.091	44.56	0.09	0.04	0.01	0.007	4959	2695	16	14	12.09	0.32	100.81
d/l (ppm)	0.006	0.004	0.012	0.003	0.003	0.0095	0.0015	0.0075	0.0025	0.0035	15	3	10	2	0.01	0.01	

All geochemistry and the reported detection limits (d/l) are expressed in wt % oxide except Cr_2O_3, Ni, V, Zn which are reported in parts per million

Table C2: Geochemical Analyses of Replicates

Sample	SiO_2	TiO_2	Al_2O_3	Fe_2O_3	MnO	MgO	CaO	Na_2O	K_2O	P_2O_5	Cr_2O_3	Ni	V	Zn	LOI	CO_2	Total
AT03-pc2^{i}	38.71	0.013	0.75	8.03	0.108	40.22	0.85	<d/l	0.02	0.007	3827	2277	34	13	11.12	0.41	100.45
AT03-pc2^{i}	38.81	0.012	0.77	8.10	0.107	40.45	0.84	<d/l	0.01	0.006	3902	2289	34	13	11.12	0.41	100.85
AT03-pc2^{i}	38.59	0.013	0.78	8.00	0.109	40.12	0.83	0.01	0.01	0.007	4100	2282	35	13	11.14	0.45	100.25
AT03-pc2^{ii}	38.78	0.013	0.78	8.06	0.108	40.35	0.85	0.06	0.01	0.008	3844	2288	33	13	11.22	0.51	100.86
AT03-pc2^{ii}	38.57	0.013	0.76	8.04	0.107	40.25	0.82	0.06	0.01	0.007	3857	2286	38	16	11.21	0.52	100.47
AT03-pc2^{ii}	38.68	0.012	0.77	8.10	0.109	40.23	0.84	0.07	0.01	0.007	3969	2280	34	13	11.23	0.52	100.69
AT03-pc2^{ii}	38.61	0.013	0.77	8.06	0.107	40.19	0.83	0.07	0.01	0.008	3878	2283	34	13	11.24	0.53	100.53
AT03-pc2^{iii}	38.61	0.014	0.77	8.08	0.106	40.28	0.85	0.04	0.01	0.007	4173	2265	38	14	11.19	0.58	100.61
AT03-pc2^{iii}	38.68	0.012	0.77	8.03	0.107	40.02	0.83	0.05	0.01	0.008	3935	2274	37	14	11.22	0.57	100.36
AT03-pc2^{iii}	38.68	0.013	0.77	8.04	0.108	40.15	0.85	0.05	0.01	0.007	3779	2271	35	12	11.22	0.56	100.51
AT03-pc2^{iv}	38.81	0.013	0.77	8.01	0.109	40.21	0.84	0.08	0.02	0.007	3918	2283	39	13	11.24	0.59	100.73
AT03-pc2^{iv}	38.75	0.012	0.77	8.08	0.111	40.24	0.83	0.06	0.01	0.008	3932	2274	38	14	11.21	0.61	100.71
AT03-pc2^{iv}	38.69	0.015	0.79	8.02	0.110	40.20	0.86	0.09	0.01	0.007	3846	2268	39	13	11.25	0.57	100.66
	0.0808	9E-04	0.01	0.033	0.001	0.1044	0.012	0.028	0.004	0.0006	109.93	7.655	2.2	1	0.045	0.07	
d/l	0.006	0.004	0.012	0.003	0.003	0.0095	0.0015	0.0075	0.0025	0.0035	15	3	10	2	0.01	0.01	
Std Error	0.0808	0.004	0.012	0.033	0.003	0.1044	0.012	0.028	0.004	0.0035	109.93	7.655	10	2	0.045	0.07	

All chemical species are reported as wt% except Cr_2O_3, Ni, V, Zn which are in ppm. i, ii, iii and iv denote replicates from four different times over a 14 month period.

Talbe C3: Geochemical Analyses of Igneous Intrusions

Sample	SiO_2	TiO_2	Al_2O_3	Fe_2O_3	MnO	MgO	CaO	Na_2O	K_2O	P_2O_5	Cr_2O_3	Ni	V	Zn	LOI	CO_2	Total	Type
AT03-04-A	49.47	1.596	14.33	12.50	0.200	6.56	8.34	4.52	0.24	0.164	195	45	300	40	2.54	0.65	100.52	A
AT03-49	49.78	1.637	14.44	12.88	0.195	6.20	10.44	3.20	0.16	0.144	138	36	358	35	1.24	0.17	100.37	A
AT03-50	43.79	1.048	10.63	7.75	0.132	11.14	8.49	2.84	0.93	0.450	845	138	178	28	12.32	9.21	99.64	A
AT04-12	49.19	1.974	13.71	14.31	0.231	6.19	9.71	3.81	0.53	0.179	57	23	381	57	0.97	0.09	100.86	A
AT04-14	50.83	1.729	14.48	13.24	0.220	5.22	7.81	4.05	0.59	0.160	32	9	355	61	2.06	0.64	100.43	A
AT03-24	52.82	1.628	14.83	12.44	0.195	4.11	8.39	4.84	0.26	0.172	<d/l	<d/l	340	37	0.61	0.19	100.33	A
AT04-5	51.22	1.944	13.92	13.91	0.236	5.22	8.42	4.10	0.17	0.171	<d/l	10	387	68	0.92	0.37	100.28	A
AT04-8B	38.39	1.508	10.79	9.35	0.149	9.51	13.61	2.16	2.43	1.307	518	71	239	7	10.13	8.14	99.42	A
AT04-7B	49.65	1.085	13.01	7.83	0.138	7.72	8.92	2.92	2.54	0.432	446	58	177	28	5.14	3.21	99.46	B
AT03-05-A	62.57	0.429	15.39	3.35	0.063	2.50	3.75	4.61	1.87	0.291	53	50	62	10	5.06	2.28	99.90	C
AT04-25	61.16	0.411	15.09	3.16	0.062	2.79	3.66	3.87	2.34	0.289	57	48	58	18	7.11	4.73	99.96	C
AT03-28	66.23	0.453	14.96	3.82	0.081	1.65	3.20	3.10	4.11	0.187	42	7	68	16	1.94	0.62	99.74	D
d/l	0.006	0.004	0.012	0.003	0.003	0.0095	0.0015	0.0075	0.0025	0.0035	15	3	10	2	0.01	0.01		

All chemical species are reported as wt% except Cr_2O_3, Ni, V, Zn which are in ppm.

A = Diabase Dyke, B = Lamprophyre, C = Light-Grey Dacite and D = Grey-Brown Dacite

Table C4: Gold Assay Results

SAMPLE	Au(ppm)	Zone	CO_2 (wt%)
AT03-20-PC2a	<0.001	Proto	0.41
AT03-42	<0.001	Proto	0.22
AT03-44-22	<0.001	Proto	3.17
AT03-21Ma	<0.001	Proto	0.68
AT03-20-PC2b	0.014	Proto	0.41
AT03-20-PC2c	0.003	Proto	0.41
AT03-44-23	0.002	Proto	0.76
AT03-20-PE3a	0.001	Proto	0.87
AT03-20-PC2d	<0.001	Proto	0.41
AT03-20-PC2e	<0.001	Proto	0.41
AT03-51A	0.003	Mgs	6.11
AT03-44-15	<0.001	Mgs	2.22
AT03-44-37	0.001	Mgs	3.70
AT03-20-CD1b	0.001	Mgs	4.05
AT03-20-CD1c	0.001	Mgs	3.98
AT03-21-EF1b	0.002	Mgs	3.04
AT03-44-19	0.001	Mgs	2.06
AT03-51D	<0.001	Mgs	2.40
AT03-20-IJ2d	<0.001	Mgs	3.72
AT03-20-IJ1C	0.001	Mgs	3.06
AT03-21-EF2d	0.005	Talc	19.85
AT03-20-CD3b	0.033	Talc	17.11

Table C4: Gold Assay Results (cont.)

SAMPLE	Au(ppm)	Zone	CO_2 (wt%)
AT03-20-IJ2a	0.002	Talc	15.60
AT03-20-IJ3a	0.030	Talc	18.08
AT03-44-40	0.001	Talc	24.49
AT03-20-IJ3b	0.027	Talc	18.70
AT03-44-27	<0.001	Talc	15.20
AT03-21-EF1d	0.001	Talc	17.77
AT03-20-CD3c	0.016	Talc	19.22
AT03-21-EF1e	<0.001	Talc	18.10
AT04-20Na	<0.001	Qtz	26.16
01AT7-1	0.003	Qtz	21.83
01AT4-1	0.005	Qtz	34.34
AT04-20i	0.002	Qtz	27.17
AT04-20Bc	0.004	Qtz	35.50
01AT5-2	0.005	Qtz	35.20
AT03-44-12	0.002	Qtz	25.86
AT04-20Bd	<0.001	Qtz	35.50
AT04-20Bb	<0.001	Qtz	35.50
AT04-20Ba	0.008	Qtz	35.50
GS2-B	0.180	GS	na
GS1-A	0.182	GS	na
GS3-C	0.230	GS	na

GS = gold standard (230 ppb)

Table C5: Stable Isotope Analyses

Number	$^{13}C_{(VPDB)}$	$^{18}O_{(VSMOW)}$	CO_2 (wt%)	Zone
01AT 1-5	-4.43	9.44	34.00	Qtz
01AT 4-1	-4.63	10.13	34.34	Qtz
01AT 5-2	-4.07	10.57	35.20	Qtz
01AT-11-1	-2.30	11.78	2.57	Mgs
01AT-11-2	-5.44	10.70	9.60	Tlc
01AT-1-2	-4.06	10.42	31.42	Qtz
01AT-13-2	-5.08	11.37	7.12	Tlc
01AT-1-5	-4.58	9.69	34.00	Qtz
01AT-1-6	-5.97	10.94	9.54	Tlc
01AT-1-7	-6.20	10.22	7.19	Tlc
01AT-1-8	-4.47	13.21	4.60	Mgs
01AT-1-9	-5.50	14.19	3.37	Mgs
01AT-4-1	-4.97	10.07	34.34	Qtz
01AT-5-2	-4.13	9.15	35.20	Qtz
01AT-5-3	-2.24	8.15	41.73	Qtz
01AT-5-4	-5.08	11.16	28.01	Qtz
01AT-6-1	-4.32	13.97	36.19	Qtz
01AT-6-3	-6.40	6.27	4.00	Mgs
01AT-7-1	-4.39	17.25	21.83	Tlc
01AT-7-3	-5.20	12.31	3.40	Mgs
01AT-9-2	-4.79	15.26	17.26	Tlc
AT03-20-CD1A	-2.51	13.07	3.17	Mgs
AT03-20-CD1B	-2.26	13.45	4.05	Mgs
AT03-20-CD1C	-2.66	13.20	3.98	Mgs
AT03-20-CD2A	-3.64	12.26	2.49	Mgs
AT03-20-CD2B	-3.88	12.97	3.57	Mgs
AT03-20-CD2C	-3.68	13.35	5.91	Mgs
AT03-20-CD2D	-1.31	13.94	15.88	Tlc
AT03-20-CD3A	-5.20	14.27	17.78	Tlc
AT03-20-CD3B	-4.93	14.23	17.11	Tlc
AT03-20-CD3C	-5.12	14.46	19.22	Tlc
AT03-20-CD3D	-5.05	14.66	19.69	Tlc
AT03-20-CD4A	-4.81	14.63	17.19	Tlc
AT03-20-CD4B	-4.27	12.91	5.21	Mgs
AT03-20-CD4C	-3.63	13.47	3.55	Srp

Table C5: Stable Isotope Analyses (cont.)

Number	$^{13}C_{(VPDB)}$	$^{18}O_{(VSMOW)}$	CO_2 (wt%)	Zone
AT03-20-CD4D	-4.31	12.80	3.21	Srp
AT03-20-DH1	-6.04	15.70	n/a	Mgs Vein
AT03-20-DH2	-5.97	14.80	n/a	Mgs Vein
AT03-20-DH3	-3.75	13.96	n/a	Mgs Vein
AT03-20-IJ1A	-3.02	12.98	2.80	Mgs
AT03-20-IJ1B	-2.30	13.42	2.97	Mgs
AT03-20-IJ1C	-2.64	14.41	3.06	Mgs
AT03-20-IJ2A	-3.13	12.87	15.60	Tlc
AT03-20-IJ2B	-2.78	12.99	4.67	Mgs
AT03-20-IJ2C	-2.30	13.40	3.92	Mgs
AT03-20-IJ2D	-4.28	12.90	3.72	Mgs
AT03-20-IJ2D	-3.67	12.72	3.72	Mgs
AT03-20-IJ2E	-4.18	12.78	3.20	Mgs
AT03-20-IJ2E	-2.80	13.62	3.20	Mgs
AT03-20-IJ3A	-5.39	14.18	18.08	Tlc
AT03-20-IJ3B	-4.88	14.49	18.70	Tlc
AT03-20-IJ3C	-5.55	15.08	18.65	Tlc
AT03-20-IJ4A	-5.19	14.87	19.43	Tlc
AT03-20-IJ4B	-4.08	13.26	4.11	Mgs
AT03-20-IJ4C	-3.40	13.32	3.91	Mgs
AT03-20-IJ4D	-3.32	13.32	4.11	Mgs
AT03-21-EF1B	-1.26	12.06	3.04	Mgs
AT03-21-EF1D	-4.69	12.04	17.77	Tlc
AT03-21-EF1E	-4.68	12.40	18.10	Tlc
AT03-21-EF2D	-4.64	13.07	19.85	Tlc
AT03-44-12	-6.05	13.01	25.86	Qtz
AT03-44-27	-5.43	11.26	15.20	Tlc
AT03-44-40	-5.18	10.64	24.49	Tlc
AT03-44-6	-0.34	11.07	21.60	Tlc
AT03-51A	-4.16	15.40	6.11	Mgs
AT04-20B	-2.99	8.29	35.50	Qtz
AT04-20I	-5.36	11.15	27.27	Qtz
AT04-20N	-4.84	11.21	26.16	Qtz
AT04-25	-3.79	8.20	4.73	dyke
AT03-50	-3.31	8.30	9.21	dyke

Appendix D: Geochronologic Results

TABLE D1: Geochronology

Sample	E UTM (NAD 83)	N UTM (NAD 83)	System	Age	Analyst	Other
AT03-5B	573283	6603671	U-Pb zircon	150.7 +/- 0.4 Ma	Richard Friedman	Population B
AT03-28	573556	6605367	$^{40}Ar/^{39}Ar$ (Biotite)	84.0 +/- 0.6 Ma	Thomas Ulrich	Plateau Age
AT03-44-7	577809	6601758	$^{40}Ar/^{39}Ar$ (Cr-Muscovite)	174.4 +/- 1.4 Ma	Thomas Ulrich	Integrated Age
01AT-1-2	574013	6603080	$^{40}Ar/^{39}Ar$ (Cr-Muscovite)	128.0 +/- 1.9 Ma	Thomas Ulrich	Plateau Age
02AT-8-1	575800	6602042	$^{40}Ar/^{39}Ar$ (Cr-Muscovite)	172.7 +/- 2.0 Ma	Thomas Ulrich	Plateau Age

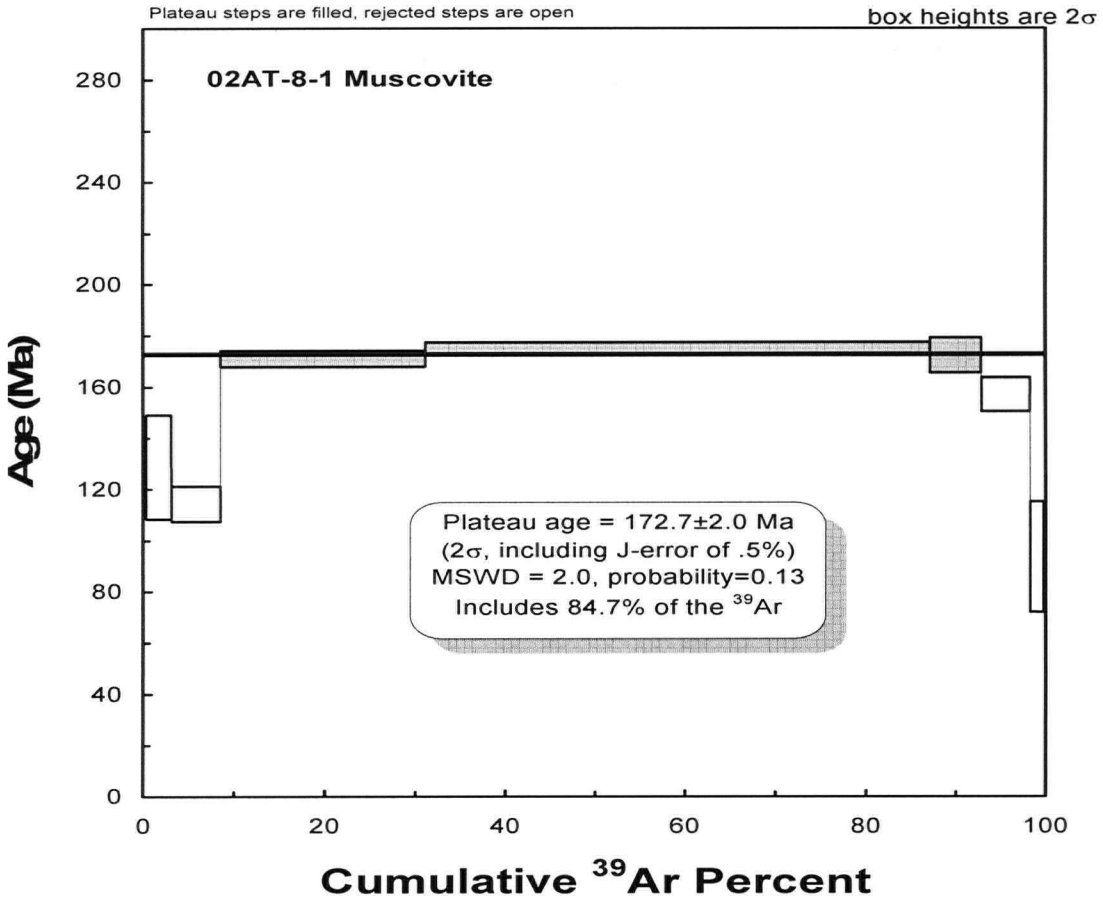

Isoplot Step-Heat Data				Isoplot Inverse Isochron Data				
Cum39Ar	Age	error	%39Ar	39/40	err	36/40	err	rho
0.26	65.83	93.27	0.26	0.010722	0.00068	0.00319	0.000281	0.253
2.97	127.91	20.5	2.71	0.029449	0.000404	0.002332	0.000174	0.022
8.38	113.3	6.81	5.41	0.055011	0.001006	0.00165	9.90E-05	0.097
31.17	170.3	3.13	22.79	0.051852	0.000532	0.000888	3.80E-05	0.107
87.29	174.24	2.45	56.12	0.065155	0.00093	0.000171	1.00E-05	0.016
93.06	171.76	6.84	5.77	0.052027	0.000739	0.000857	9.70E-05	0.053
98.52	156.29	6.77	5.46	0.056624	0.000689	0.000892	0.000108	0.008
100.01	92.38	21.74	1.49	0.037094	0.000632	0.002436	0.000228	0.027

Age = 172.7±2.0 Ma
(2s, including J-error of .5%)
MSWD = 2.0, probability = 0.13
84.7% of the 39Ar, steps 4 through 6

Model 1 Solution (±95%-conf.) on 3 points
Age = 174.9±3.0 Ma
40/36 intercept: 273±22
MSWD = 0.13, Probability = 0.71
(at J=.006959±.5% 2s)

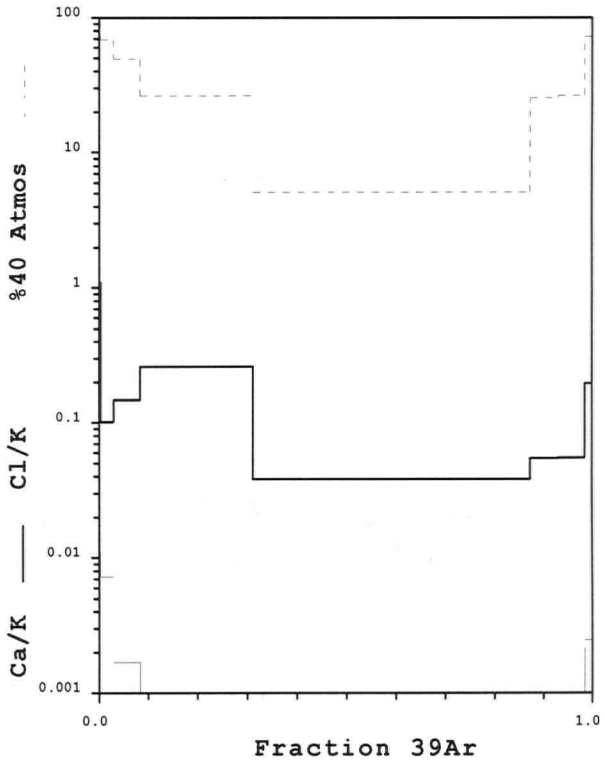

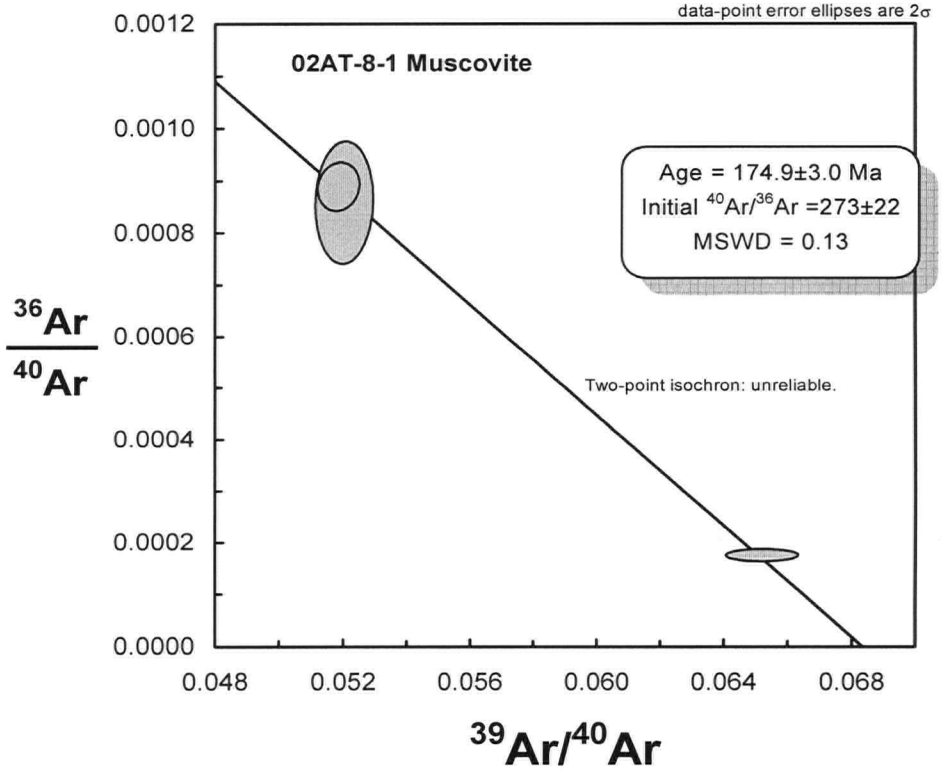

02AT-8-1 Muscovite

Laser Power(%)	Isotope Ratios 40Ar/39Ar	38Ar/39Ar	37Ar/39Ar	36Ar/39Ar	Ca/K	Cl/K	%40Ar atm	f 39Ar	40Ar*/39ArK	Age
2	100.643±0.058	0.142±0.282	0.794±0.090	0.306±0.088	1.095	0.011	94.24	0.26	5.340±7.705	65.83±93.27
2.3	34.890 0.014	0.063 0.141	0.079 0.080	0.082 0.073	0.101	0.007	68.85	2.71	10.558 1.753	127.91 20.50
2.5	18.690 0.018	0.028 0.173	0.056 0.061	0.031 0.059	0.147	0.002	48.68	5.41	9.314 0.578	113.30 6.81
2.8	19.377 0.010	0.020 0.060	0.051 0.049	0.018 0.041	0.259	0.001	26.2	22.79	14.225 0.274	170.30 3.13
3.1	15.378 0.014	0.012 0.063	0.009 0.076	0.003 0.055	0.038	-0.001	5.05	56.12	14.571 0.215	174.24 2.45
3.3	19.694 0.014	0.016 0.167	0.038 0.076	0.017 0.106	0.054	0	25.28	5.77	14.354 0.599	171.76 6.84
3.6	18.170 0.012	0.015 0.158	0.040 0.087	0.017 0.113	0.055	-0.001	26.32	5.46	13.004 0.588	156.29 6.77
4	28.800 0.017	0.042 0.144	0.146 0.074	0.069 0.089	0.195	0.002	71.91	1.49	7.550 1.823	92.38 21.74
Total/Average	17.658±0.004	0.017±0.020	0.056±0.008	0.013±0.013		0.003		100	14.463±0.078	166.26± 0.95
J =		0.006959±0.000030								

Volume 39ArK = 125.43

Integrated Date = 166.26±1.91

Volumes are 1E-13 cm3 NPT

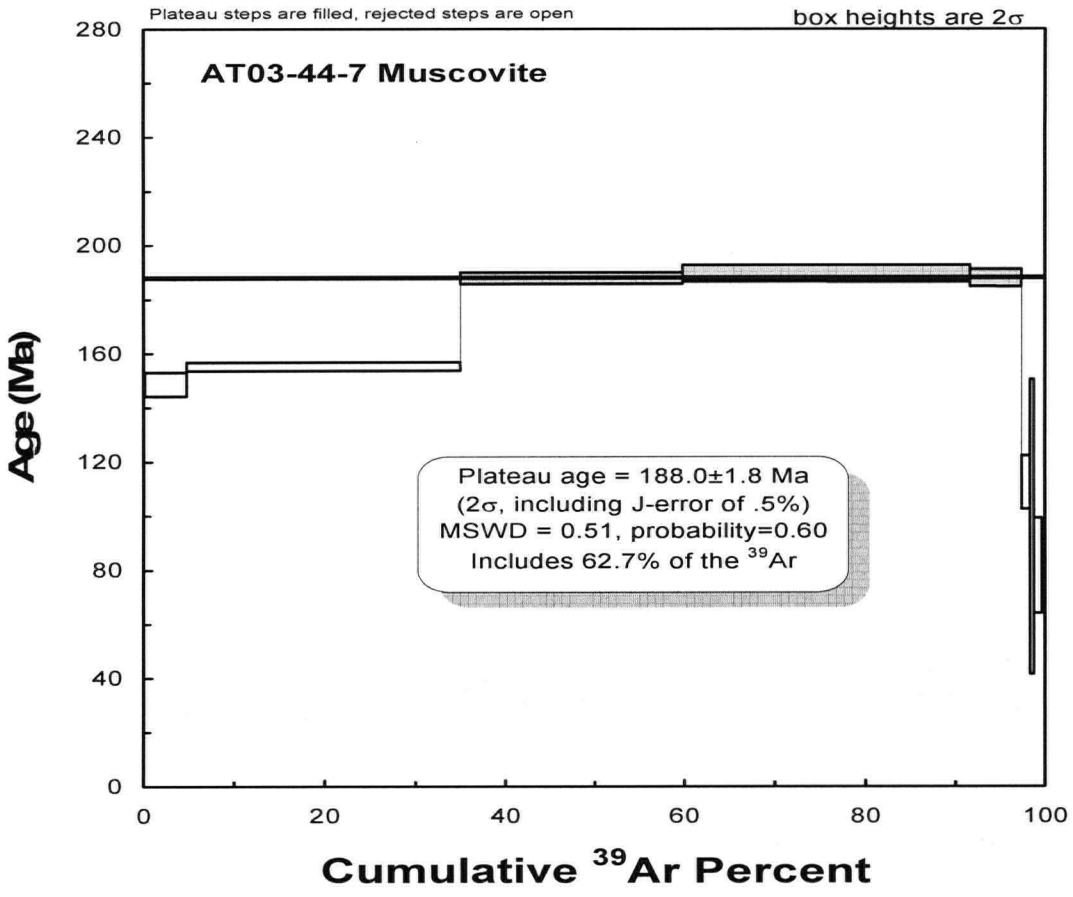

Isoplot Step-Heat Data				Isoplot Inverse Isochron Data				
Cum39Ar	Age	error	%39Ar	39/40	err	36/40	err	rho
4.65	148.29	4.49	4.65	0.041054	0.000473	0.001674	4.60E-05	0.204
35	154.76	1.43	30.35	0.05902	0.000282	0.000814	2.10E-05	0.01
60.01	187.6	2.16	25.01	0.054068	0.00054	0.000504	1.90E-05	0.008
91.89	189.36	3.15	31.88	0.057298	0.000948	0.000301	1.20E-05	0.132
97.71	187.42	3.23	5.82	0.054538	0.000794	0.000482	2.50E-05	0.141
98.73	111.82	9.85	1.02	0.042612	0.000719	0.002059	0.000115	0.102
99.11	95.25	54.62	0.38	0.027616	0.000786	0.002656	0.000427	0.055
99.98	80.96	17.65	0.87	0.023503	0.000384	0.00286	0.000116	0.154

Age = 188.0±1.8 Ma
(2s, including J-error of .5%)
MSWD = 0.51, probability = 0.60
62.7% of the 39Ar, steps 3 through 5

Model 1 Solution (±95%-conf.) on 3 points
Age = 191.8±7.6 Ma
40/36 intercept: 255±79
MSWD = 0.048, Probability = 0.83
(at J=.006961±.5% 2s)

Model 1 Solution (±95%-conf.) on 3 points
Age = 191.77 +7.25 -7.31
(MonteCarlo)
40/36 intercept: 255 +58.8 -109
MSWD = 0.048, Probability = 0.83
(at J=.006961±.5% 2s)

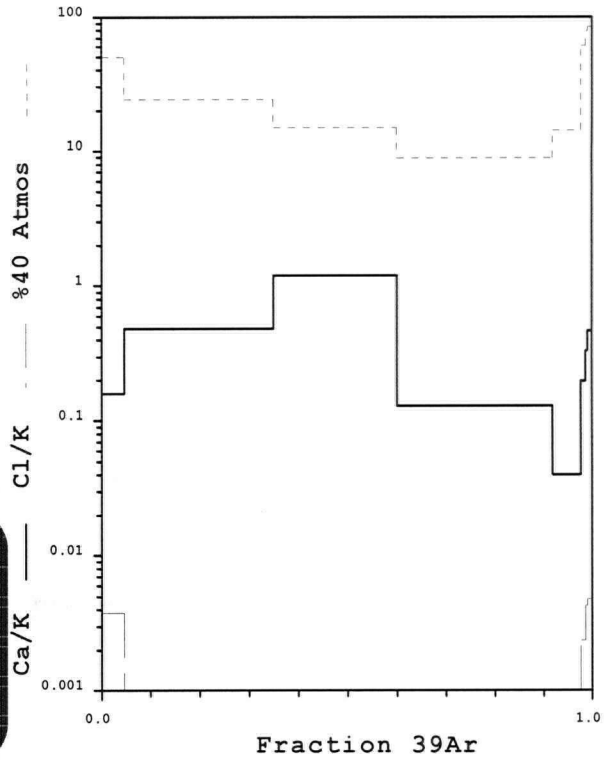

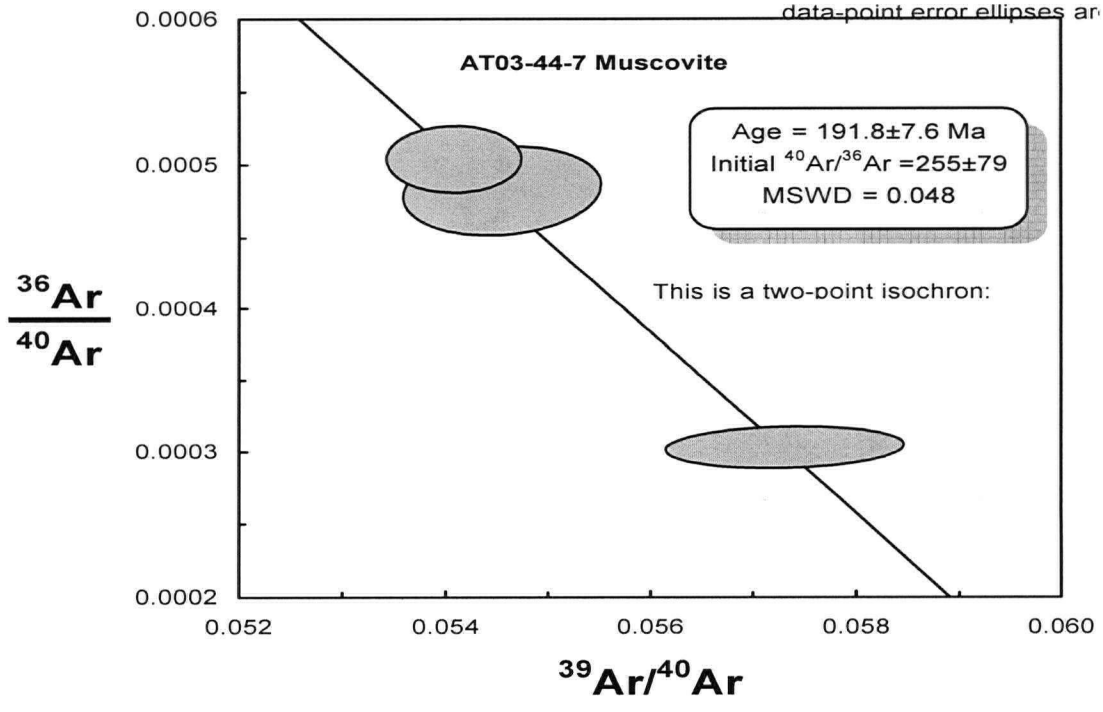

AT03-44-7 Laser Power(%)	Muscovite Isotope Ratios 40Ar/39Ar	38Ar/39Ar	37Ar/39Ar	36Ar/39Ar	Ca/K	Cl/K	%40Ar atm	f 39Ar	40Ar*/39ArK	Age
2	24.521±0.011	0.039±0.090	0.040±0.044	0.042±0.027	0.158	0.004	49.41	4.65	12.307±0.388	148.29± 4.49
2.2	16.947 0.005	0.020 0.027	0.084 0.023	0.014 0.025	0.484	0.001	24.01	30.35	12.868 0.124	154.76 1.43
2.3	18.495 0.010	0.014 0.073	0.202 0.019	0.010 0.038	1.184	-0.001	14.86	25.01	15.743 0.191	187.60 2.16
2.4	17.455 0.016	0.012 0.086	0.024 0.049	0.005 0.040	0.128	-0.001	8.89	31.88	15.898 0.279	189.36 3.15
2.5	18.481 0.014	0.013 0.153	0.017 0.072	0.009 0.050	0.04	-0.001	14.21	5.82	15.727 0.285	187.42 3.23
2.7	24.410 0.016	0.036 0.143	0.091 0.061	0.050 0.054	0.195	0.002	60.78	1.02	9.186 0.834	111.82 9.85
3	38.606 0.027	0.057 0.282	0.208 0.091	0.101 0.153	0.329	0.004	78.43	0.38	7.789 4.585	95.25 54.62
4	43.505 0.016	0.061 0.076	0.146 0.117	0.124 0.040	0.462	0.005	84.44	0.87	6.594 1.470	80.96 17.65
Total/Average	18.310±0.003	0.017±0.015	0.274±0.003	0.013±0.008		0.002		100	15.820±0.056	174.41± 0.72
J =		0.006961±0.000028								
Volume 39ArK =		356.26								
Integrated Date = Volumes are 1E-13 cm3 NPT		174.41±1.43								

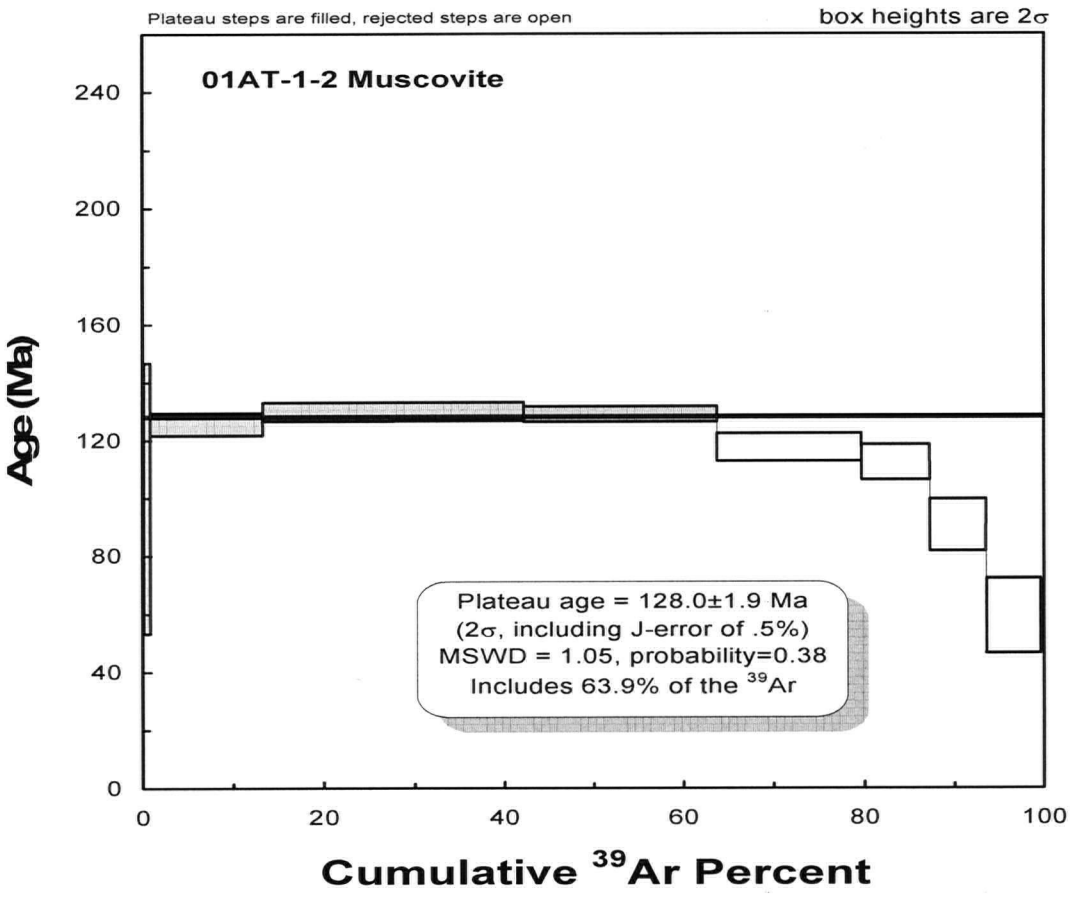

Isoplot Step-Heat Data				Isoplot Inverse Isochron Data					
Cum39Ar	Age	error		%39Ar	39/40	err	36/40	err	rho
0	ERR	ERR	step ignored	0	0.000576	0.013724	0.004574	0.005487	0.975
0.01	179.49	3712.78		0.01	0.00185	0.002464	0.00329	0.00135	0.298
0.04	684.21	1349.74		0.03	0.003468	0.002897	0.002606	0.001268	0.528
0.76	99.54	46.94		0.72	0.020385	0.000752	0.002822	0.00027	0.104
13.23	125.13	3.87		12.47	0.058432	0.000426	0.001343	6.30E-05	0.021
42.21	129.43	3.27		28.98	0.069483	0.001162	0.00087	4.00E-05	0.283
63.89	128.51	2.66		21.68	0.064922	0.000735	0.001052	3.80E-05	0.158
79.9	117	4.83		16.01	0.04971	0.000525	0.001764	6.40E-05	0.139
87.47	111.9	6.02		7.57	0.034311	0.000376	0.002316	5.70E-05	0.185
93.83	90.11	8.94		6.36	0.042402	0.000609	0.002328	0.000106	0.066
99.99	58.68	12.86		6.16	0.045527	0.001682	0.002652	0.000146	0.55

Age = 128.0±1.9 Ma
(2s, including J-error of .5%)
MSWD = 1.05, probability = 0.38
63.9% of the 39Ar, steps 1 through 6

Model 1 Solution (±95%-conf.) on 6 points
Age = 132.2±4.8 Ma
40/36 intercept: 274±23
MSWD = 0.68, Probability = 0.61
(at J=.006959±.5% 2s)

Model 1 Solution (±95%-conf.) on 6 points
Age = 132.15 +4.66 -5.19
(MonteCarlo)
40/36 intercept: 274.4 +22.4 -24.1
MSWD = 0.68, Probability = 0.61
(at J=.006959±.5% 2s)

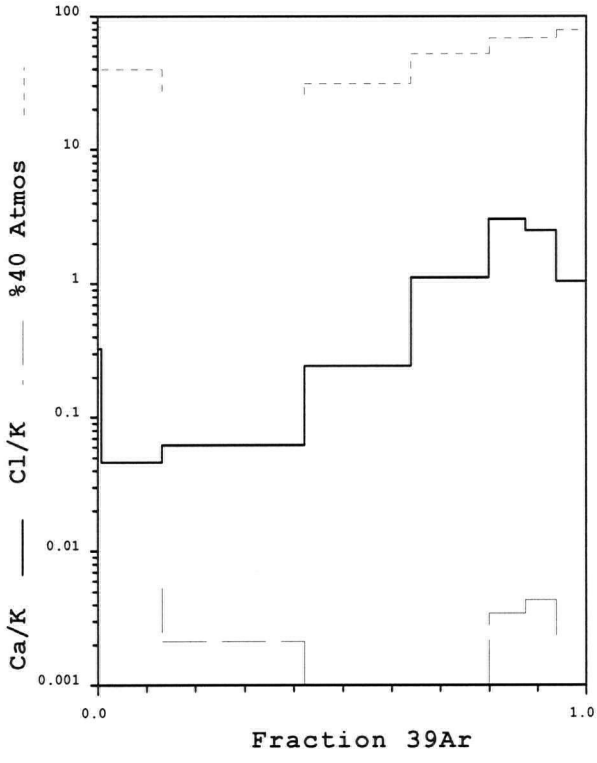

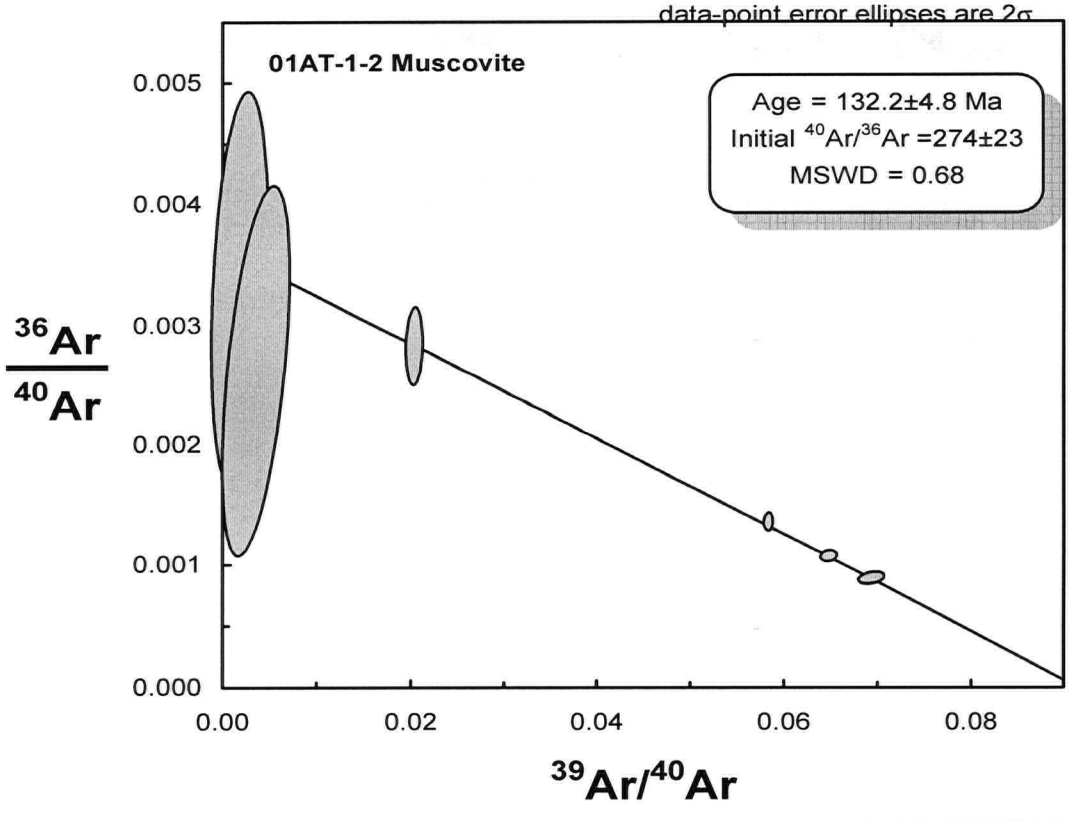

01AT-1-2 Muscovite

Laser Power(%)	Isotope Ratios 40Ar/39Ar	38Ar/39Ar	37Ar/39Ar	36Ar/39Ar	Ca/K	Cl/K	%40Ar atm	f 39Ar	40Ar*/39ArK		Age	
1.8	609.568±0.638	1.263±0.824	14.188±0.646	2.159±0.666	73.185	0.383	135.14	0	-610.328	±1039.634	----	± ----
2	415.394 0.540	1.139 0.716	8.678 0.541	1.147 0.616	19.716	0.271	97.21	0.01	15.039	326.806	179.49	3712.78
2.2	284.917 0.632	0.251 1.393	3.925 0.540	0.690 0.562	7.413	-0.003	77	0.03	66.301	157.159	684.21	1349.74
2.6	51.591 0.036	0.085 0.127	0.228 0.091	0.143 0.094	0.327	0.009	83.32	0.72	8.155	3.953	99.54	46.94
3	17.263 0.007	0.042 0.059	0.018 0.061	0.024 0.046	0.046	0.005	39.6	12.47	10.325	0.331	125.13	3.87
3.3	14.450 0.017	0.026 0.050	0.015 0.053	0.013 0.043	0.062	0.002	25.65	28.98	10.692	0.280	129.43	3.27
0.5	15.482 0.011	0.022 0.130	0.046 0.035	0.017 0.035	0.242	0.001	31.03	21.68	10.614	0.227	128.51	2.66
3.7	20.207 0.010	0.025 0.218	0.193 0.033	0.036 0.036	1.11	0.001	52.04	16.01	9.632	0.410	117.00	4.83
4	29.321 0.011	0.043 0.064	0.520 0.027	0.069 0.024	3.017	0.003	68.37	7.57	9.199	0.510	111.90	6.02
4.4	23.851 0.014	0.044 0.134	0.432 0.031	0.056 0.045	2.469	0.004	68.69	6.36	7.363	0.749	90.11	8.94
5	22.265 0.036	0.036 0.077	0.193 0.043	0.060 0.045	1.032	0.002	78.26	6.16	4.753	1.059	58.68	12.86
Total/Average	18.499±0.003	0.030±0.021	0.389±0.003	0.030±0.007		0.062		100	10.593±	0.083	118.44±	1.01
J =		0.006956±0.0000032										
Volume 39ArK =		167.42										
Integrated Date =		118.44±2.02										
Volumes are 1E-13 cm3												

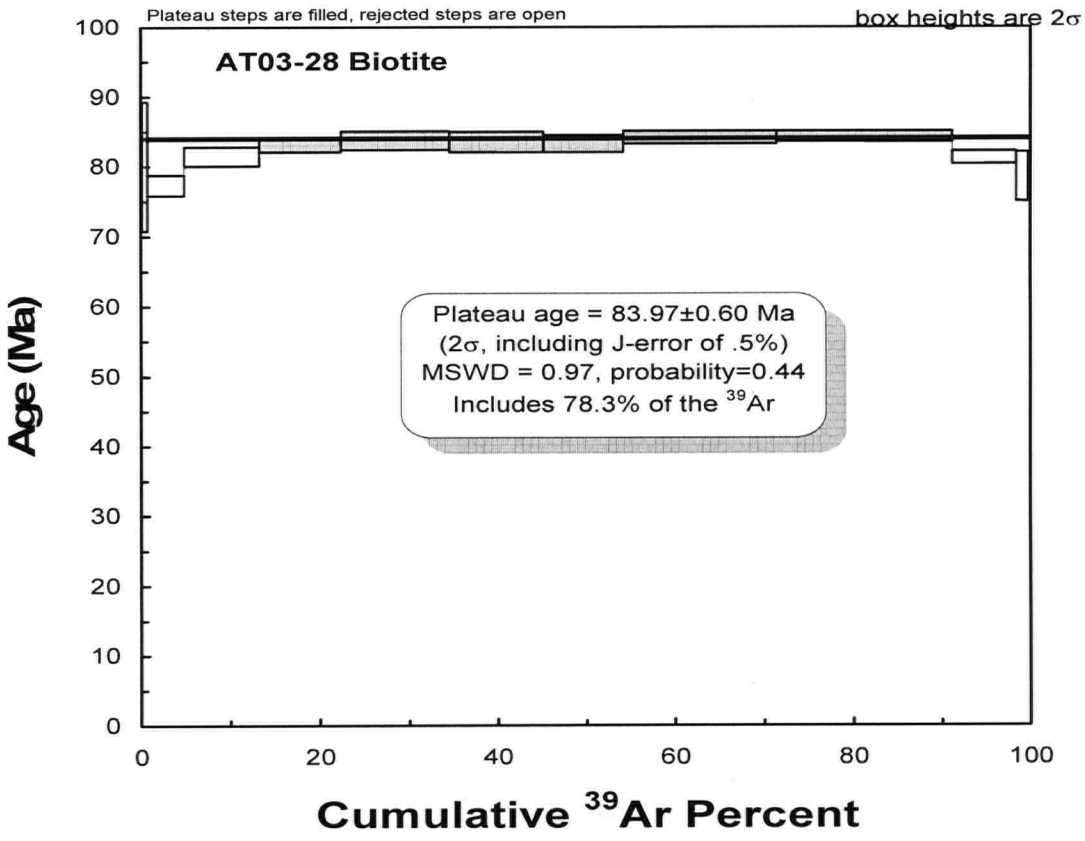

Isoplot Step-Heat Data			Isoplot Inverse Isochron Data					
Cum39Ar	Age	error	%39Ar	39/40	err	36/40	err	rho
0.69	80.24	9.32	0.69	0.06407	0.000901	0.001968	0.000167	0.008
4.69	77.44	1.48	4	0.114311	0.001412	0.000949	3.30E-05	0.108
13.15	81.61	1.38	8.46	0.13712	0.001916	0.000302	2.90E-05	0.05
22.31	83.3	0.97	9.16	0.140378	0.001313	0.000162	2.20E-05	0.028
34.46	83.97	1.33	12.15	0.140803	0.002149	0.000125	1.50E-05	0.053
45.21	83.68	1.53	10.75	0.140464	0.002462	0.000144	1.70E-05	0.06
54.31	83.46	1.26	9.1	0.140562	0.001917	0.000151	2.10E-05	0.044
71.55	84.29	0.95	17.24	0.141515	0.001591	9.60E-05	4.00E-06	0.17
91.42	84.5	0.82	19.87	0.141087	0.001325	9.80E-05	9.00E-06	0.061
98.72	81.46	0.98	7.3	0.142616	0.001659	0.000184	6.00E-06	0.24
100.01	78.66	3.52	1.29	0.123648	0.001942	0.000707	0.000113	0.045

Age = 83.97±0.60 Ma
(2s, including J-error of .5%)
MSWD = 0.97, probability = 0.44
78.3% of the 39Ar, steps 4 through 9

Model 2 Solution (±95%-conf.) on 11 points
Age = 83.0±1.6 Ma
40/36 intercept: 276±24
MSWD = 4.9, Probability = 0.000
(at J=.006963±.5% 2s)

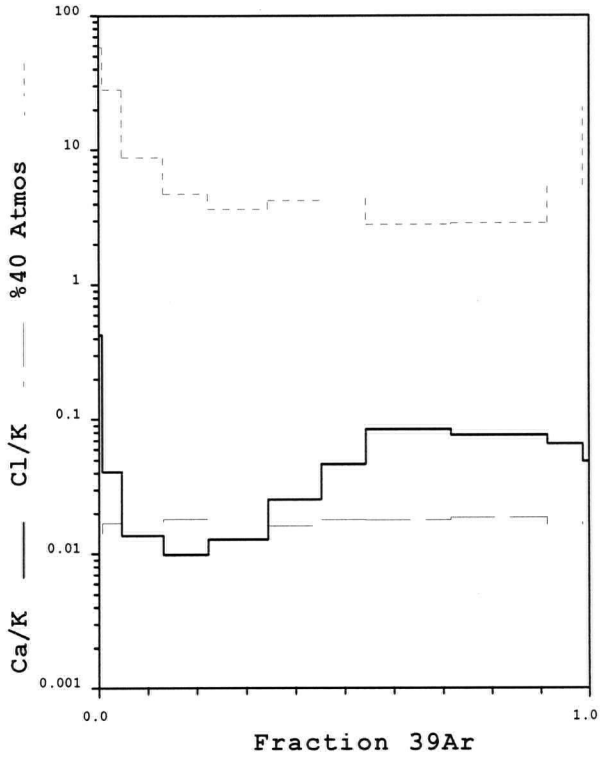

data-point error ellipses are 2σ

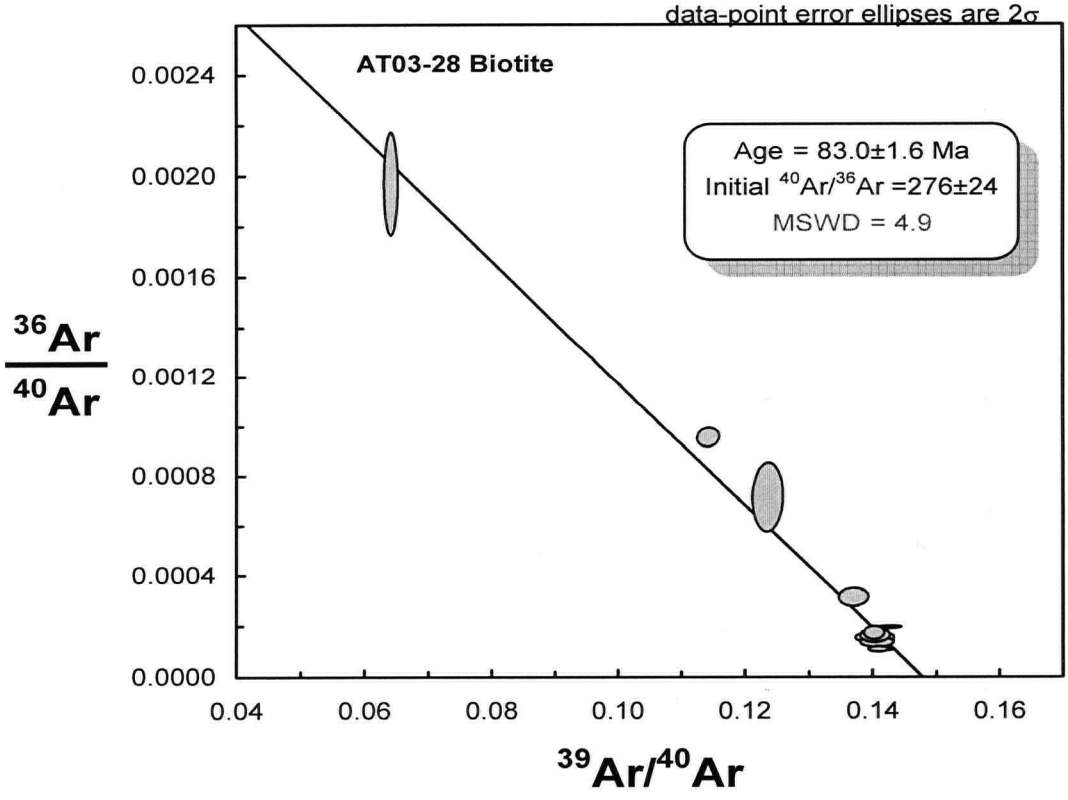

AT03-28 Biotite

Laser	Isotope Ratios									
Power(%)	40Ar/39Ar	38Ar/39Ar	37Ar/39Ar	36Ar/39Ar	Ca/K	Cl/K	%40Ar atm	f 39Ar	40Ar*/39ArK	Age
2	16.227±0.014	0.083±0.091	0.081±0.110	0.031±0.085	0.424	0.014	58.04	0.69	6.532±0.776	80.24±9.32
2.2	8.859 0.012	0.090 0.031	0.009 0.105	0.008 0.035	0.041	0.017	27.9	4	6.299 0.123	77.44 1.48
2.4	7.350 0.014	0.090 0.081	0.003 0.101	0.002 0.095	0.014	0.017	8.84	8.46	6.646 0.115	81.61 1.38
2.6	7.178 0.009	0.093 0.040	0.002 0.181	0.001 0.138	0.01	0.018	4.72	9.16	6.786 0.081	83.30 0.97
2.8	7.144 0.015	0.085 0.077	0.003 0.108	0.001 0.118	0.013	0.016	3.64	12.15	6.842 0.111	83.97 1.33
3	7.166 0.017	0.085 0.059	0.005 0.092	0.001 0.120	0.025	0.016	4.21	10.75	6.819 0.128	83.68 1.53
3.2	7.169 0.014	0.092 0.032	0.008 0.066	0.001 0.140	0.046	0.018	4.4	9.1	6.800 0.105	83.46 1.26
3.5	7.098 0.011	0.091 0.052	0.014 0.043	0.001 0.042	0.084	0.018	2.78	17.24	6.869 0.080	84.29 0.95
3.8	7.116 0.009	0.095 0.064	0.013 0.040	0.001 0.089	0.076	0.019	2.83	19.87	6.886 0.069	84.50 0.82
4	7.078 0.012	0.085 0.081	0.012 0.059	0.001 0.031	0.066	0.016	5.37	7.3	6.633 0.082	81.46 0.98
4.3	8.433 0.015	0.091 0.028	0.014 0.143	0.006 0.159	0.048	0.017	20.79	1.29	6.400 0.293	78.66 3.52
Total/Average	7.275±0.002	0.090±0.011	0.027±0.004	0.002±0.014		0.017		100	6.845±0.017	83.25±0.25
J =		0.006963±0.000026								
Volume 39ArK =		1089.19								
Integrated Date =		83.25±0.50								
Volumes are 1E-13 cm3 NPT										

$^{40}Ar/^{39}Ar$ DATING METHOD PROCEDURES

Each sample was crushed. Mineral separates were hand-picked, wrapped in aluminum foil and stacked in an irradiation capsule with similar-aged samples and neutron flux monitors (Fish Canyon Tuff sanidine, 28.02 Ma (Renne et al., 1998)).

The samples were irradiated on May 27 and 28, 2004 at the McMaster Nuclear Reactor in Hamilton, Ontario, for 56 MWH, with a neutron flux of approximately $3x10^{16}$ neutrons/cm^2. Analyses (n=54) of 18 neutron flux monitor positions produced errors of <0.5% in the J value.

The samples were analyzed on July 27 and 28, 2004, at the Noble Gas Laboratory, Pacific Centre for Isotopic and Geochemical Research, University of British Columbia, Vancouver, BC, Canada. The separates were step-heated at incrementally higher powers in the defocused beam of a 10W CO_2 laser (New Wave Research MIR10) until fused. The gas evolved from each step was analyzed by a VG5400 mass spectrometer equipped with an ion-counting electron multiplier. All measurements were corrected for total system blank, mass spectrometer sensitivity, mass discrimination, radioactive decay during and subsequent to irradiation, as well as interfering Ar from atmospheric contamination and the irradiation of Ca, Cl and K (Isotope production ratios: $(^{40}Ar/^{39}Ar)K = 0.0302$, $(^{37}Ar/^{39}Ar)Ca = 1416.4306$, $(^{36}Ar/^{39}Ar)Ca = 0.3952$, $Ca/K = 1.83(^{37}ArCa/^{39}ArK)$.). The plateau and correlation ages were calculated using Isoplot ver.3.09 (Ludwig, 2003). Errors are quoted at the 2-sigma (95% confidence) level and are propagated from all sources except mass spectrometer sensitivity and age of the flux monitor.

REFERENCES

Ludwig, K.R 2003. Isoplot 3.00 A Geochronological Toolkit for Microsoft Excel. Berkeley Geochronology Center, Special Publication No. 4

Renne, P.R., C.Swisher, C.C., III, Deino, A.L., Karner, D.B., Owens, T. and DePaolo, D.J., 1998. Intercalibration of standards, absolute ages and uncertainties in $^{40}Ar/^{39}Ar$ dating. Chemical Geology, 145(1-2): 117-152.

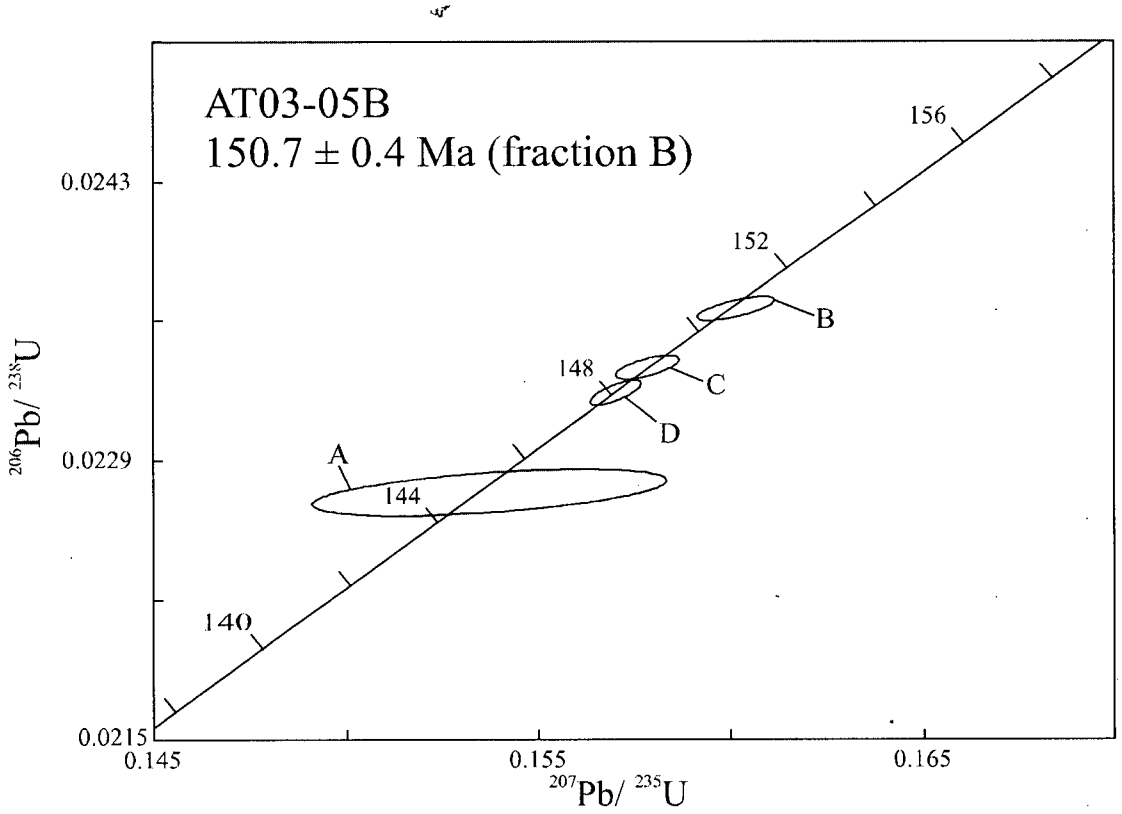

Sample AT03-05B, a quartz-K-feldspar porphyritic dacite, was dated using the U-Pb TIMS-ID technique in the Pacific Centre for Isotopic and Geochemistry Research at the University of British Columbia. Four abraded multi-grain zircon fractions were analyzed and all yielded statistically concordant results. As there is no evidence for inheritance, fraction B, which gives the oldest result of 150.7 ± 0.4 Ma ($^{206}Pb/^{238}U$ date, 2σ errors) is considered to be the best estimate for the age of the rock. Younger results from the other fractions are likely due to minor Pb loss.

U-Pb ID-TIMS analytical data for sample AT03-05B

Fraction[1]	Wt	U[2]	Pb*[3]	$^{206}Pb/^{204}Pb$[4]	Pb[5]	Th/U[6]	Isotopic ratios (±1σ,%)[7]			Apparent ages (±2σ,Ma)[7]	
	(mg)	(ppm)	(ppm)		(pg)		$^{206}Pb/^{238}U$	$^{207}Pb/^{235}U$	$^{207}Pb/^{206}Pb$	$^{206}Pb/^{238}U$	$^{207}Pb/^{235}U$
Interpreted age of 150.7 ± 0.4 Ma, based on oldest fraction B											
A 2	0.018	585	13	298	54	0.23	0.02274 (0.25)	0.1537 (1.5)	0.04903 (1.4)	144.9 (0.7)	145.2 (4.1)
B 4	0.022	469	11	991	16	0.27	0.02366 (0.13)	0.1601 (0.32)	0.04910 (0.24)	150.7 (0.4)	150.8 (0.9)
C 6	0.017	523	12	3241	4	0.26	0.02336 (0.13)	0.1579 (0.26)	0.04900 (0.20)	148.9 (0.4)	148.9 (0.7)
D 20	0.029	596	14	4580	6	0.31	0.02324 (0.14)	0.1570 (0.22)	0.04901 (0.14)	148.1 (0.4)	148.1 (0.6)

[1]Fraction identifier: single letter. Fraction ID is followed by number or approximate number of grains or fragments analysed. All analysed zircon grains were air abraded prior to dissolution and all were clear, pale pink prisms with aspect ratios of ~2-4.

[2] U blank correction of 1 pg ± 20%; U fractionation corrections were measured for each run with a double ^{233}U-^{235}U spike.

[3]Radiogenic Pb

[4]Measured ratio corrected for spike and Pb fractionation of 0.0037/amu ± 20% (Daly collector) which was determined by repeated analysis NBS Pb 981 standard throughout the course of this study.

[5]Total common Pb in analysis based on blank isotopic composition.

[6]Radiogenic Pb

[7]Blank and common Pb corrected; Pb blank corrections were 2-20 pg; U was 1 pg. Common Pb isotopic compositions are based on Stacey Kramers (1975) model Pb at the interpreted age of the rock or the $^{207}Pb/^{206}Pb$ age of the fraction.

U-Pb Geochronology: Analytical Techniques

Zircon was separated from rock samples using conventional crushing, grinding, and Wilfley table techniques, followed by final concentration using heavy liquids and magnetic separations. Mineral fractions for analysis were selected based on grain morphology, quality, size and magnetic susceptibility. All zircon fractions were abraded prior to dissolution to minimize the effects of post-crystallization Pb-loss, using the technique of Krogh (1982). All mineral separations, geochemical separations and mass spectrometry were done in the Pacific Centre for Isotopic and Geochemical Research in the Department of Earth and Ocean Sciences, University of British Columbia. Samples were dissolved in concentrated HF and HNO_3 in the presence of a mixed $^{233\text{-}235}U$-^{205}Pb tracer. Separation and purification of Pb and U employed ion exchange column techniques modified slightly from those described by Parrish et al. (1987). Pb and U were eluted separately and loaded together on a single Re filament using a phosphoric acid-silica gel emitter. Isotopic ratios were measured using a modified single collector VG-54R thermal ionization mass spectrometer equipped with a Daly photomultiplier. Measurements were done in peak-switching mode on the Daly detector. U and Pb total procedural blanks were in the range of 1 pg and 3-5 pg, respectively, during the course of this study. U fractionation was determined directly on individual runs using the $^{233\text{-}235}U$ tracer, and Pb isotopic ratios were corrected for a fractionation of 0.37%/amu for Faraday and Daly runs, respectively, based on replicate analyses of the NBS-981 Pb standard and the values recommended by Todt et al. (2000). All analytical errors were numerically propagated through the entire age calculation using the technique of Roddick (1987). Concordia intercept ages and associated errors were calculated using a modified version the the York-II regression model (wherein the York-II errors are multiplied by the MSWD) and the algorithm of Ludwig (1980). All errors are quoted at the 2σ level.

REFERENCES

Krogh, T.E, (1982): Improved accuracy of U-Pb zircon ages by the creation of more concordant systems using an air abrasion technique. Geochimica et Cosmochimica Acta, 46, p. 637-649.

Ludwig, K.R., (1980): Calculation of uncertainties of U-Pb isotopic data. Earth and Planetary Science Letters, 46, p. 212-220.

Parrish, R., Roddick, J.C., Loveridge, W.D., and Sullivan, R.W. (1987): Uranium-lead analytical techniques at the geochronology laboratory, Geological Survey of Canada. *In* Radiogenic Age and Isotopic Studies, Report 1, Geological Survey of Canada, Paper 87-2, p. 3-7.

Roddick, J.C. (1987): Generalized numerical error analysis with application to geochronology and thermodynamics. Geochimica et Cosmochimica Acta, 51, p. 2129-2135.

Stacey, J.S. and Kramers, J.D. (1975): Approximation of terrestrial lead isotope evolution by a two-stage model: Earth and Planetary Science Letters, v. 26, p. 207-221.

Appendix E: Miscellaneous Calculations and Procedures

E.1: GEOCHEMICAL POWDER PREPARATION

Accurate and precise geochemical analysis of the suite of rocks is very important for determining chemical alteration. For this reason, contamination during sample preparation must be kept to a minimum. The procedures followed for preparation of powders submitted for geochemical analysis are outlined below.

1. All weathered surfaces were cut off with a diamond rock saw generally resulting in a cubic shape.
2. The cut samples were then polished with 240 mesh-sized Al_2O_3 to remove any metal that was abraded from the rock saw during step 1.
3. Samples were then washed with distilled water in a sonic bath for 3-5 minutes to remove any Al_2O_3 and other microscopic contaminants from step 2.
4. The samples were then crushed in a rock jaw crusher. To minimize contamination during this step, the crusher was first cleaned with water and a wire brush to remove any rock, or other material (e.g. coal) from previous uses. Blank samples of the same rock type as the samples to be crushed were then sent through the machine in order to decrease the chance of contamination from other lithological types and to reduce the tendency for the metal jaws of the crusher to abrade onto the sample during crushing. The crusher and tray used to catch the sample was then blown out with compressed air before the next sample was sent through. Samples of similar type (degree of alteration) were crushed together again to reduce contamination. When samples of different alteration or type needed to be crushed, the jaws of the crusher were cleaned dry with a wire brush.
5. Before powdering the samples, the ring mill was cleaned with clean rinsing organic soap, rinsed with tap water then acetone, and finally dried with compressed air. This method of washing was also done between all samples. As with the jaw crushing step, a blank sample of similar composition as the samples powdered was powdered to minimize contamination from other lithologies during previous powdering sessions.

6. The crushed samples were placed on a blank piece of white paper and manually picked through as to obtain pieces which fit in the ring mill and contain no vein material which commonly remain in cut and polished samples. Generally the largest pieces were used. If the sample was coarse grained enough to warrant, more than one crushing step was done to increase the representativeness of the sample. During this step the crushed samples were also visually inspected to remove any pieces with abraded metal from the crusher. Metal usually abraded only the smooth cut and polished sides vs. the jagged sides produced during crushing. Abraded metal was easily identifiable.
7. The ring mill, with enclosed sample, was then placed in the shatter box and ran for 1.5 to 3 minutes until adequately powdered. This usually was when a persistent and distinctive vibrating sound was produced from the ring mill with in the shatter box.
8. The powdered sample was then homogenized using a quartering method for 3 to 5 minutes before submission to the geochemical laboratory.

Bulk geochemical samples were crushed and powdered in a tungsten carbide shatterbox. Powders were sent to the Geochemical Laboratories at McGill University, Montreal, PQ for bulk geochemical analysis by X-ray fluorescence. Results are included in the table. Samples were analyzed for major, minor and trace elements, CO_2 content by induction furnace, and total volatile content by loss on ignition (L.O.I.). Standard errors used in calculations were determined from 13 blind replicate analysis of one sample (AT03-20-PC2, Appendix C).

E.2: ERROR DETERMINATION

Knowledge of the uncertainty for each chemical species was determined by sending blind replicates of AT03-PC2 for analysis. In all, 13 blind analyses were completed (Table C-2, Appendix C); these were submitted 3 to 4 at one time accompanying other samples. The reproducibility during the same session is related to the ability of the laboratory to reproduce the same result from the same sample and the ability to adequately homogenize the sample before submitting replicates. The reproducibility

over time is a test of the ability of the laboratory to reproduce the same result for the same sample over time.

Of notable difference between the two groups are the L.O.I. and CO_2 analyses. Group 1 is consistently about 0.1 wt% L.O.I. and CO_2 below those of group 2. This is likely due to slight differences in the procedure to drive-off moisture between the two groups. Group 1 had 0.1 wt% more loosely bound CO_2 driven off than group 2. For example, 0.1 wt% less CO_2 will result in 0.1 wt% less L.O.I. as L.O.I. contains CO_2. Since both L.O.I. and CO_2 determinations are independently measured and because both L.O.I and CO_2 are consistently about 0.1 wt% lower in group 1 than in group 2, the difference must be because some CO_2 was lost in group 1 that was not lost in group 2. The other major detectible difference is in the Na_2O analyses between the two groups. Clearly there is a difference; however it is not currently known what the difference is attributed to. The standard error for Na_2O was determined only with those measurements which are above detection.

E.3: MAGNETIC SUSCEPTIBILITY MEASUREMENTS OF HAND SAMPLES VS OUTCROP MEASUREMENTS

Magnetic susceptibility measurements of hand samples were compared to the measurements made in the field at the location of each sample (Fig. E.1). The KT-9 Kappameter magnetic susceptibility meter allows for the storage and averaging of 10 measurements. The reported magnetic susceptibility for all samples and for most field locations is the average of 10 measurements made from the sample or taken over the outcrop. The highest and lowest measurements were also reported. Often only the range of magnetic susceptibility was recorded for field locations. In this case the median, generally a good approximation, was used as the magnetic susceptibility. A comparison of hand sample and field measurements, shown in Figure B2, indicates that hand sample measurements appear to be systematically lower than the field measurements for the sample. This brings into question the validity of applying algorithms relating hand sample magnetic susceptibility to alteration vs. field measurements. Up to five different KT-9 Kappameter magnetic susceptibility meters have been used throughout this study. Though unlikely, the systematic differences in magnetic susceptibility may be due to

machine calibration used between the instruments. A more likely explanation is the field measurements were not made on the exact rocks collected for hand sample measurement. Alteration in outcrop can be highly variable with a very large spread in measured magnetic susceptibility. When taking magnetic susceptibility measurements in the field, one looks for the smoothest and least weathered surfaces to take the measurements. Unfortunately these samples are near impossible to sample without a cement saw. Also, the more serpentinized an outcrop of harzburgite is, and therefore the higher the magnetic susceptibility, the harder the rock is to sample due increased fractures and alteration. Geochemical analysis can only be performed on the collected hand samples. For this reason the measurements reported from the hand samples are used as the magnetic susceptibility for any analysis involving the hand sample.

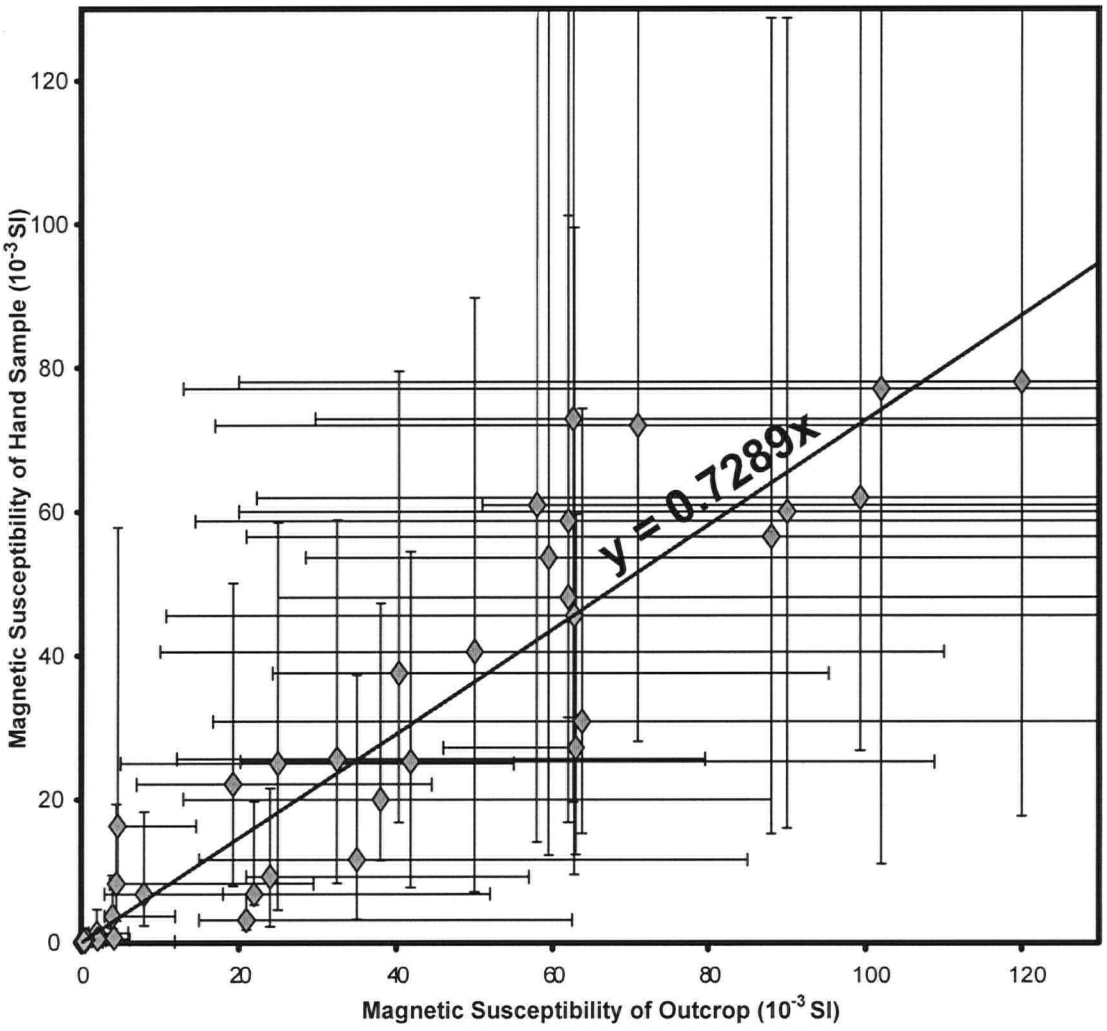

Figure E.1: Magnetic susceptibility of hand samples vs. the outcrops the hand samples were acquired from.

STABLE ISOTOPE ANALYTICAL TECHNIQUES

Carbonate samples are analyzed using the Gas Bench and a Finnigan Delta Pus XL mass spectrometer. CO_2 is extracted using continuous flow from the Gas Bench as follows. Between 150 and 300μg of crushed sample is placed in the bottom of a clean exetainer, which is sealed with a piercable septum. The exetainers flushed with Helium for 5 minutes to displace air, then 7 drops of 99% phosphoric acid are introduced using a syringe through the septum. The acid and sample are left to equilibrate at 72°C for an hour, then the CO_2 gas produced is sampled by a sampling needle attached to the gas bench. The sample run consists of 5 aliquots of reference CO_2 gas of known composition, 10 aliquots of sample gas, and one final aliquot of reference gas. In-house rock standards are distributed throughout the samples in the gas bench after every eight samples.

Raw $d^{18}O/d^{16}O$ ratios have been corrected for fractionation between phosphoric acid and calcite (from Das Sharma *et al.*, 2002) then samples that are not calcite are corrected for the appropriate acid-mineral fractionation.

The raw ratios are adjusted for machine fractionation using a factor calculated from repeated analyses of internal UBC standards BN 13, BN 83-2, H6M, which are calibrated against two international standards, NBS 18 and NBS 19.

The final results $\delta^{13}C_{(VPDB)}$ and $\delta^{18}O_{(VSMOW)}$ are corrected to VPBD and VSMOW based on an average of multiple analyses of NBS 18 and 19. The standard deviation on the average analyses of NBS 18 and 19 is > 0.1 per mil at the 2 sigma level for both $\delta^{13}C_{(VPDB)}$ and $\delta^{18}O_{(VSMOW)}$.

REFERENCES

Das Sharma, S., Patil, D.J. and Gopalan, K. (2002): Temperature dependence of oxygen isotope fractionation of CO_2 from magnesite-phosphoric acid reaction. *Geochimica et Cosmochimica Acta*, v. 66, n. 4, pp. 589–593.

Appendix F: Sample Locations

Table F1: Sample locations (NAD 83)

Sample	Eastings	Northings	Geochemistry	$^{40}Ar/^{39}Ar$	U-Pb	^{13}C	^{18}O	Au Assay
01AT-10-1	577844	6601933	x					
01AT-10-2	577844	6601933	x					
01AT-11-1	577860	6601820	x			x	x	
01AT-11-2	577860	6601820	x			x	x	
01AT-1-2	574013	6603080	x	x		x	x	
01AT-13-1	577782	6602226	x					
01AT-13-2	577782	6602226	x			x	x	
01AT-1-5	574013	6603080	x			x	x	
01AT-1-6	574013	6603080	x			x	x	
01AT-1-7	574013	6603080	x			x	x	
01AT-1-8	574013	6603080	x			x	x	
01AT-1-9	574013	6603080	x			x	x	
01AT-2-2	573954	6603058	x					
01AT-3-1	573866	6603293	x					
01AT-4-1	573552	6603542	x			x	x	x
01AT-5-2	573278	6603742	x			x	x	x
01AT-5-3	573278	6603742				x	x	
01AT-5-4	573278	6603742	x			x	x	
01AT-6-1	575352	6604258	x			x	x	
01AT-6-3	575352	6604258	x			x	x	
01AT-7-1	574956	6604734	x			x	x	x
01AT-7-3	574956	6604734	x			x	x	
01AT-8-1	575800	6602042	x					
01AT-9-1	575856	6602056	x					
01AT-9-2	575856	6602056	x			x	x	
02AT-8-1	575800	6602042		x				
AT03 - 28	573556	6605367	x					
AT03-20-CD1A	575884	6602100	x			x	x	
AT03-20-CD1B	575884	6602100	x			x	x	x
AT03-20-CD1C	575884	6602100	x			x	x	x
AT03-20-CD2A	575884	6602100	x			x	x	
AT03-20-CD2B	575884	6602100	x			x	x	
AT03-20-CD2C	575884	6602100	x			x	x	
AT03-20-CD2D	575884	6602100	x			x	x	
AT03-20-CD3A	575884	6602100	x			x	x	
AT03-20-CD3B	575884	6602100	x			x	x	x
AT03-20-CD3C	575884	6602100	x			x	x	x
AT03-20-CD3D	575884	6602100	x			x	x	
AT03-20-CD4A	575884	6602100	x			x	x	
AT03-20-CD4B	575884	6602100	x			x	x	
AT03-20-CD4C	575884	6602100	x			x	x	
AT03-20-CD4D	575884	6602100	x			x	x	
AT03-20-DH1	575884	6602100				x	x	
AT03-20-DH2	575884	6602100				x	x	
AT03-20-DH3	575884	6602100				x	x	
AT03-20-ij1a	575884	6602100	x			x	x	
AT03-20-ij1b	575884	6602100	x			x	x	
AT03-20-ij1c	575884	6602100	x			x	x	x
AT03-20-ij2a	575884	6602100	x			x	x	x

Table F1: Sample locations (NAD 83)

Sample	Eastings	Northings	Geochemistry	$^{40}Ar/^{39}Ar$	U-Pb	^{13}C	^{18}O	Au Assay
AT03-20-ij2b	575884	6602100	x			x	x	
AT03-20-ij2c	575884	6602100	x			x	x	
AT03-20-ij2d	575884	6602100	x			x	x	x
AT03-20-ij2e	575884	6602100	x			x	x	
AT03-20-ij3a	575884	6602100	x			x	x	x
AT03-20-ij3b	575884	6602100	x			x	x	x
AT03-20-ij3c	575884	6602100	x			x	x	
AT03-20-lj4a	575884	6602100	x			x	x	
AT03-20-lj4b	575884	6602100	x			x	x	
AT03-20-ij4c	575884	6602100	x			x	x	
AT03-20-ij4d	575884	6602100	x			x	x	
AT03-20-PA-1A	575884	6602100	x					
AT03-20-PA-2B	575884	6602100	x					
AT03-20-PB-2B	575884	6602100	x					
AT03-20-PB-3B	575884	6602100	x					
AT03-20-PC-1A	575884	6602100	x					
AT03-20-PC2	575884	6602100	x					x
AT03-20-PC-3A	575884	6602100	x					
AT03-20-PD-1A	575884	6602100	x					
AT03-20-PD-1B	575884	6602100	x					
AT03-20-PD-2A	575884	6602100	x					
AT03-20-PD-2B	575884	6602100	x					
AT03-20-PD-3A	575884	6602100	x					
AT03-20-PE-1A	575884	6602100	x					
AT03-20-PE-3A	575884	6602100	x					x
AT03-20-PE-3B	575884	6602100	x					
AT03-21-EF1-A	575742	6602243	x					
AT03-21-EF1-B	575742	6602243	x			x	x	x
AT03-21-EF1-C	575742	6602243	x					
AT03-21-EF1-D	575742	6602243	x			x	x	x
AT03-21-EF1-E	575742	6602243	x			x	x	x
AT03-21-EF1-F	575742	6602243	x					
AT03-21-EF2-A	575742	6602243	x					
AT03-21-EF2-B	575742	6602243	x					
AT03-21-EF2-C	575742	6602243	x					
AT03-21-EF2-D	575742	6602243	x			x	x	x
AT03-21-EF2-E	575742	6602243	x					
AT03-21-EF2-F	575742	6602243	x					
AT03-21-Ma	575742	6602243	x					x
AT03-21-PC-A	575742	6602243	x					
AT03-21-PC-B	575742	6602243	x					
AT03-21-PF-A	575742	6602243	x					
AT03-21-PF-B	575742	6602243	x					
AT03-21-PF-C	575742	6602243	x					
AT03-21-PG-A	575742	6602243	x					
AT03-21-PG-B	575742	6602243	x					
AT03-21-PH-B	575742	6602243	x					
AT03-21-PK-A	575742	6602243	x					
AT03-21-PK-B	575742	6602243	x					

Table F1: Sample locations (NAD 83)

Sample	Eastings	Northings	Geochemistry	$^{40}Ar/^{39}Ar$	U-Pb	^{13}C	^{18}O	Au Assay
AT03-24	577613	6602505	x					
AT03-28	573556	6605367		x				
AT03-42	577758	6601257	x					x
AT03-44-1	577809	6601758	x					
AT03-44-10	577809	6601758	x					
AT03-44-11	577809	6601758						
AT03-44-12	577809	6601758	x			x	x	x
AT03-44-13	577809	6601758	x					
AT03-44-14	577809	6601758	x					
AT03-44-15	577809	6601758	x					x
AT03-44-16	577809	6601758	x					
AT03-44-17	577809	6601758	x					
AT03-44-18	577809	6601758	x					
AT03-44-19	577809	6601758	x					x
AT03-44-2	577809	6601758	x					
AT03-44-20	577809	6601758	x					
AT03-44-21	577809	6601758	x					
AT03-44-22	577809	6601758	x					x
AT03-44-23	577809	6601758	x					x
AT03-44-24	577809	6601758	x					
AT03-44-25	577809	6601758	x					
AT03-44-26	577809	6601758	x					
AT03-44-27	577809	6601758	x			x	x	x
AT03-44-28	577809	6601758	x					
AT03-44-29	577809	6601758	x					
AT03-44-3	577809	6601758	x					
AT03-44-30	577809	6601758	x					
AT03-44-31	577809	6601758						
AT03-44-32	577809	6601758						
AT03-44-33	577809	6601758	x					
AT03-44-34	577809	6601758	x					
AT03-44-35	577809	6601758	x					
AT03-44-36	577809	6601758	x					
AT03-44-37	577809	6601758	x					x
AT03-44-38	577809	6601758	x					
AT03-44-39	577809	6601758	x					
AT03-44-4	577809	6601758	x					
AT03-44-40	577809	6601758	x			x	x	x
AT03-44-5	577809	6601758	x					
AT03-44-6	577809	6601758	x			x	x	
AT03-44-7	577809	6601758	x	x				
AT03-44-8	577809	6601758	x					
AT03-44-9	577809	6601758	x					
AT03-49	576020	6601915	x					
AT03-4a-b	573293	6603629	x					
AT03-50	576219	6602005	x			x	x	
AT03-51-A	575925	6602101	x			x	x	x
AT03-51-B	575925	6602101	x					
AT03-51-C	575906	6602113	x					

Table F1: Sample locations (NAD 83)

Sample	Eastings	Northings	Geochemistry	$^{40}Ar/^{39}Ar$	U-Pb	^{13}C	^{18}O	Au Assay
AT03-51-D	575906	6602113	x					x
AT03-51-E	575891	6602083	x					
AT03-51-F	575891	6602083	x					
AT03-5a-b	573283	6603671	x		x			
AT04 - 10	576330	6604222	x					
AT04 - 11	575516	6603708	x					
AT04 - 12	577894	6601135						
AT04 - 13	578966	6601258	x					
AT04 - 14	577809	6601758						
AT04 - 16	574004	6603443	x					
AT04 - 2	577809	6601758	x					
AT04 - 20 - A	573459	6603577	x					
AT04 - 20 - B	573459	6603577	x			x	x	
AT04 - 20 - C	573459	6603577	x					
AT04 - 20 - D	573459	6603577	x					
AT04 - 20 - E	573459	6603577	x					
AT04 - 20 - F	573459	6603577	x					
AT04 - 20 - H	573459	6603577	x					
AT04 - 20 - I	573459	6603577	x			x	x	x
AT04 - 20 - J	573459	6603577	x					
AT04 - 20 - K	573459	6603577	x					
AT04 - 20 - L	573459	6603577	x					
AT04 - 20 - M	573459	6603577	x					
AT04 - 20 - N	573459	6603577	x			x	x	x
AT04 - 21 - B	575660	6602200	x					
AT04 - 23	575422	6603169	x					
AT04 - 25	574050	6603084	x			x	x	
AT04 - 3	577700	6601269	x					
AT04 - 4	577817	6601847	x					
AT04 - 5	577572	6602483	x					
AT04 - 6 - B	576671	6602340	x					
AT04 - 7 - B	574838	6608489	x					
AT04 - 8 - B	574884	6608579	x					
AT04 - 9	574310	6604486	x					